



Directed self-assembly of block copolymers on chemically nano-patterned surfaces

Memòria presentada per optar al títol de Doctor en Ciència de Materials

Departament de Química

Universitat Autònoma de Barcelona

Laura Evangelio Araujo

DIRECTORS

Francesc Pérez Murano

Institut de Microelectrònica de Barcelona (IMB-CNM, CSIC)

Jordi Fraxedas Calduch

Institut Català de Nanociència i Nanotecnologia (ICN2)

TUTOR

Joan Bausells Roigé

Institut de Microelectrònica de Barcelona (IMB-CNM, CSIC)

2017

Memòria presentada per aspirar al Grau de Doctor per **Laura Evangelio Araujo**

Vist i plau dels directors **Prof. Francesc Pérez Murano** i **Dr. Jordi Fraxedas Calduch**, i tutor **Prof. Joan Bausells Roigé**

Director

Director

Tutor

Francesc Pérez Murano

Jordi Fraxedas Calduch

Joan Bausells Roigé

Autor

Laura Evangelio Araujo

Bellaterra, 31 de març de 2017

*“Caminante son tus huellas, el camino y nada más;
Caminante no hay camino, se hace camino al andar.
Al andar se hace el camino, y al volver la vista atrás,
se ve la senda que nunca se ha de volver a pisar.
Caminante no hay camino, sino estelas en la mar”*

Antonio Machado (1875-1939)

Acknowledgements

El meu camí durant la realització de la tesi, no m'ha suposat únicament un canvi professional i científic molt enriquidor, sinó que també m'ha permès conèixer gent que ha marcat d'alguna manera el camí que vaig decidir iniciar fa uns anys. És per això que vull dedicar-vos unes línies d'aquesta memòria.

En primer lloc, m'agradaria agrair els meus directors de tesi, Prof. Francesc Pérez Murano i Dr. Jordi Fraxedas Calduch, per haver-me donat l'oportunitat de començar la meva tesi, i haver pogut conèixer el fabulós i curiós món de la nanotecnologia. A en Francesc, m'agradaria agrair-li el seu esforç, suport, consells i dedicació durant tot aquest període, així com la gran quantitat de coses que he anat aprenent d'ell. Gràcies també, Jordi, per haver-me ensenyat a valorar els “petits” detalls de les coses, però sobretot per la teva dedicació en la feina.

M'agradaria agrair també a tots els membres del grup NanoNEMS, no únicament per les nostres discussions científiques, sinó per tots els nostres bons moments. En primer lloc, agrair el suport del meu tutor de tesi Prof. Joan Bausells Roigé. En segon lloc, gràcies als que ja esteu fent els vostres camins fora, però que quan vaig començar em van ajudar a començar a construir el que avui acabo: Marc, Jordi, Nerea, Giordano, Ygezu, Sophie i Nil. I en especial als meus companys de “cafè, ciència i dinar dels divendres”: Olga, Gemma, Albert, Matteo, Esteve, Steven, Angelos i Federico.

No me olvido de vosotras, Ana y Marta, que sé que una ya lo estará echando de menos. Gracias, Ani, por mostrarme siempre tu amistad, apoyo, fuerza y tus consejos. Empezamos esto juntas, y nos falta muy poquito para terminarlo. Y te agradezco a ti en especial Marti, porque no sólo me enseñaste y dejaste que volara en este camino de copolímeros de bloque, sino que también me has ayudado y aconsejado en el camino de la ciencia y la amistad, y eso se merece más que un *Science* o un *Nature*!

En especial agraïment també a la Rosa Villa i el seu grup, perquè em van acollir al vostre despatx quan vaig començar fins ara: Ana, Eli, Xavi, Jose, Anton i Gemma.

M'agradaria agrair també totes les persones que han fet possible tota la meva feina dins de Sala Blanca i a administració, perquè sempre han estat disposats a ajudar-me quan ho he necessitat; per tant, part d'aquesta feina també és vostra. En especial al nanocientífics del Nanolab: Liber, Xevi, Ana i Albert, per ensenyar-me i donar-me suport sempre que ho he necessitat. També moltes gràcies a tota la resta d'àrees de Sala Blanca i administració, perquè sense vosaltres el nostre treball no seria possible: Marta Gerbolés, Roser, Carles, Elena, Marta Duch, Jose, Javi, Josep M^a, Nuria, Annabel, Anna, Nieves, Elisenda...

Tampoco quiero dejar de lado a mi grupo de “gordis”, porque si no me van a pedir un pastel como recompensa (aunque sé que me lo pediréis igual...). Muchas gracias a todos, por todos los buenos momentos que hemos pasado en nuestros momentos de desconexión al medio día, y las grandes vivencias que hemos pasado: Sara, Liber, Maria, Sergi, Jordi i Carolina. Sarita, cuantas cosas hemos aprendido juntas eh? Gracias por nuestras largas conversaciones de soporte mañaneras y por nuestras aventuras en el coche ;)

I also want to acknowledge all the project partners I have had the opportunity to work with. Especially all the partners from CoLiSA and PLACYD projects, for having guided and encouraged me in every step of my thesis way: partners from Göttingen, Erlangen, Grenoble, Bordeaux, Athems and Arkema’s team. I have learned a lot from all of you. I would like to especially thank my supervisors, Dr. Raluca Tiron and Dr. Stefano Cabrini, during my research stays at CEA-Leti in Grenoble, and at the Molecular Foundry in Berkeley, for their support and for giving me the opportunity to work with them in a remarkable working environment. Thanks to that, I have had the chance of not only exchange knowledge with scientists from all around the world, but also to meet incredible people. Un grand merci à Maxime, Ahmed, Gaëlle et Guillaume pour leur aide et leur accueil. And thank you Alison, Hilary, Tony, Félix and Maria Elena, to share with me and make even more incredible the three months I spent in California.

También me gustaría agradecer a todos los colaboradores con los que he podido trabajar durante este último periodo de tiempo. Gracias a Tiberio, Mari Cruz, Aurora y Edgar, por enseñarme e iniciarme en el mundo del GISAXS.

Fuera del ámbito científico, y no por ello menos importante, me gustaría agradecer a todas las personas que me han ayudado, animado y compartido conmigo grandes momentos en estos años de tesis, pero sobretudo en esta última recta final: Pili, Paco, Laura, Natàlia, Carlos, Tat, Fran, Marta, Jordi, Ismi, Anna y Miriam.

El especial agradecimiento os lo debo a vosotros, mis padres, abuelos y hermano, porque siempre me habéis ayudado y apoyado en todas mis decisiones. Vosotros me animasteis a empezar mi camino, a aprender a levantarme y continuar en él hasta el final. Por eso, gracias en esto, y en todos los aspectos de mi vida.

Y por último a ti, Javi, porque decidiste iniciar y recorrer nuestro camino en la vida juntos. Gracias por todo el apoyo que me has dado durante estos años, y en especial por la infinita paciencia que has demostrado siempre, tu amabilidad y cariño.

Gràcies a tots, perquè tots formeu part d’aquest camí!

This research has been supported by the Ministry of Education of Spain with the FPU grant 13/03746.

Resum

La tesi doctoral titulada “*Auto-assemblatge de copolímers de bloc per modificació química de la superfície*”, presenta com a objectiu principal el desenvolupament, implementació i caracterització d’un mètode de guiatge de copolímers de bloc basat en la modificació química de la superfície. El desenvolupament d’aquest mètode de nanofabricació contribueix a la futura generació de dispositius i circuits nanoelectrònics.

Primer de tot, es presenten els aspectes generals sobre l’auto-assemblatge dirigit de copolímers de bloc, així com el seu rol dins del futur de la nanoelectrònica comparat amb altres tecnologies emergents. Després, per tal d’entendre i determinar les interaccions que tenen lloc durant el procés d’auto-assemblatge, es dóna una visió general sobre els processos químics i físics que tenen lloc en les pel·lícules primes de copolímers de bloc.

La part principal de la tesi es focalitza en l’estudi, desenvolupament i implementació d’un mètode de guiatge químic per tal de dirigir l’auto-assemblatge de copolímers de bloc. A banda d’estudiar el procés experimental, també es caracteritzen els mecanismes que condueixen l’alineament i s’introdueixen a un model per simular el procés d’auto-assemblatge dirigit. A més, també es presenta la transferència del procés a una línia pilot industrial de fabricació de circuits integrats.

La implementació del procés de guiatge químic s’ha provat no únicament amb materials comercials, sinó també amb nous sistemes polimèrics que permeten arribar a mides per sota dels 10 nm. Per aquests sistemes, es defineix un nou mètode de guiatge basat en la combinació de modificacions topogràfiques i químiques.

Per tal d’entendre millor el procés, s’estudien tècniques específiques de metrologia. En particular, mitjançant tècniques d’alta energia de rajos X, es descriuen les principals diferències entre patrons químics de guiatge. D’altra banda, les propietats nanomecàniques dels diferents dominis del copolímer es determinen mitjançant el mode *peak force tapping* de la microscòpia de força atòmica.

Finalment, es mostra un mètode per transferir els motius del copolímer al substrat. Aquest es basa en la infiltració d’un domini del copolímer. La infiltració canvia les propietats del material i el fa més resistent al gravat amb oxigen. D’altra banda, i com a aplicació final, es presenta un procés de fabricació de ressonadors nanomecànics, basats en el procés d’auto-assemblatge de copolímers de bloc amb infiltració.

Summary

The thesis entitled “*Directed self-assembly of block copolymers on chemically nano-patterned surfaces*”, addresses the development, implementation and characterization of a chemical epitaxy process to direct self-assemble block copolymers. This nanofabrication method contributes to the next generation of nanoelectronic devices and circuits.

Firstly, the main aspects of directed self-assembly of block copolymers and its role and status in the future of nanoelectronics is presented and compared with other powerful technologies. Then, a general overview about the physics and chemistry involved in block copolymer thin films is presented, in order to understand and determine the interactions taking place during the DSA process.

The main part of the thesis is focused on the study, development and implementation of a chemical epitaxy approach to guide the self-assembly of block copolymers. Apart from the process development, the mechanisms which drive the block copolymer alignment are characterized and simulated into a DSA model. Moreover, the process transfer to a more industrial pilot line is presented.

The implementation of the chemical epitaxy process is addressed not only with commercial block copolymers, but also with new polymer systems which allow getting sub- 10 nm resolution. For these systems, a new guiding method is presented based on the combination of a chemical and graphoepitaxy approach.

To better understand the DSA process, dedicated metrology methods are also studied. In particular, by using high-energy X-ray techniques it is possible to describe the main characteristics of the chemical guiding patterns. On the other hand, the nanomechanical properties of block copolymer domains are studied by using the peak force tapping mode in atomic force microscopy.

A reliable method to pattern transfer the block copolymer features into the substrate is showed. It is based on infiltrating one block copolymer domain which enhances its resistivity to plasma etching. Finally, as a final application, a novel fabrication process of a nanowire mechanical resonator by means of DSA and infiltration is presented.

Contents

Introduction	1
1. Introduction to nanolithography.....	5
1.1. Introduction.....	7
1.2. Status and challenges of lithography for microelectronics	8
1.2.1. Optical lithography.....	9
1.2.2. Extreme ultraviolet lithography	10
1.2.3. Maskless lithography	12
1.2.4. Nanoimprint lithography.....	18
1.2.5. Directed self-assembly of block copolymers.....	19
1.3. Summary: lithography status, issues and challenges.....	21
1.4. References	23
2. Chemistry and physics of block copolymer materials.....	27
2.1. Block copolymers and their synthesis.....	29
2.2. Physics of block copolymers	32
2.2.1. Order-disorder transition in block copolymers.....	32
2.2.2. Morphologies of diblock copolymers.....	33
2.2.3. Block copolymers in thin films	34
2.2.4. Interface neutralization.....	37
2.2.5. Thermal and solvent annealing of block copolymer films	37
2.3. Modelling of block copolymer directed self-assembly.....	39
2.3.1. Block copolymer kinetics	40
2.3.2. Field-theoretic simulations and self-consistent field theory	41
2.4. High- χ block copolymers.....	42
2.4.1. Organic based high- χ block copolymers	43
2.4.2. Inorganic based high- χ block copolymers.....	44
2.5. References	45

3. Directed self-assembly of PS-<i>b</i>-PMMA BCPs by chemical epitaxy	53
3.1. Introduction to DSA of block copolymers by chemical epitaxy.....	55
3.2. Development of chemical epitaxy by substrate functionalization.....	57
3.2.1. Materials and methods	57
3.2.2. Directed self-assembly by chemical epitaxy of PS- <i>b</i> -PMMA results.....	61
3.3. Characterization of the surface free energy of chemical guiding patterns.....	66
3.3.1. Experimental method to determine the interface interactions for modeling the chemical epitaxy DSA process.....	66
3.3.2. Role of the surface interactions by field-theoretic simulations and self-consistent field theory on chemical epitaxy DSA process	73
3.4. Manufacturability of chemical epitaxy by substrate functionalization	77
3.4.1. Materials and methods	78
3.4.2. Directed self-assembly by chemical epitaxy of PS- <i>b</i> -PMMA results.....	83
3.5. Development and implementation of chemical epitaxy by UV substrate functionalization	85
3.5.1. Chemical surface characterization of UV exposed surfaces.....	86
3.5.2. Surface free energy characterization.....	90
3.5.3. DSA of chemical epitaxy by UV surface functionalization	92
3.6. Chemical epitaxy based resistless direct writing methods	94
3.6.1. Introduction.....	94
3.6.2. E-beam lithography direct writing	94
3.6.3. Local Anodic Oxidation based AFM nanolithography.....	99
3.6.4. Summary and comparison	108
3.7. Summary and conclusions.....	109
3.8. References	111
 4. Directed self-assembly of PS-<i>b</i>PMMA BCPs by graphoepitaxy	115
4.1. Introduction to directed self-assembly of block copolymers by graphoepitaxy...	117
4.2. Development and implementation of graphoepitaxy on PS- <i>b</i> -PMMA by means of e-beam lithography	119
4.2.1. Materials and methods	119

4.2.2.	Directed self-assembly by graphoepitaxy of PS- <i>b</i> -PMMA results.....	122
4.3.	Development and implementation of graphoepitaxy on PS- <i>b</i> -PMMA by means of photolithography.....	124
4.3.1.	Materials and methods	124
4.3.2.	Directed self-assembly by graphoepitaxy results.....	128
4.4.	Surface affinity control on topographical guiding patterns.....	129
4.5.	Summary and conclusions.....	132
4.6.	References	133
5.	Directed self-assembly of high-χ block copolymers.....	137
5.1.	Introduction to high- χ block copolymers.....	139
5.2.	PS- <i>b</i> -PLA systems	139
5.2.1.	PS- <i>b</i> -PLA synthesis	139
5.2.2.	PS- <i>b</i> -PLA self-assembly.....	140
5.2.3.	PS- <i>b</i> -PLA directed self-assembly by chemical epitaxy.....	145
5.2.4.	Experimental determination of surface free energy for PS- <i>b</i> -PLA DSA	146
5.3.	PLA- <i>b</i> -PDMS- <i>b</i> -PLA systems	147
5.3.1.	PLA- <i>b</i> -PDMS- <i>b</i> -PLA synthesis.....	147
5.3.2.	PLA- <i>b</i> -PDMS- <i>b</i> -PLA self-assembly	148
5.3.3.	PLA- <i>b</i> -PDMS- <i>b</i> -PLA directed self-assembly by chemical epitaxy	150
5.3.4.	PLA- <i>b</i> -PDMS- <i>b</i> -PLA directed self-assembly by chemo/grapho epitaxy.....	151
5.4.	Summary and conclusions.....	157
5.5.	References	158
6.	Characterization of block copolymers and chemical guiding patterns using synchrotron radiation.....	161
6.1.	Chemical guiding pattern characterization by X-Ray photoemission.....	163
6.1.1.	Characterization of chemical guiding patterns created by electron beam lithography and oxygen plasma functionalization.....	166
6.1.2.	Characterization of guiding patterns by direct writing techniques.....	169
6.2.	Block copolymer morphology and self-assembly characterization by GISAXS...	172
6.2.1.	Basis of grazing incidence X-ray technique	172

6.2.2.	Block copolymer self-assembly GISAXS characterization.....	174
6.2.3.	Static GISAXS studies on block copolymer films	175
6.3.	Summary and conclusions.....	179
6.4.	References	180
 7. Pattern transfer of block copolymers and application in device fabrication.....		183
7.1.	Conventional atomic layer deposition	185
7.1.1.	Introduction.....	185
7.1.2.	Use of atomic layer deposition for block copolymer pattern transfer	187
7.2.	Sequential Infiltration Synthesis.....	190
7.2.1.	Introduction.....	190
7.2.2.	Use of sequential infiltration synthesis for pattern transfer.....	190
7.3.	Local nanomechanical properties of PS- <i>b</i> -PMMA self-assembly	194
7.3.1.	Introduction.....	194
7.3.2.	Optimal Indentation Conditions.....	195
7.3.3.	Characterization of PS- <i>b</i> -PMMA thin films.....	196
7.3.4.	Characterization PS- <i>b</i> -PMMA thin films after atomic layer deposition	197
7.3.5.	Characterization of PS- <i>b</i> -PMMA after sequential infiltration synthesis.....	199
7.4.	Fabrication of nanomechanical devices based on metallic oxide nanowires.....	201
7.4.1.	Materials and methods	201
7.4.2.	Nanomechanical resonators fabrication results.....	207
7.5.	Summary and conclusions.....	210
7.6.	References	211
 General conclusions.....		215
Conclusions generals		219
Annexes.....		223
Annex I. Acronyms List.....		225
Annex 2. Scientific contributions.....		229

Introduction

The term ‘*nano*’ means the billionth part of something, and thus *nanoscience* refers to the study of phenomena taking place in materials at atomic, molecular and macromolecular scales, where matter properties differ significantly from those at larger scale. It is a multidisciplinary science which is based on the convergence of a mix of scientific and technological domains. Its application to different techniques which allow the manipulation, fabrication and characterization of matter with an industrial objective is referred as *nanotechnology*.

The conceptual foundations of *nanotechnology* were partially inspired by the physicist *Richard Feynman*, Nobel Prize winner for Physics in 1965, during a conference of the American Physical Society in 1959. It was entitled ‘*There is plenty of room at the bottom*’, and he discussed the importance of manipulating and controlling the matter at the nanometer scale, and how they could tell us about the peculiar phenomena that occur in complex situations.

Nanofabrication is one aspect of nanotechnology that has developed from the evolution of microelectronics during the last decades on one side, and on the other side, from the incorporation of novel methods and techniques from nanoscience. Since the invention of the integrated circuit more than half a century ago, there has been an exponential growth in the number of transistors per chip and an associated decrease in the smallest width. Lithography is the central process in nanofabrication, and its tremendous technological evolution, in particular for what it concerns optical lithography, has delivered the possibility to define nanoscale patterns at high throughput and reproducibility. However, the current technological limits will soon be reached, and emerging technologies will take over.

It is in the framework of the need of new patterning methods for nanoelectronics that the present thesis arises. The initial overall objective of thesis has been the research of novel solutions for nanolithography, a topic of interest for the two research centers where the work has been developed (*IMB-CNM-CSIC*, and *ICN2*) and also for the European research community, as exemplified by the European projects where it has contributed. Actually, the work of this thesis has been, in several aspects, dictated by the involvement mainly in the CoLiSA Project (*Computational Lithography for directed self-assembly: Materials, Models and Processes - FP7-619793*) but also in SNM (*Single Nanometer Manufacturing for beyond CMOS devices - FP7-318804*) and PLACYD (*Pilot Line for Self-Assembly Copolymers Delivery - ENICAC JU-621217*) projects.

Directed self-assembly (DSA) of block copolymers (BCPs), offers very attractive characteristics from an industrial point of view: high resolution, low cost and high throughput. The ability of BCPs to self-assemble at the nanoscale makes them of interest to use as complementary solution to conventional lithographic techniques. Therefore, they are being to be exploited to form small features at low cost processing. DSA integrates *bottom-up* self-assembly with *top-down* conventional lithography responsible to direct the orientation of the BCPs. There are basically two approaches to do so: *graphoepitaxy* which uses topographical features of lithographically patterned surfaces, and *chemical epitaxy* which employs dense chemical patterns created normally on a polymeric surface.

The research reported in this thesis, concerns the overall objective of study, development, characterization and optimization of a chemical epitaxy approach to direct self-assemble BCPs for nanoelectronic applications. The outline of the thesis is divided in seven chapters, and they cover different aspects of BCPs, from the basic concepts to the application of DSA on the fabrication of a nanomechanical resonator.

The first chapter aims to give a general overview of the conventional and next generation lithography techniques, and bring together the foremost advances and challenges for the next generation logic node. It also describes which the main aspects of DSA are, and its role and status in the future of microelectronics industry.

On the other hand, in order to determine the mechanisms involved during the DSA process, an understanding of the basic concepts of BCPs is of great importance. Therefore, *chapter 2* is focused on the study of BCP physics from its bulk state to thin films.

The study, development and implantation of different chemical epitaxy processes are discussed in *chapter 3*, which covers the central part of the thesis work. This chapter, apart from giving a summary of the experimental methods and results, leads down the whole chemical characterization performed to understand the interactions which take place between the surface and the BCP domains. Furthermore, a novel experimental method which allows predicting the chemical affinities is presented. With the obtained data it has been possible to simulate and predict the DSA process by using self-consistent mean-field calculations. On the other hand, the process transfer to a more industrial focused pilot line in *CEA-Leti*, is presented.

In *chapter 4*, the implementation of graphoepitaxy process by means of photolithography, is presented. The BCP orientation is controlled by the tuning of experimental conditions and materials used. On the other side, the topographical guiding pattern designs and the subsequent DSA process are focused on the fabrication of a nanomechanical resonator presented in *chapter 7*.

In order to demonstrate the DSA implemented processes for smaller structures, the self-assembly behavior of materials which offer smaller features than the most used BCP, *poly(styrene-*b*-methacrylate)*, (PS-*b*-PMMA), is presented. Both, chemical and graphoepitaxy approaches, are implemented for the DSA of these new materials. These methods are explained in *chapter 5*.

The better understanding and characterization of DSA deserves dedicated metrology methods. In general, the improvement in nanofabrication methods allowing to produce sub-10 nm features has triggered a lot of activity to develop adapted characterization tools. In particular, high-energy X-ray techniques are capable to give information about the chemical nature of guiding patterns. Therefore, *chapter 6* describes the main differences between chemical guiding patterns created in different ways, by using X-ray techniques based on synchrotron radiation. On the other hand, the characterization of BCP pitch and shapes is corroborated by grazing incidence small-angle scattering (GISAXS). Besides of providing information about BCP morphology, this technique allows to perform in-situ analysis and give a general overview of the self-assembly mechanisms at early stages.

To take advantage of BCP DSA, an accurate pattern transfer to the substrate is needed. However, the poor contrast between most part of the polymers requires the use of alternative methods to enhance the etch resistivity of one of the blocks. *Chapter 7* demonstrates the use of sequential infiltration synthesis (SIS) to pattern transfer the BCP features. Moreover, it is described a novel fabrication process of a nanowire mechanical resonator based on the combination of DSA and SIS.

Chapter 1

Introduction to nanolithography

For many decades, Moore's Law has delivered to the microelectronic industry more functionality while decreasing production costs. However, this continuous tendency to reduce the dimensions of a device forcedly implies new challenges, hence new fabrication strategies need to be considered.

Nowadays, extreme ultraviolet lithography (EUV) using 13.5 nm wavelength, is the leading candidate to succeed 193 nm immersion lithography for the next generation logic nodes. Nevertheless, EUV is still not fully developed, and other approaches, like directed self-assembly or nanoimprint are much closer to manufacturing implementation than they used to be.

This chapter gives an overview of the different state-of-the-art lithography techniques and their status, challenges and possible driving forces for implementation.

1.1. Introduction

For many decades, many areas of science and technology are demanding the continuous resolution improvement of patterning methods. A prominent example is the semiconductor industry, where the increase of density in integrated circuits requires reducing the critical dimensions of the transistors, as dictated by *Moore's Law*.¹ This law describes the exponential growth in complexity of integrated circuits, and it dictates that the number of transistors in a dense integrated circuit (IC) was doubling every two years. In 1975, it was adjusted to a doubling every year and a half.²

For many years, the scaling has consisted in only reducing the feature size, and thus has resulted in a rapid progress in terms of functionality and cost-effectiveness. This has meant that, every two years, devices have become more powerful, smaller and cheaper. Nevertheless, this exponential growth is approaching physical limits, and transistors are getting too small to actually manufacture efficiently.

In the early 2000s, it was realized that chips began to become too hot during operation. Therefore, manufacturers had to redesign the IC, so that each chip contained not only one processor, but more. It enabled microelectronics industry to continue shrinking the IC size and follow *Moore's* path. Nevertheless, there is still unknown what will happen in the next years, when scaling will be no longer available due to quantum effects leading to interferences and coupling between paths.

The international technology roadmap for semiconductors (ITRS) is a document produced by semiconductor experts with the aim to enable equipment and materials suppliers to know about the future requirements. According to the ITRS, there are two directions for further progress in the microelectronics industry. The first trend is called *More Moore*, and it is based on the continuous miniaturization, but reinforced by the incorporation of new materials and processes. On the other hand, the second direction is called *More than Moore*, and it is characterized by the addition of non-digital functionalities which contribute to the miniaturization of electronic systems, although not at the same rate. *More than Moore* technologies do not represent an alternative, but an integration of digital and non-digital functionalities which can be used in a very extensive list of application fields (chemical sensors, smart cities, self-driving cars...), which do not require an extreme scaling demand.

Therefore, microelectronics not only needs to provide performance on its traditional market, but also to develop new markets, based on non-electronic functions of IC. For example, microelectronics can be extended as a platform for biological and medical science, in order to develop new applications and capabilities.³

1.2. Status and challenges of lithography for microelectronics

Lithography is derived from *Ancient Greek*, ‘*lithos*’ and ‘*graphia*’, which mean *stone* and *to write*, respectively. It was invented around 1796 in Germany by *Alois Senefelder*. He discovered that he could duplicate his scripts by writing them in grey crayon on slabs of limestone, and then printing them with rolled-on ink. From this seminal discovery to the current lithography processes many efforts in research and development have been dedicated.

In microelectronics, lithography refers to a micro/nano fabrication technique used to make IC, as well as micro and nano electromechanical systems (MEMS and NEMS). It is a highly specialized process used to transfer the patterns from a mask to a layer.

For many technological generations, the scaling of physical dimensions has been enabled by the continuous improvements of optical lithography. It has been achieved thanks to the reduction of the wavelength and to the increase of the numerical aperture (NA). Nevertheless, its physical limits are coming closer due to intrinsic limitations in resolution, and alternative non-optical lithography approaches are taking over.

Figure 1.1 shows a graph with the lithography scaling as a function of the time and wafer size. Nowadays, extreme ultraviolet (EUV) lithography seems to be almost ready for high-volume manufacturing, while new technologies like DSA or nanoimprint lithography (NIL) are gaining consensus.

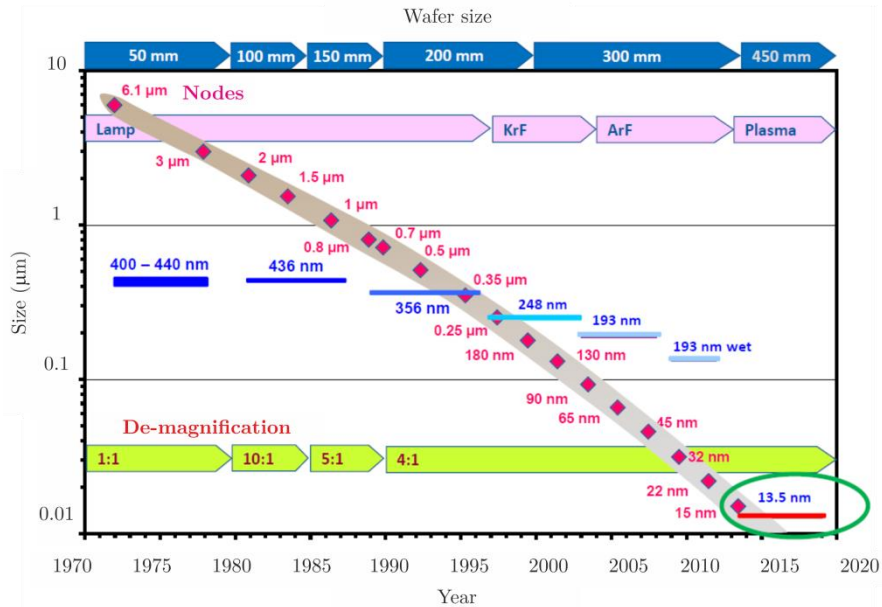


Figure 1.1. Lithography scaling map as a function of time and wafer size

In the next sections, the next generation lithography (NGL) techniques will be discussed, according to their challenges and their current status on the industry.

1.2.1. Optical lithography

Optical lithography has been the primary patterning method for semiconductor industry, since it has provided high-volume manufacturing and high-resolution chip production, as compared to other approaches.

As in other lithography approaches, the goal is to generate a pattern on a thin layer of resist, which is deposited on a substrate. Figure 1.2 shows a schematic representation of a general photolithography process.

The desired pattern is created on a photomask normally larger than the final pattern in the resist (4x in most systems), and the system has a projection optical system which provides a demagnification ratio. Then, the resist is exposed to a pattern of intense light, which causes a chemical change on the exposed areas. Finally, the resist is developed. Thus, the final pattern on the resist is binary: there are parts covered with the resist, and others completely un-covered. This binary pattern is used for pattern transfer into the underlying layer.

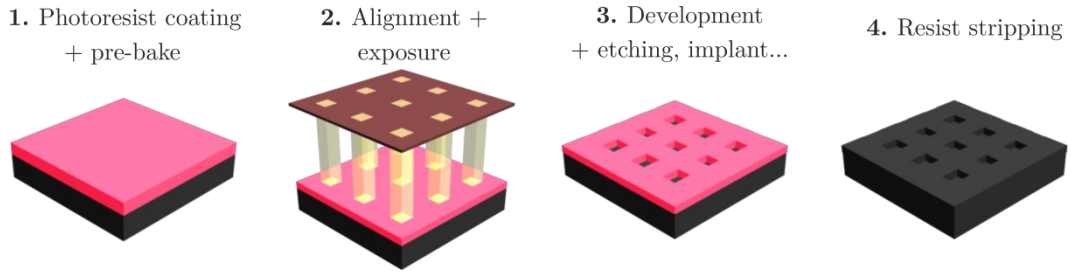


Figure 1.2. Schematic representation of a general photolithography process

The optical resolution R , is a key parameter in optical lithography, which depends on the illumination light wavelength, λ , and the NA of the projection lens, as shown in equation (1.1).

$$R = k \cdot \frac{\lambda}{NA}, \quad (1.1)$$

where k is a constant which depends on the resist and process technology NA is proportional to the medium index of refraction, n , and to the largest angle of converging rays subtended at the resist, θ . R can be reduced by reducing the wavelength and/or increasing NA.

When using optical lithography, changes in the NA, or in the material can improve the resolution, getting structures at fractional wavelength sizes.^{4,5} The choice of the wavelength is determined by the radiation source. Figure 1.3 shows a schematic representation of the wavelength exposure systems. Until the late 1980s, optical lithography was performed with high-pressure Hg discharge lamps, which operated at 436 nm (g-line) and 365 nm (i-line), respectively.

Then, these lamps were substituted by more powerful excimer lasers, called deep-ultraviolet (DUV) systems, which have been the main pillar of the industry for the last past years. The excimer laser wavelengths for DUV are 248 nm (KrF) and 193 nm (ArF), respectively.⁶ The 193 nm wavelength has allowed achieving resolutions of 50 nm. An important element of 193 nm lithography is the use of pellicles, which protect the mask from the contamination of particles, and maintains the manufacturing yield. On the other hand, another related wavelength parameter is the resist, which cannot be too thin if it has to be used in pattern transfer. Therefore, large efforts on the development of new resists have to be performed, particularly in the chemically amplified resists (CAR).

As the resolution demands were increasing, the exposure wavelength was reduced to 157 nm by using F₂ lasers. Nevertheless, the development of lenses, masks, pellicles and resists took a considerable amount of time, and an alternative was found by introducing the ArF immersion system.⁷ Immersion lithography replaces the air gap between the lens and wafer with a liquid which refractive index is greater than 1. By this way, the resolution is increased by a factor equal to the refractive liquid index.

The water immersion with ArF exposure allowed to overcome better the resolution limit of the ArF exposure, since it permitted getting wavelengths smaller than 157 nm, and resolutions of 39 nm.⁸ 193 immersion lithography has displaced the 157nm technology, and has been the choice for printing critical dimensions of the 45 and 32 nm nodes.

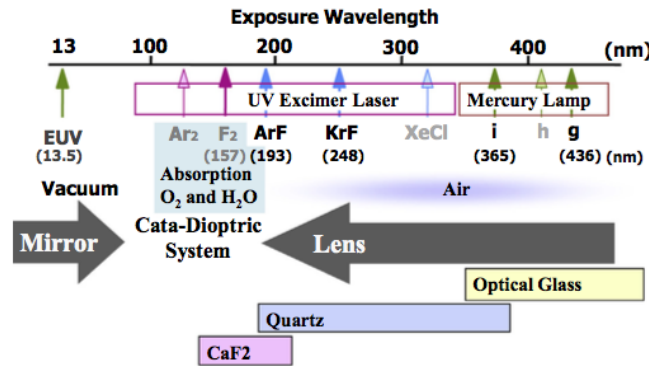


Figure 1.3. Wavelengths in projection exposure systems. Hg lamps are used for g-line and i-line exposure. In DUV, KrF and ArF excimer lasers are used⁹

1.2.2. Extreme ultraviolet lithography

EUV lithography development started in 1985, and it extends optical lithography to a higher resolution, since it utilizes a shorter wavelength ($\lambda = 13.5$ nm), as depicted in the scheme of Figure 1.3.

Moreover, EUV can greatly enhance the feature density of chips without using additional layers or multi-patterning, and it is currently developed for high volume manufacturing of the 7 nm logic node by 2020 (Intel, Globalfoundries, Samsung and TSMC).

The principle of EUV, is similar to optical lithography, in which the light is refracted through lenses onto the wafer. Nevertheless, because light radiation is strongly absorbed at this wavelength, all the EUV system must be in vacuum, and the optics must be reflective.

The EUV beam can be taken out from high-temperature and high-density plasma. There are mainly two methods to produce the plasma: the laser produced plasma (LPP) which produces plasma by condensing a strong laser beam into a material, and the discharge produced plasma (DPP) which produces plasma by a pulsed high-current discharge between electrodes in a certain atmosphere. The first one is the most commonly used in the industry, and its principle of operation is represented in Figure 1.4.

To generate the EUV light by the LPP system, the light source hits a rapid-fire stream of droplets with CO₂ laser pulses, which generates a plasma. The most common target material for laser-plasma are ⁵⁰Sn, ⁵³I, and ⁵⁴Xe. The EUV excited from the plasma, is collected then by a condensing mirror, which directs the resulting radiation into the scanner, going through an intermediate focus which illuminates a reflection mask.

In summary, this means that, in order to generate EUV light of 13.5 nm wavelength, there is the need of a powerful laser, added to the disadvantage of having to work in vacuum and with specialized multilayer mirrors.

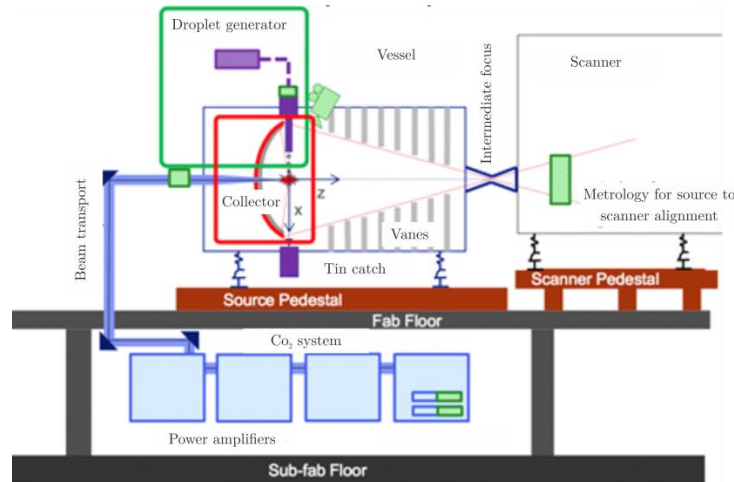


Figure 1.4. EUV generation principle (Image taken from ASML)

The major drawback of EUV, is that it does not only require new scan-systems, but also new chemicals and new mask infrastructure. Moreover, it has the big challenges of making masks free of defects, and on the other hand, of designing resists able to absorb EUV five times as faster.

All of these requirements make this technology to be very complex and expensive; more than twice that of an average 193 nm scanner. Although EUV presents these big challenges, there is being a very solid progress, and the industry is very optimistic about EUV lithography to be implemented into 7 nm logic node production.

Currently, manufacturers are using immersion lithography and multi-patterning at 16 nm, 14 nm and 10 nm logic nodes, respectively. However, for the 7 nm node, it seems that 193 immersion lithography is being replaced by EUV scanners due to its simplicity. Nevertheless, the 7 nm node will be costly not only for fabrication but for wafer, mask, design and development times costs.

1.2.3. Maskless lithography

Maskless lithography refers to the lithography approaches in which the radiation used to expose the resist is not projected or transmitted through a mask. The various forms of maskless lithography include: electron beam lithography (EBL), focused ion beam (FIB), interference lithography (IL) and scanning probe lithography (SPL).

1.2.3.1. Electron beam lithography

EBL is a complementary solution to optical lithography, because it offers a very high resolution (sub-10 nm) due to the achievable small wavelength (10-50 keV electrons). Nevertheless, it has a low throughput, and therefore its use is limited to mask fabrication, low-volume production and research and development.

Figure 1.5 shows a plot with the required time to expose an area of 1 cm^2 , as a function of the minimum feature size. As observed in the graph, for linewidths below 600 nm, the exposure time does not meet with the minimum requirement of semiconductor industry ($1 \text{ cm}^2/\text{s}$).

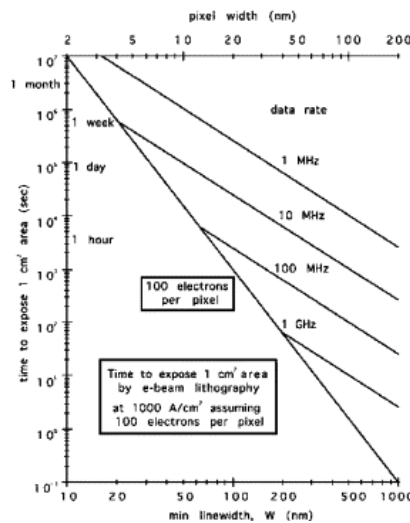


Figure 1.5. Required time to expose 1 cm^2 area with EBL as a function of the linewidth¹⁰

For research applications, normally an electron microscope equipped with an e-beam system is used, avoiding thus the extremely high costs of those used for commercial applications. These fully dedicated patterning systems present the advantage of offering very high resolution added to the ability of creating patterns without a mask. Moreover, despite presenting the drawback of using very long writing times, projection EBL^{11,12} and the use of massive parallel beams¹³ have been recently introduced to overcome these limitations.

The EBL fabrication principle involves the exposure of a highly focused electron beam to a resist in order to chemically modify its solubility and enabling the selective removal of either the exposed or non-exposed parts of the resist. The general fabrication process is depicted in Figure 1.6, which includes the (i) resist deposition, (ii) e-beam exposure, (iii) development and (iv) resist stripping. In between (iii) and (iv) other processes can be performed like etching or metallization.

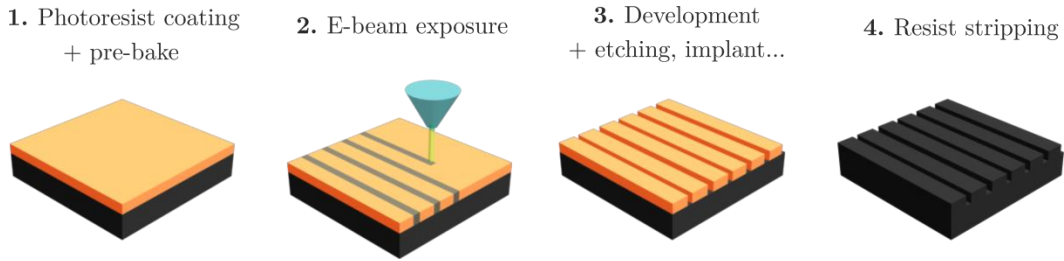


Figure 1.6. Schematic representation of a general e-beam process

The quality of the guiding patterns depends on the quality of the optics, resist, substrate and processing conditions (e-beam energy and dose, development time and temperature). On the other hand, the column containing the electron optics must operate in vacuum in order to reduce gas scattering of the beam.

The quality of the e-beam spot is determined by the electron optics and the degree of focus.¹⁴ When the electrons go inside the resist, they start a sequence of collisions which produces the deflection of the beam. This effect, represented in Figure 1.7, increases with thickness and it is more pronounced at low energies.¹⁵

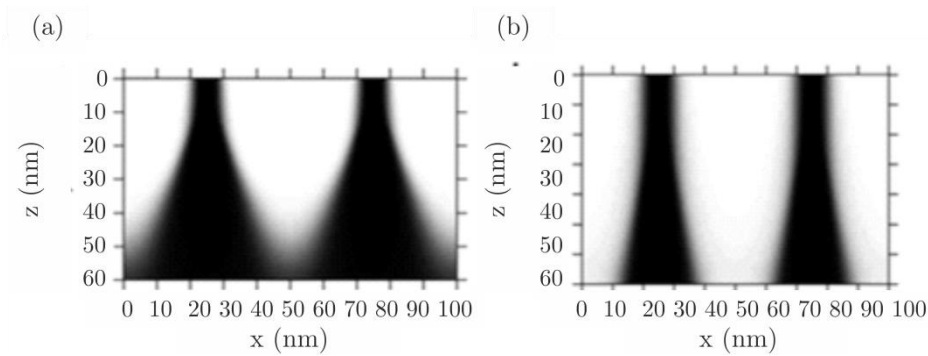


Figure 1.7. Simulations of electron beam broadening caused to scattering effects at (a) low and (b) high incident energies¹⁶

A part from the scattering effect, there is a need to control also the backscattering, produced by some electrons which eventually re-emerge into the resist (see Figure 1.8). This effect leads to beam broadening and proximity effects, causing pattern alterations and overexposure.^{17,18}

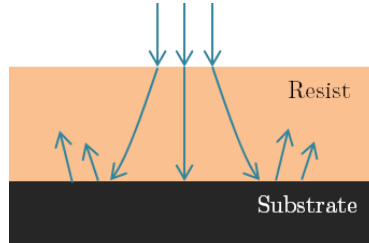


Figure 1.8. Backscattering of electrons and substrate

As shown in Figure 1.7 simulations, higher voltages produce high energy electrons which penetrate deeper and can spread laterally due to backscattering, increasing thus, the proximity effect. Although high voltages provide significantly high resolution and sharp resist profiles, low voltages (0.5 - 5 keV) are sometimes more convenient to reduce proximity effects, improve throughput and reduce the substrate damage caused to underlying materials.^{19,20}

In summary, the EBL is a technique which although not used in high volume manufacturing, it is very suitable for research and development, and for masks production.

1.2.3.2. Focused ion beam

FIB instruments use an ion beam rather than electrons. The focused ion beam can directly mill the surface, with a nanometer controlled sputtering process. The ion source is normally Ga^+ , since gallium has a low melting point, low volatility, low vapor pressure, and excellent mechanical, electrical and vacuum properties. Another ion source commercially available uses He ions, which are less damaging than Ga ions, but with low sputtering rates. Moreover, since He ions can be focused into small probe sizes, it offers higher resolution images.

FIB is normally assembled to a scanning electron microscopy (SEM) system, allowing thus, the generated features to be in situ visualized. In these systems, the electron and ion beams intersect at a 52° angle at a coincident point close to the sample surface.

The principle of operation is described in Figure 1.9. As observed in the scheme, applying an electrical field, the Ga ions are extracted from the metal surface by field transmission. These ions, are accelerated and focused through electrostatic lenses and then they hit the surface. Due to the interaction of the impinging ions with the surface, secondary electrons are generated and detected to produce an image. There are some ions which penetrate the sample and get trapped inside, producing their implantation. Ion implantation is commonly

used to introduce dopants into a semiconductor material. On the other hand, there are other ions, which transfer enough energy to the surface, inducing physical sputtering.

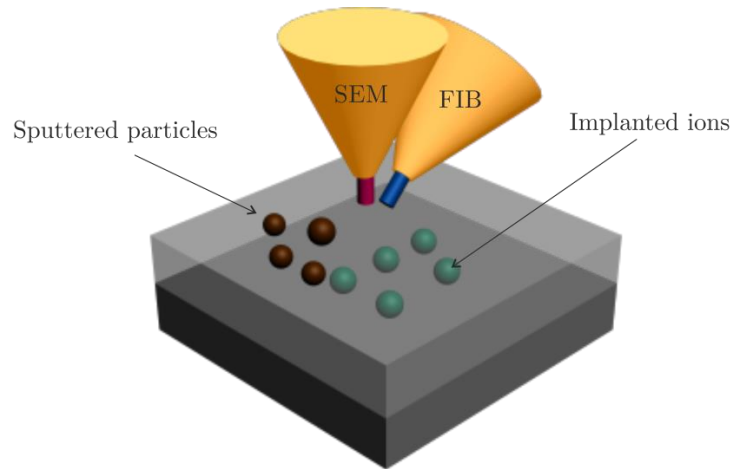


Figure 1.9. Schematic representation of a general FIB process

Figure 1.9 schematizes the different effects that can be produced simultaneously during the process: ion implantation, sputtering and secondary electrons due to the ion-matter collisions.

Another advantage of the FIB technique relies on the possibility of depositing material by directly adding a gas phase organometallic compound in the path of the ion beam. It decomposes when hits the ion beam generating volatile organic compounds which are removed by the vacuum system, and metal remains which are deposited on the surface creating a thin film.

In summary, FIB offers numerous advantages to the semiconductor industry, like the ability to perform both milling and imaging, flexibility (different shapes and deposition of different materials), and fabrication of thin cuts around 100 nm thick. Moreover, its capabilities can be increased by building an in-situ electrical measurement, thus offering the possibility of performing electrical measurements while the FIB is operating.

1.2.3.3. Interference lithography

IL is a technique which uses two interfering light beams to produce periodic structures. Its basic principle is the same as interferometry introduced by *Thomas Young* in 1801, in which the light is divided and recombined, forming periodic intensity patterns that are recorded into the substrate (see Figure 1.10). Then, the resist is exposed to the two superimposed single laser beams.

For two interfering beams, the periodicity of the patterns is given by equation (1.2).

$$P = \lambda / (2 \cdot \sin \theta), \quad (1.2)$$

where λ is the wavelength, and θ is the angle between the two interfering waves.

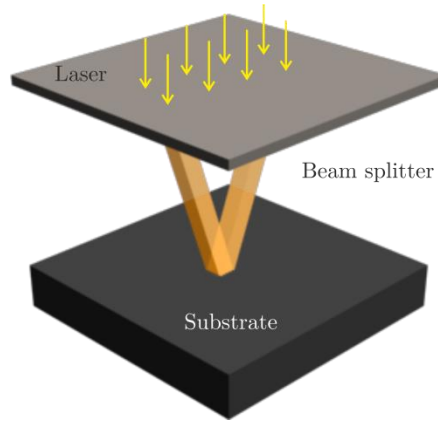


Figure 1.10. Interference of two coherent laser beams

The most interesting advantage is that dense features over a wide area can be produced without losing the focus. Therefore, it is commonly used for the fabrication of molds in NIL²¹, or for testing resist processes for lithography approaches with new wavelengths. Nevertheless, its use is limited to patterning features uniformly distributed, and other types of lithography have to be used if arbitrarily shaped patterns are desired.

1.2.3.4. Scanning probe lithography

SPL emerged in the late 1980s. It is based in scanning tunneling microscopy (STM) or atomic force microscopy (AFM), and they are used to pattern features in the nanometer range. Its mechanism is based on using a sharp tip in proximity to the sample to pattern the desired features.

Figure 1.11 shows the general SPL generation system. As observed, a local tip is brought close to the surface (nanometric distance), and the resulting tip-sample interactions (electrical, optical or mechanical) are measured in real time.

The position of the tip is controlled in the three directions by means of piezoelectric tubes. In AFM, the interaction signal is the deflection of a laser beam focused on a cantilever on which the tip is attached, whereas in STM, the interaction signal is the measurement of the tunnel current between the tip and the surface of the conducting surface.

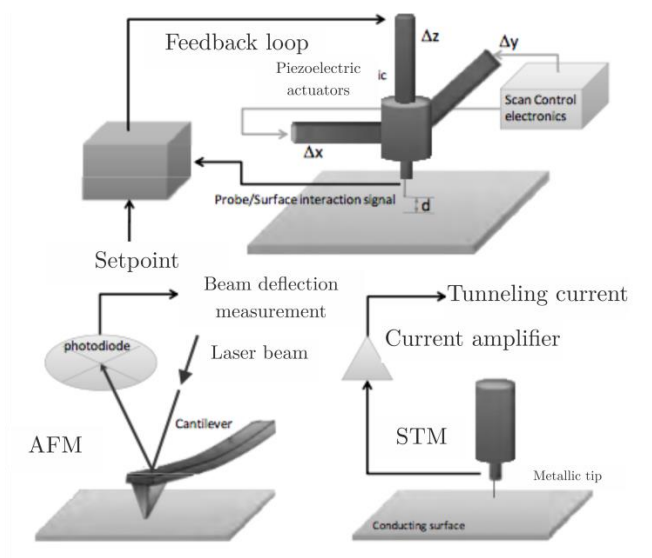


Figure 1.11. Schematic representation of a general SPL process

Apart from providing information about the surface local properties, SPL can be also used to modify the surface in a permanent way. These processes can be thermal, electrical, mechanical or diffusive.²² Figure 1.12, shows the classification of the SPL methods depending on the tip-surface interaction.

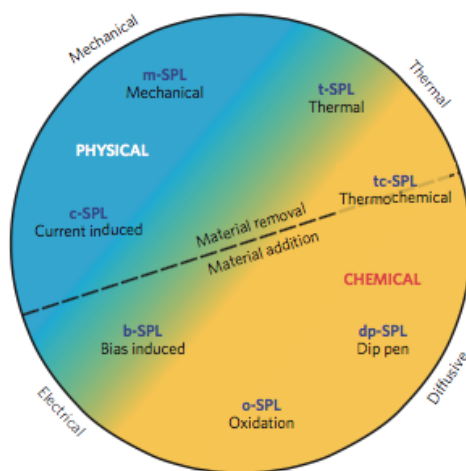


Figure 1.12. Classification of the SPL methods depending on the tip-surface interactions²²

SPL techniques offer a wide range of approaches to modify the surface, and thus leads to a high variety of patterning methods. On the other hand, as compared with other techniques, it presents the advantage of patterning in ambient conditions with no special material requirements and with high resolution.

Nevertheless, it has very low throughput is unsuitable out of the laboratory environment. To overcome these issues, different approaches are being studied, like the use of multiple probes, which can read and write in parallel.²³

1.2.4. Nanoimprint lithography

NIL is a low cost process, which offers high throughput and resolution. Its basic principle has been known for hundreds of years. However, its sub-100 nm application was introduced by *Stephen Chou* in 1995.²⁴

The fabrication process of NIL is depicted in Figure 1.13, and it consists in imprinting nanostructures from a mold to a surface, pressed into a thin resist deposited on the substrate. There are different NIL techniques, but the mostly used are the thermal NIL (Figure 1.13.a) and the UV NIL (Figure 1.13.b), respectively.

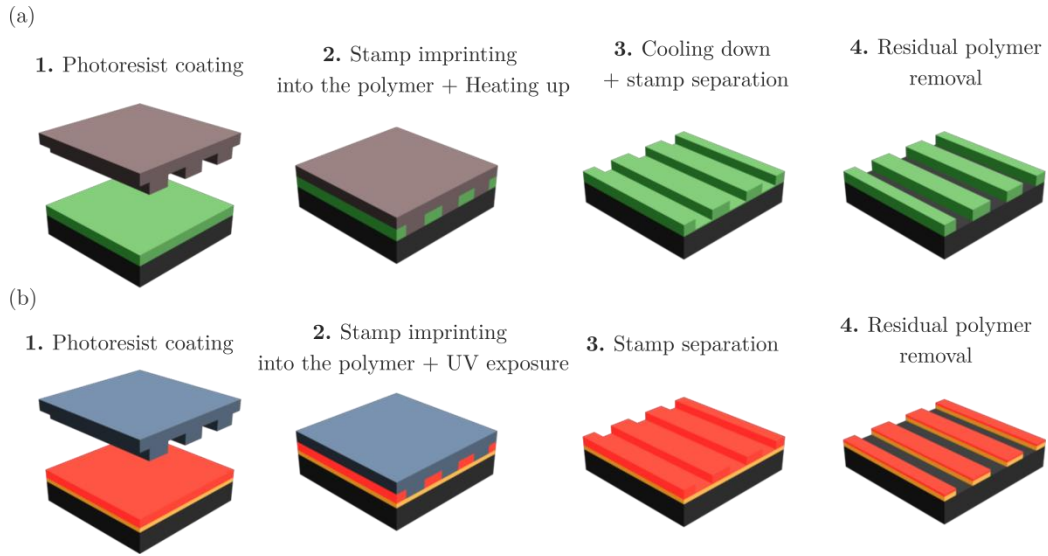


Figure 1.13. Schematic representation of a general (a) thermal and (b) UV nanoimprint process

The thermal NIL is the conventional process developed by *Stephen Chou*. During the imprint process, the mold is kept in contact with the resist, and they are heated up above the glass transition temperature of the polymer in order to make it softer.²⁴ Hereafter, the polymer is cooled down and the mold is removed, leaving the pattern resist left on the substrate.

On the other hand, in UV NIL transparent molds are imprinted into UV curable liquid resists at room temperature. Then, the mold and the substrate are put in contact and pressed. During this process, the resist is cured in UV light and becomes solid. Subsequently, the mold is removed.

Unlike conventional lithography methods, NIL does not require the use of energetic beams. Therefore, the mold used can be made by a high-resolution and low-throughput lithography, and the NIL can be used for low-cost high-volume manufacturing. Furthermore, it is a versatile technique with applications that go beyond microelectronics, including optics, plasmonics or biotechnology.

Despite the amount of benefits, there are still important challenges to overcome: throughput, overlay and defect density. For quite a long time, the throughput has improved, coming from faster filling times of the resist into the mold (80 wafers per hour). On the other hand, the overlay (ability of the lithography scanner to align and print the various layers accurately on top of each other) is also improving by the development of new wafer chucks to improve the flatness around the wafer meeting the production standards by 2018. Regarding the defectivity, it is expected to improve, as the technology develops, by improving the template cleaning, resist materials and by employing antistiction layers on the stamp to reduce the adhesion between it and the resist.

1.2.5. Directed self-assembly of block copolymers

Lithography using BCPs was first introduced by *Mansky et al.*, in 1995.²⁵ The most interesting feature of a BCP is the ability to self-assemble into domains with dimensions that are very expensive to fabricate with conventional lithographic tools. The first study with BCPs, was with a poly(styrene-*b*-butadiene) (PS-*b*-PB) system, in which the BCP film was annealed to form a single layer of PB spheres into a PS matrix.²⁵

DSA has become a relevant alternative lithographic technique for the creation of nanometer scale patterns due to its high throughput and process simplification compared to other approaches.^{26,27} It is important to remark that DSA is not a stand-alone lithography, but a combination of a lithographic tool with the ability of BCPs to self-assemble into nanoscale features. Moreover, DSA is a potentially viable patterning technique for the semiconductor industry since it offers higher throughput and simpler and lower cost processes compared to other techniques.²⁸

Even though, the major drawbacks of DSA are related with placement and defectivity. However, significant progress has been achieved in the past few years up to the extent that defect levels have been dramatically reduced (defectivity values around 24 defects/cm²).^{29,30} The industry is struggling nowadays with DSA design and integration challenges.³¹

There are two main approaches to control the orientation and alignment of self-assembled BCP domains: *graphoepitaxy*^{32,33} and *chemical epitaxy*.³⁴⁻³⁶ Figure 1.14 shows a schematic representation of a general DSA process by graphoepitaxy (Figure 1.14.a) and by chemical epitaxy (Figure 1.14.b).

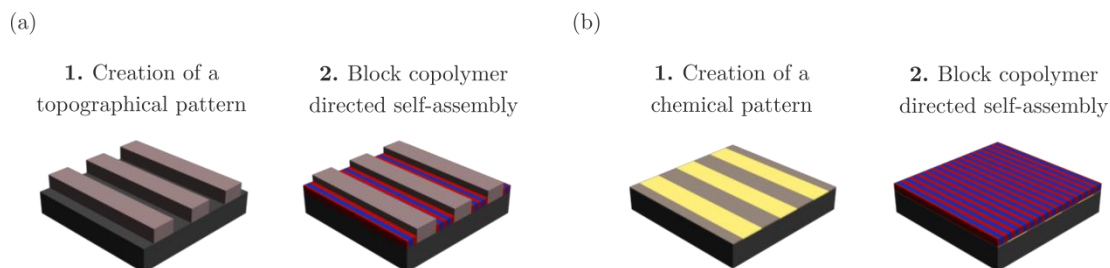


Figure 1.14. Schematic representation of a general DSA process by (a) graphoepitaxy and (b) by chemical epitaxy

On the one hand, graphoepitaxy is based on using topographic patterns (usually holes or trenches) and confine the BCP on it. It is commonly used in combination with cylindrical BCPs in order to shrink the size of contact holes or to achieve contact-hole multiplication.

On the other hand, chemical epitaxy consists of creating chemical patterns on a neutral surface so that the modified areas would present larger affinity to one of the blocks, determining the position and orientation of the molecules. The major difference between topographical and chemical DSA is the relative length scale between the pattern and the pitch of the BCP.

Until now, the multiplication factors in graphoepitaxy can be four times larger than the BCP pitch, which are much larger than in chemoepitaxy. One of the major advantages of chemical epitaxy with respect to graphoepitaxy is the reduction of the edge roughness due to the self-healing of BCPs, which means that the irregularities of the guiding patterns are not certainly transferred to the BCP pattern.³⁷

Some years ago, the original projections were all for DSA, and it was supposed to move into the logic production flow from the 14 nm to 7 nm node. However, together with its principal problem, the defectivity, pattern roughness, placement accuracy and material quality control, are still challenges that need to be overcome.

Currently, DSA of PS-*b*-PMMA defined on chemical guiding patterns is the primary focus of activities, and therefore, the main research objectives involve demonstrations that DSA can meet manufacturing requirements in terms of defectivity. On the other hand, the industry is also working on other DSA materials which scale beyond 11 nm, the minimum size achievable for PS-*b*-PMMA.

For the near future, DSA is not ready for insertion into industry for conventional patterning, but it will be used for pattern healing or repair. Nevertheless, by reducing the defectivity and improving patterning reliability, DSA patterning can push 193 nm lithography beyond its limits, especially for space/line applications by using chemical epitaxy.

1.3. Summary: lithography status, issues and challenges

Lithography is a key technology for semiconductor industry since it determines the device critical dimensions. The permanent quest for miniaturization is becoming increasingly difficult, since the cost and functionality of the fabrication processes are increasing and becoming more complex.

The recent ITRS lithography roadmap shows a big technology decision about how to lead the next generation logic node. As shown in Figure 1.15, multiple patterning and all the NGL techniques have enough resolution to reach the 10-nm half-pitch and better.

Although EUV seemed to be the preferred option for the next generation nodes, some required improvements are taking longer than expected, and NIL and DSA are becoming much closer to manufacturing implementation. Especially DSA has demonstrated improved defectivity and progress in process flow integration.

Experts on the field, support the idea that EUV is the most suitable technique for the next generation node, but it probably has one more generation before having to add multi-patterning or much larger NA.

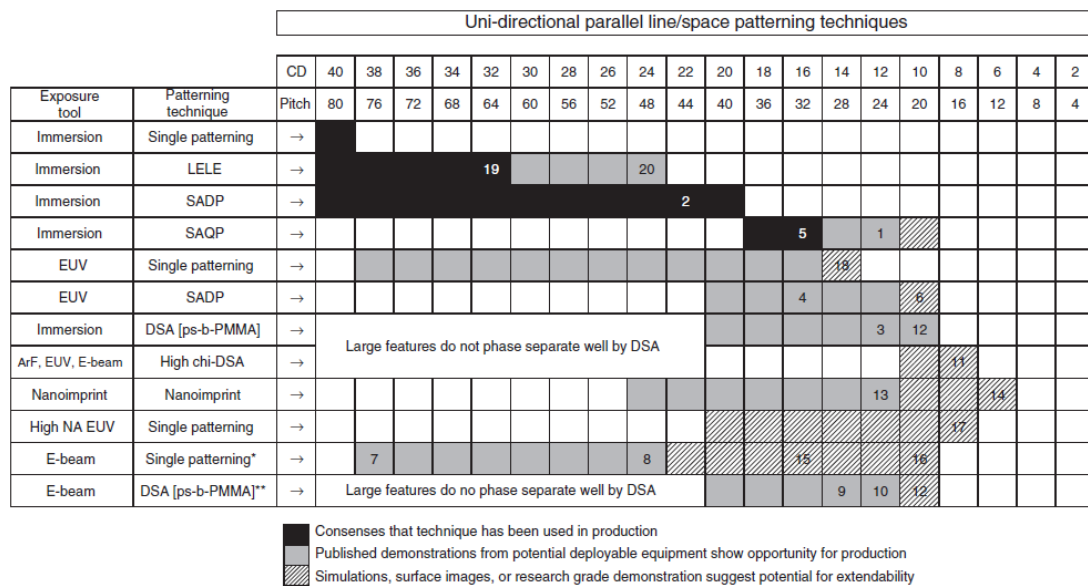


Figure 1.15. Potential solutions for line/space applications by pitch and half pitch published in the 2013 ITRS Roadmap for Lithography

To summarize, DSA and NIL are very promising techniques at lower cost, EUV promises simpler and shorter processes, and mask-less lithography is becoming more focused for chip personalization and cost effective for low volume chip designs.³⁸ Nevertheless, EUV is still not ready for high-volume manufacturing at 7 nm node, which is predicted for 2018 to 2019. Although it is making a noticeable progress, there are still some challenges ahead, such as power source, resists and pellicles.

In any case, it seems that bringing technology from the laboratory to the fabrication is becoming more difficult at each node, probably because technology has been pushed much further than it was predicted to be.

1.4. References


1. Moore, G. E. Cramming more components onto integrated circuits. **38**, (1965).
2. Moore, G. E. Progress in Digital Integrated Circuits. *IEDM Tech. Dig.* (1975).
3. Jackson, T. N. Beyond Moore ' s Law. *Nat. Mater.* **4**, 581–583 (2005).
4. Ito, T. *et al.* Pushing the limits of lithography. *Nature* **406**, 1027–1031 (2000).
5. Yoo, P. J., Suh, K. Y., Kim, Y. S., Brugger, J. & Legget, G. J. (2005).
6. Rothschild, M. *et al.* Excimer projection lithography at 193 nm wavelength. *Proc. SPIE* **922**, (1988).
7. Bloomstein, T. M. *et al.* Lithography with 157 nm Lasers. *J. Vac, Sci. Technol. B* **15**, (1997).
8. Lin, B. J. Semiconductor foundry, lithography, and partners. *Proc. SPIE* **4688**, (2002).
9. Okazaki, S. High resolution optical lithography or high throughput electron beam lithography: The technical struggle from the micro to the nano-fabrication evolution. *Microelectron. Eng.* **133**, 23–35 (2015).
10. Menon, R., *et al.* Maskless lithography. *Mater. Today* **8**, 26–33 (2005).
11. Liddle, J. A. *et al.* High-throughput projection electron-beam lithography employing SCALPEL. *Proc. SPIE* **2014**, 66–76 (1993).
12. Pfeiffer, H. C. *et al.* PREVAIL – IBM's e-beam technology for next generation lithography. *Futur. Fab Int.* **12**, (2002).
13. Hakkennes, E. A. *et al.* Demonstration of real-time pattern correction for high-throughput maskless lithography. in **7970**, 79701A–79701A–11 (2011).
14. Goldstein, J. *et al.* *Scanning Electron Microscopy and X-ray Microanalysis*. (Springer US, 2003).
15. Lee, Y. H. *et al.* Low voltage alternative for electron beam lithography. *J. Vac. Sci. Technol. B Microelectron. Nanom. Struct. Process. Meas. Phenom.* **10**, 3094–3098 (1992).
16. Stepanova, M. *et al.* *Nanofabrication: Techniques and principles*. *Nanofabrication: Techniques and Principles* (2014).
17. Chang, T. H. P. Proximity effect in electron-beam lithography. *J. Vac. Sci. Technol.* **12**, 1271–1275 (1975).
18. Lo, C. W. *et al.* Resists and processes for 1 kV electron beam microcolumn lithography. *J. Vac. Sci. Technol. B Microelectron. Nanom. Struct. Process. Meas. Phenom.* **13**, 812–820 (1995).

19. Yau, Y. W. *et al.* Generation and applications of finely focused beams of low-energy electrons. *J. Vac. Sci. Technol.* **19**, 1048–1052 (1981).
20. Sugita, A. *et al.* Resist Exposure Characteristics by a Focused Low Energy Electron Beam. *J. Electrochem. Soc Solid-State Sci. Technol.* **135**, 1741–1746 (1988).
21. Bläsi, B. *et al.* Large area patterning using interference and nanoimprint lithography. *Proc. SPIE* **9888**, (2016).
22. Garcia, R., *et al.* Advanced Scanning Probe Lithography. *Nat. Nanotechnol.* **9**, 577. (2014).
23. Vettiger, P. *et al.* the ‘Millipede’-Nanotechnology Entering Data Storage. *Trans. Nanotechnol.* **1**, 39–55 (2002).
24. Chou, S. Y., *et al.* Imprint Lithography with 25-Nanometer Resolution. *Science.* **272**, 85–87 (1996).
25. Mansky, P., *et al.* Monolayer films of diblock copolymer microdomains for nanolithographic applications. *J. Mater. Sci.* **30**, 1987–1992 (1995).
26. Liu, G., T *et al.* Integration of Density Multiplication in the Formation of Device-Oriented Structures by Directed Assembly of Block Copolymer-Homopolymer Blends. *Adv. Funct. Mater.* **20**, 1251–1257 (2010).
27. Rathsack, B. *et al.* Advances in directed self assembly integration and manufacturability at 300 nm. **8682**, 86820K (2013).
28. Hinsberg, W. *et al.* Self-Assembling Materials for Lithographic Patterning: Overview, Status and Moving Forward. *Proc. SPIE* **7637**, (2010).
29. Rincon Delgadillo, P. *et al.* Defect source analysis of directed self-assembly process (DSA of DSA). *Proc. SPIE* **8680**, 86800L–86800L–9 (2013).
30. Gronheid, R. *et al.* Defect reduction and defect stability in IMEC’s 14nm half-pitch chemo-epitaxy DSA flow. **9049**, 904905 (2014).
31. Somervell, M. *et al.* Driving DSA into Volume Manufacturing. **9425**, 1–11
32. Park, S. *et al.* Macroscopic 10-terabit-per-square-inch arrays from block copolymers with lateral order. *Science* **323**, 1030–1033 (2009).
33. Tiron, R. *et al.* Pattern density multiplication by direct self assembly of block copolymers: toward 300nm CMOS requirements. *Proc. SPIE* **8323**, 83230O–83230O–7 (2012).
34. Tada, Y. *et al.* Directed Self-Assembly of Diblock Copolymer Thin Films on Chemically-Patterned Substrates for Defect-Free Nano-Patterning. *Macromolecules* **41**, 9267–9276 (2008).
35. Kim, S. O. *et al.* Epitaxial self-assembly of block copolymers on lithographically defined nanopatterned substrates. 411–414 (2003).

- 36. Edwards, *et al.* Long-Range Order and Orientation of Cylinder-Forming Block Copolymers on Chemically Nanopatterned Striped Surfaces. 3598–3607 (2006).
- 37. Stoykovich, M. P. *et al.* Directed Assembly of Block Copolymer Blends into Nonregular Device-Oriented Structures. **1442**, (2014).
- 38. Neisser, M. *et al.* ITRS lithography roadmap: 2015 challenges. *Adv. Opt. Technol.* **4**, 235–240 (2015).

Chapter 2

Chemistry and physics of block copolymer materials



Block copolymers are macromolecules formed by two or more chemically distinct polymer chains joined by inter-block covalent bonds that microphase separate due to a balance between intermolecular repulsive and attractive forces. Due to the continuous trend to reduce the dimensions of integrated electronic circuits, these materials are of special interest since they have the intrinsic property of forming dense nanoscale structures at length scales not accessible using traditional lithographic techniques.

This chapter aims to give the fundamentals of block copolymers, including their synthesis and self-assembly properties.

2.1. Block copolymers and their synthesis

A copolymer is the result of a polymerization between two or more different monomers, and they are classified based on how these monomers are arranged in the chain¹, as shown in Figure 2.1. More complex architectures also exist, where different chains can form each branch.

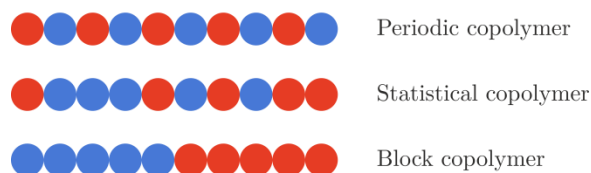


Figure 2.1. Representation of the different copolymer types

BCPs are macromolecules formed by two or more chemically distinct repeat units joined together by covalent bonds.² These materials have attracted special interest in the last few years because of their ability to self-assemble into ordered structures at the nanometer scale.³⁻⁶ The most characteristic feature of a BCP is the strong repulsion that exists between the different domains. As a result of this repulsion, BCPs tend to segregate, but as they are chemically bonded, even with a complete segregation, they cannot lead to a macroscopic phase separation, as in the case of a polymer blend. Rather, different polymers chains minimize their repulsive energy by segregating into microdomains with a length scale on the order of tens of nanometers or less. At low temperatures, the enthalpic effect drives the blocks to phase-separate, while at high temperatures entropic effects dominates and results in an homogenous mixture, as depicted in Figure 2.2.

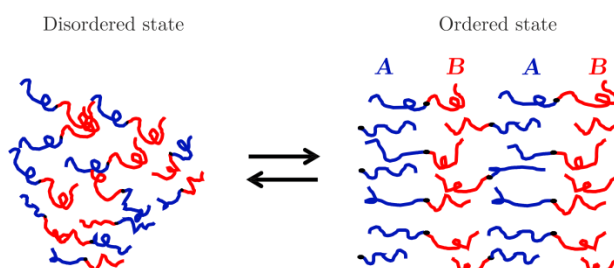


Figure 2.2. Schematic representation of disordered and ordered states of an A-B diblock copolymer

In order to synthesize a well-defined BCP, a controlled chain-growth polymerization method is needed together with an appropriate purification method. There are numerous routes to synthesize BCPs, but radical polymerization is one of the most used for commercial production of high molecular weight polymers, since it is more competitive by providing simple and reproducible mechanisms.⁷ Methods involving radical processes have been the most relevant and widely used since they can be used by a large variety of monomers and they allow very broad range of processing conditions. Nevertheless, the

conventional processes present some drawbacks regarding the molecular weight distribution, composition, and the fact that some residual monomer chains remain even after long reaction times.

In the radical polymerization processes, as depicted in Figure 2.3, the first step consists on the production of free radicals by thermal or photochemical decomposition of specific compounds, or by using high energy radiation and reduction-oxidation reactions. These free radicals react with a monomer in a way that the new molecule becomes the new free radical. Therefore, the growth of a polymer chain consists in the successive addition of monomers during propagation. The propagation step continues until all monomers are consumed. Then, the polymerization process is finished either by combination in which two growing polymer chains react with each other, or by disproportionation in which an hydrogen atom is transferred from one radical to the other resulting in two polymers. In this conventional polymerization method, the molecular weight increases rapidly at early stages and then it is reduced because of monomer exhaustion. However, in an ideal polymerization process all the chains have to grow at the same time and survive the polymerization. This can only be possible in the presence of reagents that react with radicals ($RM\cdot$) by reversible deactivation or reversible chain transfer, as described in Figure 2.4. In that case, the lifetime of an individual chain as an active specie will be lower.

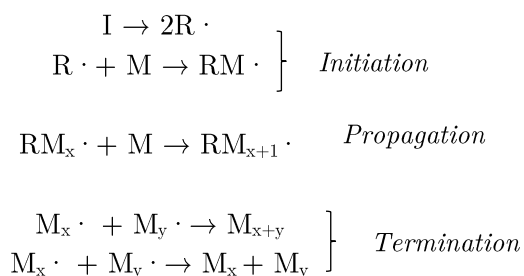


Figure 2.3. Schematic representation of conventional radical polymerization process (I , $R\cdot$ and M denote the initiator, radical and monomer species, respectively)

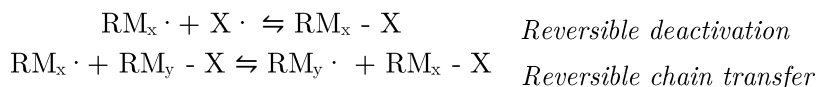


Figure 2.4. Schematic representation of radical polymerization process with reversible deactivation and chain transfer

Different living polymerization techniques have been used for the synthesis of BCPs, like nitroxide-mediated polymerization (NMP)⁸, atom-transfer polymerization (ATRP)^{9,10} or reversible addition-fragmentation chain transfer (RAFT)^{11,12}, being this last one the most convenient and useful^{13,14} since it is applicable under a large number of experimental conditions. RAFT process involves conventional radical polymerization in the presence of a suitable chain transfer agent (thiocarbonylthio RAFT agent) which mediates the polymerization process by a reversible chain-transfer process, allowing the production of low polydispersity (PDI) and high-functionality polymers. Normally, the suitable RAFT agent

described in Figure 2.5, has a thiocarbonylthio group with substituents R and Z that influence the polymerization reaction kinetics.

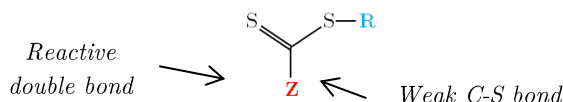


Figure 2.5. General structure of RAFT agent. R and Z are group substituents of the molecule

Figure 2.6 shows a schematic representation of how the RAFT polymerization mechanism takes place. During the initiation process (shown in the first step of Figure 2.3) the initiator is decomposed into fragments ($R\cdot$) which react with a single monomer molecule, growing a polymeric radical ($RM_x\cdot$). Polymeric radicals react in the next step with the RAFT agent to create an intermediate RAFT product which can lose either the R group ($R\cdot$) or the polymeric species ($RM_x\cdot$). After, the leaving group reacts with another monomer to create a new propagating radical referred as RM_y . Then, there is a rapid equilibrium between the active radicals and all the species that have not undertaken termination. This is the most important step in the RAFT process, and it provides equal probability to all chains to grow with narrow PDI. Finally, when the polymerization is completed, active chains react to form chains that cannot react further.¹⁵ For BCPs, there is the additional limitation that the RAFT agent must be suitable for both monomers.¹⁶

The RAFT process has emerged as one of the most important methods of living polymerization for BCP synthesis, since it can provide control over the way of initiation and termination steps and have a better chain length polymer control, a part of presenting versatility in the use of a wide number of monomers and processing conditions.

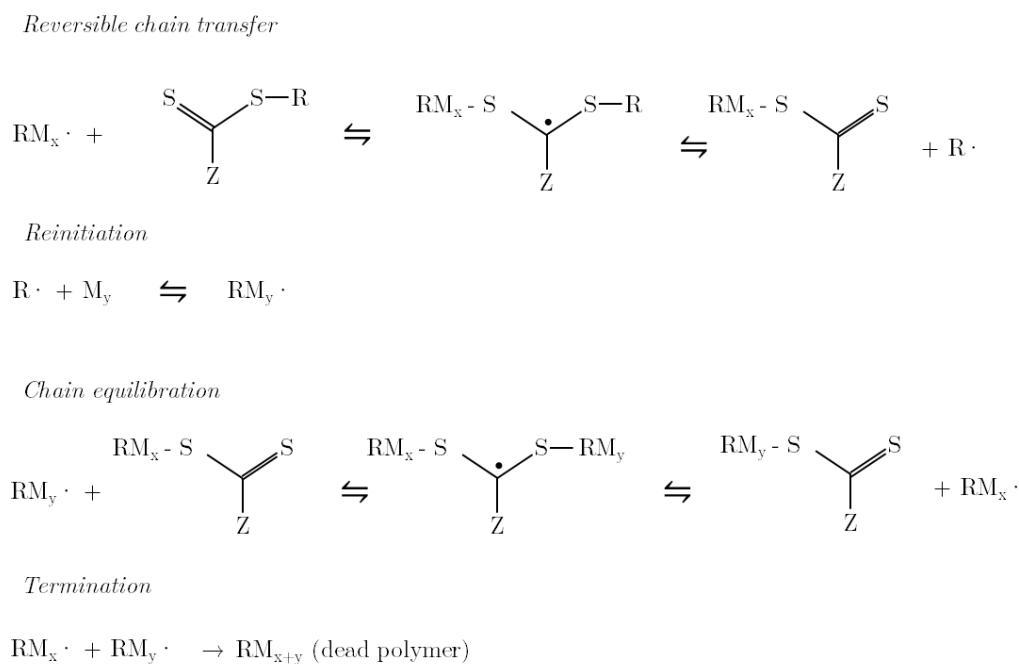


Figure 2.6. Schematic representation RAFT mechanism process

2.2. Physics of block copolymers

2.2.1. Order-disorder transition in block copolymers

The change in free energy of mixing (ΔF_m) when applied to polymer blends is described by the *Flory-Huggins* theory¹⁷ in which it is assumed that components are incompressible and mix at constant volume.¹⁸ Equation (2.1) represents the dependence of ΔF_m with the entropy contribution (ΔS_m , first two terms) and the enthalpy input (ΔH_m , third term) which includes the *Flory-Huggins* parameter, χ .

$$\frac{\Delta F_m}{k_B T} = \frac{\phi_A}{N_A} \ln \phi_A + \frac{\phi_B}{N_B} \ln \phi_B + \chi \phi_A \phi_B, \quad (2.1)$$

where ϕ_A and ϕ_B are the volume fractions of species A and B in the blend, N_A and N_B are the degree of polymerization of species A and B, $k_B T$ is the thermal energy, and χ is the *Flory-Huggins* parameter.

In contrast with homopolymer blends, diblock copolymers cannot separate macroscopically, but form ordered microphase separated morphologies due to the fact that the blocks are joined by covalent bonds and this leads to the formation of different phases depending on the volume fraction of each domain. Therefore, the *Flory-Huggins* theory is unsuitable to study the microphase separation of a BCP. *Bates and Fredrickson* have reviewed the extensive experimental and theoretical thermodynamics of BCPs.³

The phase behavior of an A-B BCP is determined by three main parameters: (i) the overall degree of polymerization, N , (ii) the volume fraction of each domain in the BCP, f , and (iii) the *Flory-Huggins* interaction parameter, χ , which represents the energy cost of two species to be mixed homogeneously and is inversely proportional to temperature. The first two parameters are dictated by the polymerization stoichiometry and the translational and configurational entropy, whereas χ is determined by the selection of the material, which has a largely enthalpic contribution. Thus, the strength of the BCP segregation power is normally expressed by the reduced parameter χN , which reflects both enthalpic and entropic contributions. By increasing χ , which favors a reduction in A-B contacts, and N , which is related to some loss of translational and configurational entropy, a local compositional ordering frequently referred to as *microphase separation* is induced. On the contrary, if either N or χ are not large enough, the entropic contributions will dominate leading to a disordered phase.

The critical point predicted by mean-field calculations for symmetric diblock copolymers is $\chi N = 10.5$.¹⁹ There exist two regimes in BCPs microphase segregation: strong^{20,21} and weak^{19,22} segregation regimes. In the strong segregation limit (SSL), where $\chi N \gg 10.5$, the interaction energy drives the blocks to segregate into well-defined microdomains and the A-B interface is narrow. In the weak segregation limit (WSL), which occurs in the vicinity of the order-disorder transition, the entropic terms are larger than the interaction term.

Therefore, the two blocks are miscible since the segregation power is not strong enough to form a sharp phase boundary between the two phases, thus the interface becomes diffuse. The boundary between the melted and segregated structures is determined by the order-disorder temperature, T_{ODT} , where the thermal energy is comparable to the interaction energy of the two blocks.

For $f = 0.5$, the transition between ordered and disordered states occurs when χN is approximately 10.5.²³ Therefore, when $\chi N \ll 10.5$, entropy dominates the energetic penalty of mixing A and B segments, resulting in a disordered phase. As this value increases, A and B domains remain ordered in the microscopic scale since they are chemically joined.

2.2.2. Morphologies of diblock copolymers

As previously described, the structure resulting from the BCP microphase separation will depend on the degree of polymerization, the composition of the BCP and the chemical interaction between blocks. The phase behavior of an A-B diblock copolymer has been studied experimentally²⁴ and a successful theoretical correlation has been found by using the self-consistent field theory (SCFT).^{21,25-27} Based on SCFT, *Matsen and Bates*²⁷ constructed a phase diagram for an A-B copolymer from the WSL to the SSL, and it was observed that for the WSL the SCFT results agree with *Leibler* who first showed the phase diagram in this region.¹⁹

Figure 2.7 shows the most updated phase-diagram for an A-B diblock copolymer²⁸ which consists on a representation of χN as a function of f . The BCP morphology will depend basically on the strength of the interactions between monomers and the bulk fraction of each domain. The phase diagram shows that by increasing f , body-centered cubic (bcc) spherical (S), hexagonal-close packed (hcp) spherical (S_{cp}), cylindrical (C), gyroid (G) and lamellar (L) structures are predictable. Figure 2.8 shows a schematic of the most useful microphase arrangements of blocks in an A-B diblock copolymer as a function of f .

Over the years, there have been several contributions to the phase diagram, and lately another morphology has been identified both theoretically²⁹ and experimentally corresponding to the *orthorhombic Fddd* phase (O^{70}).³⁰⁻³³ On the other hand, it can be inferred that for a symmetric system, below $\chi N = 10.5$ the system is disordered, and between 10.5 and 12.5 it is found the WSL, in which it is expected to appear some disordered regions due to thermal effects derived from the fact that the thermodynamic driving force, is small.

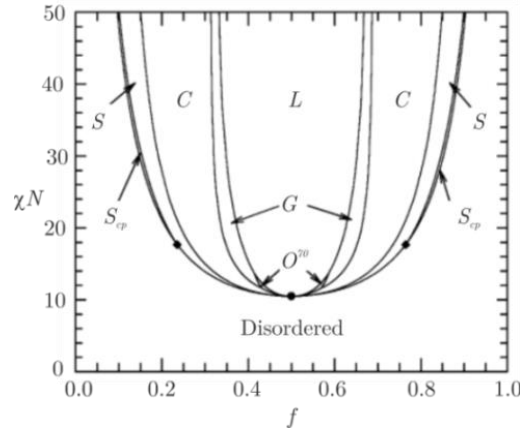


Figure 2.7. Phase diagram for an A-B diblock copolymer showing the ordered lamellar (L), cylindrical (C), spherical (S), gyroid (G) and $Fddd$ (O^{70}) morphologies²⁸

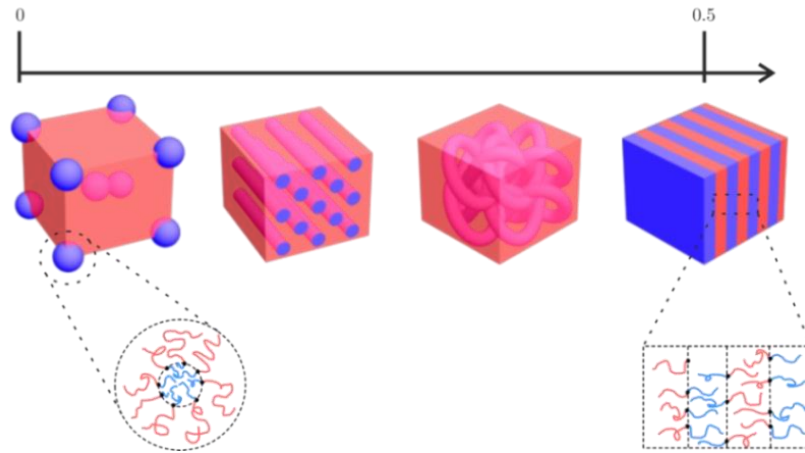


Figure 2.8. Schematics of the most common ordered-state morphologies found in an A-B diblock copolymer as a function of f . Above $f = 0.5$, the hierarchy reverses, i.e. the morphology phases repeat with the blocks reversed

For non-crystallizable homopolymers there is a thermal transition where upon heating, the material changes from a vitreous solid to the viscous or rubbery liquid state. This temperature is called *glass transition temperature*, T_g , and above it polymer chains have greater mobility since polymer free volume increases. BCPs exhibit two T_g corresponding to their constituent blocks, so in order to allow BCP molecules diffuse freely, it has to be heated above the largest T_g , and the film becomes more ordered over time. Nevertheless, there is a limit on temperature which is set by the stability of the polymer that can undergo crosslinking or chain scission.

2.2.3. Block copolymers in thin films

In lithographic applications, BCPs are used to form thin films, so the phase behavior is actually richer than in bulk, since there are effects induced by the interfaces involving air and the substrate. Generally, thin films are produced by coating a substrate with a dilute polymer solution in an appropriate solvent for both blocks. BCPs show the same

morphology as in bulk, but the orientation of the phase strongly depends on the boundaries, i.e. on the interaction between the domains and the substrate.

2.2.3.1. Role of surface affinity

Figure 2.9 shows a cylindrical A-B diblock copolymer self-assembled onto two different systems. When the substrate has a neutral attraction for both domains, the cylinders are oriented perpendicular to the substrate, whereas if the substrate strongly attracts one of the domains, the free energy is minimized by forming a layer with cylinders oriented parallel to the substrate.

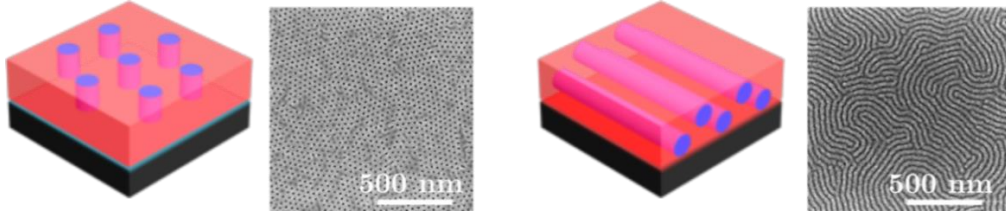


Figure 2.9. Schematic and SEM images of cylindrical PS-b-PMMA block copolymer, showing different polymer blocks-surface interactions

2.2.3.2. Role of block copolymer film thickness

In a thin film, the BCP morphology is strongly influenced by the boundary conditions determined by the surface and the interface of the film. The total free energy of an A-B diblock copolymer thin film can be expressed as a sum of the contributions from its internal structure, F_{bulk} , and from its surface/interface, F_{surf} , as shown in equation (2.2):

$$F = F_{bulk} + F_{surf} = (F_{A/B} + F_{conf}) + (F_{A/subs} + F_{B/subs} + F_{A/air} + F_{B/air}), \quad (2.2)$$

where $F_{A/B}$ is the interfacial energy between A and B, F_{conf} is the conformational entropy of A and B, and $F_{A/air}$, $F_{B/air}$, $F_{A/subs}$ and $F_{B/subs}$ are the interaction energies between each domain and the air or substrate, respectively.

Normally, in a DSA process, BCP film thickness, d , is less than few nanometers the BCP pitch, L_0 , and hence the contribution of the surface to the total free energy, F , becomes significant. Therefore, the effect of commensurability between BCP film thickness, d , and its natural period, L_0 , is critically important, and it makes the film thickness to be an integer or half-integer of L_0 . If not, the energy due to the conformational entropy of the A and B polymer chains becomes too high and leads to non-homogeneous BCP films.

Figure 2.10 shows a general overview of the different morphologies that a lamellar diblock copolymer can present depending on the interface energies between the domains and the air and substrate, respectively. As it can be observed, the surface and air are in contact with the polymer which presents lower interface energy and the BCP is oriented parallel to the substrate when domains present different interface energies with air and substrate. In that

situation, one has to take into account that the film thickness has to be equal to $n \cdot L_0$ or $(n+0.5) \cdot L_0$, in order to not change the natural bulk period, L_0 . When film thickness does not commensurate with $n \cdot L_0$ or $(n+0.5) \cdot L_0$, the system tends to minimize its free energy by forming spontaneously macroscopic islands or holes. On the other hand, perpendicular lamellae are observed when both the air and the substrate present equal affinity for both BCP domains, and no commensurability effect due to film thickness is present.

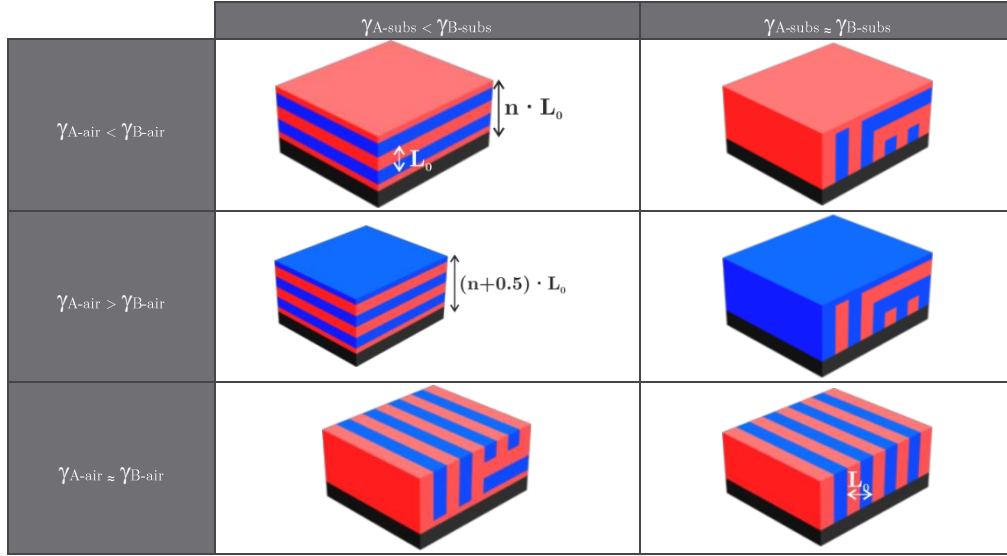


Figure 2.10. Schematic illustrations of a lamellar A-B BCP thin film varying interfacial affinities. γ_{A-sub} , γ_{B-sub} , γ_{A-air} and γ_{B-air} represent the interfacial energies of A and B with respect to the substrate and air, respectively

As described in Figure 2.11, when BCP do not accomplish the film thickness commensurability condition, because of stretching or compression effects which are energetically unfavorable, BCP tends to mitigate them and fulfill the commensurability condition, by creating some holes or terraces with different number of layers. As it can be observed in the SEM image, in the region where the BCP has a perpendicular orientation, the BCP does not fit the commensurability condition, and therefore it adopts the morphology in which there is no restriction with the film thickness.

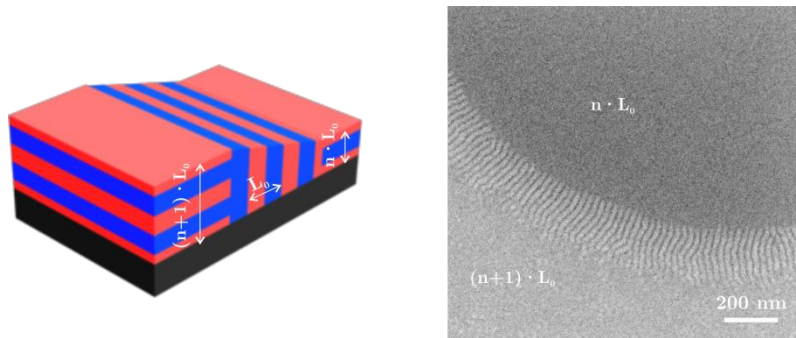


Figure 2.11. Schematics of a lamellar A-B diblock copolymer confined in a system with preferential affinity to red domains on the substrate and air with initial thickness of $(n+0.5) \cdot L_0$

2.2.4. Interface neutralization

Technological applications require transferring the patterns into a functional material and therefore, there is the need to control the BCP morphology. In general, strong preferential interactions occur between one of the BCP domains and the substrate, which leads to wetting morphologies at the polymer-brush interface. Therefore, the surface has to be able to balance the surface free energies for both BCP domains. This can be overcome by creating a neutral substrate and thus, controlling the interface energies in order to promote the desired morphology uniformly over the whole sample. The most used technique to achieve this goal was first introduced by Mansky,³⁴ and it consists in using a *brush polymer* based on the use of random copolymers to induce the perpendicular orientation of BCPs. By properly tuning the brush layer composition, the interface energies can be well controlled and thus, the final BCP morphology.

On the other hand, high- χ BCPs have normally a large surface energy between the two blocks, and this leads to a parallel oriented morphology.³⁵ Therefore, it is important to have a balance between the film thickness, the substrate and the interface energies.^{34,36,37} In order to control the interface energy between the air and the BCP and thus its orientation, there exist other different approaches that can be used, including solvent annealing^{38,39}, electric^{40,41} or magnetic⁴² fields, or the use of top-coats.^{6,43} The use of top-coats is more compatible with lithographic processes, but top-coats must be soluble in a solvent that do not disturb the BCP self-assembly.

2.2.5. Thermal and solvent annealing of block copolymer films

As it has been mentioned previously, in order to promote and enhance the ordering of the BCP microdomains it is necessary to introduce some mobility on polymer chains to facilitate the microphase separation process. Furthermore, when using BCP thin films, the molecules are in a non-equilibrium state, trapped on a solvent, and cannot form an ordered large area.^{3,44} In order to promote the equilibrium morphology, either thermal treatments or processes in which a solvent vapor is used can be employed.

2.2.5.1. Thermal annealing processes

BCP phase-separation is promoted by the strength of the repulsive interaction between blocks, χN , where χ depends on the temperature as:

$$\chi = \left(\frac{Z}{k_B T} \right) \left[\epsilon_{AB} - \frac{(\epsilon_{AA} + \epsilon_{BB})}{2} \right], \quad (2.3)$$

where Z is the number of nearest neighbors per monomer in the polymer, $k_B T$ is the thermal energy, and ϵ_{AB} , ϵ_{AA} , ϵ_{BB} are the interaction energies between A and B, A and A, and B and B, respectively.

Taking account equation (2.3), χ decreases as function of temperature, but at high temperatures, χ is high enough to induce microphase separation. Thermal treatments consist on annealing the BCP above its T_g but below T_{ODT} , in order to increase the mobility of the molecules and promote the microphase separation. These processes are strictly controlled by the BCP film thickness since the compression of polymer chains is energetically unfavorable. Therefore, the microphase separation occurs in the way to reduce the entropic penalty; that is, if the initial film thickness is commensurate with the boundary conditions (see Figure 2.10), then the film is stable and homogeneous. Additionally, in order to minimize the total free energy, the system develops different morphologies. As compared with other processes, thermal treatments are preferred since there is equipment already implemented in industry and there is no waste stream.⁴⁴ Nevertheless, thermal treatments are not very effective for some systems which require very long annealing time due to their high T_{ODT} ⁴⁵ and sometimes they are not suitable for systems which undergo degradation under high temperatures. To address these issues, processes involving the use of a solvent are used.

2.2.5.2. Solvent annealing processes

Solvent vapor annealing processes offer flexibility regarding the choice of the solvent and processing conditions, and they permit avoiding the budget temperature that thermal processes involve, since the BCP glass transition temperature is decreased by exposing the sample to a vapor.^{46,47} In these processes, polymer thin films are exposed to one or more solvents at temperatures below T_g for a period of time to form a swollen and mobile polymer film.^{48,49} During the evaporation process, there exists a gradient of solvent concentration which goes from the surface to the inside of the film, thus occurring first the ordering at the film surface.

When solvent annealing processes are used, one has to take into account that the solvent may affect the interaction between BCP domains⁵⁰ and polymer interaction with the substrate. The miscibility between a polymer and a solvent is governed by the interaction *polymer-solvent* parameter, χ_{ps} , which can be estimated with the molar volume of the solvent, and the solubility parameters of the solvent and polymer. By using the *Flory-Huggins* interaction criteria, the complete miscibility between polymer and solvent is achieved when $\chi_{ps} < 0.5$, and the affinity between them is stronger when the χ_{ps} value is decreased. Therefore, the selection of a solvent may induce some changes in the degree of microphase separation. On the other hand, it presents a disadvantage in the kinetics when using high- χ BCP systems and therefore, some works have been reported to improve processing time up to some minutes. These results show that a previous heating of the solvent induces a smaller activation energy for the BCP diffusion and thus well-ordered nanostructures can be formed in shorter times.^{51,52}

By conveniently combining both processes, highly ordered structures with low defectivity and by using shorter annealing times can be achieved. In this process, known as *solvothermal annealing processes*, the BCP sample is exposed to a solvent vapor and consequently irradiated with microwave energy.^{53,54}

2.3. Modelling of block copolymer directed self-assembly

The phase behavior of simple BCPs is understood rather well, although there are some disagreements between theoretical and experimental results.^{19,55,56} Therefore, the role of computational modeling consists mainly on exploring parameter variations on the DSA physical mechanism which are difficult to obtain in experiments.

Modelling the DSA process requires a hierarchical approach, since polymeric materials exhibit structure on very different scales, ranging from Ångströms to micrometers, and thus the modelling challenge consists in devising models and combining information provided by the different DSA models. It follows that they cannot be included in the same theoretical framework, and different theoretical approaches have been developed depending on the length and time scales.

On the one hand, *atomistic models* provide an accurate prediction of local properties of self-assembled systems with dimensions around 10 nm, and on the other hand, *coarse-grained models* describe the microphase separation in mixed systems by field-theoretic representations of polymer molecules in combination with self-consistent-field calculations on scales in the order of 10 nm to 1 μm .

The atomistic information (statistical segment length, *Flory-Huggins* parameter, the surface energies and the self-diffusion coefficient) is used to parameterize the coarse-grained models, which, in turn, allow predicting the free energy of defects, the DSA kinetics and the mechanisms of defect generation and annihilation. Then, the information provided by the coarse-grained models can be used to calibrate a reduced model that can be integrated into a lithographic process simulation, by coarse-graining or reverse-mapping the information.

Figure 2.12 shows a schematic representation of the three models as a function of the length and time scale. As observed, there is a need of different models and simulation techniques that target properties at different length and time scales, since there is no single model capable of simultaneously extracting all relevant DSA parameters.⁵⁷

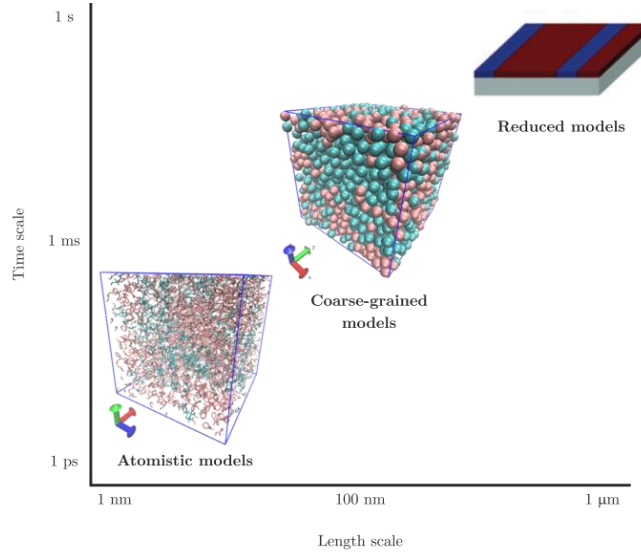


Figure 2.12. Adapted schematic illustration of the different models as a function of time and length scales⁵⁸

2.3.1. Block copolymer kinetics

From the disordered to the ordered state, as the BCP films equilibrate, the individual BCP chains move diffusing through the ever-growing domain interfaces adopting more energetically favorable states. This means that low free-energy defect structures, such as dislocations, can persist but eventually move to the lowest energy state at equilibrium.

Experimentally it is observed that DSA processes induces a diversity of defects which limits the application of BCP DSA into the industry (industry standards require less than 0.01 defects/cm²).⁵⁹ Defects can be conceived as thermal fluctuations in the vicinity of the order-disorder transition where the excess of free energy is comparable to the thermal energy scale, $k_B T$. Outside the vicinity of the order-disorder transition, where the defect excess of free energy is significantly larger than $k_B T$, they directly come from the kinetics of structure formation.⁶⁰ Additionally to the thermodynamic equilibrium properties, the kinetics of BCP formation is also important since BCPs do not usually form spontaneously long-range-ordered features and they require a thermal or solvent annealing. Therefore, since diffusivity exhibits an Arrhenius dependence (equation (2.4)) annealing times determine the ability of the BCP to eliminate defects.⁶¹ On the other hand, the difference of free energy between the defective and the defect free state is the driver for eliminating defects and it decreases as χN increases.⁶² The higher χN the greater is the penalty for mixing in an exponential decrease in diffusion:

$$D = D_0 e^{-0.28(\chi N - 3.5)}, \quad (2.4)$$

where D_0 is the diffusion coefficient of the corresponding non-phase separated polymer.

Equation (2.4) explains why in high- χ BCPs the self-assembly kinetics is very slow (exponential decrease of BCP chain mobility with respect to χN). Therefore, solvent annealing processes are very suitable because they can offer polymer chain mobility at low temperature, thus avoiding the problem of slow self-assembly behavior.

On the other hand, when the BCP self-assemble on a chemical guiding pattern, it can strongly influence the kinetics by modifying the free energy background. The self-assembly kinetics is much slower when the guiding pattern dimensions do not commensurate with L_0 , when the chemical interactions between the BCP domains and substrate are weak or when using high density multiplication patterns. Therefore, it is important to understand and control the self-assembly kinetics to annihilate the final trapped defect states, especially observed in line/space patterns. The use of a soft, coarse-grained polymer model is suitable to describe the kinetics of the structure formation since it evolves in time scales of minutes or hours, which are non-accessible for atomistic modeling.⁶³

2.3.2. Field-theoretic simulations and self-consistent field theory

The coarse-grained model denotes the polymer conformations and their interactions through a coarse-grained bead-spring representation. In this modelling, the atomistic information is used to correlate material properties to the thermodynamics and kinetics of the DSA process.^{64,65} Coarse-grained models study complex and three-dimensional DSA processes on the scale of hundreds of nanometers and minutes since the interactions between segments are weak. Small number of atoms are grouped into segments, and then the interactions between these coarse-grained segments are calculated.^{57,66,67} These softer interactions arise as a consequence of coarse-graining and can be explained because of the excluded volume interactions, due to the fact that in the microscopic scale atoms cannot overlap (Pauli's principle).^{68,69} Therefore, these soft volume interactions allow for an overlap between the coarse-grained segments.

In the case of a binary blend, the coarse-grained parameters which describe the interactions and correlations on short length scales are, the incompatibility between molecules, χN , the compressibility, κN , the chain dimensions, R_{eo} , and the invariant degree of polymerization, \bar{N} , which quantifies the number of neighbors a molecule interacts with:

$$\bar{N} \equiv \left(\frac{\rho_o}{N_{cg}} R_{eo}^3 \right)^2, \quad (2.5)$$

where ρ_o is the number density of segments and N_{cg} represents the number of coarse-grained interaction centers. N is a dimensionless parameter and it is smaller than the smallest length scale of physical interest and it is on the range between 16 and 128. χN determines the phase behavior, κN limits the fluctuations of the total density, R_{eo} depicts the length scale, and \bar{N} controls the strength of long wavelength composition fluctuations.⁶³

On the other hand, in order to characterize the contact of the DSA domains with the confining boundaries, the surface and interface tensions are used as the coarse-grained invariant parameters. These interactions are represented by convenient force fields and the strength of each of those interactions as depicted in Table 2.1.

Additionally, in order to compute the free energy and the thermodynamic forces that drive the structure formation self-consistent field calculations are used. These calculations are based on a mean-field approximation which allows for the calculation of free energies of self-assembled morphologies.⁷⁰

Table 2.1. Invariant parameters of the coarse-grained model

Interactions	Invariant coarse-grained parameters
Chain connectivity	R_{eo} : mean squared end-to-end distance of non-interacting polymer coils
	f : fraction of polymer domains
Polymer melt	κN : isothermal liquid compressibility · Invariant degree of polymerization
Repulsion between unlike species	χN : Flory Huggins parameter · Invariant degree of polymerization
Interaction of the domains with the guiding pattern	Geometry of confinement (measured in units of R_{eo} or L_o)
	γ_{SA} , γ_{SB} : Surface free-energies of the segments species with the confining boundaries
Dynamics of macromolecules	D : Self-diffusion coefficient which defines time scale

These particle-based models described before provide detailed information of the macromolecular conformations, but they are too expensive to explore the DSA on large-scale lithographic processes. Therefore, new reduced models are being studied since they can be integrated into a lithographical process flow: *Continuum models*^{71–73} and *interface Hamiltonians*.^{74,75} On the one hand, continuum models describe DSA processes by collective variables in space and time in order to predict the three-dimensional BCP structure, and they can be derived from the SCFT in the WSL between domains. On the other hand, interface Hamiltonians describe the DSA process by only the evolution of the interfaces between the copolymer domains, and they provide an appropriate description on the SSL. They overcome the limitations of continuum models in dealing with the disparity between interfaces, although it is difficult to derive these interactions in complex geometries

2.4. High-chi block copolymers

Currently, microelectronics industry is demanding the development of new methods focused on the production of ever-smaller structures. DSA is an alternative technique which provides a complementary solution to the resolution limitation of conventional lithography. PS-*b*-PMMA has been the most studied BCP system, principally due to the fact that both PS and PMMA have almost equal surface energies which allows forming morphological and

uniform patterns all the way through the film.³⁴ On the other hand, PMMA can be easily etched by oxygen plasma or UV exposure + wet etching, and then the remaining material can be used as a mask for pattern transfer.^{76,77} Moreover, new techniques based on using SIS have been recently reported showing very high aspect ratio structures after pattern transfer, due to the fact of an enhancement on the etch selectivity between PS and PMMA.⁷⁸⁻⁸⁰

As discussed previously, when the enthalpic contributions are sufficiently large to overcome the entropy to mix the blocks, the microphase segregations occurs originating different nanostructures depending on the relative volume fraction of the two blocks. For lamellar block copolymer ($f = 0.5$), this condition occurs when the product χN is above 10.5, which means that every BCP has a minimum achievable size.^{3,19} Therefore, in order to obtain smaller features, the degree of polymerization, N , has to be reduced since it reduces the characteristic BCP length scale, and the χ value has to be increased to balance the product χN and keep constant the level of phase segregation. In that sense, since PS-*b*-PMMA has a low χ value (0.041 at 25°C),¹⁸ its minimum feature size is around 12 nm and therefore, its utility for the next generation nodes is restricted.^{6,38,81} Therefore, in order to achieve smaller domains, a BCP with larger interaction parameter has to be used. Nevertheless, the design of high- χ systems which provide sub-20 nm resolution has to be demonstrated with a controlled BCP synthesis and with a good etching selectivity.

The generation of high- χ BCP systems can be performed by introducing polymer domains which have stronger interactions among identical monomers and high incompatibility among different domains. Normally it can be achieved by introducing very highly polar groups, fluorine or silicon-rich blocks.

2.4.1. Organic based high- χ block copolymers

Organic based BCP usually present low χ values. Moreover, these BCP share similar chemistries which it is translated in a low etching contrast between blocks, and consequently low aspect ratio features.⁸² An example of organic high- χ BCP system is poly(styrene-*b*-D,L-lactide), PS-*b*-PLA, with both hydrophobic (PS) and hydrophilic (PLA) domains. This amphiphilic nature gives rise to a χ value of 0.23.⁸³ Other organic high- χ BCP are depicted in Table 2.2.

However, such materials are generally difficult to generate due to their dissimilar polarities and properties between blocks. This means that they cannot easily show the perpendicular morphology with a thermal annealing as does PS-*b*-PMMA, and they need either a solvent annealing or an additional top-coat layer.

2.4.2. Inorganic based high- χ block copolymers

Inorganic based BCP are being intensively studied due to the high etching contrast between domains. They are normally formed by one organic domain and one inorganic block which is resistant to oxygen plasma. The inorganic part is normally a silicon or iron containing domain which forms the corresponding oxide after oxygen plasma exposure and retains the pattern from the original features. The first polymer used was polydimethylsiloxane (PDMS)-containing BCP with a backbone formed by Si-O bonds.⁸⁴

The highest- χ BCP system synthesized so far, is an ABA triblock copolymer containing PLA and PDMS end and midblock, respectively.⁸⁵ These domains are extremely incompatible ($\chi = 1.4$) and PDMS provides a high etch resistivity, while PLA is almost twice as susceptible to be etched compared to PS. Other inorganic high- χ systems are summarized in Table 2.2.

Table 2.2. Organic and inorganic high- χ BCP systems collected from several works at 25°C

Organic BCPs		Inorganic BCPs	
BCP system	χ value	BCP system	χ value
PS- <i>b</i> -PMMA	0.041 ¹⁸	PS- <i>b</i> -PFS	0.08 ⁸⁴
PS- <i>b</i> -PEO	0.077 ⁸⁶	PS- <i>b</i> -PDMS	0.26 ⁸⁴
PS- <i>b</i> -P2VP	0.178 ⁸⁷	PTMSS- <i>b</i> -PLA	0.46 ³⁹
PS- <i>b</i> -PLA	0.233 ⁸³	PS- <i>b</i> -MH	0.58 ⁸⁸
PS- <i>b</i> -PI	0.110 ⁸⁹	PLA- <i>b</i> -PDMS- <i>b</i> -PLA	1.4 ⁸⁵

There are other high- χ systems which combine BCPs with inorganic species to form an hybrid material.⁹⁰ *Park et al.* describe a system consisting of a mixture of poly(styrene-*b*-ethylene oxide), PS-*b*-PEO, and a low molecular weight organosilicate forming 7 nm pitch lamellae morphology. On the other hand, there are other examples in which a metal salt is selectively added to a PS-*b*-PEO, reducing its size to 3 nm.⁹¹ Nevertheless, the fact of adding a metal salt can bring complications during the processing steps.

Once the basis of BCP chemistry and physics has been studied, in the next chapters the different chemical and graphoepitaxy processes developed and optimized at IMB-CNM will be described. These processes will be implemented for both PS-*b*-PMMA and high- χ materials. All these results, lead to implement the chemical epitaxy process at larger scale in the cleanroom of CEA-Leti which operates with a wafer scale of 300 mm. Moreover, the role of the chemical interactions which take place between the guiding pattern and the BCP domains will be experimentally characterized and modelled.

2.5. References

1. Jenkins, A. D., *et al.* Glossary of Basic Terms in Polymer. *Pure Appl. Chem.* **68**, 2287–2311 (1996).
2. Hamley, I. W. *The physics of block copolymers*. (Oxford University Press, 1998).
3. Bates, F. S. *et al.* Block copolymer thermodynamics: theory and experiment. *Annu. Rev. Phys. Chem.* **41**, 525–557 (1990).
4. Park, C., *et al.* Enabling nanotechnology with self assembled block copolymer patterns. *Polymer*. **44**, 6725–6760 (2003).
5. Segalman, R. Patterning with block copolymer thin films. *Mater. Sci. Eng. R Reports* **48**, 191–226 (2005).
6. Bates, C. M. *et al.* Polarity-switching top coats enable orientation of sub-10-nm block copolymer domains. *Science* **338**, 775–9 (2012).
7. Moad, G. *et al.* The Chemistry of Radical Polymerization. Oxford Editions (2006).
8. Solomon, D. H., *et al.* Polymerization process and polymers produced thereby. US patent (US4581429) (1986).
9. Kato, M., *et al.* Polymerization of Methyl Methacrylate with the Carbon Tetrachloride Dichlorotris- (triphenylphosphine)ruthenium(II)/Methylaluminum Bis(2,6-di-*tert*-butylphenoxide) Initiating System: Possibility of Living Radical Polymerization. *Macromolecules* **28**, 1721–1723 (1996).
10. Wang, J. S. *et al.* Controlled ‘living’ radical polymerization. Atom transfer radical polymerization in the presence of transition-metal complexes. *J. Am. Chem. Soc.* **117**, 5614–5615 (1995).
11. Le, T. P., *et al.* Polymerization with living characteristics. (WO1998001478) (1998).
12. Chiefari, J. *et al.* Living Free-Radical Polymerization by Reversible Addition - Fragmentation Chain Transfer : The RAFT Process We wish to report a new living free-radical polymerization of exceptional effectiveness and versatility, *Macromolecules* **31**, 5559–5562 (1998).
13. Rizzardo, E. *et al.* Tailored polymers by free radical processes. *Macromol. Symp.* **143**, 291–307 (1999).
14. Chiefari, J. *et al.* *Handbook of radical polymerization*. (John Wiley & Sons, 2002).
15. Moad, G., *et al.* Living radical polymerization by the RAFT process. *Aust. J. Chem.* **58**, 379–410 (2005).
16. Perrier, S. *et al.* Macromolecular design via reversible addition-fragmentation chain transfer (RAFT)/xanthates (MADIX) polymerization. *J. Polym. Sci. Part A Polym. Chem.* **43**, 5347–5393 (2005).

17. Flory, P. J. Principles of Polymer Chemistry. C. Press (1953).
18. Russell, T. P. Temperature Dependence of the Interaction Parameter of Polystyrene and Poly (methyl methacrylate). *Macromolecules* **890**–893 (1990).
19. Leibler, L. Theory of microphase separation in block copolymers. *Macromolecules* **13**, 1602–1617 (1980).
20. Meier, D. J. Theory of Block Copolymers. I. Domain Formation in A-B Block Copolymers. *J. Polym. Sci. Part C* **26**, 81–98 (1969).
21. Helfand, E. Block Copolymer Theory. III. Statistical Mechanics of the Microdomain Structure. *Macromolecules* **8**, 552–556 (1975).
22. Fredrickson, G. H. *et al.* Fluctuation effects in the theory of microphase separation in block copolymers. *J. Chem. Phys.* **87**, 697 (1987).
23. Bates, F. S. Polymer-Polymer Phase Behavior. *Science*. **251**, (1990).
24. Bates, F. S. *et al.* Fluctuations, Conformational Asymmetry and Block Copolymer Phase Behaviour. *Faraday Discuss.* **98**, 7–18 (1994).
25. Vavasour, J. D. *et al.* Self-consistent mean field theory of the microphase diagram of block copolymer/neutral solvent blends. *Macromolecules* **25**, 2041–2045 (1992).
26. Matsen, M. W. *et al.* Stable and unstable phases of a diblock copolymer melt. *Phys. Rev. Lett.* **72**, 2660–2663 (1994).
27. Matsen, M. W. *et al.* Unifying Weak- and Strong-Segregation Block Copolymer Theories. *Macromolecules* **29**, 1091–1098 (1996).
28. Matsen, M. W. Effect of architecture on the phase behavior of AB-type block copolymer melts. *Macromolecules* **45**, 2161–2165 (2012).
29. Tyler, C. A. *et al.* Orthorhombic Fddd network in triblock and diblock copolymer melts. *Phys. Rev. Lett.* **94**, 1–4 (2005).
30. Bailey, T. S., *et al.* A noncubic triply periodic network morphology in poly(isoprene-*b*-styrene-*b*-ethylene oxide) triblock copolymers. *Macromolecules* **35**, 7007–7017 (2002).
31. Kim, M. I. *et al.* Stability of the Fddd phase in diblock copolymer melts. *Macromolecules* **41**, 7667–7670 (2008).
32. Im Kim, M. *et al.* Determination of the FDDD phase boundary in polystyrene-block-polyisoprene diblock copolymer melts. *Macromolecules* **42**, 5266–5271 (2009).
33. Takenaka, M. *et al.* Directed self-assembly of block copolymers. *Curr. Opin. Chem. Eng.* **2**, 88–94 (2013).
34. Mansky, P. Controlling Polymer-Surface Interactions with Random Copolymer Brushes. *Science*. **275**, 1458–1460 (1997).

35. Maher, M. J. *et al.* Interfacial design for block copolymer thin films. *Chem. Mater.* **26**, 1471–1479 (2014).
36. Huang, E., *et al.* Neutrality conditions for block copolymer systems on random copolymer brush surfaces. *Macromolecules* **32**, 5299–5303 (1999).
37. Hur, S.-T., *et al.* H. Investigation for correlation between elastic constant and thermal stability of liquid crystalline blue phase I. *Soft Matter* **7**, 8800 (2011).
38. Cushen, J. D. *et al.* Oligosaccharide/silicon-containing block copolymers with 5 nm features for lithographic applications. *ACS Nano* **6**, 3424–3433 (2012).
39. Cushen, J. D. *et al.* Thin Film Self-Assembly of Poly(trimethylsilylstyrene- b - d , l - lactide) with Sub-10 nm Domains. *Macromolecules* **45**, 8722–8728 (2012).
40. Boker, A. *et al.* Large scale domain alignment of a block copolymer from solution using electric fields. *Macromolecules* **35**, 1319–1325 (2002).
41. Olszowka, V. *et al.* Electric field alignment of a block copolymer nanopattern: direct observation of the microscopic mechanism. *ACS Nano* **3**, 1091–1096 (2009).
42. Gopinadhan, M. *et al.* Thermally switchable aligned nanopores by magnetic-field directed self-assembly of block copolymers. *Adv. Mater.* **26**, 5148–5154 (2014).
43. Maher, M. J. *et al.* Directed Self-Assembly of Silicon-Containing Block Copolymer Thin Films. *ACS Appl. Mater. Interfaces* **7**, 3323–3328 (2015).
44. Bates, C. M., *et al.* Block copolymer lithography. *Macromolecules* **47**, 2–12 (2014).
45. Han, E. *et al.* Perpendicular Orientation of Domains in Cylinder-Forming Block Copolymer Thick Films by Controlled Interfacial Interactions. *Macromolecules* **42**, 4896–4901 (2009).
46. Bang, J. *et al.* Defect-free nanoporous thin films from ABC triblock copolymers. *J. Am. Chem. Soc.* **128**, 7622–7629 (2006).
47. Jeong, J. W., *et al.* Highly Tunable Self-Assembled Nanostructures from a Poly(2-vinylpyridine-b-dimethylsiloxane) Block Copolymer. *Nano Lett.* **11**, 4095–4101 (2011).
48. Sinturel, C., *et al.* Solvent vapor annealing of block polymer thin films. *Macromolecules* **46**, 5399–5415 (2013).
49. Park, W. I. *et al.* Tunable and rapid self-assembly of block copolymers using mixed solvent vapors. *Nanoscale* **6**, 15216–21 (2014).
50. Yu, X. *et al.* Morphology development of ultrathin symmetric diblock copolymer film via solvent vapor treatment. *Macromolecules* **37**, 7301–7307 (2004).
51. Lodge, T. P. *et al.* Mechanisms of chain diffusion in lamellar block copolymers. *Phys. Rev. Lett.* **75**, 657–660 (1995).

52. Ruiz, R., *et al.* Effect of structural anisotropy on the coarsening kinetics of diblock copolymer striped patterns. *Phys. Rev. B - Condens. Matter Mater. Phys.* **77**, 1–5 (2008).
53. Zhang, X., *et al.* Fast assembly of ordered block copolymer nanostructures through microwave annealing. *ACS Nano* **4**, 7021–7029 (2010).
54. Gotrik, K. W. *et al.* Solvothermal annealing of block copolymer thin films. *Nano Lett.* **13**, 5117–5122 (2013).
55. Semenov, A. N. Contribution to the theory of microphase layering in block-copolymer melts. **1256**, 733–742 (1985).
56. Fredrickson, G. H. Dynamics and rheology of inhomogeneous polymeric fluids: A complex Langevin approach. *J. Chem. Phys.* **117**, 6810–6820 (2002).
57. Praprotnik, M., *et al.* Multiscale simulation of soft matter: from scale bridging to adaptive resolution. *Annu. Rev. Phys. Chem.* **59**, 545–571 (2008).
58. Computational Lithography for directed Self Assembly: Materials, Models and Processes (CoLiSA: 619793). European Union Seventh Framework Programme
59. Jeong, S. J., *et al.* Directed self-assembly of block copolymers for next generation nanolithography. *Mater. Today* **16**, 468–476 (2013).
60. Li, W. *et al.* Defects in the Self-Assembly of Block Copolymers and Their Relevance for Directed Self-Assembly. *Annu. Rev. Chem. biomol. Eng.* 187–218 (2015).
61. Takahashi, H. *et al.* Defectivity in laterally confined lamella-forming diblock copolymers: Thermodynamic and kinetic aspects. *Macromolecules* **45**, 6253–6265 (2012).
62. Peters, A. J., *et al.* Understanding defects in DSA: calculation of free energies of block copolymer DSA systems via thermodynamic integration of a mesoscale block-copolymer model. *Proceeding SPIE* **9049**, 90492E (2014).
63. Daoulas, K. C., *et al.* Morphology of multi-component polymer systems: single chain in mean field simulation studies. *Soft Matter* **2**, 573 (2006).
64. Stoykovich, M. P. *et al.* Directed Self-Assembly of Block Copolymers for Nanolithography: Essential Integrated Circuit Geometries. **1**, 168–175 (2007).
65. Müller, M. Geometry-controlled interface localization-delocalization transition in block copolymers. *Phys. Rev. Lett.* **109**, 1–5 (2012).
66. Baschnagel, J. *et al.* Computer simulations of polymers close to solid interfaces: Some selected topics. *Interface Sci.* **11**, 159–173 (2003).
67. Mullinax, J. W. *et al.* Generalized Yvon-Born-Green Theory for Molecular Systems. *Phys. Rev. Lett.* **103**, 1–4 (2009).

68. Noid, W. G. *et al.* The multiscale coarse-graining method. I. A rigorous bridge between atomistic and coarse-grained models. *J. Chem. Phys.* **128**, 1–11 (2008).
69. Müller, M. *et al.* Computing free energies of interfaces in self-assembling systems. *Phys. Chem. Chem. Phys.*, **11** (2009)
70. Matsen, M. W. The standard Gaussian model for block copolymer melts. *J. Phys. Condens. Matter* **14**, 21–47 (2002).
71. Petera, D. *et al.* Effect of patterned surface on diblock-copolymer melts and polymer blends near the critical point. *J. Chem. Phys.* **107**, 9640 (1997).
72. Chen, H. *et al.* Morphology of thin block copolymer films on chemically patterned substrates. *J. Chem. Phys.* **108**, 6897 (1998).
73. Tsori, Y. *et al.* Diblock Copolymer Ordering Induced by Patterned Surfaces above the Order - Disorder Transition. 2719–2727 (2001).
74. Wang, Q., *et al.* Symmetric diblock copolymer thin films confined between homogeneous and patterned surfaces: Simulations and theory. *J. Chem. Phys.* **112**, 9996–10010 (2000).
75. Edwards, E. W., *et al.* Precise control over molecular dimensions of block-copolymer domains using the interfacial energy of chemically nanopatterned substrates. *Adv. Mater.* **16**, 1315–1319 (2004).
76. Stuen, K. O., *et al.* Dimensional scaling of cylinders in thin films of block copolymer-Homopolymer ternary blends. *Macromolecules* **42**, 5139–5145 (2009).
77. Ruiz, R. *et al.* Density Multiplication and Improved Copolymer Assembly. *Science*. **321**, 936–940 (2008).
78. Peng, Q., *et al.* Nanoscopic patterned materials with tunable dimensions via atomic layer deposition on block copolymers. *Adv. Mater.* **22**, 5129–5133 (2010).
79. Peng, Q., *et al.* A route to nanoscopic materials via sequential infiltration synthesis on block copolymer templates. *ACS Nano* **5**, 4600–4606 (2011).
80. Moon, H. S. *et al.* Atomic layer deposition assisted pattern multiplication of block copolymer lithography for 5 nm scale nanopatterning. *Adv. Funct. Mater.* **24**, 4343–4348 (2014).
81. Yue, Z., *et al.* SAXS analysis of the Order-disorder transition and the interaction parameter of Polystyrene-block-poly(methyl methacrylate). *Macromolecules* **41**, 9948–9951 (2008).
82. Delcambre, *et al.* Mechanical properties of antiplasticized polymer nanostructures. *Soft Matter* **6**, 2475 (2010).
83. Keen, I. *et al.* Control of the Orientation of Symmetric Poly(styrene)-block-poly(D,L-lactide). *Langmuir*, **28** (2012).

84. Hartney, M. A., *et al.* Block copolymers as bilevel resists. *J. Vac. Sci. Technol. B J. Chem. Phys.* **3**, 1346–1241 (1985).
85. Rodwogin, *et al.* Polylactide-poly(dimethylsiloxane)-polylactide triblock copolymers as multifunctional materials for nanolithographic applications. *ACS Nano* **4**, 725–732 (2010).
86. Frielinghaus, H. *et al.* Micro - vs . macro-phase separation in binary blends of poly (styrene)-poly(isoprene) and poly(isoprene)-poly(ethylene oxide) diblock copolymers. *Eur. Lett.* **53**, 680–686 (2001).
87. Dai, K. H. *et al.* Determining the temperature-dependent Flory interaction parameter for strongly immiscible polymers from block copolymer segregation measurements. *Polymer.* **35**, 157–161 (1994).
88. Otsuka, I. *et al.* Control of 10 nm scale cylinder orientation in self-organized sugar-based block copolymer thin films. *Nanoscale* **5**, 2637–41 (2013).
89. Lecommandoux, S. *et al.* Microphase Separation of Linear and Cyclic Block Copolymers Poly(styrene-*b*-isoprene): SAXS Experiments. *Macromolecules* **37**, 1843–1848 (2004).
90. Park, S.-M., *et al.* Patterning sub-10 nm line patterns from a block copolymer hybrid. *Nanotechnology* **19**, 455304 (2008).
91. Park, S. *et al.* Macroscopic 10-terabit-per-square-inch arrays from block copolymers with lateral order. *Science* **323**, 1030–1033 (2009).
92. Moore, G. E. Cramming more components onto integrated circuits. *Electronics*, **38**, (1975).
93. Jan, C. H. *et al.* A 22nm SoC platform technology featuring 3-D tri-gate and high-k/metal gate, optimized for ultra low power, high performance and high density SoC applications. *Electron Devices Meet. IEDM* 44–47 (2012).
94. Neisser, M. *et al.* ITRS lithography roadmap: 2015 challenges. *Adv. Opt. Technol.* **4**, 235–240 (2015).
95. Liu, G., *et al.* Integration of Density Multiplication in the Formation of Device-Oriented Structures by Directed Assembly of Block Copolymer-Homopolymer Blends. *Adv. Funct. Mater.* **20**, 1251–1257 (2010).
96. Rath sack, B. *et al.* Advances in directed self assembly integration and manufacturability at 300 mm. *Proceeding SPIE* **8682**, 86820K (2013).
97. Hinsberg, W., *et al.* Self-Assembling Materials for Lithographic Patterning: Overview, Status and Moving Forward. *Proc. SPIE* **7637**, 76370G–76370G–11 (2010).
98. Rincon Delgadillo, P. *et al.* Defect source analysis of directed self-assembly process (DSA of DSA). *Proc. SPIE* **8680**, 86800L–86800L–9 (2013).

99. Gronheid, R. *et al.* Defect reduction and defect stability in IMEC's 14nm half-pitch chemo-epitaxy DSA flow. *Proceeding SPIE* **9049**, 904905 (2014).
100. Somervell, M. *et al.* Driving DSA into Volume Manufacturing. *Proceeding SPIE* **9425**, 1–11 (2015).
101. Tiron, R. *et al.* Pattern density multiplication by direct self assembly of block copolymers: toward 300mm CMOS requirements. *Proc. SPIE* **8323**, 83230O–83230O–7 (2012).
102. Tada, Y. *et al.* Directed Self-Assembly of Diblock Copolymer Thin Films on Chemically-Patterned Substrates for Defect-Free Nano-Patterning. *Macromolecules* **41**, 9267–9276 (2008).
103. Kim, S. O. *et al.* Epitaxial self-assembly of block copolymers on lithographically defined nanopatterned substrates. *Letters to nature*, 411–414 (2003).
104. Edwards, E. W., *et al.* Long-Range Order and Orientation of Cylinder-Forming Block Copolymers on Chemically Nanopatterned Striped Surfaces. *Macromolecules*, 3598–3607 (2006).
105. Stoykovich, M. P. *et al.* Directed Assembly of Block Copolymer Blends into Nonregular Device-Oriented Structures. *Science*, **1442**, (2014).

Chapter 3

Directed self-assembly of PS-*b*-PMMA block copolymers by chemical epitaxy

In directed self-assembly by chemical epitaxy, block copolymers are guided by chemical patterns created on the substrate. Thus, by tuning the chemical interactions between the block copolymer domains and the chemical pattern, an optimal BCP alignment with high density multiplication factors can be achieved.

In this chapter, the development, optimization and characterization of a chemical epitaxy process based on substrate functionalization is presented. To demonstrate its industrial applicability, the process initially developed at IMB-CNM has been transferred to the cleanroom of CEA-Leti, which is more focused towards industrial production, and has a pilot line intended to the fabrication of CMOS integrated circuits.

On the other hand, two other novel approaches based on chemical direct writing techniques by means of electron beam lithography and atomic force microscopy lithography are presented.

3.1. Introduction to directed self-assembly of block copolymers by chemical epitaxy

DSA of BCPs is becoming a very promising approach to overcome the conflict between the continuous demanding to decrease the size of electronic devices and processing costs of traditional lithographic techniques, since it is a very effective and simple method to pattern dense arrays of features with dimensions in the nanoscale.¹⁻⁶ Several recent studies have shown that DSA is an emerging technique that can be used to improve the line-width roughness (LWR)⁷ and line-edge roughness (LER)⁸, apart from enhancing the resolution of the currently patterning methods. Nevertheless, it remains a challenge to fulfill the rigorous requirements of defectivity from the semiconductor industries. Chemical and topographical guiding patterns provide highly oriented and ordered features, and have demonstrated to offer satisfying structures demanded by the semiconductor industry.^{7,9-15}

Chemical epitaxy consists of a combination of a top-down method to create chemical patterns with a self-assembled periodic process, which allows getting higher resolutions than the lithographic ones. In chemical epitaxy, the guiding patterns consist of guiding areas that preferentially wet one of the domains of the BCP and that are separated by interspatial regions which are normally referred to as background areas. These guiding and background lines are characterized for having different interactions with the domains of the BCP. Therefore, in chemical epitaxy DSA, the chemistry and the guiding pattern geometries determine the generation of microstructures with the lowest free energy.¹⁶ Consequently, there has to be a high control of the thermodynamic forces which fine tune the patterning order, by controlling the critical parameters on the fabrication of chemical guiding patterns.

Several materials can be used as background layers to create the guiding patterns: self-assembled monolayers¹⁷, HSQ resist⁷ and end-grafted homopolymers or random copolymer brushes.^{13,15,18-20} The most widely used technique consists on using end-grafted homopolymers or random copolymer brushes. Different approaches are currently used to create the guiding patterns. The first chemoepitaxy approach based on substrate functionalization was presented by *Kim et al.* in 2003 where a self-assembled monolayer (SAM) was used to chemically create the guiding patterns.¹⁷ In this approach, the photoresist was patterned by EUV-IL, with alternating lines and spaces of period L_0 , and then the topographic resist pattern was converted to a chemical pattern by irradiating the sample with X-rays. However, this method presents some disadvantages regarding the lithography step, since it has to nominally be at the same feature density as that achieved by the BCP. Therefore, *Ruiz et al.* reported a viable technique based on the use of EBL and oxygen plasma functionalization for cylindrical BCP with pattern density

multiplication of $2L_0$ (see Figure 3.1.a).¹³ Later on, *Cheng et al.* developed a technique to increase the density multiplication factor of a lamellar PS-*b*-PMMA BCP, based on 193 nm immersion lithography.⁷ In 2010, *Sanders et al.* from IBM presented a chemical epitaxy DSA flow using sparse chemical pre-patterns made by a pattern-first, neutralize-last approach.²¹ Based on these works, industry focused BCP DSA as a potential complementary technique for the next generation logic nodes. However, the defect density has to be decreased down to 0.01 defects/cm², and thus, in order to achieve the defectivity level required by the industry, *Liu and Nealey* in 2011 developed the LiNe process. In this process, two materials with different chemical affinities are employed to create the chemical guiding pre-patterns. As shown in the scheme from Figure 3.1.b, the process flow starts by spin-coating a cross-linkable polystyrene (X-PS) on a substrate and after a lithography step, the material is etched. Then, a random hydroxyl terminated poly(styrene-*b*-methyl methacrylate) (PS-*r*-PMMA-OH) brush is spin-coated and grafted to the substrate between the X-PS guiding stripes, creating thus a chemical pattern. The X-PS guiding stripes are more affine to PS domains while the PS-*r*-PMMA background stripes have equal affinity for both domains.¹⁸ Other approaches combining the use of topographical and chemical patterns have been also presented by *Kim et al.* in which the BCP is self-assembled on top of grapho-chemical pre-pattern.²²

Nowadays, the main research objective for DSA on chemical patterns is to meet the manufacturing requirements of the semiconductor industry (low defectivity, process integration and device design with DSA patterns). Nevertheless, new processes and materials must be developed to demonstrate resolutions up to 5 nm of BCP half-pitch, to serve DSA manufacturing processes able for more than two future node generations. Therefore, for the complete incorporation of DSA processes it is necessary to understand the physics and chemistry that enables the integration of BCPs with traditional manufacturing processes.²³

In this chapter, the implementation, characterization and modelling of a chemical epitaxy process for PS-*b*-PMMA based on the functionalization of the substrate after an EBL is presented. First, this method has been implemented at laboratory scale, at the IMB-CNM cleanroom. Then, and in order to demonstrate the industrial scalability of the process, it has been transferred to CEA-Leti's cleanroom, which is more industrial focused and has a compatible pilot line for the fabrication of CMOS integrated circuits.

On the other hand, two other novel chemical epitaxy approaches based on direct writing techniques are presented. These two direct writing techniques are based on using EBL and AFM directly on the substrate, thus avoiding the use of resist and the corresponding development and stripping steps.

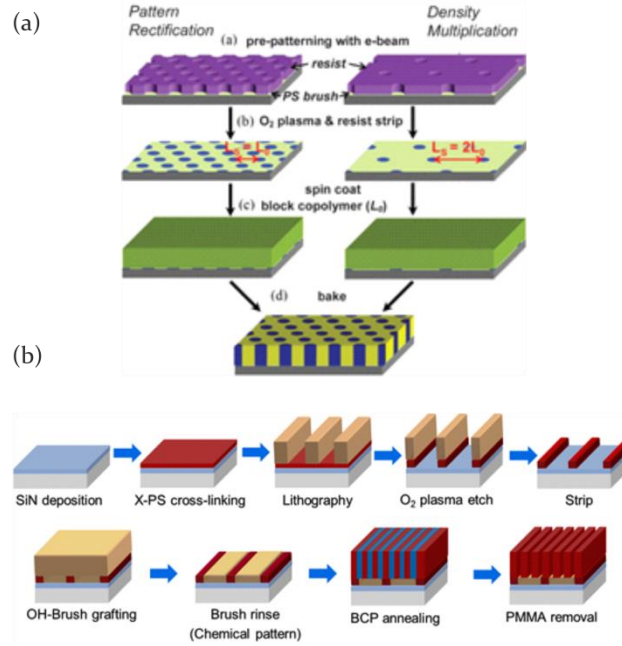


Figure 3.1. Schematic of the chemical epitaxy process developed by (a) *Ruiz et al.* using e-beam lithography and O₂ plasma functionalization¹³ and by (b) *Liu and Nealey* using an alternate pattern of two polymers (LiNe process)¹⁸

3.2. Development and implementation of chemical epitaxy by substrate functionalization

Chemical epitaxy based lithography and substrate functionalization methods are those in which an end-grafted homopolymer or random brush polymer is first deposited on top of the substrate, and then patterned by means of a top-down approach. Then, the defined regions are selectively functionalized to change their chemical affinity. This functionalization can be performed by using either oxygen plasma or UV exposure.

In this section, a chemical epitaxy process defined by EBL and oxygen plasma functionalization is presented. First, the process is defined and optimized at the IMB-CNM cleanroom for three different PS-*b*-PMMA materials, and then for high- χ BCPs (see *chapter 5*). Since chemical epitaxy processes are mainly driven by the difference on the surface free energy between the substrate and the BCP domains, a new experimental process to determine these interactions is also presented. Then, based on these experimental results, the simulation and modelling of this DSA method is performed.

3.2.1. Materials and methods

3.2.1.1. Description of the chemical epitaxy process

A new technique based on using the EBL and oxygen plasma functionalization has been developed and optimized to promote the alignment of PS-*b*-PMMA and also high- χ BCPs.

The process flow is depicted in Figure 3.2. It consists of the following steps: (i) polymer brush grafting on the top of a silicon substrate, (ii) e-beam writing on PMMA resist, (iii) resist development and substrate functionalization by oxygen plasma, (v) resist removal and (vi) BCP spin-coating.

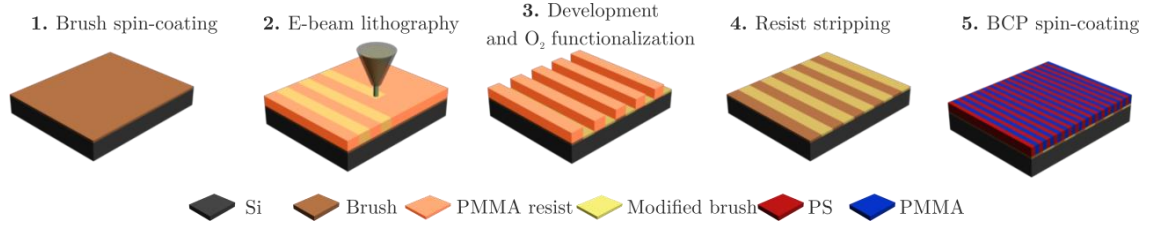


Figure 3.2. Schematic of the chemical epitaxy process based on using EBL and oxygen plasma functionalization

3.2.1.2. Brush and block copolymer materials

Lamellae PS-*b*-PMMA BCPs with different polymer chain lengths have been used for the DSA process, each one processed with its own polymer brush and annealing conditions in order to fine-tune the interface energies that provide an optimal alignment (see Table 3.1 and Table 3.2 for brush and BCP specifications).

For each BCP, different brush layers based on PS-*r*-PMMA and PS-OH, and in consequence different processing conditions, have been tested. The brush layer and processing conditions used for each BCP are specified in Table 3.3.

Table 3.1. Specifications of brush layer materials used for chemical epitaxy DSA

Material	Molecular weight	PDI
PS-OH	4.5 kg/mol	1.34
PS _{70%-r} -PMMA	9.9 kg/mol	1.09
PS _{60%-r} -PMMA	7.9 kg/mol	1.85

Table 3.2. Specifications of PS-*b*-PMMA BCP used for chemical epitaxy DSA

BCP chemical nature	PS- <i>b</i> -PMMA	PS- <i>b</i> -PMMA	PS- <i>b</i> -PMMA
PDI	1.09	1.12	1.1
Molecular weight	79 kg/mol	45 kg/mol	42.3 kg/mol
PS fraction	50 %	50%	48%
Pitch	38 nm	28 nm	22 nm

Table 3.3. Processing conditions used for PS-*b*-PMMA BCP DSA

		L ₀ = 38 nm	L ₀ = 28 nm	L ₀ = 22 nm
Brush	Brush material	PS-OH	PS-OH	PS _{70%-r} -PMMA
	Processing conditions	260°C for 5 min, N ₂ environment	260°C for 5 min, N ₂ environment	230°C for 5 min, N ₂ environment
	Film thickness	4.7 nm	4.7 nm	8.6 nm
BCP	Film thickness	0.9L ₀	0.75L ₀	1.3L ₀
	Processing conditions	230°C for 10 min, N ₂ environment	200°C for 20 min, O ₂ environment	230°C for 10 min, N ₂ environment

3.2.1.3. Substrate preparation and creation of the chemical guiding patterns

The starting substrates are 0.9 x 0.9 cm² chips bearing a native silicon oxide layer ({100}, p-type silicon wafers of 4-40 $\Omega \cdot \text{cm}$ resistivity). Previously to the grafting process, the sample surface is cleaned and activated by an oxygen plasma for 10 min at 500 W and 50 sccm oxygen flow. Then a 2% PGMEA brush solution is spin-coated at 5000 rpm on the top of the surface and annealed by using the processing conditions depicted in Table 3.3.

Consequently, the non-grafted brush is removed by dipping the sample in PGMEA for 5 min in an ultrasound bath at 40°C. The brush film thickness grafted after PGMEA rinsing depends on brush molecular weight (see Table 3.3). Then, a 2% 950k PMMA solution is spin-coated on the top of the brush at 2000 rpm giving rise to an 80 nm film thickness. Once the resist has been deposited, the guiding patterns are defined by EBL in a *RAITH 150Two* equipment. Figure 3.3 depicts the definitions regarding guiding pattern dimensions and BCP specifications that are going to be used from now on through the manuscript (d denotes the BCP film thickness, L_0 is the BCP pitch, and L_s and L_b refer to guiding and background stripe widths, respectively). Guiding patterns for line/space applications with guiding stripes widths between $0.5L_0$ to $3.5L_0$ and density multiplication factors of $2L_0$ to $7L_0$ have been designed.

The EBL has been performed by exposing the desired patterns at 20 kV and 110 pA of beam current with a nominal beam diameter of 2 nm. The exposure has been defined as a set of single line exposures and e-beam doses between 225 and 675 $\mu\text{C}/\text{cm}^2$ have been used in order to obtain the desirable line width. This means that the writing speed has been varied between 4.9 $\mu\text{m}/\text{s}$ and 1.6 $\mu\text{m}/\text{s}$ by using a line step size of 10 nm.

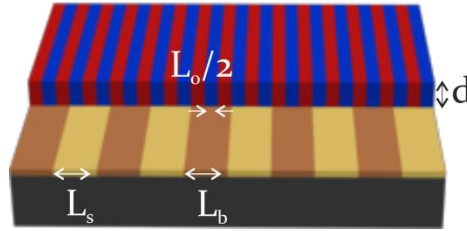


Figure 3.3. Guiding pattern dimensions and BCP specifications scheme

After the exposure, the resist is developed by dipping the sample in a methyl isobutyl ketone (MIBK) and isopropanol (IPA) solution at 1:3 for 30 s and then, in IPA for a further 30 s. Subsequently, the sample defined areas are exposed to oxygen plasma in order to chemically change their structure.

3.2.1.4. Functionalization of the surface and PS-*b*-PMMA spin-coating

Once the sample has been developed after the EBL exposure, it is subjected to a brief dose of oxygen plasma in order to chemically change the substrate affinity. It is known that

oxygen plasma induces polar groups on the brush creating regions more affine to PMMA (see Figure 6.4.c from *chapter 6*).²⁴

The functionalization is performed in an *Alcatel AMS 110 DE* reactive ion etching (RIE) equipment by using two different conditions denoted as soft and strong (see specifications in Table 3.4). Two different conditions have been used in order to study how the BCP morphology changes as a function of the interactions between the BCP domains and the different functionalized regions.

Table 3.4. O₂ plasma conditions for brush functionalization

	Soft O ₂ plasma	Strong O ₂ plasma
[O ₂] (sccm)	10	50
Power Source (W)	150	300
Time (s)	5	10
Pressure (Pa)	1.33	1.33
Temperature (°C)	20	20
Brush removed	0.6 nm	4.5 nm

After performing the brush functionalization, the resist is removed by dipping the sample into acetone for 2 min in an ultrasound bath at 40°C. Figure 3.4 shows AFM images of the topography and phase signals of a chemical guiding pattern created on a PS-OH brush layer by soft oxygen plasma functionalization after removing the PMMA resist. Brighter and darker areas correspond to the background and guiding stripes, respectively.

The chemical contrast revealed by the AFM phase image is a signature of the fact that the un-exposed PS-OH domains (background regions) are slightly affine to polystyrene, while the stripes exposed to oxygen plasma are slightly affine to PMMA due to the oxidation of the polymer. Furthermore, it is observed that oxygen plasma exposure induces a removal of around 0.5 nm of PS-OH (Figure 3.4.a).

The presence of some topography between stripes may enhance the guiding efficiency of the chemical patterns, although it is not enough to induce the alignment of the BCP.^{9,25}

Finally, a 1.5% PGMEA solution of BCP is spin-coated on the top of the chemical guiding pattern and it self-assembles with respect to the previous pattern after a thermal annealing treatment. Processing conditions (brush material, BCP film thickness, annealing temperatures and time) for each BCP are summarized in Table 3.3.

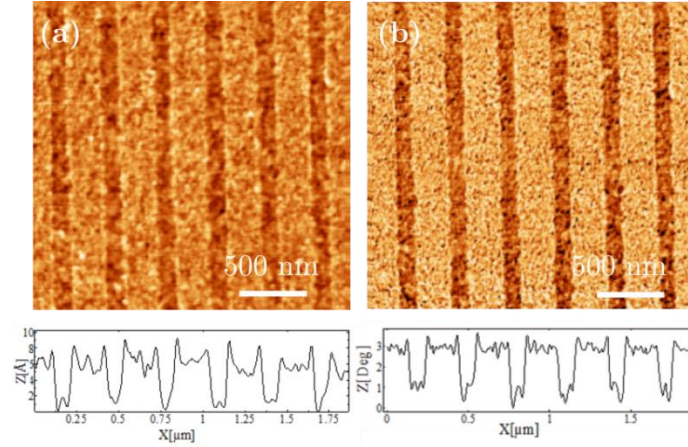


Figure 3.4. AFM topography (a) and phase (b) images of a chemical guiding pattern created by e-beam exposure followed by oxygen plasma modification

3.2.2. Directed self-assembly by chemical epitaxy of PS-*b*-PMMA results

The PS-*b*-PMMA DSA process has been studied for three molecular weight systems. First, the results for the 28 nm pitch are presented, and then those for the 38 nm and 22 nm, respectively.

PS-*b*-PMMA 28 nm pitch directed self-assembly

First DSA experiments were performed with PS-*b*-PMMA of 14 nm half-pitch by varying the multiplication factor and by keeping constant the guiding stripe width at $0.5L_0$. Figure 3.5 shows an example of PS-*b*-PMMA DSA for a guiding stripe width of $0.5L_0$ and density multiplication factors of $3L_0$ and $4L_0$. As it can be observed, the BCP is well self-assembled with respect to the previous chemical pattern as a function of the guiding pattern pitch. Furthermore, Figure 3.6 shows that the process is transferable to larger guiding patterns showing low defectivity.

On the other hand, when the guiding pattern dimensions are not in registry with the BCP pitch, the alignment is lost all along the guiding pattern (Figure 3.7). For this later example, guiding and background stripe widths are 0.5 and $4L_0$, respectively, and because the background stripe width does not fit with $(0.5+n) \cdot L_0$, the accurate BCP alignment is not achieved.

Nevertheless, despite being an appropriate method to guide this 28 nm pitch BCP, the required resolution of the beam is 14 nm since the guiding stripe dimensions are set to be the half of the BCP pitch. Therefore, the method is somehow disadvantageous due to the fact that it introduces a lithographic step, nominally at the same feature density as that achieved by the BCP.

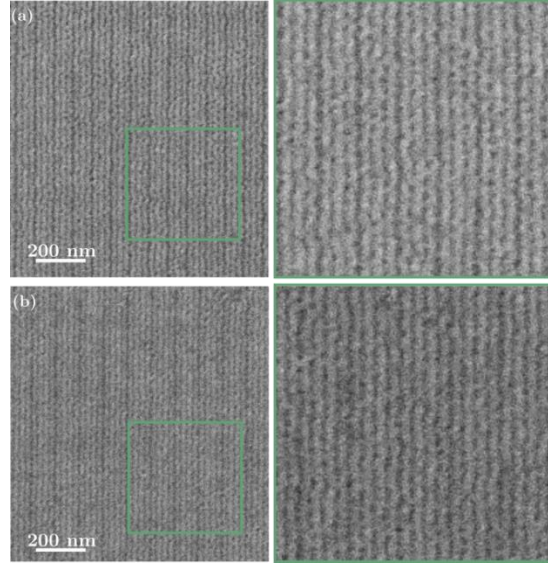


Figure 3.5. PS-*b*-PMMA ($L_0 = 28$ nm) DSA for $L_s = 0.5L_0$ and density multiplication factors of (a) $3L_0$ and (b) $4L_0$

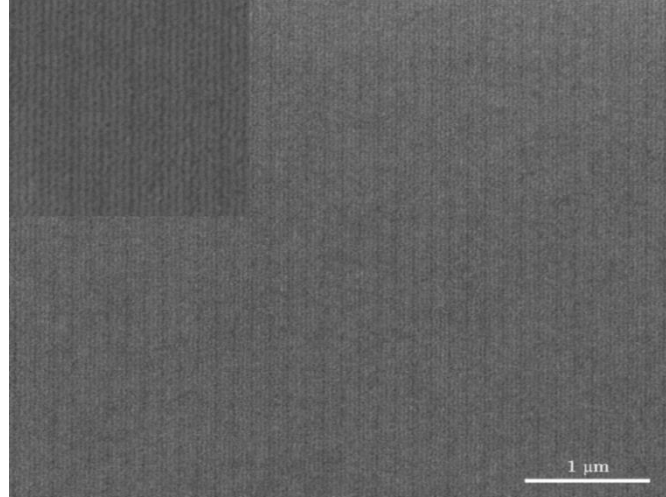


Figure 3.6. PS-*b*-PMMA ($L_0 = 28$ nm) DSA in a large area for $L_s = 0.5L_0$ and density multiplication factor of $3L_0$

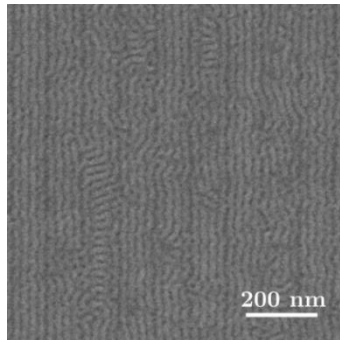


Figure 3.7. PS-*b*-PMMA ($L_0 = 28$ nm) DSA for $L_s = 0.5L_0$ and $L_b = 4L_0$ showing no BCP alignment due to the non-commensurability of the pattern with the BCP pitch

As a solution, guiding patterns with wider guiding stripes have been designed in order to relax the lithography resolution requirements and extend the implementation of the process

for the next generation BCP materials with smaller pitch. Figure 3.8 illustrates the density multiplication concept when using $0.5L_0$ or $(0.5+n) \cdot L_0$ guiding stripe widths. The concept behind this approach is that by properly tuning the brush functionalization, when using wide guiding stripes, more than one standing perpendicular lamellae is located on top of guiding stripes, thus avoiding lying lamellae.

To experimentally demonstrate the effect of the brush functionalization on the BCP alignment, guiding patterns with the same dimensions have been exposed to two different oxygen plasma conditions (referred to *soft* and *strong*), depicted previously in Table 3.4, and using the same BCP material. As shown in Figure 3.9.a, when soft oxygen plasma conditions are used slightly PMMA affine regions can be obtained, favoring standing perpendicular lamellae. In that situation, $3.5L_0$ wide guiding stripes were exposed and thus, four PMMA and three PS stripes are on top of them. On the other hand, the non-exposed regions ($1.5L_0$) which are slightly affine to PS, have three PS and two PMMA stripes. When stronger conditions are used, lying lamellae is promoted due to the strong surface affinity for PMMA, as shown in Figure 3.9.b. Based on these DSA results, it can be concluded that by properly tuning the oxygen plasma conditions, the BCP wetting behavior can be accurately controlled, enabling the possibility of achieving and controlling different alignment morphologies.

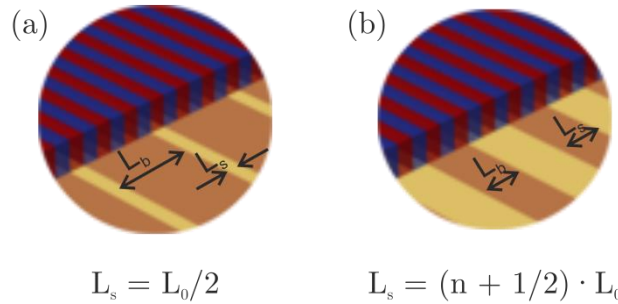


Figure 3.8. DSA by chemical epitaxy schemes showing the concept of density multiplication. L_s denotes the width of the chemical guiding stripes, and L_b represents the separation between guiding stripes (background). The density multiplication factor is defined as the ratio between the period of the guiding pattern and that of the BCP

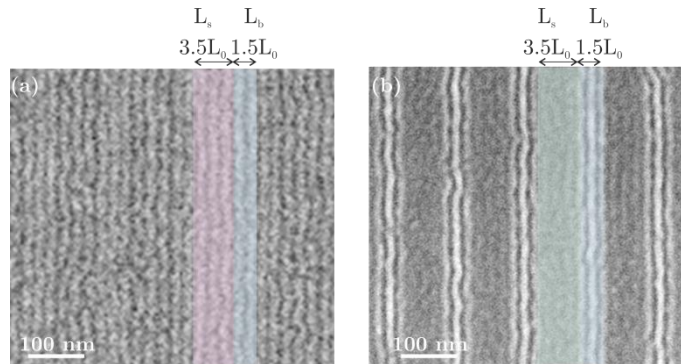


Figure 3.9. PS-*b*-PMMA ($L_0 = 28$ nm) DSA when using (a) soft and (b) strong plasma conditions. Red and green colors refer to soft and strong functionalization, respectively, while blue color depicts background regions

*PS-*b*-PMMA 38 and 22 nm pitch directed self-assembly*

To demonstrate that the process is scalable to other BCP polymer chain lengths, two additional BCPs with 38 nm and 22 nm pitch have been used with a guiding and background stripe widths of $0.5L_0$ and $1.5L_0$, respectively (material specifications and processing conditions are depicted in Table 3.1, Table 3.2 and Table 3.3, respectively).

As shown in the SEM images from Figure 3.10, the BCP has been aligned by following the chemical pre-pattern, although different processing conditions have had to be used for each BCP. This is attributed to the fact that depending on the BCP molecular weight the interactions taking place between the domains and the surface are different. This effect will be later on studied by the experimental characterization of surface free energies.

Moreover, the DSA method has been also tried for guiding patterns with wider guiding stripes, but it has not been successful for the case of 38 nm pitch PS-*b*-PMMA, as it has been for the case of 22 nm pitch demonstrated in Figure 3.11. In this later situation, guiding stripe widths of $1.5L_0$ have kept constant while the guiding pattern pitch has been varied up to density multiplication factors of $5L_0$. Above $5L_0$ pitch, fingerprint morphology is started to be seen in between background regions because the chemical pattern is not strong enough to drive the BCP alignment.

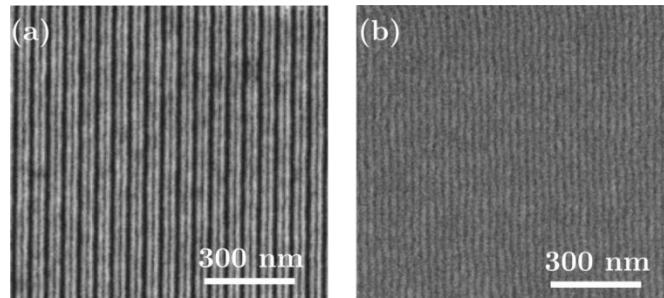


Figure 3.10. PS-*b*-PMMA DSA when using $0.5L_0$ width guiding stripes and density multiplication factor of $2L_0$ for BCP pitch of (a) 38 nm and (b) 22 nm

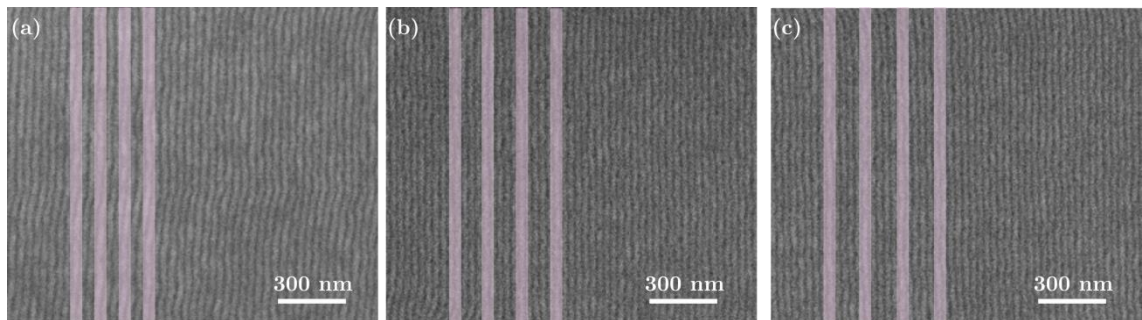


Figure 3.11. PS-*b*-PMMA ($L_0 = 22$ nm) DSA for $L_s = 1.5L_0$ and density multiplication factors of (a) $3L_0$, (b) $4L_0$ and (c) $5L_0$. Red color refers to guiding stripes width ($L_s = 1.5L_0$)

On the other hand, it is known that BCP morphology depends on the BCP film thickness. In order to find out the optimal film thickness which provides the best DSA results, a range of different thicknesses has been studied for each BCP. As an example of it, Figure 3.12

shows SEM images of PS-*b*-PMMA ($L_0 = 38$ nm) on top of the same chemical guiding pattern ($L_s = 0.5L_0$ and $L_b = 1.5L_0$) by using different values of film thickness. It is clearly observed that the morphology and phase separation behavior strongly depends on the BCP film thickness. For this BCP, the best result is obtained when the film thickness is $0.9L_0$.

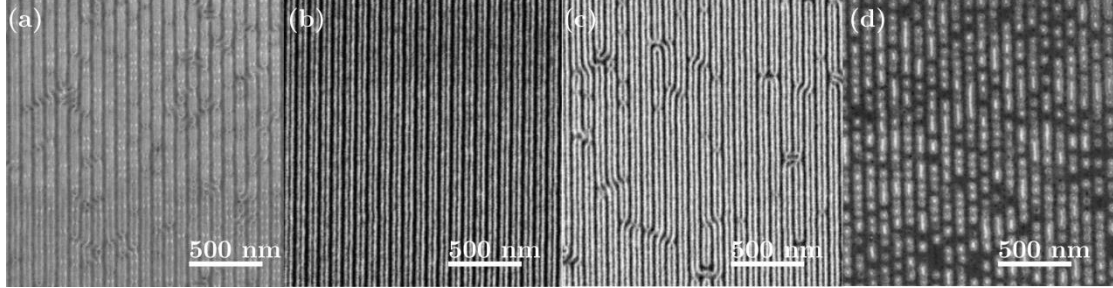


Figure 3.12. PS-*b*-PMMA ($L_0 = 38$ nm) DSA for $L_s = 1.5L_0$ and density multiplication factor of $2L_0$ with film thickness values of (a) $0.8L_0$, (b) $0.9L_0$, (c) $0.96L_0$ and (d) $1.1L_0$

In short, it has been demonstrated that the DSA of PS-*b*-PMMA by chemical epitaxy with oxygen plasma functionalization has been successfully implemented with different BCP chain lengths and high density multiplication factors, although the largest pitch BCP has not been possible to align by using wide guiding stripes patterns and high density multiplication factors. This may be attributed to the high interaction that exists between the stripes and the domains of the BCP.

In order to understand how the BCP behaves at the bottom of the guiding pattern and thus check which interactions are taking place between the blocks and the chemical pattern, a cross-section SEM image, after selectively removing the PMMA domains by an oxygen plasma has been taken.

From Figure 3.13 it can be gathered that PS domains slightly wet the PS-OH brush layer in non-modified regions (brown stripes). That means that the interaction between the brush and the PS domains is too strong to ensure the perpendicular BCP morphology from the top to the bottom, promoting a PS wetting layer at the bottom of the guiding pattern. Therefore, it is difficult to direct self-assemble the BCP through the entire guiding pattern with higher density multiplication factors.

On the other hand, to avoid this wetting behavior on background regions different random copolymer brush layers (PS-*r*-PMMA) with PS contents between 0.6 and 1 have been tried for different processing conditions. Nevertheless, there has not found an optimal alignment condition for any of the brush layers used.

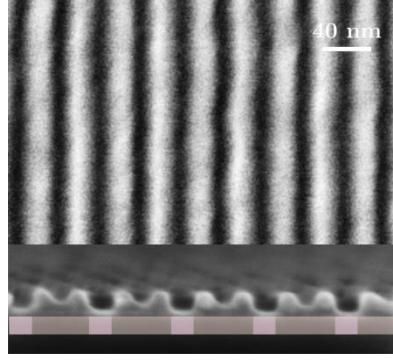


Figure 3.13. SEM cross-section of PS-*b*-PMMA ($L_0 = 38$ nm) DSA for $L_s = 0.5L_0$ and density multiplication factor of $2L_0$

3.3. Characterization of the surface free energy of chemical guiding patterns

As discussed in previous chapters, the self-assembly of BCPs oddly leads to perfect structures without defects. Sometimes the system is kinetically trapped into a metastable morphology.¹² Therefore, computer simulations are used to optimize the self-assembly process on the guiding patterns by using SCFT or Ginzburg-Landau theory (TDGL) of the Ohta-Kawasaki model.²⁶

In chemical epitaxy DSA, the achievement of the proper BCP alignment with high density multiplication factors depends on the chemical pattern dimensions and on the interface energies between the guiding features and the BCP domains. By controlling the interactions between the substrate and the BCP domains together with an accurate guiding pattern design, large aligned BCP areas have been experimentally demonstrated.^{17,27}

3.3.1. Experimental method to determine the interface interactions for modeling the chemical epitaxy DSA process

3.3.1.1. Materials and methods

Description of the overall process to determine the surface free energy

The difference of surface free energy between homopolymers A and B, can be experimentally determined by performing homopolymer blend dewetting experiments.

This novel approach, depicted in Figure 3.14, allows measuring the contact angle between homopolymers in a polymer blend, and thus calculating the difference on the surface free energy. First, a 50:50 A:B homopolymer blend is spin-coated on the top of a brush layer (un-modified and chemically modified), and it is subsequently annealed under the same conditions than those for which the BCP is optimally aligned.

After the annealing, if the substrate is not attractive enough to both homopolymers, a set of droplets is obtained. In most of the cases, the homopolymer blend layer dewetts, forming a drop-in-drop structure which contains both homopolymers.

As it can be seen in more detail in the cross-section of Figure 3.14, the droplets are generally formed by one polymer droplet surrounded by the other polymer. Then, one of the two domains is selectively removed and the contact angle is characterized by SEM cross-section imaging.

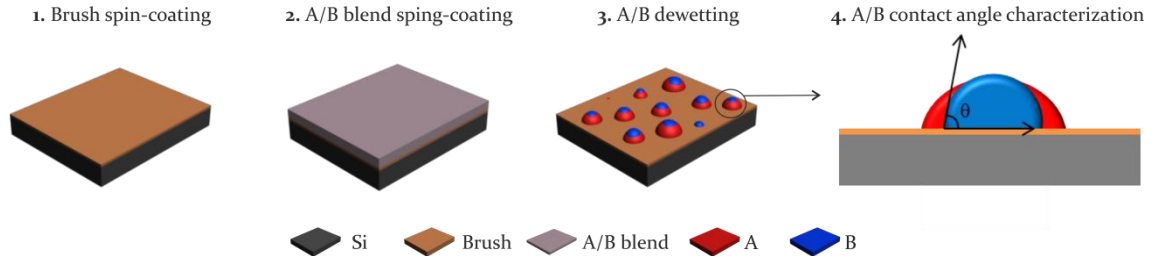


Figure 3.14. Overall fabrication process to determine the contact angle between homopolymers

The contact angle between homopolymer determines the surface affinity for both BCP domains. If $\Phi_{A-B} < 90^\circ$, then the surface is more affine to B and if $\Phi_{A-B} = 90^\circ$, then the surface presents equal affinity for both homopolymers.

Polymer brush and processing conditions

In order to find out the interactions taking place at the surface in the different chemical epitaxy processes described in section 3.2, PS/PMMA contact angle experiments are carried out. Different brush layer materials and BCP, and surface processing conditions (non-modified and chemically modified surfaces by using soft and strong oxygen plasma conditions) have been used.

The systems chosen to characterize the surface free energies have been those in which the different BCPs have shown an optimal DSA behavior (Table 3.5). The optimal DSA conditions have been selected according with the experimental results shown in the previous section.

The performed experiments are detailed in Table 3.6. These experiments have been selected in accordance to brush material/annealing and BCP. Then for each optimized DSA system (pair of brush/annealing and BCP), modified and un-modified surfaces have been characterized (three first rows of Table 3.6). Additionally, to compare the DSA results, two further systems in which none of BCPs has shown DSA, have been analyzed (two last rows of Table 3.6).

Table 3.5. Optimal DSA processing conditions obtained for PS-*b*-PMMA of 38, 28 and 22 nm pitch

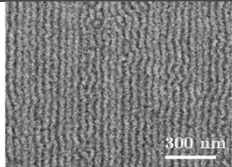
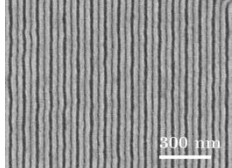
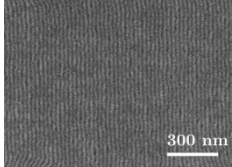
Block copolymer	Brush layer + annealing	BCP annealing	SEM image
PS- <i>b</i> -PMMA $L_0 = 38$ nm	PS-OH 260°C, 5 min in N ₂	230°C, 10 min in N ₂	
PS- <i>b</i> -PMMA $L_0 = 28$ nm	PS-OH 260°C, 5 min in N ₂	200°C, 20 min in hot-plate	
PS- <i>b</i> -PMMA $L_0 = 22$ nm	PS _{70%} - <i>r</i> -PMMA 230°C, 5 min in N ₂	230°C, 10 min in N ₂	

Table 3.6. PS/PMMA contact angle experiments performed, describing the processing conditions (brush layer and BCP processing)

	Brush + annealing	PS/PMMA annealing	Chemical functionalization	BCP DSA
A	PS-OH 260°C, 5 min in N ₂	230°C, 10 min in N ₂	- Non-modified	PS- <i>b</i> -PMMA 28 nm
B	PS-OH 260°C, 5 min in N ₂			PS- <i>b</i> -PMMA 38 nm
C	PS _{70%} - <i>r</i> -PMMA 230°C, 5 min in N ₂			PS- <i>b</i> -PMMA 22 nm
D	PS _{60%} - <i>r</i> -PMMA 230°C, 5 min in N ₂		- Modified with strong O ₂ conditions	Not achieved
E	PS _{80%} - <i>r</i> -PMMA 230°C, 5 min in N ₂			

3.3.1.2. Experimental determination of surface free energy

After PS/PMMA spin-coating and annealing, PMMA domains are selectively removed by oxygen plasma in order to characterize the samples by SEM cross-section imaging. Figure 3.15 shows a schematic representation of the drop-in-drop structure that the homopolymer blend takes after the annealing in both un-modified and modified surfaces. Figure 3.15.a represents a surface slightly more attractive to A domains (red), whereas Figure 3.15.b strongly to B (blue). The wetting behavior is not strong in Figure 3.15.a, and therefore there is no polymer wetting layer, as there is in Figure 3.15.b where the surface is strongly B affine.

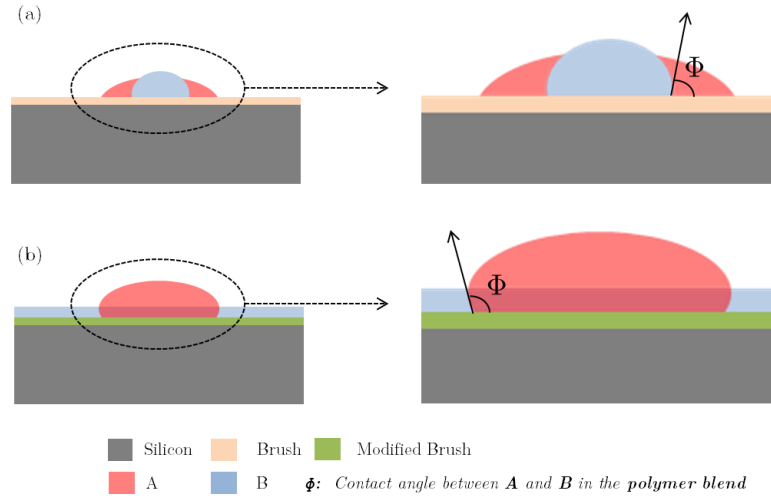


Figure 3.15. Schematics of the drop-in-drop structure of A/B blend after annealing on top of (a) un-modified and (b) modified surface

SEM images of PS/PMMA polymer blend droplets on top of un-modified and modified (soft) PS-OH brush layers after removing PMMA domains are shown in Figure 3.16 (SEM images correspond to the PS/PMMA experiment depicted in the first row of Table 3.6). From Figure 3.16.a it can be observed that the measured contact angle between PS and PMMA is 60.6° indicating a more PS affine surface. On the contrary, when the surface is functionalized by oxygen plasma exposure, the chemical affinity becomes more PMMA attractive, as revealed by the contact angle value of 140.5° .

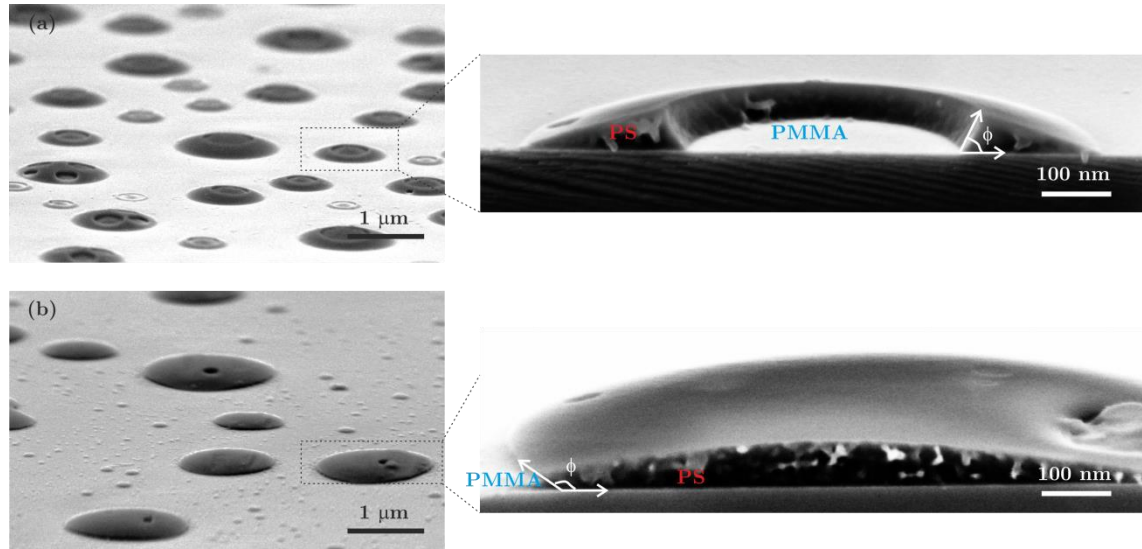


Figure 3.16. SEM images of PS/PMMA polymer blend droplets on the top of (a) un-modified and (b) modified PS-OH brush layers taken after removing PMMA domains

The behavior of the polymer blend not only depends on the substrate functionalization (depicted in Figure 3.15), but also on the brush chemistry. Figure 3.17 shows SEM images of PS/PMMA homopolymer blend on top of different brush layer materials which present different PS content. It can be observed, that the higher the content of PMMA in the brush, the higher the value of the contact angle due to the increase of PMMA affinity.

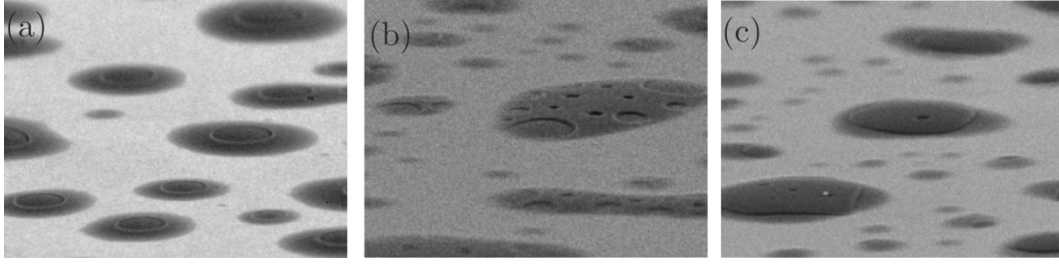


Figure 3.17. SEM images of PS/PMMA polymer blend droplets on the top of different brush layers (a) PS_{80%}-*r*-PMMA ($\Phi = 37.9^\circ$), (b) PS_{70%}-*r*-PMMA ($\Phi = 42.1^\circ$) and (c) PS_{60%}-*r*-PMMA ($\Phi = 61.9^\circ$)

From the contact angle between homopolymers, the difference on the surface free energy is determined by the *Young's Equation*:

$$\gamma_s = \gamma_{sl} + \gamma_l \cdot \cos \theta, \quad (3.1)$$

where γ_s and γ_l , represent the surface free energy of the surface and the liquid, respectively, γ_{sl} is the surface tension between the surface and the liquid, and θ is the contact angle between the liquid and the surface.

For homopolymer blends, equation (3.1) becomes:

$$\gamma_{A-Surface} - \gamma_{B-Surface} = \gamma_{A-B} + \gamma_l \cdot \cos \theta_{AB}, \quad (3.2)$$

where $\gamma_{A-surface}$ and $\gamma_{B-surface}$ are the interface tensions between homopolymers, and γ_{AB} is the surface free-energy between A and B which depends on the annealing temperature and can be obtained from the literature. The interfacial tension between PS and PMMA as a function of the annealing temperature reported in the literature is (3.3).²⁸

$$\gamma_{PS/PMMA} [\text{mN/m}] = 3.6 - 0.013T [^\circ\text{C}], \quad (3.3)$$

For each system described in Table 3.6 and by using equations (3.2) and (3.3), the difference on the surface free energy is calculated. Table 3.7 and Table 3.8 show the values of the experimental interface energies obtained from the contact angle measurements.

Table 3.7. Values of experimental interface energies obtained from contact angle measurements and the corresponding alignment results achieved after the optimal DSA process (A, B, C)

System	A (PS-OH _A)			B (PS-OH _B)			C (PS _{70%} - <i>r</i> -PMMA)		
	Un- modified	Soft O ₂ plasma	Strong O ₂ plasma	Un- modified	Soft O ₂ plasma	Strong O ₂ plasma	Un- modified	Soft O ₂ plasma	Strong O ₂ plasma
Φ	60.6°	140.5°	156.6°	55°	128°	147.1°	77.7°	145°	155.8°
$\cos \Phi$	0.49	-0.77	-0.91	0.57	-0.62	-0.84	0.21	-0.82	-0.91
$\gamma_{PS/PMMA}$	1 mN/m			0.61 mN/m					
$\gamma_{PMMA-Brush}$ - $\gamma_{PS-Brush}$	0.49 mN/m	-0.77 mN/m	-0.92 mN/m	0.35 mN/m	-0.38 mN/m	-0.51 mN/m	0.13 mN/m	-0.50 mN/m	-0.56 mN/m

Table 3.8. Values of experimental interface energies obtained from contact angle measurements of two polymer brush (D, E)

System	D (PS _{60%} - <i>r</i> -PMMA)			E (PS _{80%} - <i>r</i> -PMMA)		
	<i>Un-modified</i>	<i>Soft O₂ plasma</i>	<i>Strong O₂ plasma</i>	<i>Un-modified</i>	<i>Soft O₂ plasma</i>	<i>Strong O₂ plasma</i>
Φ	107.7°	154.5°	159.7°	64.9°	141.6°	155.3°
$\cos \Phi$	-0.30	-0.90	-0.94	0.42	-0.78	-0.91
$\gamma_{PS/PMMA}$	0.61 mN/m					
$\gamma_{PMMA-Brush} - \gamma_{PS-Brush}$	-0.19 mN/m	-0.55 mN/m	-0.57 mN/m	0.26 mN/m	-0.48 mN/m	-0.55 mN/m

From the values of Table 3.7 it can be observed that for the systems A, B and C, the surface is PS affine in the background regions, and this affinity is higher as the PS content of the brush is larger. On the other hand, after the functionalization, the guiding stripes become more PMMA affine. It can be observed that this interaction is higher when the oxygen conditions are stronger.

Comparing the oxygen plasma treatments, the different value of $\gamma_{PMMA-Brush} - \gamma_{PS-Brush}$ explains the different morphologies that the BCP takes depending on the chemical guiding pattern strength (experimental results from Figure 3.9, which correspond to system A depicted in Table 3.7). When the guiding stripes are created by soft oxygen plasma, they are slightly affine to PMMA domains ($\gamma_{PMMA-Brush} - \gamma_{PS-Brush} = -0.77$ mN/m), promoting not a strong but a slight interaction with the guiding pattern, and forming perpendicular lamellae. In turn, when using strong oxygen plasma, the guiding stripes become strongly affine to PMMA ($\gamma_{PMMA-Brush} - \gamma_{PS-Brush} = -0.92$ mN/m), favoring laying lamellae. On the other hand, as discussed before, background stripes present slightly affinity to PS domains ($\gamma_{PMMA-Brush} - \gamma_{PS-Brush} = 0.49$ mN/m). Moreover, by comparing B to E systems (different brush, and same BCP processing conditions), it can be observed that the higher the content on PS in the brush the higher is the difference on the surface free energies.

From the characterization of the surface free energies, it can be first concluded that the surfaces becomes more PMMA attractive after the functionalization of the brush, but the chemical interaction that takes place strongly depends on the processing conditions used. Therefore, by properly tuning these chemical modifications on the substrate, an optimal set of interface energies which provides a DSA with very low defectivity can be found. It has been demonstrated that for each BCP, an optimal set of interface energies is determined by the brush layer material, its corresponding processing conditions, and by the block copolymer annealing.

On the other hand, it is also important to remark that in order to have a good alignment by chemical epitaxy, background areas need to be slightly affine to the contrary domain the guiding regions are. This is demonstrated when using PS_{60%}-*r*-PMMA brush (depicted by system D in Table 3.8), in which the DSA is lost since both regions (modified and unmodified) are PMMA attractive.

Figure 3.18 shows a graph illustrating the difference of surface free energy ($\gamma_{\text{PMMA-Brush}} - \gamma_{\text{PS-Brush}}$) on background (pink) and guiding (blue and green) regions, as a function of the brush PMMA content. When the same BCP processing conditions are used (systems B to E), it is observed that the higher the PMMA content on the brush layer, the lower is the difference on the $\gamma_{\text{PMMA-Brush}} - \gamma_{\text{PS-Brush}}$, between soft and strong functionalization. This occurs because the higher the PMMA content on the brush, the less PS molecules, the oxygen has to react with. On the other hand, for this situation, it can also be drawn that the lower the PMMA content, the higher is the difference between modified and un-modified regions, being this situation more suitable for the highest molecular weight BCP (system B).

On the other hand, it is seen that the final DSA behavior strongly depends on the BCP annealing. It is reflected in systems A and B, in which the same brush conditions but different BCP conditions are used. This happens because the interfacial energy between PS and PMMA depends on the BCP annealing (equation (3.3)), and it is higher when the BCP annealing temperature decreases. This increase in the interfacial energy between PS and PMMA, makes the system to have a larger difference between guiding and background surface free energies.

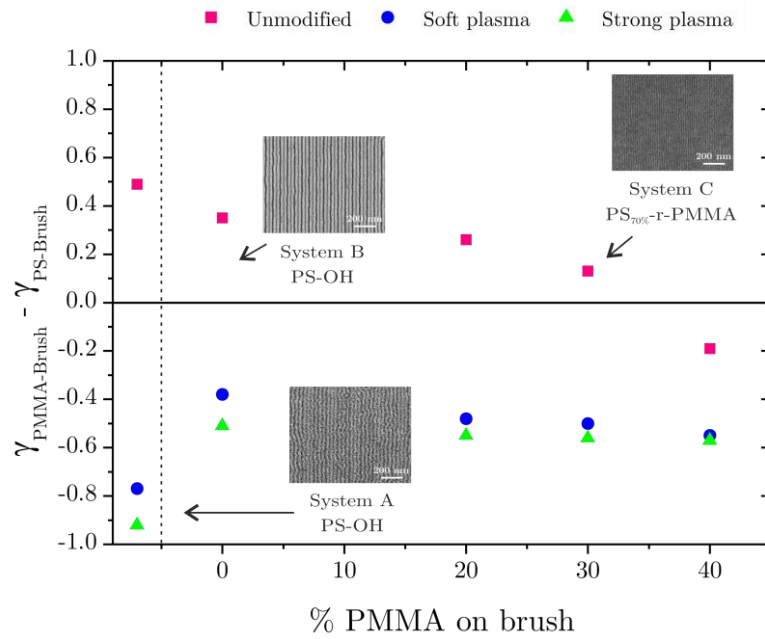


Figure 3.18. Representation of the difference free energy ($\gamma_{\text{PMMA-Brush}} - \gamma_{\text{PS-Brush}}$) on background (pink) and guiding (blue and green) regions, as a function of the brush PMMA content. SEM images correspond to the optimal DSA results obtained for each BCP pitch (systems A, B and C)

To demonstrate that a specific BCP system requires a particular set of interface energies, each BCP has been processed by using the optimal alignment conditions of the other two BCPs. Figure 3.19, shows SEM images of each BCP (38 nm, 28 nm and 22 nm pitch) aligned by using the processing conditions A, B and C. It can be observed from the results, that each BCP only gets an optimal DSA under specific processing conditions, and it becomes disordered when either the brush or the BCP annealing conditions are changed.

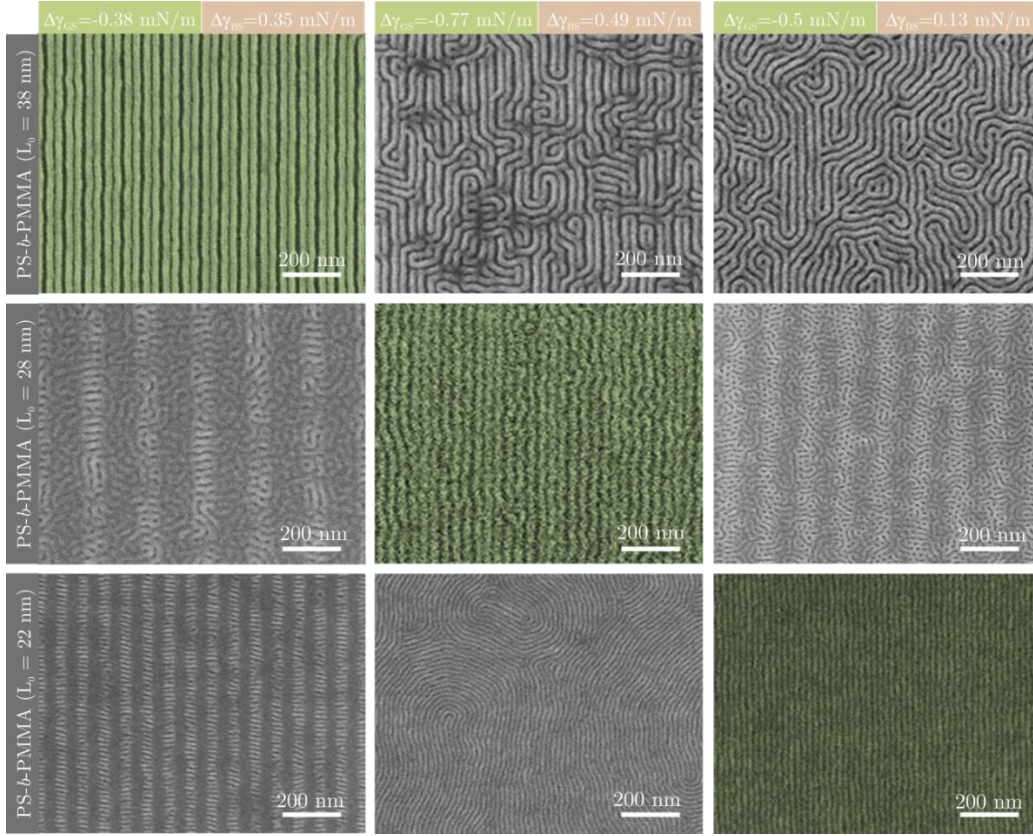


Figure 3.19. Comparison of the BCP DSA results obtained for the three optimal set of interface energies found (A, B and C). $\Delta\gamma_{bs}$ and $\Delta\gamma_{gs}$, denote the difference of surface free energy on background and guiding stripes, respectively

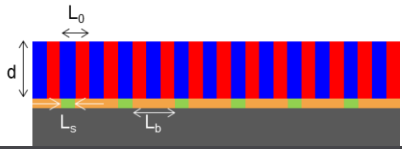
3.3.2. Role of the surface interactions by field-theoretic simulations and self-consistent field theory on chemical epitaxy DSA process

The chemoepitaxy process has been modeled by using a soft coarse grained model, as described previously in section 2.3. Single-Chain-in-Mean-Field (SCFM) simulations of the soft, coarse-grained model have been carried out to study the BCP structure formation on chemical patterned substrates. Additionally, self-consistent calculations have been used to compute the free-energy and the thermodynamic forces that drive the structure formation. This work has been performed in collaboration with *Marcus Müller* group (*Computational Soft Condensed Matter*) at the *Georg-August-Universität* of Göttingen.

The achievement of high density multiplication factors on DSA chemical epitaxy processes, requires considering multiple parameters. The most relevant ones are of dimensional nature, material and process related, all of them depicted in Table 3.9. While most of these parameters are known either because they are unequivocally experimentally determined, from the literature or from modelling/simulation, the surface free-energies are sensitively dependent on the experimental conditions, and the accurate quantitative estimation of their values has almost not been addressed up to now. Furthermore, it has been reported that the main driving force of the chemical epitaxy process is the difference on the surface-free energy of BCP domains with the confining boundaries, and therefore it is very important to

determine them. In order to run simulations and model the chemical epitaxy DSA process, surface free energy experimental data reported in the previous section, has been introduced into the DSA model.

Table 3.9. Description of the pattern dimensions and invariant parameters of the coarse-grained model

Dimensional parameters		
L_s	Width of guiding stripe	
L_b	Width of background stripe	
L_0	Bulk lamellae period	
d	BCP film thickness	
Material parameters		
χ^N	Flory Huggins parameter \cdot degree of polymerization	
R_{eo}	Mean square end-to-end BCP chains distance	
κ^N	Inverse isothermal compressibility of the liquids \cdot degree of polymerization	
D	Self-diffusion coefficient	
γ_{SA}, γ_{SB}	Surface free-energies of the segments species with the confining boundaries	

The molecular connectivity of the chain molecules is described by discretized Edwards Hamiltonian, and the non-bonded interactions are modeled by a local free-energy function that depends on the local density of A and B beads. The confining surfaces at the top and bottom of the film are represented by impenetrable walls where the top wall is neutral and the bottom wall has a chemical stripe pattern that symmetrically attracts one segment species and repels the other. An incompressible melt of symmetric AB diblock copolymers confined between a neutral surface and a bottom surface with a chemical guiding pattern is studied in the simulations.

In the soft, coarse-grained model, the strength of the affinity for wetting is characterized by the parameter ΛN . Assuming a trivial density profile at the confining surface, Young's equation yields the following prediction in SSL:

$$\cos(\theta_{AB}) = \frac{\Delta\gamma}{\gamma_{AB}} = \sqrt{\frac{12\pi}{\chi N}} \cdot \left(1 - \frac{4\ln 2}{\chi N}\right)^{-1} \cdot \Lambda N = c \cdot \Lambda N, \quad (3.4)$$

By this way, the interactions between the blocks and the surface are determined by two parameters, $\Lambda_s N$ and $\Lambda_b N$, quantifying the preference of the guiding and background stripes, respectively. By knowing these values, it can be easily determined which will be the BCP domains behavior with respect to the modified and un-modified regions. To validate the linear relation between the cosine of the contact angle and the surface preference, and thus accurately determine the constant of proportionality, c , as a function of incompatibility and chain length, simulations have been performed. Then, the relation between the contact angle and the strength of the surface affinity for a symmetric homopolymer blend can be mapped.

The simulated system is defined by the parameters depicted in Table 3.10 with linear assignment between particle positions and grid points, hard walls on top and bottom, and antisymmetric surface fields of strength ΛN , i.e. $\Lambda_s N = -\Lambda_b N$. The antisymmetric set-up gives rise to a nearly straight AB interface that runs from the bottom to the top surface. The minimization of interface curvature allows to accurately measuring the contact angle between the AB interface and the surface. In contrast to a macroscopic droplet set-up, the line tension does not influence the contact angle and the AB interface is not curved.

Table 3.10. Simulation system parameters

Parameter	Value
N	32
χN	16, 20 and 30
$\sqrt{N} = \frac{nR_{eo}^3}{V}$	90 and 128
V	$2.56 \times 10 \times 2 R_{eo}^3$

Figure 3.20 presents the $\cos(\phi_{AB})$ as a function of the strength of the surface interaction ΛN , as obtained from the simulation data compared with the analytical prediction (dashed lines). Simple linear fits (solid lines) yield $\cos(\phi_{AB}) = c \cdot \Lambda N$ with $c = 1.58$ (green), 1.4 (red) and 1.15 (black). Deviations from the analytical prediction arise from discretization effects of the chain contour and space, and from the fact that the analytical formula is obtained in the SSL. Figure 3.21 shows an example of the simulation results for obtaining the relation between the contact angle and surface strength.

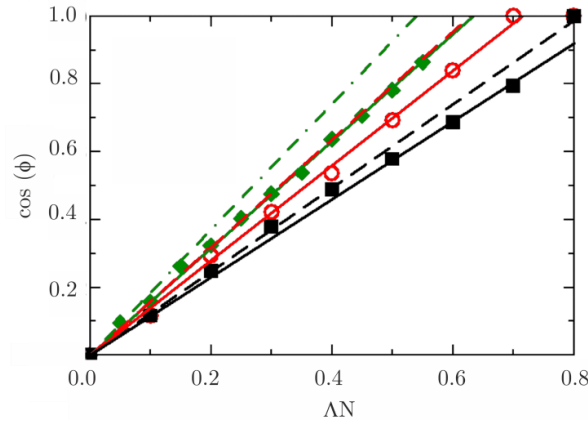


Figure 3.20. Relationship between contact angle and surface strength from the analytical prediction (dashed lines) and from simulations. Green, red and black colors represent the values of χN 16 ($c = 1.58$), 20 ($c = 1.4$) and 30 ($c = 1.15$), respectively.

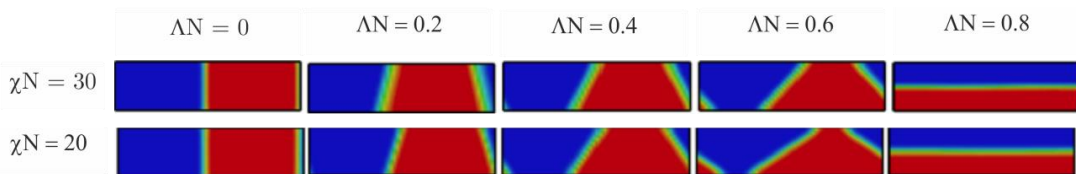


Figure 3.21. Examples of simulation of symmetric homopolymer blends for two values of χN as a function of the surface strength.

The comparison of the experimental DSA process and simulations has been performed for PS-*b*-PMMA 22 nm when using wide guiding stripes ($L_s=1.5L_0$ and $L_b=1.5L_0$) and soft oxygen plasma conditions. The experimental DSA result is shown in Figure 3.22, and the values of difference in surface free energy used are summarized in system C of Table 3.7.

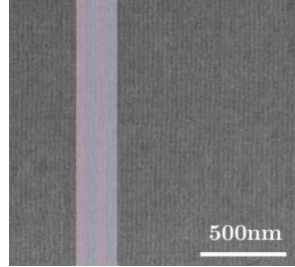


Figure 3.22. PS-*b*-PMMA ($L_0 = 22$ nm) DSA for L_s and $L_b = 1.5L_0$. Red and blue stripes denote guiding and background stripes, respectively

To carry out the simulations, it has to be established a process window where the guiding pattern is strong enough to direct the structure but weak enough to not result in parallel lamellae. However, first simulation results showed that by using the experimental strength values, the guiding pattern was too strong and it gave rise to lying lamellae. This was attributed to the fact that the brush layer is not only characterized by the contact angle, but also for its responsiveness. That is, that there is an interdigitation between the brush and BCP before the structure formation.

Figure 3.23 shows a graph representing the relation between the contact angle and the brush composition (%PMMA) for different brush grafting densities. Black, blue and red color lines represent a high ($h=0.7R_{eo}$), intermediate ($h=0.5R_{eo}$) and low ($h=0.35R_{eo}$) grafting density, whereas the dashed and solid blue lines limit the process window with the contact angle values of guiding and background regions, respectively. The simulations have been carried out for a system with $L_0=1.67R_{eo}$, $\chi N=17$ and $D=\frac{3}{4}L_0$. From the graph, it can be observed that intermediate grafting density is closer to experimental results.

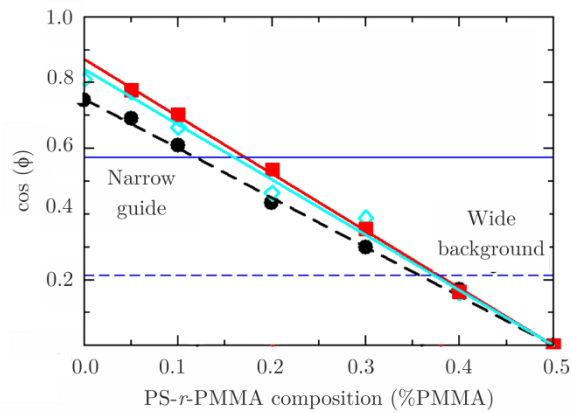


Figure 3.23. Relation between contact angle and brush composition for different brush grafting densities (black, blue and red colors refer to high, intermediate and low grafting density, respectively, and dashed and solid blue lines represent the $\cos(\phi_{AB})$ of background and guiding stripes)

Figure 3.24 show the SCMF simulation results as a function of the brush grafting density. As discussed previously, standing lamellae are favored when the brush thickness is decreased.

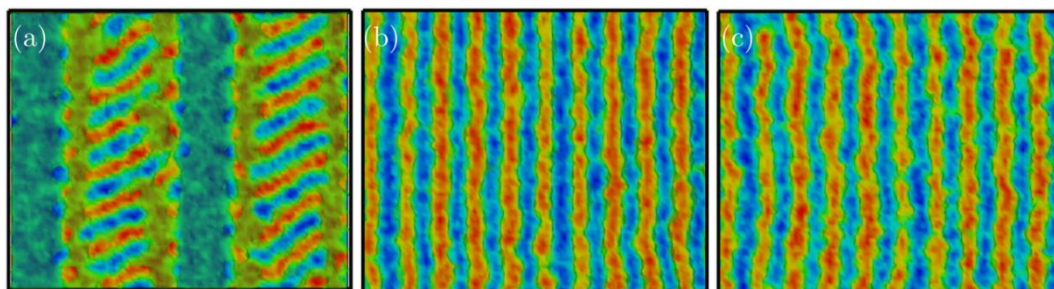


Figure 3.24. SCMF simulation results for a thin BCP film and using (a) high, (b) intermediate and (c) low grafting density

In conclusion, a model has been introduced which validates the DSA chemical epitaxy process when wide guiding stripes are used. Experimental values of surface free energies, determined by using a novel approach, are introduced on the DSA model to run the simulations. From the results obtained, it has been observed that the role of the interfacial free energy is not only the key parameter for the simulation, but also the brush responsiveness.

3.4. Manufacturability of chemical epitaxy by substrate functionalization

As a further step towards, the industrialization chemical epitaxy process developed at IMB-CNM (CSIC) for PS-*b*-PMMA systems has been transferred to CEA-Leti (Grenoble, France).

CEA-Leti is a Laboratory for Electronics and Information Technology which is operated by the *Direction de la Recherche Technologique* at CEA. It mainly aims at helping companies to increase their competitiveness through technological innovation and transfer of its technical know-how to industry. CEA-Leti benefits from 8000 m² cleanrooms in which are working not only people employed by CEA but also co-workers from different industrial companies within the framework of bilateral collaborations. These straight collaborations with industry partners together with the extensive experience on the DSA lithography, makes CEA-Leti a suitable place to study the implementation and manufacturability of the chemical epitaxy process developed at IMB-CNM to a CMOS compatible 300 mm process line.

3.4.1. Materials and methods

3.4.1.1. Description of the chemical epitaxy process

The overall chemical epitaxy process described in Figure 3.2 has been transferred to CEA-Leti's pilot line with slight modifications in order to make the process CMOS compatible. Figure 3.25 shows the overall process implemented at Leti's Pilot line in a *SOKUDO DUO* lithography track. It consists of 6 steps and except from the EBL and functionalization steps, all the rest have been performed in the same lithography track (SiARC-SOC layers spin-coating, brush grafting, resist development and stripping, and BCP spin-coating and annealing).

It can be noted that the main differences between this process and the one implemented at IMB-CNM, are the use of CMOS compatible materials, CMOS compatible e-beam positive resist and standard stack for lithography (SiARC-30 nm/SOC-95 nm).

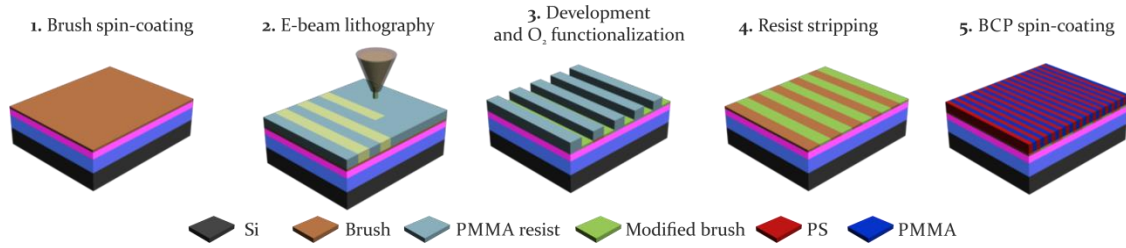


Figure 3.25. Schematic of the chemical epitaxy process based on using EBL and oxygen plasma functionalization implemented at Leti's pilot line

3.4.1.2. Brush and block copolymer materials

To study the DSA process and make it to be as similar as possible to the already implemented at IMB-CNM, the same brush and BCP materials have been used (Table 3.1 and Table 3.2). Nevertheless, the PS-OH brush layer was not available at CEA-Leti, and therefore another hPS (homopolymer polystyrene) brush with different specifications had to be used (molecular weight of 12 kg/mol and PDI of 1.2). As a consequence of having higher molecular weight, the film thickness after removing the non-grafted material results in 5.6 nm.

Regarding BCP materials, PS-*b*-PMMA of 38 nm and 22 nm pitch BCPs with the same specifications as the ones at IMB-CNM (Table 3.2) have been used. Since PS-*b*-PMMA of 28 nm pitch was not available, there has been used a BCP blend (40:60) of 38 nm and 22 nm pitch BCPs.

On the other hand, because the different processing steps involve the use of different solvents, equipment and processing conditions, all the surface free energies have been characterized for different brush layer materials to accurately transfer the DSA process.

3.4.1.3. Substrate preparation and creation of the chemical guiding patterns

The starting substrates are 300 mm silicon wafers ({100}, p-type). Previously to the grafting process, 30 nm silicon-containing antireflection coating (SiARC) and 95 nm spin-on carbon (SOC) layers are spin-coated onto the silicon. The coatings are from *JSRmicro* under the trademark of ISX and HM series, respectively.

The use of these layers has been widely used for advanced semiconductor manufacturing since the 45 nm node.²⁹ SiARC and SOC layers work as bottom anti-reflection layers for the photoresist during exposure and the combination of both of them offers a higher reflection control and etch selectivity.³⁰ The total reflectivity at the interface must be controlled to be as small as possible in order to have a good critical dimension (CD) control. On the other hand, the thickness of the layers is determined depending on the desired optical and etch requirements. Regarding the etching, fluorine plasma is used to transfer the resist pattern into the SiARC, and then transferred to SOC by oxygen plasma etching.

After the preparation of the substrates, a 2% PGMEA solution of brush is spin-coated at 1500 rpm, annealed at 230°C for 10 min and rinsed away by PGMEA in the same step-process in the track. After rinsing the brush with PGMEA, 50 nm of a compatible CMOS resist (EP555), is deposited on the top of SiArc/SOC substrates and annealed at 130°C. It is important to highlight, that this is a chemically amplified resist (CAR) which enhances the efficiency of e-beam exposure, and thus reduce the effective dose. Then the guiding patterns are defined by using a *Vistec SB3054DW* EBL tool with an energy of 5 keV and e-beam dose of 156 $\mu\text{C}/\text{cm}^2$. After the e-beam exposure, a resist post-bake is performed at 110°C. The guiding patterns have been designed in order to study different multiplication factors and by using wide guiding stripes for the different BCP dimensions. Figure 3.26 shows a schematic representation of the designed guiding patterns, consisting of arrays of thirty lines by varying the L_s and L_b from 20 to 125 nm with steps of 5 nm, in column and row, respectively.

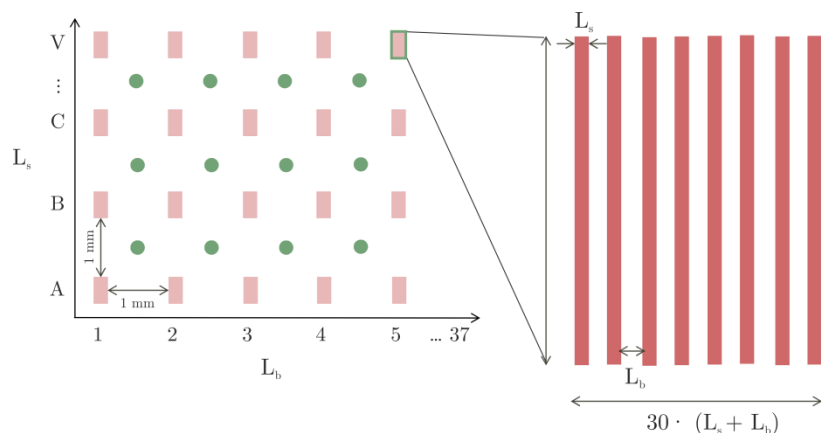


Figure 3.26. Schematic representation of the guiding patterns by varying L_s and L_b

3.4.1.4. Functionalization of the surface and PS-*b*-PMMA spin-coating

The functionalization conditions used at IMB-CNM have not been possible to implement, because the 300 mm RIE tool available at Leti does not allow the use of very low oxygen flows. Therefore, two of the lowest conditions available for the 300 mm tool have been studied in an inductive (ICP) *LAM VERSYS* tool (Table 3.11).

Table 3.11. Oxygen plasma conditions for brush functionalization used at CEA-Leti

	Conditions A	Conditions B
[O ₂] (sccm)	100	50
Power Source (W)	200	200
Time (s)	5	5
Pressure (Pa)	1.33	1.33
Temperature (°C)	20	20

To determine the interactions of the chemical guiding pattern, a surface characterization has been performed on different modified and non-modified brush materials by analyzing their surface free energy. This characterization has been experimentally carried out by contact angle measurements with the sessile drop method. The *Young's equation* (3.1) describes the balance of the three phase contact of a solid-liquid and gas as:

The surface tension of the liquid and the solid, γ_L and γ_S , can be easily measured, but the value of γ_{SL} cannot be measured directly and there has to make more assumptions of the relationship between γ_L , γ_S , and γ_{SL} . Figure 3.27 shows a schematic representation of the liquid and solid surface tensions and the solid-liquid boundary tension.

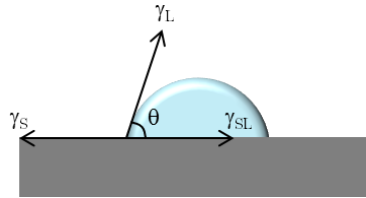


Figure 3.27. Schematic of a droplet showing the three phase contact of a solid, liquid and gas

In order to determine the surface free energy from the contact angle, there are multiple models developed by various researchers. The *Owens, Wendt, Rabel and Kaelble* theory (OWRK) shows a standard method for calculating the surface free energy of a solid from the contact angle with several liquids.^{31,32} This theory assumes that surface free energy is a sum of independent components, associated with the different interactions (dispersion and polar) that take place:

$$\gamma_{SL} = \gamma_S + \gamma_L - 2\sqrt{(\gamma_L^D \cdot \gamma_S^D)} - 2\sqrt{(\gamma_L^P \cdot \gamma_S^P)}, \quad (3.5)$$

where γ_L^D , γ_S^D , γ_L^P and γ_S^P are the dispersive and polar components of the surface tensions of the liquid and solid, respectively.

The result equation of combining equation (3.1) and (3.5) is:

$$\frac{\gamma_L \cdot (\cos \theta + 1)}{2\sqrt{\gamma_L^D}} = \sqrt{\gamma_L^P} \cdot \frac{\sqrt{\gamma_L^P}}{\sqrt{\gamma_L^D}} + \sqrt{\gamma_S^D}, \quad (3.6)$$

Because γ_S^D and γ_S^P are unknown, at least two liquids with known disperse and polar parts of the surface tension are required to determine the surface free energy of the solid wherein at least one of the liquids must have a polar part higher than 0. Normally, water, glycerol and formamide can be used as polar liquids and diiodomethane and α -bromonaphthalene as dispersive. Table 3.12 shows the surface tension values for the three experimental liquids used.

Table 3.12. Surface tension values for water, diiodomethane and ethylene glycol^{33,34}

	γ_L^D [mN/m]	γ_L^P [mN/m]	γ_L [mN/m]
Water (H₂O)	22.1	50.7	72.8
Diiodomethane (CH₂I₂)	49.0	1.8	50.8
Ethylene glycol (C₄H₁₀O₂)	23.6	5.0	28.6

The surface free energy of the two modified and un-modified brush layer materials (hPS and PS_{70%-*r*}-PMMA) has been determined by the sessile drop method using the liquids described above. The values are depicted in Table 3.13. It can be observed that after oxygen plasma functionalization the substrate becomes more attractive to PMMA domains since the polar component of the free energy is larger. Moreover, for the strongest oxygen plasma conditions, it has not been possible to measure the value for the hPS brush probably because the film thickness was thinner (5.6 nm) than for PS_{70%-*r*}-PMMA (8.6 nm) and almost all brush was removed after the functionalization step.

On the other hand, the substrate was again characterized after the resist stripping with PGMEA in order to see if it induced some hydrophobicity to the surface. Nevertheless, the values of surface free energy in Table 3.14 show that there is almost no change on the surface after rinsing.

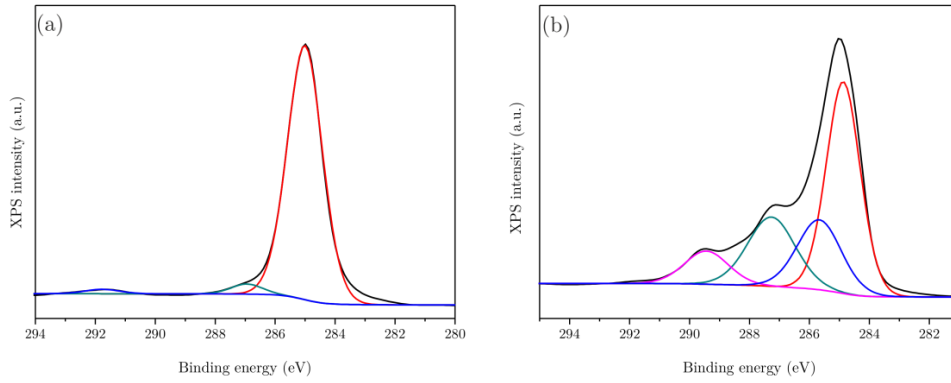
Table 3.13. Surface free energy of modified and non-modified hPS and PS-*r*-PMMA brush layers.

	Substrate	γ_L^D [mN/m]	γ_L^P [mN/m]	γ_L [mN/m]
hPS	<i>Non-modified</i>	38.5±0.22	1.3±0.05	39.8±0.27
	<i>Modified (Conditions A)</i>	31.3±0.14	20.4±0.12	51.7±0.26
	<i>Modified (Conditions B)</i>	-	-	-
PS-<i>r</i>-PMMA (70% PS)	<i>Non-modified</i>	35.6±0.27	5.2±0.1	40.7±0.37
	<i>Modified (Conditions A)</i>	34.5±0.27	14.6±0.14	49.1±0.41
	<i>Modified (Conditions B)</i>	28.9±0.53	42.6±0.55	71.5±1.09

Table 3.14. Surface free energy of modified hPS and PS-*r*-PMMA brush layers after PGMEA rinsing

	Substrate	γ_L^D [mN/m]	γ_L^P [mN/m]	γ_L [mN/m]
hPS	<i>Modified (Conditions A)</i>	30.2±0.12	20.1±0.11	50.3±0.23
	<i>Modified (Conditions B)</i>	-	-	-
PS-<i>r</i>-PMMA (70% PS)	<i>Modified (Conditions A)</i>	33.3±0.14	17.4±0.11	50.7±0.24
	<i>Modified (Conditions B)</i>	28.8±0.07	40.6±0.15	69.3±0.21

The chemistry of the surface has been analyzed with X-Ray Photoelectron Spectroscopy (XPS) on both modified and un-modified surfaces to demonstrate the chemical affinity change on the polymer after the functionalization step. As shown in Figure 3.28.b, after oxygen plasma functionalization there is an increase in intensity towards higher binding energies in the ca. 286-291 eV region, which corresponds to contributions from different carbon-oxygen configurations, characteristic from the brush oxidation (blue, green and pink features corresponding to hydroxyl, carbonyl and carboxyl contributions, respectively).

**Figure 3.28.** XPS spectra corresponding to C1s region of (a) hPS and (b) modified hPS using *conditions A*, by using a PHOIBOS150 analyser and monochromatic 1486.6 eV photons

On the other hand, the surface has been also characterized by studying the BCP behavior on top of un-modified and modified brush layers. It is known that the neutral brush layer for lamellar PS-*b*-PMMA is PS_{60%}-*r*-PMMA, denoting that it takes the fingerprint morphology on free-free-surface. Therefore, when using PS_{70%}-*r*-PMMA the surface is affine to PS, and when it is modified, it changes its affinity to neutral or more PMMA affine due to the oxidation of the substrate.

To carry out the experiment, PS-*b*-PMMA 22 nm pitch BCP is spin-coated on the top of PS_{70%}-*r*-PMMA brush from a 1.5% PGMEA solution and spin-coated at 1500 rpm. Then it is annealed at 230°C for 5 min. Figure 3.29 shows the BCP morphology on top of modified and non-modified PS_{70%}-*r*-PMMA. From Figure 3.29.a it is observed that, as previously predicted by the surface free energy characterization, before the treatment the surface is slightly affine to PS and it changes its affinity to strongly attract PMMA when it is oxidized by the oxygen treatment (Figure 3.29.b and c). Despite having modified the affinity of the surface by chemically oxidizing it, in order to guide the BCP by using wide

guiding stripes, softer oxygen plasma conditions which creates a surface not strong but slight affine to PMMA are needed.

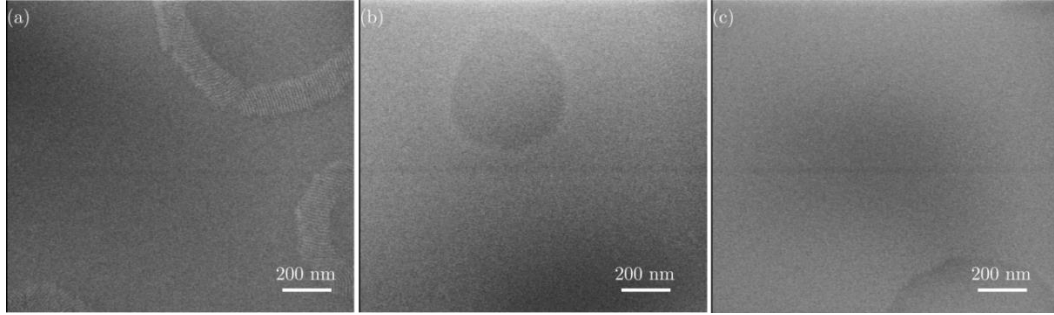


Figure 3.29. PS-*b*-PMMA ($L_0 = 22$ nm) self-assembly on PS_{70%}-*r*-PMMA un-modified (a) and modified with *conditions A* and *B* (b and c, respectively)

3.4.2. Directed self-assembly by chemical epitaxy of PS-*b*-PMMA results

Nevertheless, the DSA process was anyway tested with “*conditions A*” depicted in Table 3.11 since these were the softest conditions available. As Figure 3.30 shows, the DSA process did not work because the resist is somehow modified during the functionalization process and conventional strippers are not efficient enough to remove the whole resist. Therefore, in the SEM images it is observed that BCP is blended with the rests of e-beam resist not allowing thus, the precise BCP DSA.

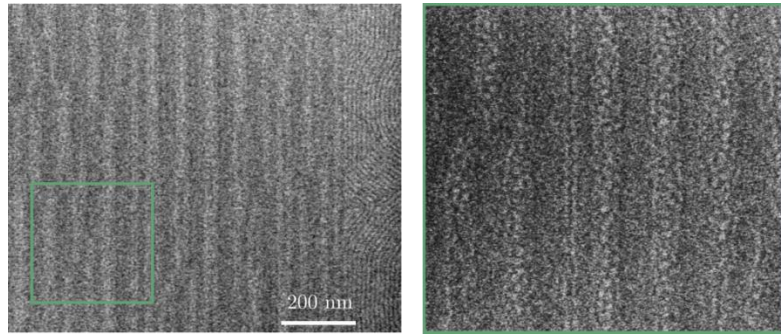


Figure 3.30. PS-*b*-PMMA ($L_0 = 22$ nm) DSA on hPS chemical guiding patterns created when using oxygen plasma conditions A.

In order to demonstrate that the process is easily implementable at larger scales and that the problem is coming from the oxygen plasma equipment availability, the functionalization process has been performed at IMB-CNM in small samples from guiding patterns created at 300 mm. Thus, samples which had been previously patterned in a 300 mm e-beam tool have been functionalized at IMB-CNM by using the soft conditions depicted in Table 3.4.

The BCPs (38 nm, 28 nm and 22 nm pitch) and processing conditions have been the same as the ones used at CEA-Leti. Figure 3.31 shows the DSA results of the three BCPs aligned with CEA-Leti’s guiding patterns ($L_s = 1.5L_0$ and $L_b = 0.5L_0$). That proves, therefore, that

the process can be easily scaled to 300 mm almost without defects, although an accurate oxygen plasma condition has to be found. Moreover, as Figure 3.32 demonstrates, high density multiplication factors when using chemical epitaxy can be obtained (in all cases L_s is constant to $1.5L_0$, and L_b is varied). The DSA results shown are for BCP length chains of 38 nm and 28 nm and density multiplication factors, up to $5L_0$. As compared to the results obtained at IMB-CNM for PS-*b*-PMMA of 38 nm pitch, there have been obtained high density multiplication factors when using wide stripes. This is attributed to the different specifications of the brush layer used (hPS) which had a higher molecular weight, and a thus a thicker film.

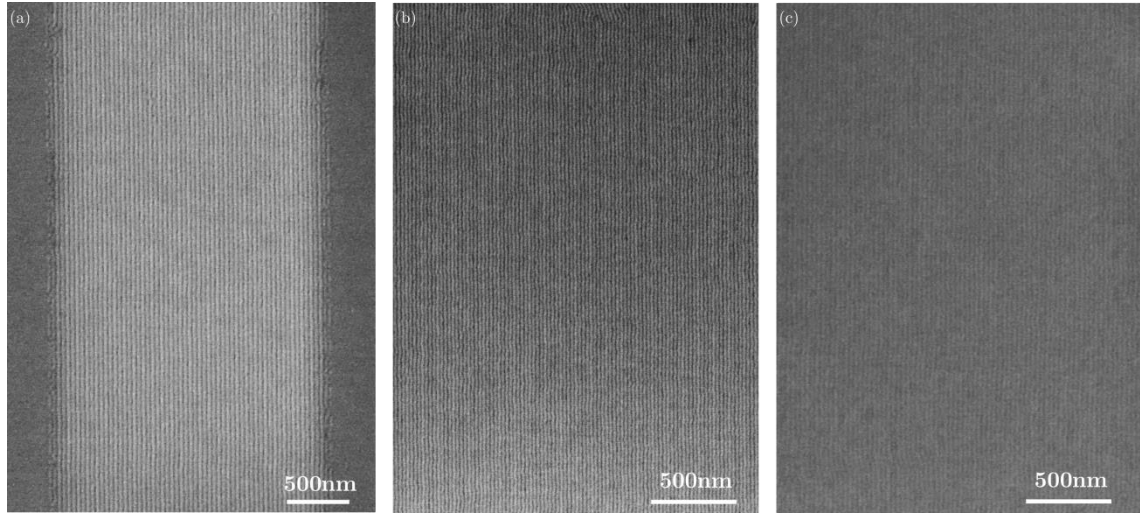


Figure 3.31. PS-*b*-PMMA DSA on chemical guiding patterns created at CEA-Leti and functionalized at IMB-CNM (a) $L_0 = 38$ nm, (b) $L_0 = 28$ nm and (c) $L_0 = 22$ nm

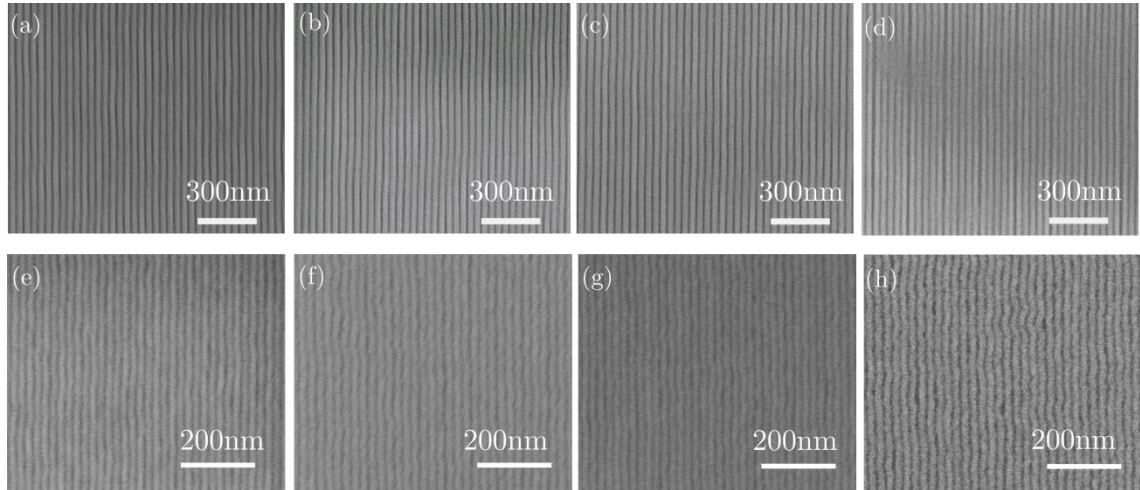


Figure 3.32. PS-*b*-PMMA DSA with density multiplication factors between 2 and $5L_0$ for (a-d) 38 nm and (e-h) 28 nm pitch BCP

3.5. Development and implementation of chemical epitaxy by UV substrate functionalization

In this section, a novel approach of creating chemical guiding patterns by means of exposing the desired areas of the pattern to UV, is presented. It has been previously demonstrated that there is the need to tune the surface energies, to precisely control the orientation of the BCP morphology.^{35,36} When creating chemical guiding patterns, there is the need to chemically change the affinity of the guiding stripes. This can be performed by exposing the surface to a controlled oxygen plasma exposure¹³, as demonstrated in the previous section, or by using two brush layer materials with different chemical affinities.¹⁸ However, this last approach presents the drawback of involving a large number of processing steps. On the other hand, when using oxygen plasma to functionalize the substrate, the process window is very tight.

Therefore, a new strategy to chemically modify the brush is presented. It consists on exposing the polymer surface to UV light, which undergoes to a photochemical reaction. It is known that UV photons interact with PS, leading to carbon-carbon scissions and generating C-O bonds (C-O, C=O, COOH...) at the polymer surface.^{37,38}

From surface characterization techniques, it has been demonstrated that the surface reactions which take place during the UV irradiation, result in a loss of aromaticity, produced by the formation of radicals, PS cross-linking and oxidative degradation (Figure 3.33).^{39,40} Furthermore, it has been published that the level of oxidation during a UV exposure is less than during an oxygen plasma.³⁵

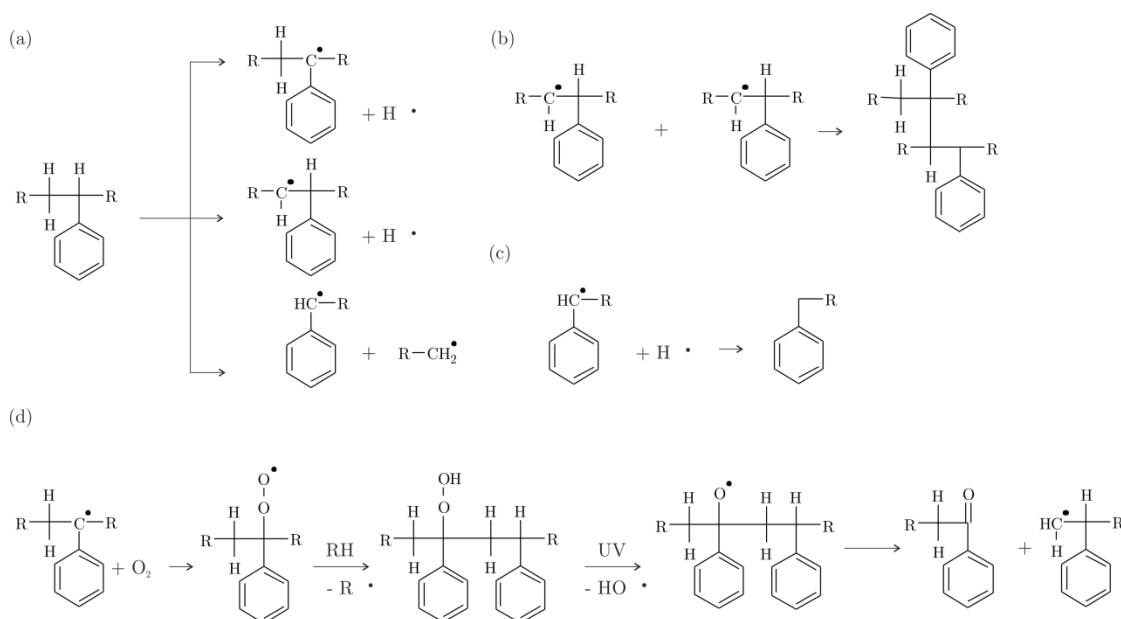


Figure 3.33. Photochemical reactions of PS due to UV exposure: (a) formation of radicals, (b) cross-linking and (c) oxidative degradation³⁸

Figure 3.34 shows XPS spectra of polystyrene, plasma-treated and UV-irradiated polystyrene from *Zhang et al.* work. It is observed that the main changes are due to the oxidation of the surface, more intense when the sample is exposed to oxygen plasma.

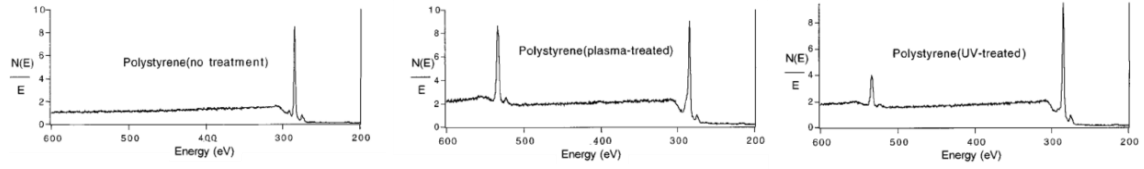


Figure 3.34. XPS spectra of (a) polystyrene and (b) plasma-treated polystyrene and (c) UV-irradiated polystyrene, presented by *Zhang et al.*³⁵

This means that, UV surface modification results in an easy a rapid approach to control the interfacial interactions providing a wider process window, as compared with conventional oxygen plasma treatments. Moreover, although the number of processing steps is higher than in the direct writing approaches because there is the need to use a resist, this method results very suitable to be implemented on a single track, thus making easier its industrial application.

3.5.1. Chemical surface characterization of UV exposed surfaces

3.5.1.1. UV exposure by using a lamp

In order to implement this approach to create chemical guiding patterns and align BCPs, the technique is first tried and characterized on free-surface. This work has been performed at CEA-Leti's pilot line by using an UV lamp of the SOKUDO DUO lithography track. The overall process is depicted in Figure 3.35. The starting substrates are 300 mm silicon wafers ($\{100\}$, p-type), in which 30 nm SiARC and 95 nm SOC layers have been deposited.

Then, PS_{70%}-*r*-PMMA and hPS brush layers have been used to perform the UV tests on 300 mm. Their specifications are depicted in Table 3.1. The brush layers have been spin-coated from a 2% PGMEA solution at 1500 rpm, and annealed at 230°C for 10 min. Consequently, in the same process step, the non-grafted brush is rinsed away with PGMEA, and the sample is exposed with a certain UV dose.

Finally, PS-*b*-PMMA of two molecular weights (depicted in Table 3.2), are deposited on top of the modified brush, and annealed in the same track at 230°C for 5 min.

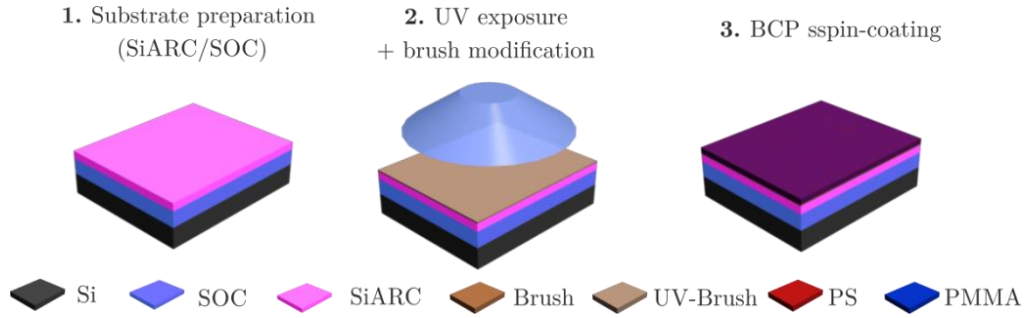


Figure 3.35. Schematic of the PS-*b*-PMMA self-assembly process on UV modified brush polymers

Figure 3.36 and Figure 3.37 show SEM images of PS-*b*-PMMA self-assembly, on top of different UV exposed hPS and PS-*r*-PMMA surfaces, respectively. When hPS brush is used (Figure 3.36), it can be observed that the surface without UV exposure is, as expected, PS affine. Nevertheless, the surface becomes neutral when it is briefly exposed to UV dose, as fingerprint morphology SEM images reveal (from 10 to 80 mJ/cm² dose of process window). At doses higher than 80 mJ/cm², the brush is overexposed and it becomes more PMMA affine. It can be also drawn, that when higher molecular weight BCPs are used, the process window becomes narrower (at doses higher than 20 mJ/cm², the surface starts being PMMA affine).

On the other hand, these results have been compared with PS_{70%}-*r*-PMMA brush. Figure 3.37 shows the self-assembly results when using PS_{70%}-*r*-PMMA. As the brush is PS affine, when there is no exposure, the surface is more attractive to PS. Nevertheless, when it is briefly UV exposed it becomes rapidly PMMA attractive, without going through a neutral affine state. Since UV tends to react with PS inducing its cross-linking and oxidation, making it little by little more PMMA affine, the process window when using PS_{70%}-*r*-PMMA, is narrower due to its lower PS content.

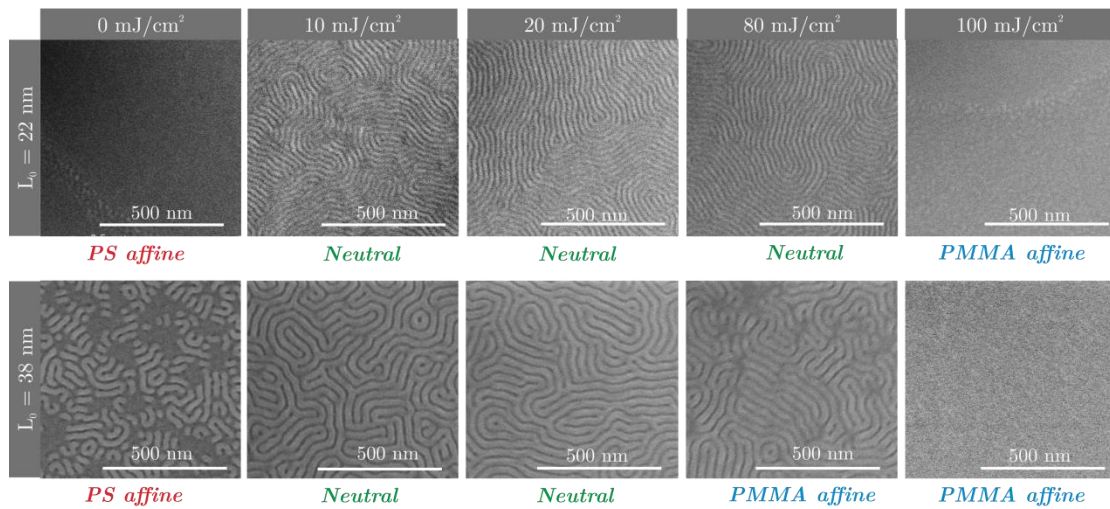


Figure 3.36. PS-*b*-PMMA self-assembly as a function of UV dose on hPS brush

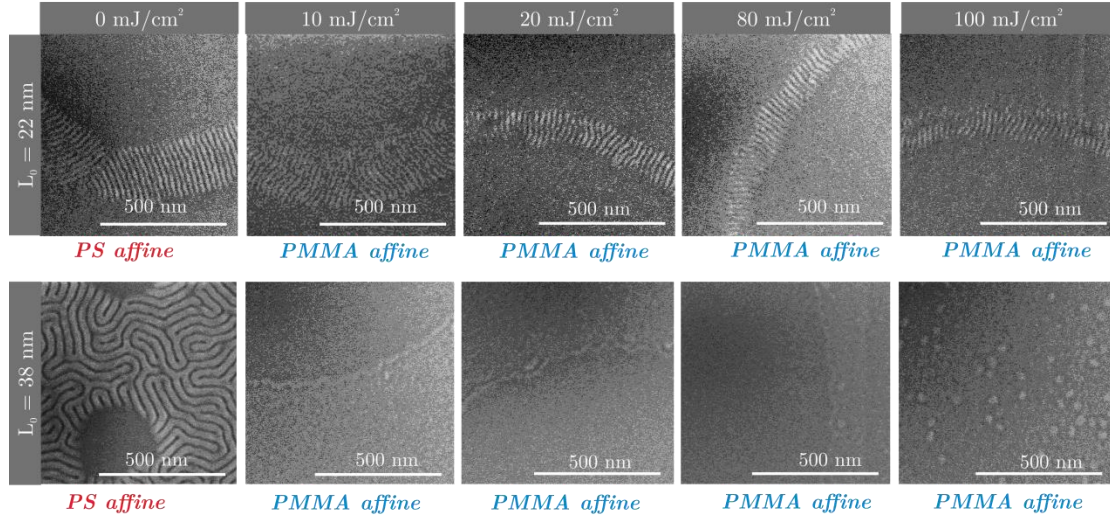


Figure 3.37. PS-*b*-PMMA self-assembly as a function of UV dose on PS-*r*-PMMA brush

3.5.1.2. UV exposure by using a laser

In order to test the impact of the UV exposure on the surface interactions, another UV source has been used. The experiments have been performed in a DUV tool, *Nikon 5307E*, which operates at a wavelength of 193 nm.

Both, the starting substrates and processing conditions have been the same as the ones described in the last experiments. Figure 3.38 and Figure 3.39 show the results of PS-*b*-PMMA of 22 nm and 38 nm, respectively. As observed for both BCPs, the process window is wider than when using the UV lamp. On the other hand, the exposure doses are a little bit higher due to the difference on the light wavelength.

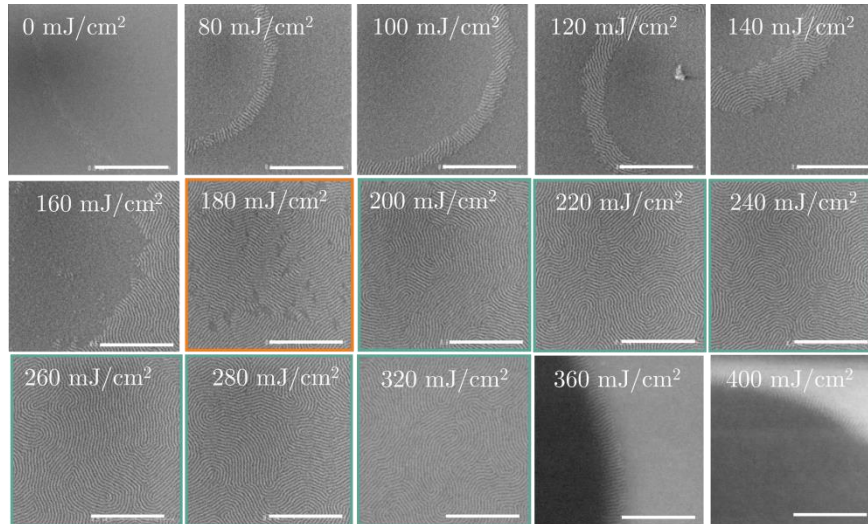


Figure 3.38. PS-*b*-PMMA ($L_0 = 22$ nm) self-assembly as a function of UV dose ($\lambda = 193$ nm) on hPS brush (Scale bar corresponds to 500 nm)

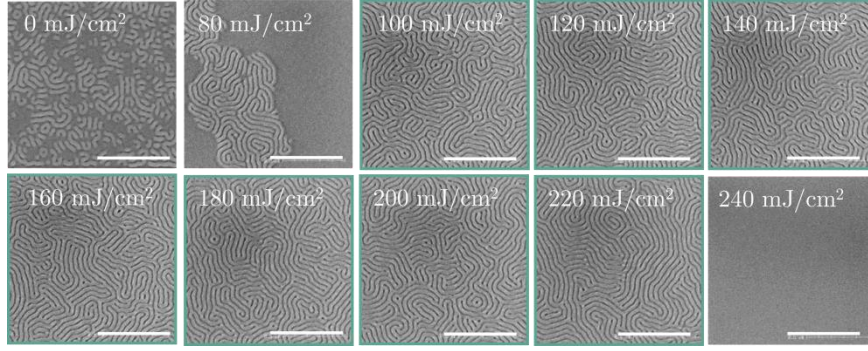


Figure 3.39. PS-*b*-PMMA self-assembly ($L_0 = 38$ nm) as a function of UV dose ($\lambda = 193$ nm) on hPS brush (Scale bar corresponds to 500 nm)

Furthermore, as the process window becomes wider when varying the light wavelength, the experiments have been also tried when using PS-*r*-PMMA brush. Figure 3.40 shows the PS-*b*-PMMA self-assembly when modifying PS_{70%}-*r*-PMMA brush with a UV light source of ($\lambda = 193$ nm).

As observed in the images, and in agreement with the results for hPS brush, the process window in which the surface is neutral, is wider than when modifying the surface with the UV lamp. Moreover, as also already observed in the last experiments, when comparing both BCPs, the process window is wider when using the lowest molecular weight material.

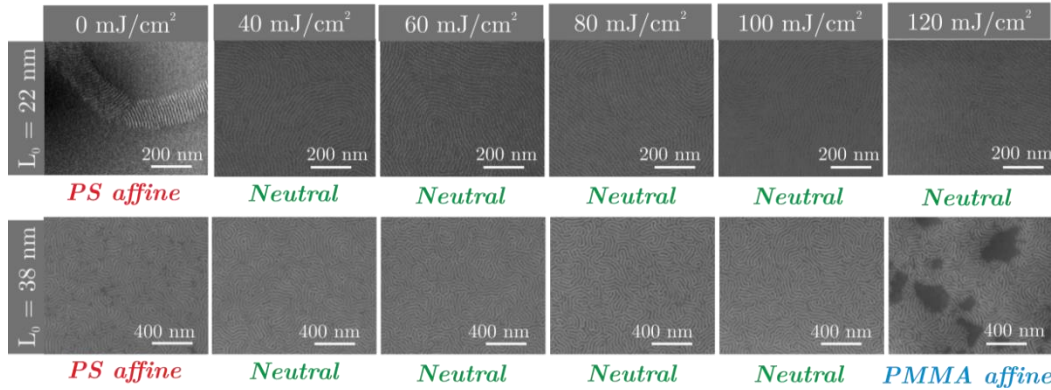


Figure 3.40. PS-*b*-PMMA self-assembly as a function of UV dose ($\lambda = 193$ nm) on PS-*r*-PMMA brush

On the other hand, in order to study the effect of the antireflective layer on the PS modification, there has been performed a test on a silicon substrate. This test has been done with PS-*b*-PMMA of 22 nm and 38 nm on hPS brush surfaces. The obtained results are shown in Figure 3.41, for 38 nm BCP pitch.

It is interesting to observe from the results, that the process window has been considerably reduced, and shifted to lower doses. This effect is explained due to the absence of the antireflective layer. It is known that a high reflective substrate like silicon, can cause light from the exposure to bounce back into the brush. This effect is however, mitigated when using an antireflective coating, since it absorbs part of the UV light.⁴¹ Therefore, during the UV exposure, the energy is partially absorbed by the *ARC*, and then the effect on the

brush layer is reduced. Table 3.15 summarizes the process window in terms of UV dose, for each BCP as a function of the UV source, brush layer and substrate.

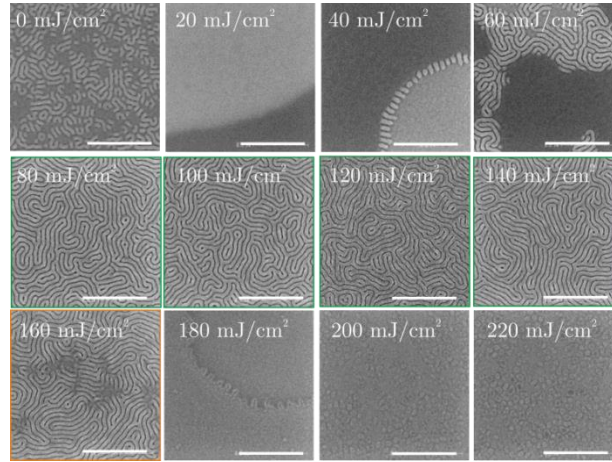


Figure 3.41. PS-*b*-PMMA self-assembly ($L_0 = 38$ nm) as a function of UV dose ($\lambda = 193$ nm) on hPS brush when using a silicon substrate (Scale bar corresponds to 500 nm)

Table 3.15. UV dose range for neutral surface as a function of BCP, brush, substrate and UV source

	UV Lamp (SiARC/SOC)		UV Laser (SiARC/SOC)		UV Laser (Si)
	hPS	PS _{70%} - <i>r</i> -PMMA	hPS	PS _{70%} - <i>r</i> -PMMA	hPS
22 nm	10 - 80 mJ/cm ²	-	200 - 320 mJ/cm ²	40 - 120 mJ/cm ²	180-240 mJ/cm ²
38 nm	10 - 20 mJ/cm ²	-	100 - 220 mJ/cm ²	40 - 100 mJ/cm ²	80-140 mJ/cm ²

3.5.2. Surface free energy characterization

In order to further characterize the surface exposed to UV light and have a more quantitative result, the surface free energy has been analyzed. The surface characterization has been performed by using the sessile drop method, described previously in section 3.4.1.4. The UV exposure method to carry out the characterization has been performed with the lamp due to the easiest accessibility to the tool.

The analysis of the UV exposure has been performed on different treated hPS and PS_{70%}-*r*-PMMA samples. Figure 3.42 represents the total surface free energy, γ , as a function of the UV dose for both brush materials. As observed, for both materials, the increase of surface free energy with the UV exposure dose is exponential, but much more slower for hPS. This allows determining a process window for hPS (dashed line), whereas it is not possible for PS_{70%}-*r*-PMMA. In Figure 3.43, there is a further characterization of the hPS brush layer, representing the two components (polar and dispersive) of the surface free energy. As clearly observed from the graph, the major change on the surface free energy is due to the polar component, owing to the oxidation reaction taking place at the surface.

On the other hand, the surface free energy value in which the surface is neutral to both homopolymers, has been considered to be the corresponding for the lamellae neutral brush

layer, PS_{60%}-*r*-PMMA, which corresponds to a polar surface free energy, γ_P , of 5.2 mN/m. The horizontal dashed line on the graph represents the value of the polar surface free energy of PS_{60%}-*r*-PMMA. As observed it fits inside the process window in which the hPS presents a neutral behavior.

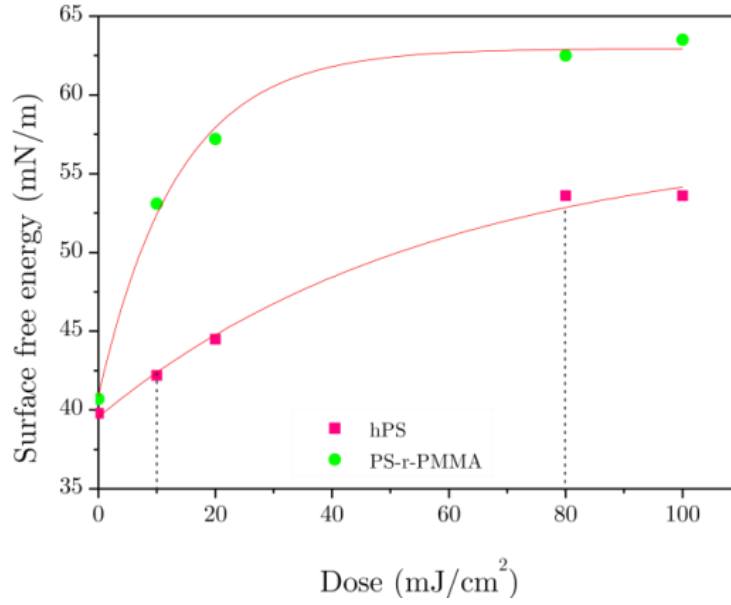


Figure 3.42. Surface free energy - UV dose curve plot performed on hPS and PS_{70%}-*r*-PMMA samples exposed to UV lamp (dashed line represents the process window for hPS brush)

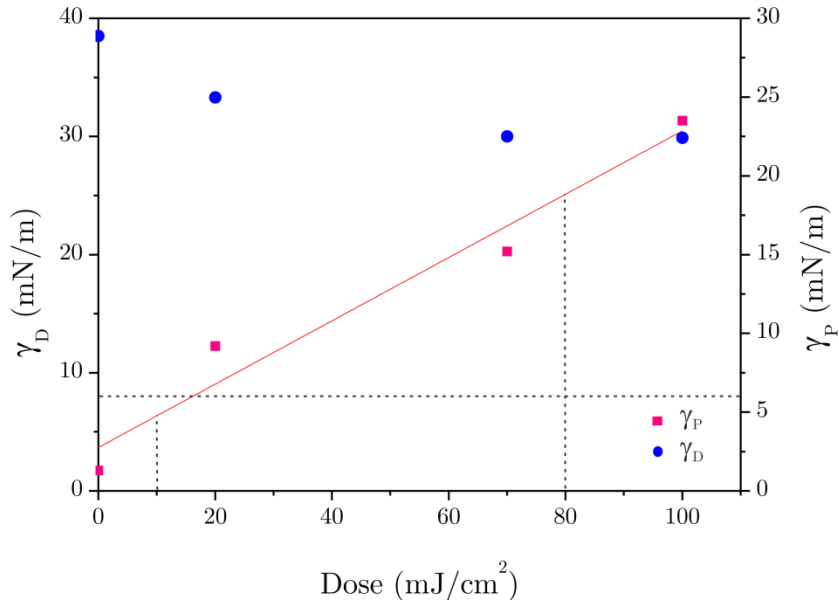


Figure 3.43. Polar and dispersive components of the surface free energy - UV dose curve plot performed on hPS samples exposed to UV lamp (vertical dashed lines represent the process window and horizontal dashed line represents the polar component of the surface free energy of PS_{60%}-*r*-PMMA)

In addition, the surface has been also characterized by XPS. There have been studied three UV-exposed samples, and the chemical changes have been compared with bare PS. As

shown in Figure 3.44, after the UV functionalization, there is an increase in intensity towards higher binding energies, which corresponds to the contributions of carbon-oxygen bonding. Nevertheless, the oxidation level present on the surface is much more lower than the one observed when the sample was oxidized by oxygen plasma (Figure 3.28.b). This is in agreement with the statement, that UV modification allows getting a wider processing window than the one provided by other functionalization methods.

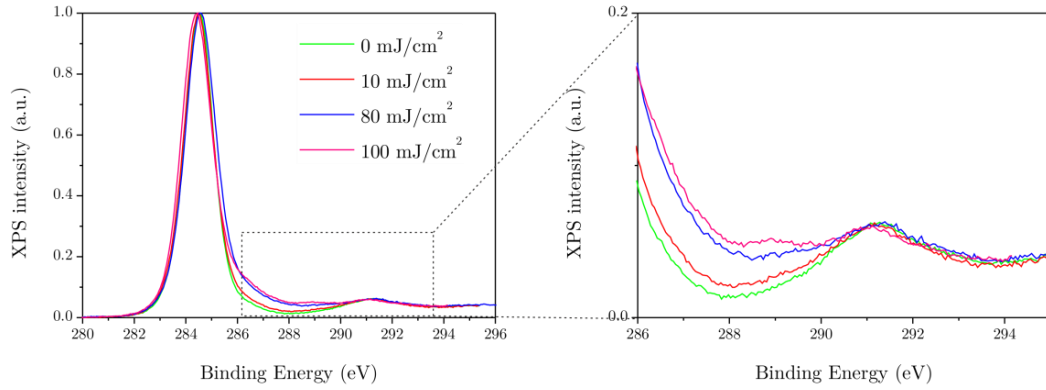


Figure 3.44. XPS spectra corresponding to C1s region of different UV exposed hPS surfaces, using a PHOIBLOS150 analyser and monochromatic 1486.6 eV photons

3.5.3. Directed self-assembly of chemical epitaxy by UV surface functionalization

3.5.3.1. Description of the chemical epitaxy process

In order to find the final DSA application with this novel approach, the surface and the BCP self-assembly behavior, have had first to be characterized. The overall implemented DSA chemical epitaxy process is the one depicted in Figure 3.45. It consists of 6 steps: (i) brush spin-coating, (ii) DUV lithography on negative tone resist (NTR), (iii) resist development, (iv) UV exposure, (v) resist stripping and (vi) BCP spin-coating.

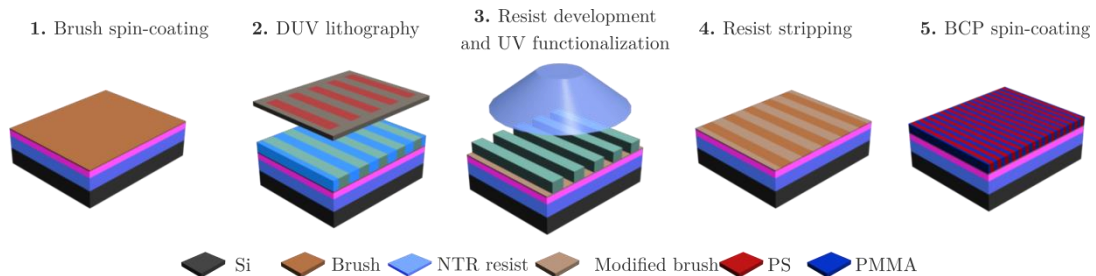


Figure 3.45. Schematic of the chemical epitaxy process based on DUV and UV functionalization implemented at Leti's pilot line

3.5.3.2. Substrate preparation and creation of the chemical guiding patterns

The DSA process has been performed with the same substrates and materials, as the ones used for the surface characterization. First, in order to optimize the lithography step, a Focus/Energy matrix (FEM) is performed.

Then, the substrate is prepared, and an hPS brush layer is deposited on the top of the surface in order to define the chemical guiding patterns on it. The 193nm deep UV lithography is performed by using a NTR, *JSR AIM8630JN*, which is pre-baked at 85°C for 1 min. Consequently, the 193nm deep UV lithography is performed in a *Nikon 5307E* tool, with a dose of 51 mJ/cm². Subsequently, the resist is post-baked at 85°C for one further minute, and developed with butyl acetate.

Once the lithography is performed, the substrate is chemically modified by exposing the sample to the UV lamp at 20 mJ/cm², since it is the value in which the surface presented a neutral surface. Finally, the resist is stripped with IPA, and PS-*b*-PMMA of 22 nm pitch is deposited and annealed.

Nevertheless, when the wafer was inspected, there was no evidence of chemical pattern and the entire surface seemed to be PS affine. Therefore, the effect of the resist stripping on the UV modified surface was inspected by characterizing its surface free energy. Table 3.16, shows the values of the surface free energy of different treated hPS surfaces. As commented previously, the surface free energy increases after UV exposure, but it turns back to the reference value after dipping the sample in BA or IPA. This is attributed mainly to a change on the polar component of the surface free energy which decreases considerably. This is explained because the solvents used to strip the resist, affect the chemical changes performed on the surface by stripping the polar groups created on the brush layer. Looking at the surface free-energy values, it is clarified therefore, the fact that there is no chemical contrast on the guiding patterns when using 20 mJ/cm².

Table 3.16. Surface free energies of different hPS treated surfaces

	hPS	hPS + UV (20 mJ/cm ²)	hPS + UV + BA	hPS + UV + IPA
γ	39.8 mN/m	48.5 mN/m	38.8 mN/m	38.8 mN/m
γ_D	38.5 mN/m	33.3 mN/m	37.9 mN/m	37.9 mN/m
γ_P	1.3 mN/m	9.2 mN/m	0.9 mN/m	0.8 mN/m

The solvent effect on different UV doses, has been widely studied by characterizing the surface free energy, in order to force the contrast on the chemical guiding patterns. The optimal value found, which is within the hPS process window and which does not damage the brush layer (the brush thickness remains the same) has been to 50 mJ/cm². When using this dose, the surface free energy after stripping the resist with IPA is 43.8 mN/m, which is within the hPS process window (see Figure 3.42). The DSA results are shown in Figure

3.46, where the darker areas are the ones covered by the NTR (non-modified and PS-affine).

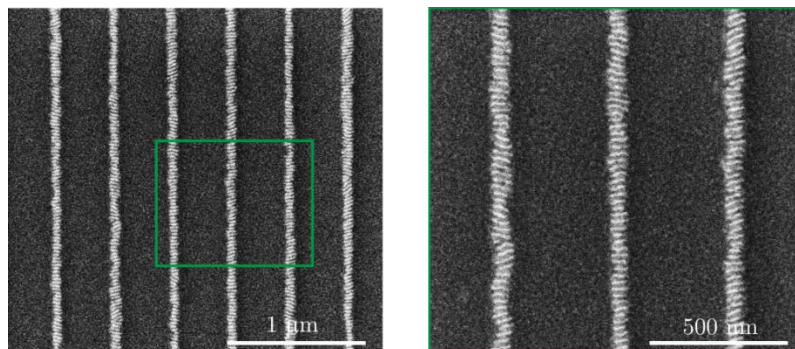


Figure 3.46. Schematic of the chemical epitaxy process based on DUV and UV functionalization implemented at Leti's pilot line

In summary, it has been demonstrated a viable process to create chemical guiding patterns, which allows using a wider process window. This method allows controlling with precise accuracy the interactions between the guiding pattern and the BCP blocks by properly tuning the UV exposure dose. Therefore, it permits avoiding non-desired morphologies as may appear with the oxygen modification approach. However, as it has been demonstrated by the surface free energy characterization, the effect of the solvents during the processing has to be taken into account.

3.6. Chemical epitaxy based resistless direct writing methods

3.6.1. Introduction

Direct writing methods involve the preparation of the desired patterns avoiding any issues related with resists. In these methods, the radiation that is used to expose the surface is not transmitted through a resist but directly to the substrate. Direct writing techniques can achieve resolutions below 6 nm, high precision for pattern placement and a reduction in the number of process steps because the use of a resist is not needed.

Two novel methodologies based on direct writing lithography have been developed and optimized. The guiding patterns are directly created on the top of the brush layer inducing its chemical modification by means of EBL and AFM.

3.6.2. E-beam lithography direct writing

EBL is normally used in surfaces covered with electron-sensitive films, since the electron beam changes the chemistry of the resist, enabling the selective removal of the exposed or non-exposed regions. Despite being a limiting technique for high-volume production due to its low throughput, the major advantage of EBL is that patterns below 10 nm resolution

can be exposed. Therefore, this makes it a very suitable technique for research and development.

3.6.2.1. Materials and methods

Description of the chemical epitaxy process

In a conventional EBL, the step sequence of depositing, developing and removing the resist makes the process larger and may induce some chemical changes on the substrate and its functionalization. In direct e-beam writing, the creation of the guiding patterns is performed by directly exposing the polymer brush layer to electrons in order to induce its chemical modification, without the use of a resist. Indeed, by accurately tuning the e-beam parameters, highly precise and resolution patterns can be created, which is one of the critical factors in the microelectronics industry. Besides this, the developed process of e-beam direct exposure becomes simpler since the sequence of resist deposition, exposure, development, substrate functionalization and resist strip is substituted by a single step.

Figure 3.47 shows the overall fabrication process for PS-*b*-PMMA DSA using guiding patterns created by direct e-beam exposure on top of the brush layers made of PS-OH. It consists of a three-step process: (i) PS-OH brush grafting on top of silicon substrate, (ii) creation of guiding patterns by e-beam exposure and (iii) BCP self-assembly.

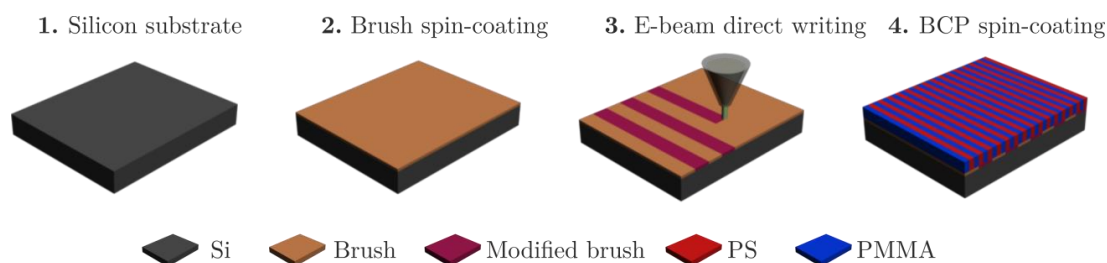


Figure 3.47. Overall fabrication process for DSA by e-beam direct writing

Brush and block copolymer materials

The starting substrates are 0.9 x 0.9 cm chips bearing a native silicon oxide layer (p-type silicon wafers of 4-40 $\Omega \cdot \text{cm}$ resistivity). The brush layer used is PS-OH with a $M_n = 4.5 \text{ kg} \cdot \text{mol}^{-1}$ and $\text{PDI} = 1.09$, purchased from *Polymer Source, Inc* and the BCP material is PS-*b*-PMMA of 28 nm pitch. The specifications of both the brush and the BCP are depicted in Table 3.17.

Table 3.17. Specifications of brush layer and BCP materials used for direct writing chemical epitaxy DSA

	Molecular weight	PDI
PS-OH	4.5 kg/mol	1.34
Lamellar PS- <i>b</i> -PMMA	45 kg/mol	1.12

Substrate preparation and creation of chemical guiding patterns

In a first step, a 40 nm thick PS-OH layer from a 1.5% toluene solution is spin-coated at 5000 rpm for 1 min on the top of a silicon substrate which has been previously activated by using oxygen plasma at 500W for 10 min in order to enable the reaction between the hydroxyl PS-OH groups and the native oxide of the surface. In order to accelerate the reaction, an annealing step at 260°C for 5 min in a continuous N₂ gas flow. It is important to avoid oxygen during the annealing step, since it could react with the brush layer producing its oxidation and thus, inducing a chemical modification that could affect after to the DSA process.

After, the non-reacted PS-OH brush is rinsed away with toluene by ultrasounds bath at 40°C for 5 min, leaving a grafted 4.7 nm PS-OH film. Then, the chemical guiding patterns are created on the grafted PS-OH by direct e-beam exposure in a *RAITH150Two* tool without using any kind of resists. The e-beam process is performed by exposing the desired patterns at 20 kV and 330 pA of beam current with a nominal beam diameter of 2 nm. On the other hand, a wide range of e-beam factors, between 4 mC/cm² and 4 C/cm², has been studied in order to find the optimal width of the guiding stripes that guide the assembly of the BCP. This means that the line writing speed is varied between 0.825 and 0.0001 mm/s by using a line step of 10 nm. The exposure is defined as a set of single line exposures. The pattern pitch employed is $4L_0$ (where L_0 is the BCP pitch), and the widths of the guiding and background stripes are determined by the dose factor applied in each case. Figure 3.48 shows the chemical guiding patterns specifications for a $4L_0$ pattern pitch, in which L_s and L_b represent the guiding and background stripe widths, respectively. In all the tests, the pattern pitch has been set at $4L_0$, and the guiding stripe width is defined by the dose factor.

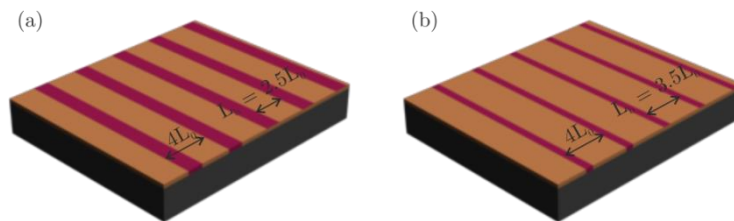


Figure 3.48. Chemical guiding patterns specifications created by direct e-beam writing. Schemes represent (a) wide and (b) narrow guiding stripes exposed. The guiding stripes are colored in magenta and the pristine PS-OH surface in brown. L_0 refers to the pitch of the BCP and L_b to the separation between guiding stripes

In order to see how the guiding patterns look like after e-beam exposure, an array of 112 nm pitch lines ($4L_0$) with a line width of 42 nm ($1.5L_0$) which corresponds to an e-beam dose of 184,000 $\mu\text{C}/\text{cm}^2$, has been characterized by AFM, as it is shown in Figure 3.49. It is important to highlight that the contrast in the phase image (Figure 3.49.c) is larger than in the topographic image (Figure 3.49.a), indicating that the guiding pattern creation mainly involves a brush chemical change. On the other hand, the observed topographic

change may be an artifact due to the effect of the chemical change on the interaction forces between the tip and surface that determine how the amplitude of the tip oscillation is reduced.

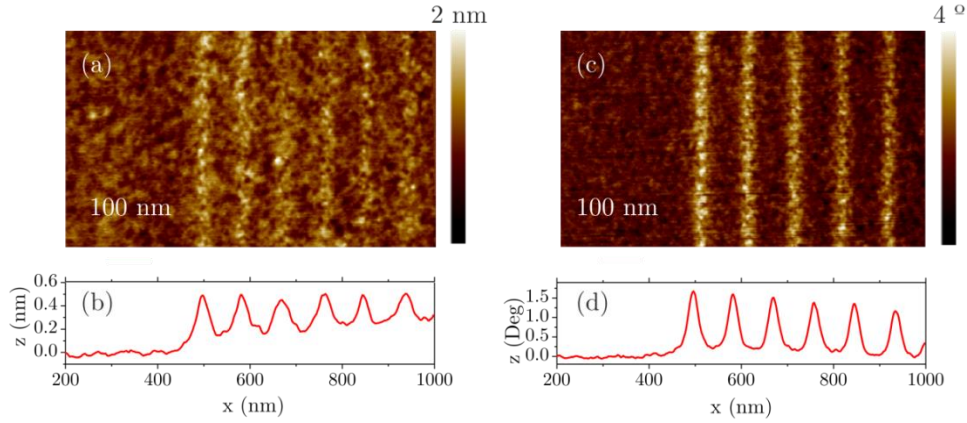


Figure 3.49. AFM images and profiles of guiding patterns created by e-beam direct exposure (20 kV, 30 μm , 184,000 $\mu\text{C}/\text{cm}^2$) (a) Topographic AFM image of an array of 112 nm pitch ($\Delta z = 2$ nm) and (b) extracted average profile (c) Phase AFM image acquired simultaneously to image (a) ($\Delta\Phi = 4$ Deg) and (d) extracted average profile

In order to characterize the chemical affinity between the different areas of the guiding pattern and each domain of the BCP, the contact angle between homopolymers, polystyrene (PS) and poly(methyl methacrylate) (PMMA), with the brush has been experimentally determined.

Figure 3.50 shows the procedure to determine the chemical interaction characterization between different species and it consists of depositing a thin homopolymer layer on top of both unmodified and modified brush.⁴² The samples are annealed at 190°C for 24h in a vacuum environment in order to accelerate the dewetting of the polymer. Droplets of the homopolymer are formed on top of brush layer, and then the contact angle of these droplets is determined by AFM as depicted in Figure 3.51. As it is revealed in the figure, e-beam exposed areas present larger affinity to PS domains. This is explained by the cross-linking of PS due to e-beam exposure, as reported in the literature.^{43,44} PS is found to be resistant to electron beams, but beyond a certain e-beam dose, it undergoes cross-linking with the possible scission of the phenyl groups.

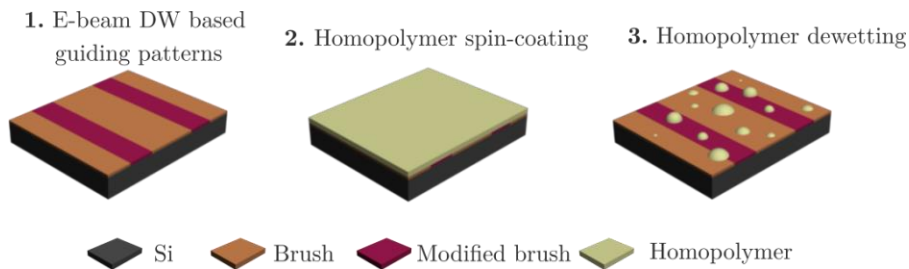


Figure 3.50. Overall fabrication process to determine the contact angle between homopolymers and brush

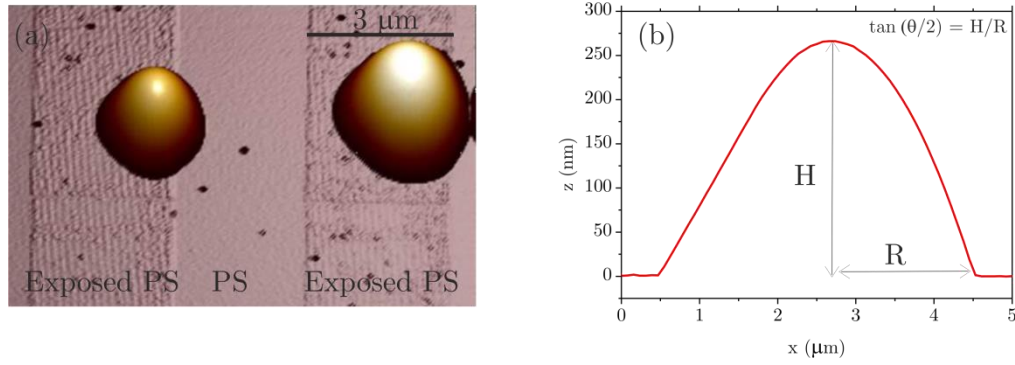


Figure 3.51. Procedure to determine the contact angle between homopolymers and the brush layer (e-beam modified and un-modified) (a) Topographic AFM image of PS droplets on top of patterned and unpatterned areas (b) Profile of a PS droplet on PS-OH

PS-*b*-PMMA spin-coating

After e-beam parameters were optimized to achieve the precise guiding pattern dimensions ($L_s = 1.5L_0$ and $L_b = 2.5L_0$), a lamellar PS-*b*-PMMA BCP of 28 nm pitch from a 1.15% toluene solution is spin-coated at 2750 rpm for 1 min. Afterwards, in order to promote the self-assembly, the sample is annealed at 200°C for 20 min in hot-plate.

*3.6.2.2. Directed self-assembly by chemical epitaxy of PS-*b*-PMMA results*

Figure 3.52 shows the DSA results for a 28 nm BCP when different e-beam doses were applied to create the chemical guiding patterns. It can be seen that the best alignment of the BCP is achieved when a dose factor of 184,000 $\mu\text{C}/\text{cm}^2$ is used Figure 3.52.c), which corresponds to a guiding stripe width of $1.5L_0$ and a density multiplication factor of $4L_0$.

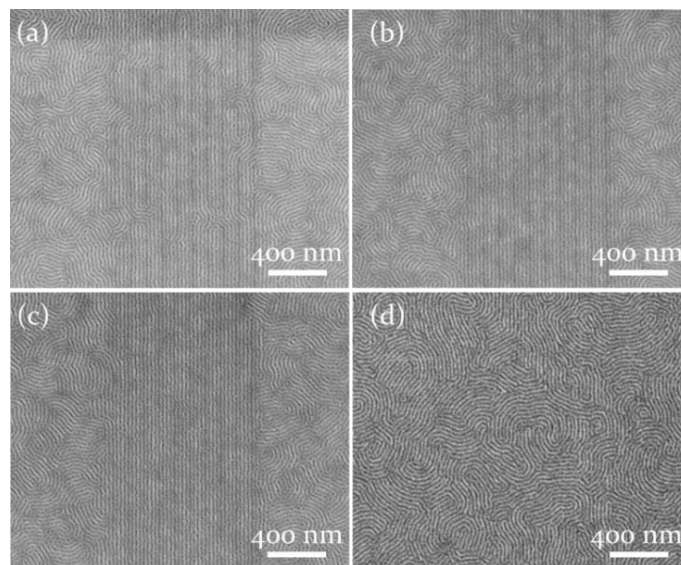


Figure 3.52. DSA of PS-*b*-PMMA of 28 nm pitch for different e-beam doses. (a) dose = 256,000 $\mu\text{C}/\text{cm}^2$; (b) dose = 196,000 $\mu\text{C}/\text{cm}^2$; (c) dose = 184,000 $\mu\text{C}/\text{cm}^2$; (d) dose = 40,000 $\mu\text{C}/\text{cm}^2$

As discussed previously, in accordance with contact angle results it can be better observed in the zoomed image (Figure 3.53) that on the top of exposed areas (red stripes) there are two PS domains and one PMMA domain in the middle, indicating that the e-beam modified surface has become slightly more affine to PS. This behavior is better described in the scheme where one block of PMMA (blue colored) is at the center of the guiding stripe, while two PS domains (red colored) also stand on the top of the guiding stripe, thus demonstrating the slightly affinity of the guiding stripes to PS. In *chapter 6* the chemical interactions taking place between the domains and the chemical guiding pattern are discussed in more detailed from HAXPES experiments characterization.

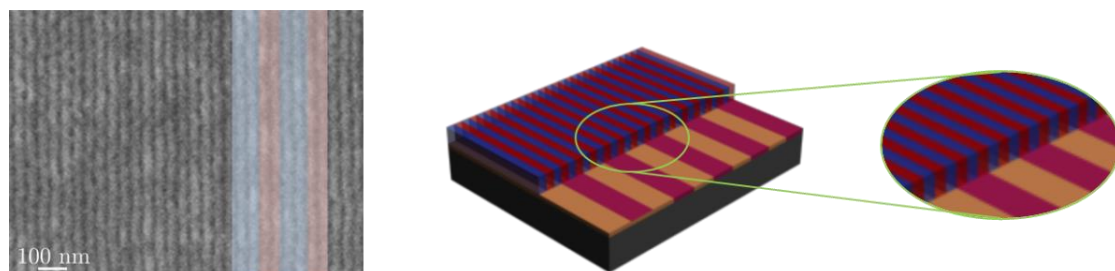


Figure 3.53. Zoom SEM image of PS-*b*-PMMA DSA ($L_0 = 28$ nm) for an e-beam dose of 184,000 $\mu\text{C}/\text{cm}^2$. Guiding stripes are colored in red ($1.5L_0$) and the pristine PS-OH surface in blue ($2.5L_0$)

3.6.3. Local Anodic Oxidation based AFM nanolithography

Aside from e-beam lithography, AFM-based local anodic oxidation (LAO) can be used as a direct lithography approach. In contrast with e-beam direct writing, in which the high e-beam doses employed prevent from high resolution guiding patterns and involve large e-beam writing times, the unique capabilities of AFM, in terms of resolution and position accuracy, makes it very suitable for the investigation of the guiding behavior of novel polymer materials, in view of obtaining a half-pitch resolution around 10 nm or below.

Few efforts of creating guiding patterns by means of AFM lithography for DSA applications have been previously reported.^{45,46} In these works, a self-assembled layer of octadecyltrichlorosilane (OTS) was chemically modified by contact-mode AFM while applying a voltage and then cylindrical BCP were directly self-assembled on top of it.

LAO is a modality of AFM lithography in which a voltage is applied between the tip and the surface that leads to an electrochemical reaction. As depicted in Figure 3.54, for a silicon substrate and under certain environment conditions, between the tip and the surface there is always a water absorption layer which covers both the tip and the substrate. When the tip is approached some nanometers to the surface a water meniscus is formed, and then by applying a voltage an electrochemical cell, in which the tip acts as a cathode and the water as the electrolyte, is generated.⁴⁷

The chemical reactions that take place in the cell are water hydrolysis and the subsequent oxidation of the silicon. The overall reaction is depicted in (3.7).



LAO is performed by operating AFM in noncontact mode, increasing thus the tip throughput and lifetime.⁴⁸

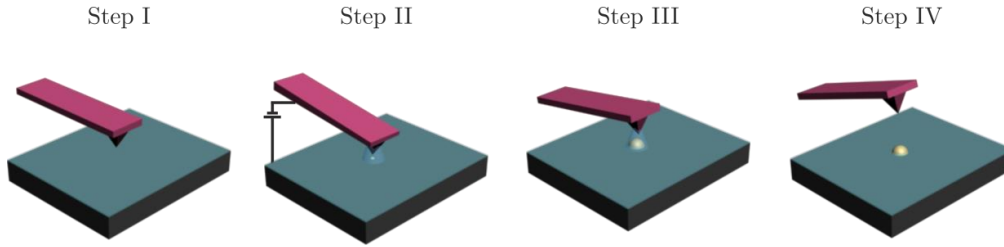


Figure 3.54. Local anodic oxidation steps in noncontact mode

The application of LAO AFM method can be used as a technique to create chemical guiding patterns on top of a brush layer by increasing the tip throughput and lifetime.^{48,49} Furthermore, patterns with density multiplication factors up to 7 can be created in a very efficient, precise and routinely way by using commercial equipment. On the other hand, because of the achievable resolution of oxidation scanning probe lithography, this approach has great potential to become very useful to study next generation DSA of BCP.

3.6.3.1. Materials and methods

Description of the chemical epitaxy process

Figure 3.55 shows the overall process for the fabrication of chemical guiding patterns on top of PS-OH brush layers by LAO. It consists in a three-step process: (i) PS-OH brush grafting on top of silicon substrate, (ii) creation of guiding patterns by AFM-based LAO and (iii) BCP self-assembly.

As in the case of e-beam direct writing, the whole process contains fewer single processes than the normal methods used to create guiding patterns, since the sequence of resist, exposure, development and resist removal is discarded/eliminated by the single process of o-SPL patterning.

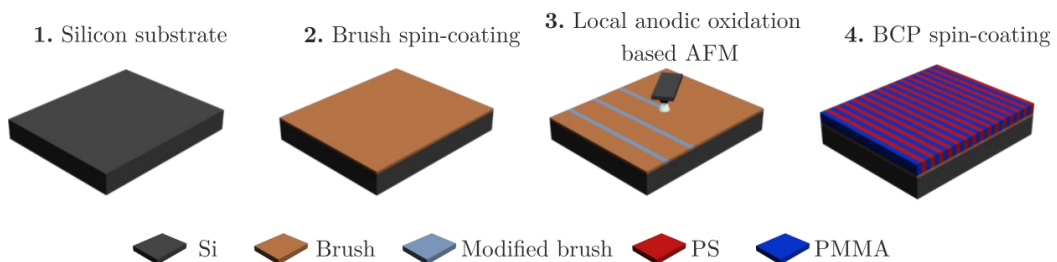


Figure 3.55. Overall fabrication process for DSA by o-SPL

Brush and block copolymer materials

To directly compare both direct writing techniques, the same materials (brush and BCP) and processing conditions are used in the fabrication process.

When using the LAO-AFM based approach, the chemical guiding patterns are created directly on top of PS-OH after being removed the non-reacted brush with toluene.

Substrate preparation and creation of the chemical guiding patterns

The AFM instrument (*Dimension Icon*, Bruker) is operated under noncontact mode using standard tapping cantilevers (*OTESPA* with nominal tip radius of 7 nm), with a close loop control of x, y and z displacement which avoids piezo-induced dimensional distortions. A homemade humidity control system is used in order to control the humidity during the oxidation process. As depicted in Figure 3.56, it maintains the humidity constant in the range of 20-60% by introducing inside the chamber a constant N₂ flow.

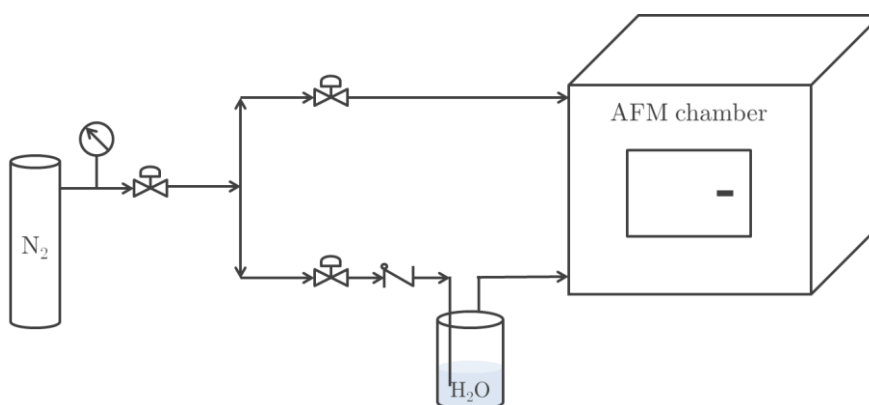


Figure 3.56. Humidity control system installed next to the AFM chamber

In order to create the chemical guiding patterns the AFM is operated in soft-tapping mode, at an oscillation amplitude around 15 nm and then moved to the desired position to start the creation of a line. After, the feedback loop is disconnected and a positive voltage is applied to the sample through the AFM chuck. When the voltage pulse is applied, the electric field induces the formation of a liquid meniscus between the sample and the tip in which a redox reaction takes place.

During the oxidation process, the tip is moved along the line at a selected speed, and when it reaches the end of the line the bias voltage is switched to zero and the feedback loop is connected (the feedback is off during writing). When the voltage is off, the liquid meniscus is broken and the tip recovers its original amplitude and it is moved to the new position to fabricate a new line.

It is important to highlight that in order to maintain constant the separation between the tip and the surface, the lines are fabricated following the direction where the lateral movement of the tip is parallel to the surface.

Figure 3.57 shows a scheme in which the local oxidation process is used when a polymer brush layer is grafted on top of a silicon substrate. Under the application of a voltage to the sample with respect to the tip, the water molecules are ionized ($2\text{H}_2\text{O} \rightarrow 2\text{OH}^- + 2\text{H}^+$) and the OH^- ions are accelerated through the surface where the electrochemical reaction takes place oxidizing the underneath silicon.

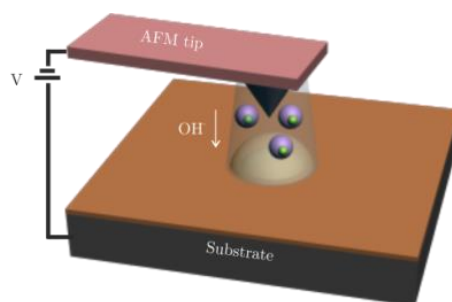


Figure 3.57. Local anodic oxidation process on polymer brush layer

Figure 3.58 shows an example of a large $15 \times 15 \mu\text{m}^2$ guiding pattern made up of an array of lines of 400 nm pitch. The magnified image reveals that the pattern consists of 15 nm width lines and roughly 1 nm height. The fact that the modified areas appear raised from the background indicates that the underneath silicon has been oxidized.

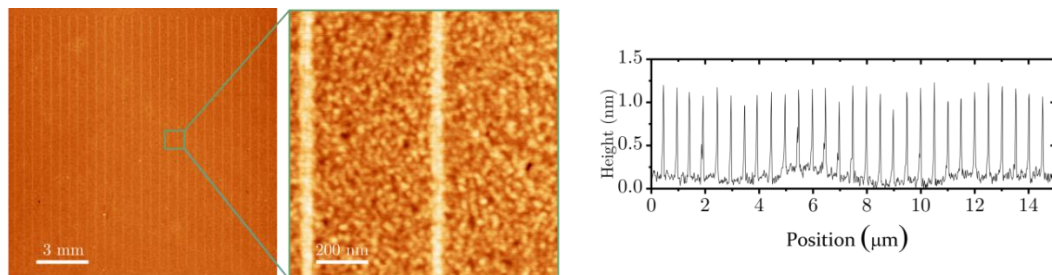


Figure 3.58. AFM images and profile of high resolution guiding patterns created by o-SPL (a) Array of lines covering an area of $15 \times 15 \mu\text{m}^2$

The resolution of the guiding patterns is determined by the AFM radius, the water meniscus size and the relative velocity of the tip with respect to the surface. By keeping constant the humidity, the tip-speed and the gap between the tip and the surface, it can be observed in Figure 3.59 that the higher the bias voltage applied, the wider the oxidized lines are. Therefore, the bias voltage has to be precise in order to control the accurate and desired line width. On the other hand, the line width can be also tuned by varying the humidity and keeping constant all other parameters, as it is seen in Figure 3.60, where the relative humidity used is 20% and 40%, respectively.

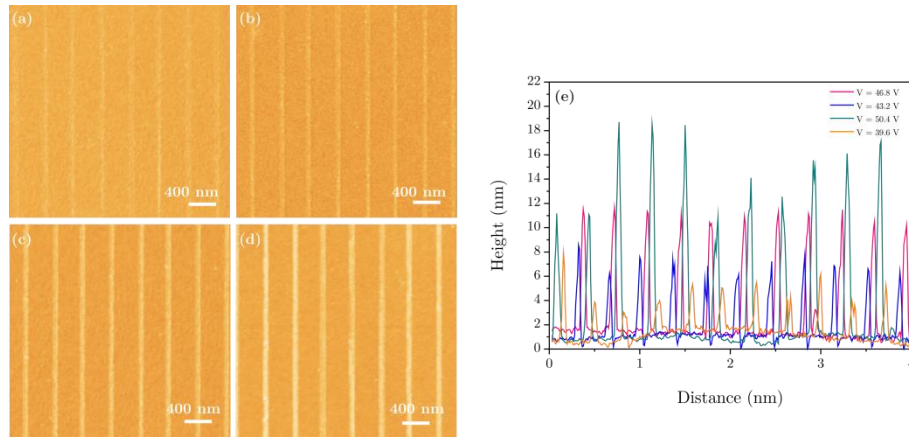


Figure 3.59. AFM images of guiding patterns created by o-SPL at bias voltages of (a) 39.6 V, (b) 43.2 V, (c) 46.8 V and (d) 50.4 V, by keeping a constant humidity of 17%, a tip-speed of 2 $\mu\text{m/s}$ and a tip-surface distance of -6 nm

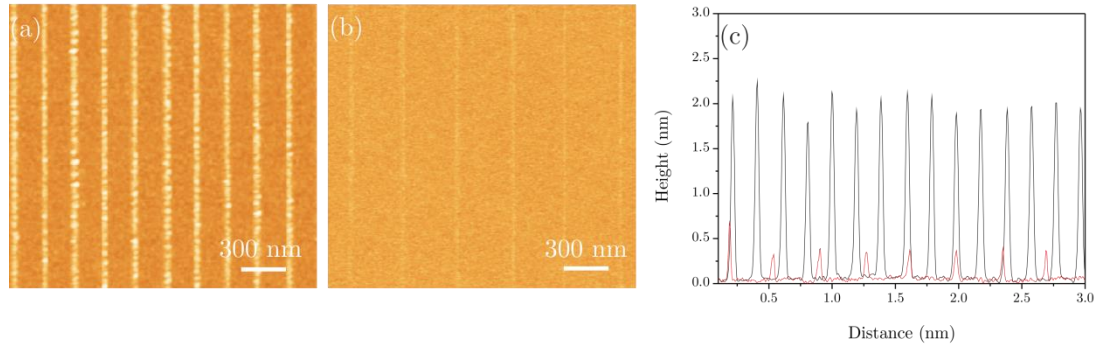


Figure 3.60. AFM images of guiding patterns created by o-SPL at (a) 40% and (b) 20% humidity, by keeping a constant bias voltage of 32.4 V, a tip-speed of 5 $\mu\text{m/s}$ and a tip-surface distance of -8 nm. Red and black profiles in (c) correspond to low and high humidity, respectively, in order to highlight the effect of relative humidity on the guiding pattern creation

High resolution guiding patterns are achieved when high tip velocity and low humidity are used. Figure 3.61 shows an example of high resolution guiding patterns consisting of an array of lines of 20 nm pitch with a line width resolution below 10 nm. It is remarkable that the contrast in the phase image is larger than in the topographic image, showing that the patterning involves changes in the surface chemical properties. The origin of compositional contrast in phase imaging AFM is related to changes in energy dissipation, meaning that in the oxidized regions of the pattern the tip dissipates more energy. This is also indicative of differences in the chemical and/or physical properties between the oxidized and non-oxidized regions.⁵⁰ A closer inspection of the patterns reveals that its roughness is basically due by the surface roughness of the brush layer, which is the limiting factor for the present pattern resolution.

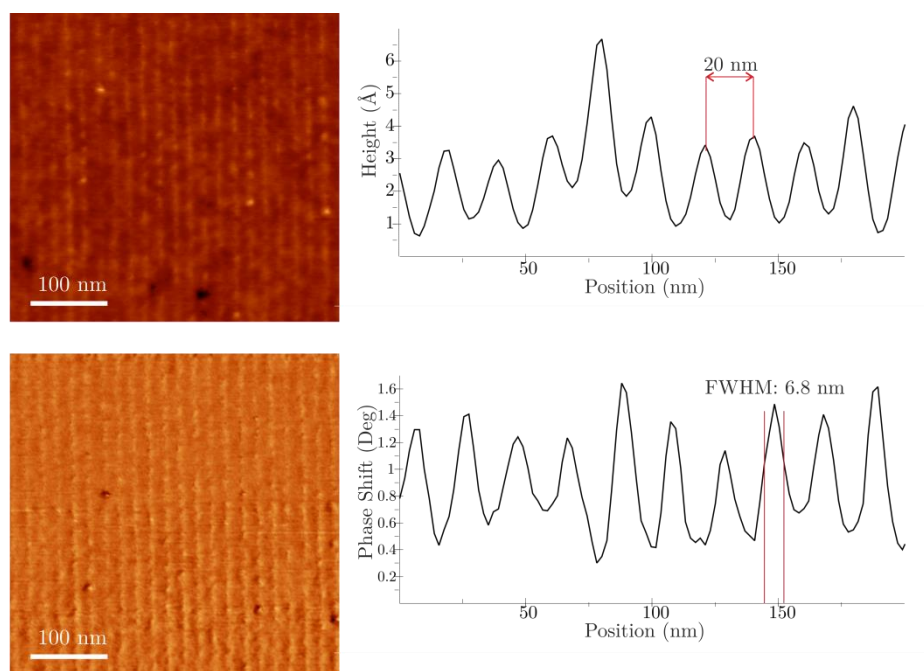


Figure 3.61. Topographic and phase AFM images of an array of lines of 20 nm pitch ($\Delta z = 4$ nm) and the respective profiles.

The guiding patterns created by α -SPL on the brush layer can be of diverse chemical/physical nature depending on the oxidation conditions used: (i) chemical surface modification of the top brush polymer chemical groups (similar to what it has been reported on tip-induced electro-oxidation for constructive nanolithography⁵¹), (ii) chemical modification of the brush and oxidation of the underlying silicon and (iii) oxidation of the underlying silicon together with the brush polymer degradation.

When the first situation occurs, there is only a slight change not in topography but in phase AFM images, which means that there is no underneath oxide grown. In order to prove that there is only a chemical change on the surface, an additional experiment has been performed. Specifically, square type guiding patterns are formed at low oxidation conditions on top of PS-OH brush layers and then they are characterized using the peak-force tapping mode of the AFM. Figure 3.62 shows AFM topography (a) and adhesion (b) images with two squares patterns oxidized at 8V and 5V, respectively, by keeping constant all other parameters. Whilst enough contrast for the square oxidized at highest voltage is observed in both topography and adhesion images, the bottom AFM topography image (Figure 3.62.a) reveals that there is not enough contrast for the square oxidized at the lowest voltage. On the other hand, the bottom AFM adhesion image (Figure 3.62.b) shows a slightly contrast, indicating the presence of a chemically modified surface. Friction AFM images were not used since it has been observed that scanning in contact mode induces some chemical and topographical changes on the brush layer.

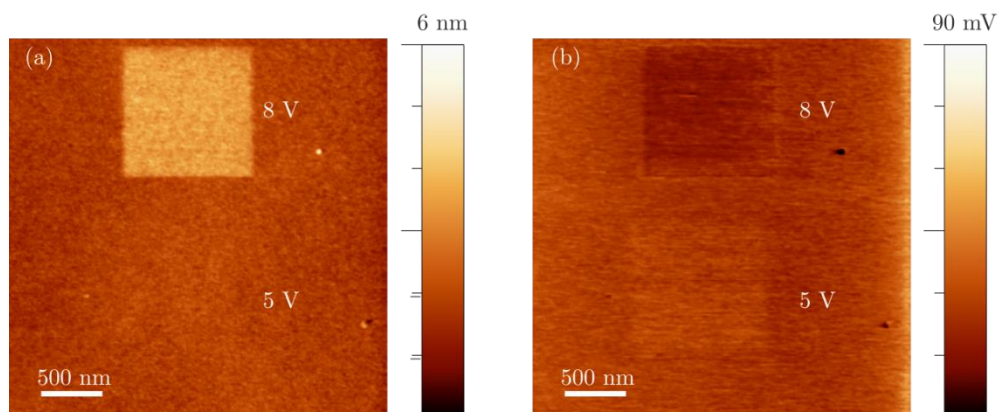


Figure 3.62. Peak-Force tapping AFM images corresponding to squared patterns created by o-SPL at bias voltages of 8 V (top square) and 5 V (bottom square)

In order to prove when the second and third situations take place, the PS-OH stability to hydrofluoric acid (HF) has been tested. It is known that at 5% concentration and at 20°C, PS-OH is not altered under HF attack⁵², thus it protects the silicon oxide grown by o-SPL to be etched. However, when the PS-OH becomes degraded because of the effect of applying high voltages, it loses its resistivity to HF and the underlying oxide reacts to HF.

To test the PS-OH resistance to HF, o-SPL has been performed on a PS-OH sample by using different bias voltages. Figure 3.63.a and b show the topographic and friction AFM images before HF dipping for 10 seconds, and it can be observed that for medium voltages, the patterns show a good chemical contrast. However, in Figure 3.63.b it is observed that for bias voltages higher than 34 V, the chemical contrast is large but the pattern does not sustain the HF etching. In that case, the patterns appear to be as a depressed area after HF etching, and the depth of the depression is consistent with the thickness of the brush layer (4.7 nm) and the native silicon oxide (1-2 nm). In consequence, it can be concluded that the use of high voltages damages the polymer layer inducing its degradation.

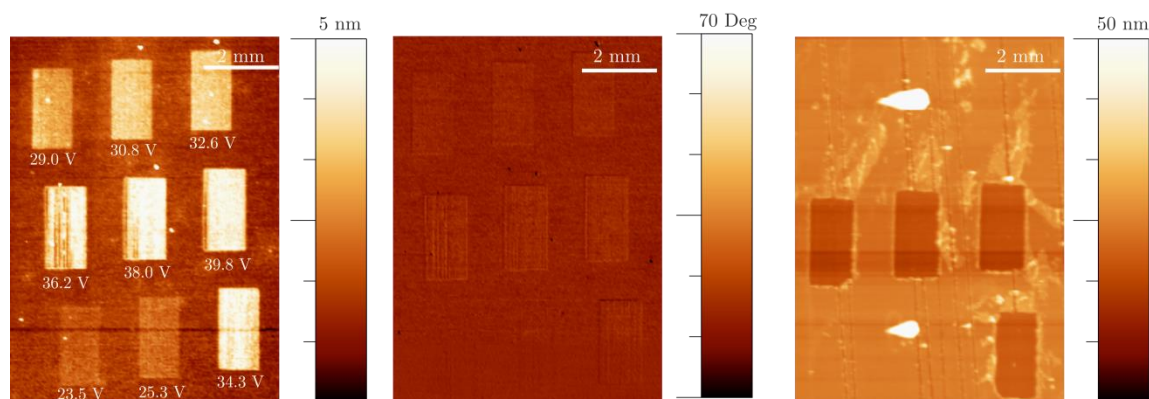


Figure 3.63. AFM images of chemical patterns performed on a PS-OH by o-SPL at different bias voltages. Images (a) and (b) show the topography and phase images of the sample before HF etching, and (c) shows the topography image after immersing the sample in an HF solution for 10 seconds

*PS-*b*-PMMA self-assembly*

After optimizing the AFM lithography to achieve the precise guiding pattern specifications, a lamellar PS-*b*-PMMA BCP of 28 nm pitch from a 1.15% toluene solution is spin-coated at 2750 rpm for 1 min.

Afterwards, in order to promote the self-assembly, the sample is annealed at 200°C for 20 min in hot-plate.

*3.6.3.2. Directed self-assembly by chemical epitaxy of PS-*b*-PMMA results*

Figure 3.64 shows the results of PS-*b*-PMMA ($L_0 = 28$ nm) DSA when using o-SPL for the fabrication of guiding patterns. Figure 3.64.a shows a comparison between the guiding pattern (top, AFM topography image) and the BCP DSA (bottom, SEM image) for different multiplication factors.

The guiding pattern consists of an array of lines with variable pitch in order to demonstrate the different multiplication factors achievable for this BCP. The line width has been set to 14 nm which is the half-pitch of the BCP used, and density multiplication factors between $3L_0$ and $5L_0$ have been tested. On the other hand, Figure 3.64.b demonstrates the effectiveness of the o-SPL for BCP DSA, in which the boundary between the fingerprint and the aligned area is perfectly differentiated.

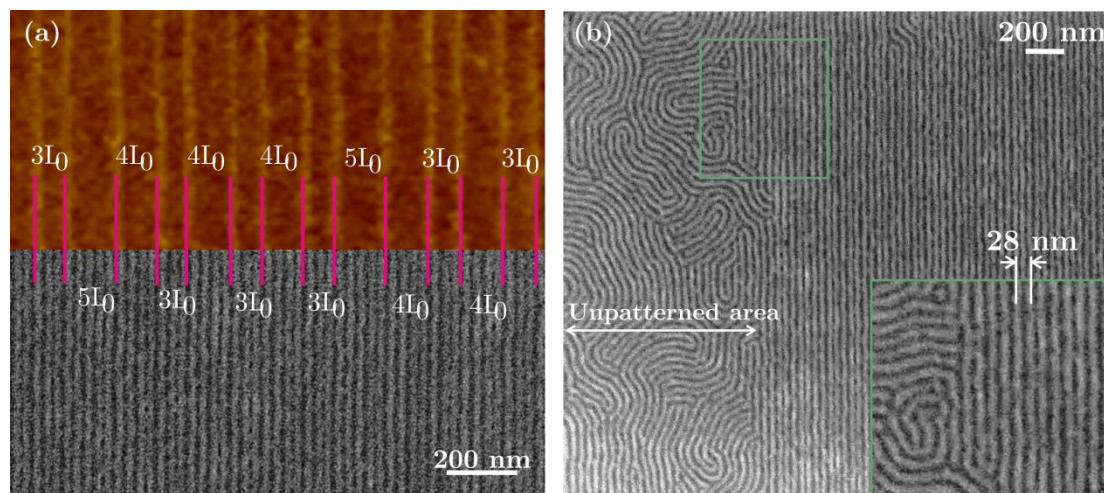


Figure 3.64. Different density multiplication factors for PS-*b*-PMMA BCP ($L_0 = 28$ nm) with chemical guiding patterns created by o-SPL ($V = 36$ V, tip-speed = $3 \mu\text{m/s}$ and RH = 23%) (a) Comparison between the guiding pattern (top, AFM topography image) and the aligned BCP (bottom, SEM image) SEM images have been taken after removing PMMA domains by oxygen plasma etching (b) SEM image showing the aligned BCP on top of the guiding pattern and the non-aligned BCP on top of unpatterned area

In order to obtain higher density multiplication factors, the oxidation strength has to be increased since the conditions used to align the BCP in Figure 3.64 do not have the oxidation strength needed to enforce the BCP DSA with a density multiplication factor of

$7L_0$. However, when the oxidation strength is increased (by increasing the humidity or the bias voltage), the line width becomes wider and larger than the half BCP pitch, and thus $1.5L_0$ lines width have to be created in order to not promote the alignment of only one BCP stripe, but three. Figure 3.65.a shows an example of a chemical guiding pattern created to achieve a $7L_0$ density multiplication factor for PS-*b*-PMMA of 28 nm pitch. The pattern consists of an array of 196 nm pitch lines. As it can be better observed in the zoomed image (Figure 3.65.c), the oxidized lines appear wider than in previous showed DSA results in order to promote the alignment with high density multiplication factor.

On the other hand, the experiments point out that the simple chemical modification of the brush layer (oxidation conditions (i)) is not enough to induce the BCP alignment, while patterns showing at least 0.5 nm of topographic height contrast, efficiently allows its alignment. The influence of topography-induced alignment on chemical patterns has been previously reported⁵³.

A closer inspection of the aligned patterns discloses that there are three aligned stripes on the top of the oxidized line (one PMMA stripe surrounded by two PS stripes) indicating that the oxidized lines become not strongly but slightly affine to PS domains. This behavior is better depicted in the scheme of Figure 3.65.d and later on, explained and demonstrated by surface characterization techniques. This situation is different from the one reported in other works of BCP DSA by using AFM lithography^{54,55}, where the oxidized areas become more PMMA affine. In these works, an octadecylthriclorosilane (OTS) self-assembled monolayer is used, instead of PS-OH, and the methyl layer is transformed to a carboxylic terminated layer, which is more affine to PMMA.

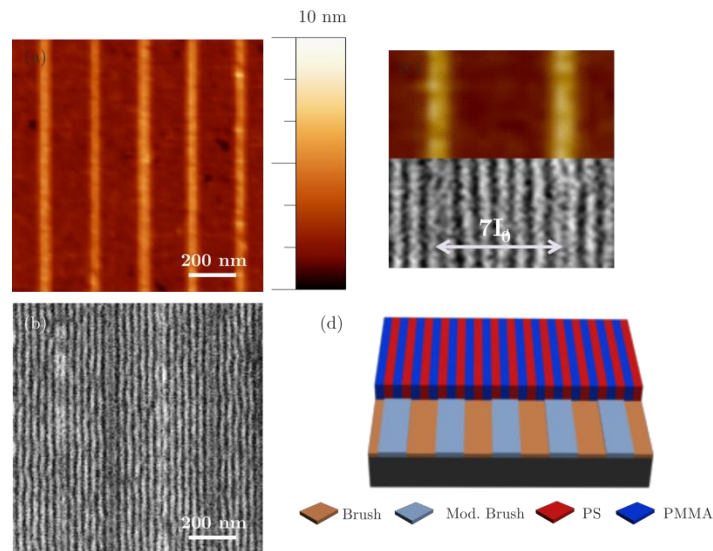


Figure 3.65. (a) AFM image of chemical guiding pattern created by o-SPL ($V = 34.2$ V, tip-speed = $2 \mu\text{m/s}$ and $\text{RH} = 38\%$). (b) SEM image of PS-*b*-PMMA DSA with $7L_0$ density multiplication factor. (c) Comparison between the guiding pattern (top, AFM topography image) and the aligned BCP (bottom, SEM image). (d) Scheme of the DSA process by o-SPL for high density multiplication factors. SEM images have been taken after removing PMMA domains by oxygen plasma etching

3.6.4. Summary and comparison

In summary, two methods based on the creation of a chemical guiding pattern directly on the brush layer without using a resist have been presented. Both methods have the advantage of simplifying the processing sequence by reducing the number of single processing steps.

On the one hand, by e-beam direct writing it has been demonstrated that the dimensions of the guiding patterns can be controlled with accuracy by varying the e-beam dose and with a much more simpler processing than other methods reported in the literature. However, the major drawback is the low throughput coming from the high e-beam doses employed to chemically modify and cross-link the structure of PS.

On the other hand, DSA by AFM-based nanolithography process relies on the unique resolution performance of AFM, although it has low throughput arising from the limited scan size and speed, which at present, limits its industrial application. However, diverse actions are taken in order to improve it, such as parallelization of AFM lithography by the use of multiple probes⁵⁶ or the use of local oxidation of high-resolution stamps.^{57,58} Moreover, it is a very promising technique to study the behavior of high- χ BCP which have half-pitches below 10 nm, since line widths of 7 nm can be obtained under controlled environmental and processing conditions.

In any case, the creation of guiding patterns either by o-SPL or direct writing EBL are a rather simple and affordable methods to study the alignment behavior of BCPs.

3.7. Summary and conclusions

Three different approaches based on chemical epitaxy processes have been designed and implemented at IMB-CNM to direct self-assemble PS-*b*-PMMA systems of different molecular weights.

In the first approach, the process is based on the definition of the guiding patterns by means of EBL and subsequent functionalization by oxygen plasma, thus creating a chemical contrast on the surface strong enough to guide the BCP self-assembly. This process has been successfully implemented to three PS-*b*-PMMA systems with different polymer chain lengths. First, the process has been demonstrated for guiding stripes of half L_0 widths, and then for wider guiding stripes with $(n + 1/2) \cdot L_0$ widths. This has allowed to relax the lithography requirements in terms of resolution, enabling the process integration to smaller PS-*b*-PMMA and high- χ materials.

Furthermore, an extensive characterization of the chemical guiding pattern has been performed in order to define the role of the interface energies between the substrate and the BCP domains. To do so, a novel experimental method by using homopolymer blends has been designed to determine the contact angle between the homopolymers in the blend, and thus calculate the difference on surface free energies by using *Young's equation*. This characterization has led to the conclusion that the main driving force in a chemical epitaxy process comes from the chemical interactions taking place at the surface. Moreover, it has been demonstrated that depending on the BCP system there is the need of a specific set of interface energies which are given by the brush layer and BCP annealing conditions.

On the other hand, the definition of the contact angles has been used to implement the experimental data on a DSA model and simulate a specific chemical epitaxy process. From the simulation results, it can be concluded that a good correlation between the experimental DSA process and the one predicted by the theory has been demonstrated. On the other hand, it has been found out that the responsiveness of the brush layer plays a very important role on the self-assembly process, favoring the standing lamellae when using an intermediate or low brush density, due to the interdigitation between it and the BCP domains.

In the two last chemical epitaxy approaches, the chemical guiding patterns have been defined directly on the brush thus avoiding the use of resists. These novel methods present the advantage of simplifying the processing sequence by reducing the number of single processing steps.

On the first direct writing method, the guiding patterns are created by means of EBL, and it has been demonstrated that the feature dimensions can be accurately controlled by varying the e-beam dose using a much simpler processing as compared to other methods reported in the literature. On the second approach, the guiding patterns are created by

locally oxidation of the surface with AFM nanolithography. This method, as compared with EBL direct writing, presents the advantage of the unique resolution performance of AFM.

Nevertheless, the major drawback of both methods is the low throughput arising from the limited writing speed which at present limits their industrial application. In any case, the creation of guiding patterns either by AFM or direct writing EBL can be considered as simple and affordable methods to study the alignment behavior of BCPs.

Further characterization by X-ray techniques of the different chemical guiding patterns is presented in *chapter 6*.

3.8. References

1. Bates, F. S. *et al.* Block copolymer thermodynamics: theory and experiment. *Annu. Rev. Phys. Chem.* **41**, 525–557 (1990).
2. Bates, F. S. *et al.* Block Copolymers—Designer Soft Materials. *Phys. Today* **52**, 32 (1999).
3. Park, C., *et al.* Enabling nanotechnology with self assembled block copolymer patterns. *Polymer (Guildf)*. **44**, 6725–6760 (2003).
4. Segalman, R. Patterning with block copolymer thin films. *Mater. Sci. Eng. R Reports* **48**, 191–226 (2005).
5. Black, C. T. Polymer self-assembly as a novel extension to optical lithography. *ACS Nano* **1**, 147–50 (2007).
6. Ross, C. a *et al.* Patterned Magnetic Media Made by Lithography. *MRS Bull.* **33**, 838–845 (2008).
7. Cheng, J. K., *et al.* Dense self-assembly on sparse chemical patterns: Rectifying and multiplying lithographic patterns using block copolymers. *Adv. Mater.* **20**, 3155–3158 (2008).
8. Stoykovich, M. P. *et al.* Remediation of line edge roughness in chemical nanopatterns by the directed assembly of overlying block copolymer films. *Macromolecules* **43**, 2334–2342 (2010).
9. Segalman, B. R. A., *et al.* Graphoepitaxy of Spherical Domain Block Copolymer Films. *Adv. Mater.* **13**, 1152–1155 (2001).
10. Kim, S. O. *et al.* Epitaxial self-assembly of block copolymers on lithographically defined nanopatterned substrates. 411–414 (2003).
11. Cheng, J. Y., *et al.* Nanostructure engineering by templated self-assembly of block copolymers. *Nat. Mater.* **3**, 823–828 (2004).
12. Bitai, I. *et al.* Graphoepitaxy of Self-Assembled Block Copolymers on two-dimensional periodic patterned patterns. *Science*. **321**, 939–943 (2008).
13. Ruiz, R. *et al.* Density Multiplication and Improved Copolymer Assembly. *Science*. **321**, 936–940 (2008).
14. Tavakkoli, K. G. A. *et al.* Templating Three-Dimensional Self-Assembled Structures in Bilayer Block Copolymer Films. *Science*, **336**, 1294–1298 (2012).
15. Liu, C. *et al.* Chemical Patterns for Directed Self-Assembly of Lamellae-Forming Block Copolymers with Density Multiplication of Features. *Macromolecules*, **46** (2013).

16. Detcheverry, F, *et al.* Interpolation in the Directed Assembly of Block Copolymers on Nanopatterned Substrates: Simulation and Experiments. *Macromolecules* **43**, 3446–3454 (2010).
17. Kim, S. O. *et al.* Epitaxial self-assembly of block copolymers on lithographically defined nanopatterned substrates. *Nature* **424**, 411–414 (2003).
18. Liu, C.-C. *et al.* Fabrication of Lithographically Defined Chemically Patterned Polymer Brushes and Mats. *Macromolecules* **44**, 1876–1885 (2011).
19. Oria, L., *et al.* Polystyrene as a brush layer for directed self-assembly of block copolymers. *Microelectron. Eng.* **110**, 234–240 (2013).
20. Fernández-Regúlez, M., Evangelio, *et al.* Sub-10 nm Resistless Nanolithography for Directed Self-Assembly of Block Copolymers. *ACS Appl. Mater. Interfaces* **6**, 21596–21602 (2014).
21. Cheng, J. Y. *et al.* Simple and versatile methods to integrate directed self-assembly with optical lithography using a polarity-switched photoresist. *ACS Nano* **4**, 4815–23 (2010).
22. Kim, J., *et al.* The SMART™ Process for directed block copolymer self-assembly. *Photopolymer Science and Technology*, **26**, 573–579 (2013).
23. Gronheid, R. & Nealey, P. F. *Directed Self-assembly of Block Copolymers for Nanomanufacturing*. (Elsevier, 2015).
24. Dulcey, C. S. *et al.* Photochemistry and Patterning of Self-Assembled Monolayer Films Containing Aromatic Hydrocarbon Functional Groups. *Langmuir* **12**, 1638–1650 (1996).
25. Tiron, R. *et al.* Pattern density multiplication by direct self assembly of block copolymers: toward 300mm CMOS requirements. *Proc. SPIE* **8323**, 83230O–83230O–7 (2012).
26. Qin, J. *et al.* Evolutionary pattern design for copolymer directed self-assembly. *Soft Matter* **9**, 11467 (2013).
27. Edwards, E. W., *et al.* Precise control over molecular dimensions of block-copolymer domains using the interfacial energy of chemically nanopatterned substrates. *Adv. Mater.* **16**, 1315–1319 (2004).
28. Winesett, D. A., *et al.* Tuning Substrate Surface Energies for Blends of Polystyrene and Poly (methyl methacrylate). *Langmuir*, **19**, 8526–8535 (2003).
29. Wei, Y. *et al.* Performance of tri-layer process required for 22nm and beyond. *Proc. SPIE* 79722L (2011).
30. Burns, S. *et al.* Silicon containing polymer in applications for 193nm high NA lithography processes. *Proceeding SPIE* **6153**, 61530K–61530K–12 (2006).

31. Owens, D. K. *et al.* Estimation of the surface free energy of polymers. *J. Appl. Polym. Sci.* **13**, 1741–1747 (1969).
32. D. H. Kaelble. Dispersion-Polar Surface Tension Properties of Organic Solids. *J. Adhes.* **2**, 66–81 (1970).
33. Dann, J. R. Forces involved in the adhesive process: I. Critical surface tensions of polymeric solids as determined with polar liquids. *J. Coll. Interface Sci* **32**, (1970).
34. Yu, S. *et al.* *Polymer Interface and Adhesion*. ISBN 9780824715335 (1982).
35. Zhang, D., *et al.* Effects of UV Irradiation and Plasma Treatment on a Polystyrene Surface Studied by IR–Visible Sum Frequency Generation Spectroscopy. *Langmuir* **16**, 4528–4532 (2000).
36. Pfleging, W., *et al.* Laser-assisted modification of polystyrene surfaces for cell culture applications. *Appl. Surf. Sci.* **253**, 9177–9184 (2007).
37. Lopez-gejo, J., *et al.*, Vacuum-ultraviolet Photochemically Initiated Modification of Polystyrene Surfaces: Chemical Changes. *Photochemistry and photobiology* 777–782 (2005).
38. Chada, S. *et al.* Self-assembled nanostructures from homopolymer induced by UV and solvent exposure. *Soft Matter* **4**, 2164–2167 (2008).
39. Onyiriuka, E. C. The effects of high-energy radiation on the surface chemistry of polystyrene: A mechanistic study. *J. Appl. Polym. Sci.* **47**, 2187–2194 (1993).
40. France, R. M., *et al.* X-ray photoelectron spectroscopy (XPS) and time-of-flight secondary ion mass spectrometry (ToF-SIMS) analysis of UV-exposed polystyrene. *Macromol. Chem. Phys.* **196**, 3695–3705 (1995).
41. Burns, S. *et al.* Trilayer development for 193 nm immersion lithography. *J. Photopolym. Sci. Te* **20**, (2007).
42. Kim, B., *et al.* Dewetting of PMMA on PS–Brush Substrates. *Macromolecules* **42**, 7919–7923 (2009).
43. Varlot, K., *et al.* Physical and chemical changes in polystyrene during electron irradiation using EELS in the TEM: Contribution of the dielectric function. *J. Microsc.* **191**, 187–194 (1998).
44. Massey, S., *et al.* Chemical Modification of Polystyrene by Low-Energy (<100 eV) Electron Irradiation Studied by Mass Spectrometry. *J. Appl. Polym. Sci.* **108**, 3163–3168 (2008).
45. Xu, J. *et al.* Directed self-assembly of block copolymers on two-dimensional chemical patterns fabricated by electro-oxidation nanolithography. *Adv. Mater.* **22**, 2268–72 (2010).

46. Xu, J., Russell, *et al.* Block copolymer self-assembly in chemically patterned squares. *Soft Matter* **7**, 3915 (2011).
47. Garcia, R., *et al.* Nano-chemistry and scanning probe nanolithographies. *Chem.Soc.Rev.* **35**, 29–38 (2005).
48. Pérez-Murano, F. *et al.* Nanometer-scale oxidation force microscopy of Si (100) surfaces by tapping mode atomic. *J. Appl. Phys.*, **78** 6797–6801 (1995).
49. Martínez, R. V., *et al.* Patterning polymeric structures with 2 nm resolution at 3 nm half pitch in ambient conditions. *Nano Lett.* **7**, 1846–1850 (2007).
50. García, R., *et al.* Nanoscale compositional mapping with gentle forces. *Nat. Mater.* **6**, 405–411 (2007).
51. Maoz, B. *et al.* "Constructive Nanolithography": Inert Monolayers as Patternable Templates for In-Situ Nanofabrication of Metal Semiconductor Organic Surface Structures. 725–731 (2000).
52. J-drain. Chemical Resistance Chart. 1–3 Available at: www.j-drain.com. (Accessed: 7th July 2014)
53. Kodera, K. *et al.* Defect-aware process margin for chemo-epitaxial directed self-assembly lithography using simulation method based on self-consistent field theory. *Proc. SPIE* **9049**, 904926-1-904926–8 (2014).
54. Xu, J. *et al.* Directed self-assembly of block copolymers on two-dimensional chemical patterns fabricated by electro-oxidation nanolithography. *Adv. Mater.* **22**, 2268–72 (2010).
55. Xu, J., *et al.* Block copolymer self-assembly in chemically patterned squares. *Soft Matter* **7**, 3915 (2011).
56. Vettiger, P. *et al.* the 'Millipede'-Nanotechnology Entering Data Storage. *Trans. Nanotechnol.* **1**, 39–55 (2002).
57. Cavallini, M., *et al.* Parallel Writing by Local Oxidation Nanolithography with Submicrometer Resolution. *Appl. Phys. Lett.* **83**, 5286–5288 (2003).
58. Albonetti, C. *et al.* Parallel-local anodic oxidation of silicon surfaces by soft stamps. *Nanotechnology* **19**, 435303 (2008).

Chapter 4

Directed self-assembly of PS-*b*-PMMA block copolymers by graphoepitaxy

Graphoepitaxy generates topographical structures that guide the self-assembly of BCPs. It is well known that in order to obtain an optimal BCP alignment, not only the topographical guiding pattern specifications have to be taken into account, but also the chemical interactions between the block copolymer domains and the topographical pattern (bottom and walls).

*In this chapter, the implementation, optimization and characterization of a graphoepitaxy process for PS-*b*-PMMA is presented. The definition of the guiding patterns is introduced first, using e-beam lithography, and then by photolithography to demonstrate a simpler and less time-consuming process.*

On the other hand, an experimental demonstration to control the orientation of the block copolymer depending on the surface affinities is presented.

4.1. Introduction to directed self-assembly of block copolymers by graphoepitaxy

Self-assembly of BCPs exhibits random domain orientation, as already shown in previous sections. It limits their applicability, and therefore, topographical or chemical guiding patterns are used to guide the nanostructures and overcome such random distribution.¹⁻³ While *chapter 3* is focused on the description and characterization of the different implemented chemical epitaxy processes, the present chapter aims to briefly discuss about the graphoepitaxy approach to guide BCPs, including the influence of topographical surfaces on DSA and the different ways to control the BCP orientation.

Graphoepitaxy consists in creating topographical features on the substrate to enforce the self-assembly of BCPs, thus enhancing the lateral order on the BCP microdomains.⁴⁻⁸ However, not only the commensurability has to be taken into account, but also the interfacial interactions between the substrate and the polymer, as well as substrate roughness. The first graphoepitaxy DSA process was introduced by *Kramer et al.* in 2001, and it is schematized below in Figure 4.1.⁹

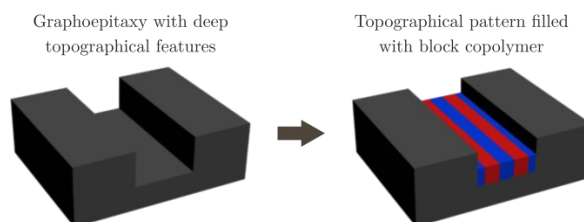


Figure 4.1. Scheme of the overall graphoepitaxy process developed by *Kramer et al.* using topographical guiding patterns to direct BCP self-assembly⁹

After the creation of the topographical pre-pattern, the brush is deposited to control the BCP affinity, and then the BCP fills the topographical regions confining the BCP. Normally, the distances filled by the BCP are larger than L_0 , thus achieving high density multiplication factors. This means that the effective pitch of the patterning is considerably reduced, thus relaxing the lithography step in terms of resolution.

There are different methodologies to create the guiding patterns, all of them based on the use of a top-down approach. The most commonly used technique is photolithography^{4,6,9,10}, but also IL¹¹⁻¹³ or EBL¹⁴⁻¹⁶ are used. An alternative method to create the guiding patterns is by using a NIL template into a resist rather than on the substrate.¹⁷

As discussed in *chapter 1*, in photolithography, the guiding pattern size is limited by the wavelength and the lens numerical aperture (when using 193 nm wavelength, the minimum pattern size is limited to 37 nm)¹⁸, whereas in IL shorter wavelengths can be used, thus

increasing the photolithography resolution. It has been demonstrated that resolutions below 10 nm when using EUV light of wavelength 13.5 nm, have been obtained.^{19,20} Nevertheless, compared with the high equipment cost and process complexity of IL, photolithography presents the added benefit of being a rapid and easy lithography process.

On the other hand, EBL offers resolutions below 10 nm, determined by the voltage, beam spot size, resist and e-beam dose.²¹ Despite having lower throughput as compared to the other two lithographic techniques, EBL does not require the use of a photomask. On the other hand, as compared with the last two discussed methods, it presents the advantage of fabricating less LER trenches, thus enabling the applicability of the process for smaller BCPs.

As it has been previously discussed, graphoepitaxy DSA is rather simple and cost-effective approach. However, it has the limitation of requiring a minimum trench width to have order in the self-assembly process. This implies a compromise in the storage space for being used in bit patterned media fabrication.^{22,23} To solve this problem, the use of shallow features to control BCP ordering has been demonstrated, and first introduced by *Park et al.*²⁴

In the mentioned work, described in Figure 4.2, single crystalline wafers of silicon with a given miscut orientation are used. Upon thermal annealing an atomic-scale periodic topography over the substrate is generated. Then the BCP is guided by the confinement effect of the planes. Nevertheless, the precise alignment of the BCP does not occur since the BCP period is normally not commensurate with the underlying guiding pattern period.

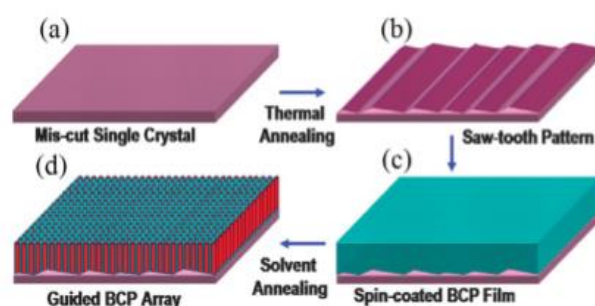


Figure 4.2. Schematic representation of graphoepitaxy process using the strategy developed by *Parker et al.* of creating patterns based on highly oriented crystalline facets on a single crystal surface²⁴

Normally topographical guiding patterns are created on hard-substrates which present the inconvenient of remaining after pattern transfer, being undesirable for device fabrication. Recently, there have been presented other graphoepitaxy approaches where organic pre-patterns are used.²⁵⁻²⁷ This novel approach was introduced in 2009 by *Jeong et al.* in which they used an organic negative-tone photoresist to create the guiding patterns.²⁶

4.2. Development and implementation of graphoepitaxy on PS-*b*-PMMA by means of e-beam lithography

In graphoepitaxy DSA, the geometry of the guiding pattern plays a key role during the process. Nevertheless, as in chemical epitaxy, there is also need to control the interfacial interactions of the substrate (bottom and walls) with the BCP. This interaction is normally controlled with the use of random copolymers to generate a neutral surface, and with the BCP processing conditions.

On the other hand, it is also important to consider the defectivity of the process with respect to the guiding pattern dimensions. It has been demonstrated that, as the separation between trenches grow larger, defect density increases^{9,28}. Furthermore, the lateral order on edges presents less defectivity compared to the middle of the trench, when trench widths are larger.^{4,29,30}

4.2.1. Materials and methods

4.2.1.1. Description of the graphoepitaxy process

The technique implemented at IMB-CNM to direct self-assemble PS-*b*-PMMA and high- χ BCPs, is depicted in Figure 4.3. It consists of 6-steps: (i) e-beam writing on PMMA resist, (ii) PMMA development, (iii) silicon etching, (iv) resist removal, (v) polymer brush grafting on silicon, and (vi) BCP spin-coating.

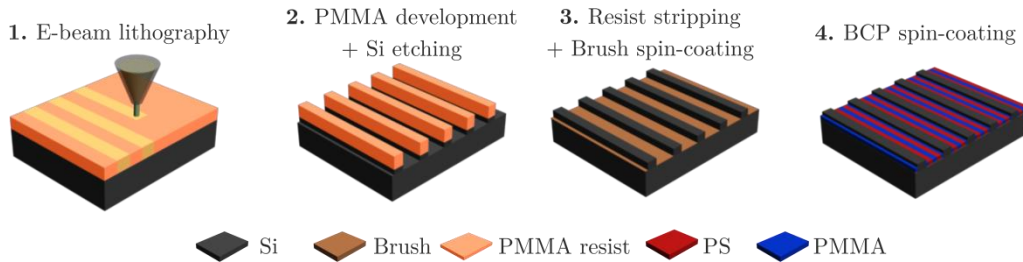


Figure 4.3. Schematic of the graphoepitaxy process for PS-*b*-PMMA by means of e-beam lithography

4.2.1.2. Brush and block copolymer materials

Lamellae PS-*b*-PMMA of 22 nm pitch has been used for the DSA process, with a PS_{60%}-*r*-PMMA brush, processed under different conditions depending on the final desired structure. The specifications of brush and BCP material are depicted in Table 4.1.

Table 4.1. Specifications of brush and BCP used for graphoepitaxy DSA

Material	Molecular weight	PDI	Pitch (SEM)
PS _{60%} - <i>r</i> -PMMA	7.9 kg/mol	1.85	-
PS- <i>b</i> -PMMA	42.3 kg/mol	1.10	22.5 nm

4.2.1.3. Creation of the topographical guiding patterns

The aim of using graphoepitaxy is to, later on, obtain a novel class of nanowires based mechanical resonators (*chapter 7*). It is depicted in Figure 4.4. The fabrication process of the mechanical resonators will be based on the use of graphoepitaxy DSA and therefore, there is a need to study first the DSA process.

The guiding patterns designed to study the DSA graphoepitaxy process are those which will be used at a later stage to fabricate the mechanical resonators. These are first defined by EBL in order to demonstrate the applicability of the process, and then by photolithography in order to validate a possible industrial scalability.

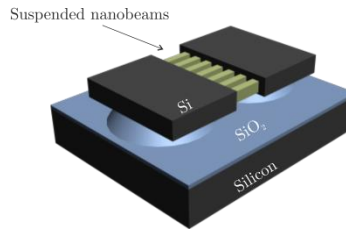


Figure 4.4. Schematic representation of a device based on an array of identical nanobeams made by directed self-assembly of block copolymers

The starting substrates are $0.9 \times 0.9 \text{ cm}^2$ chips bearing a native silicon oxide layer ($\{100\}$, p-type silicon wafers of $4\text{--}40 \text{ } \Omega \cdot \text{cm}$ resistivity). Previously to the lithography process, the sample surface is cleaned and activated by an oxygen plasma for 10 min at 500 W and 50 sccm of oxygen flow.

Figure 4.5 shows the pattern designs used to create the guiding patterns with a negative-tone resist. It consists of two $10 \times 10 \text{ } \mu\text{m}^2$ pads separated from each other a w distance. In the different designs, the length of the guiding patterns has been kept constant, and then the w has been varied from 60 nm to $1 \text{ } \mu\text{m}$. This wide range has been selected in order to, later on, reproduce the results by using photolithography in which the minimum resolution is 350 nm.

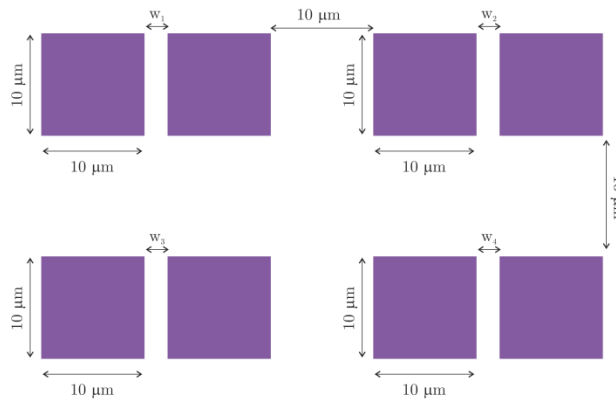


Figure 4.5. Schematic representation of the design used to study the PS-*b*-PMMA DSA by graphoepitaxy

After the substrate cleaning process, a negative-tone resist, *AR-N7500-08*, is spin-coated on the top of the silicon at 4000 rpm for 1 min, and annealed at 85°C for one further min, to get a 150 nm thick film. Then, the guiding patterns are defined by EBL in a *RAITH 150Two* equipment. The exposure has been performed at 20 kV and 110 pA beam current, with a nominal beam diameter of 2 nm. The exposure has been defined with the designs depicted in Figure 4.5 with an e-beam dose of 150 $\mu\text{C}/\text{cm}^2$. The writing speed has been, therefore 7.33 m/s by using a line step of 10 nm.

Once the exposure has been completed, the samples have been developed by using the resist developer *AR-300-47*. The samples are dipped into the developer for 2 min, and then into water for two further minutes. Finally, the samples are annealed at 135°C for 5 min.

To finally define the topographic guiding patterns, a silicon etching of 120 nm is performed on the surface by using the negative-tone resist as a mask. The silicon etching conditions are depicted in Table 4.2.

Table 4.2. RIE conditions for silicon etching

[SF ₆] (sccm)	35
[C ₄ F ₈] (sccm)	45
Power Source (W)	100
Chuck Power (W)	20
Time (s)	40
Pressure (Pa)	2
Temperature (°C)	20
Silicon etched	120 nm

Figure 4.6 shows a SEM image of the guiding patterns after having etched 120 nm of silicon. In the image, 100 nm of resist are still present. It is removed by exposing the sample to oxygen plasma at 500 W for 10 min with an oxygen flow of 50 sccm, prior to BCP spin-coating.

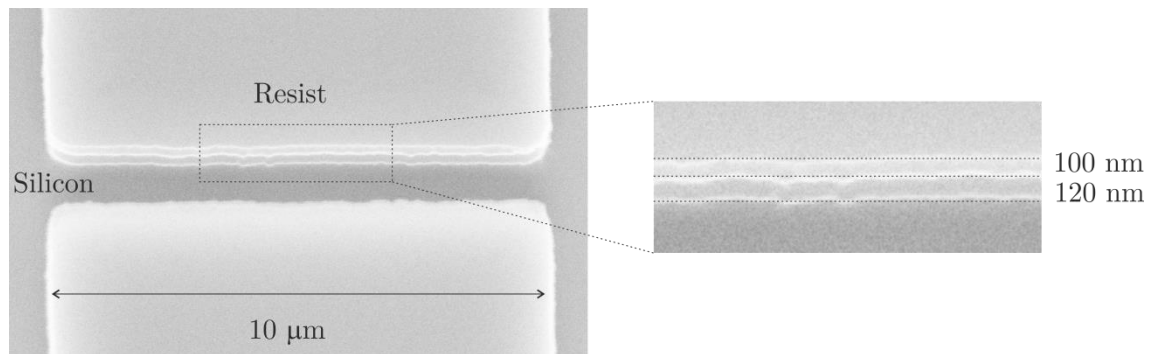


Figure 4.6. SEM cross-section image of the graphoepitaxy guiding pattern created by e-beam lithography after silicon etching

4.2.1.4. Deposition of the brush layer

As previously discussed, for the fabrication of the mechanical resonators, a perpendicular oriented BCP morphology is required. Therefore, in order to avoid the parallel oriented morphology, both the bottom and the walls of the guiding pattern need to have neutral affinity for the BCP.

Depending on the brush solution concentration and spin-coating speed, the brush grafting can be controlled (Figure 4.7). If the brush solution is diluted and it is spin-coated at very high spin speeds, its grafting occurs only at the bottom of the guiding patterns (Figure 4.7.a). This means that the bottom of the guiding pattern presents a neutral affinity for both BCP domains, whereas the walls (silicon is not grafted) are more PMMA affine. On the other hand, if the brush concentration is increased, it is grafted in the whole silicon surface, thus presenting neutrality in both surfaces (Figure 4.7.b).

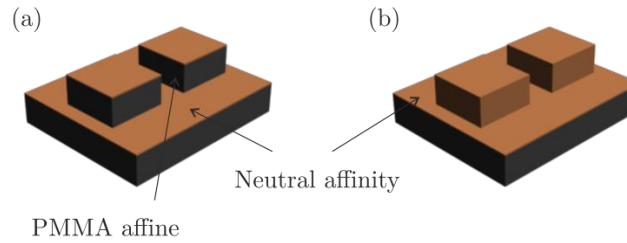


Figure 4.7. Schematics of graphoepitaxy patterns with brush (a) only at the bottom and (b) at the bottom and walls

As discussed above, the desired situation is the one depicted in Figure 4.7.b. Therefore, a 2% PS_{60%}-*r*-PMMA at 1500 rpm is spin-coated on the top of the guiding patterns and consequently annealed at 230°C for 5 min in a nitrogen environment. Then, the non-grafted brush is removed by dipping the sample in PGMEA for 5 min at 40°C in an ultrasonic bath. Finally, a 0.5% PS-*b*-PMMA solution is spin-coated at 2500 rpm and annealed at 230°C for 10 min under a nitrogen flow to promote the BCP self-assembly.

4.2.2. Directed self-assembly by graphoepitaxy of PS-*b*-PMMA results

The DSA experiments have been performed for PS-*b*-PMMA of 22 nm pitch on topographical guiding patterns by varying their separation width. The separation range width has been studied between 60 nm and 1 μm. It has to be pointed out, that after the BCP deposition, the solution tends to go inside the trenches due to the topographical confinement effect. Therefore, the defectivity on edges is strongly reduced, as compared with the middle of the trench when its width is larger, or with the rest of the sample.^{4,29,30}

Figure 4.8 shows the SEM images of the corresponding DSA process when using different separation widths. It can be observed that the maximum separation width at which the

BCP shows a perpendicular orientation with respect to the guiding patterns is between 500 nm and 600 nm.

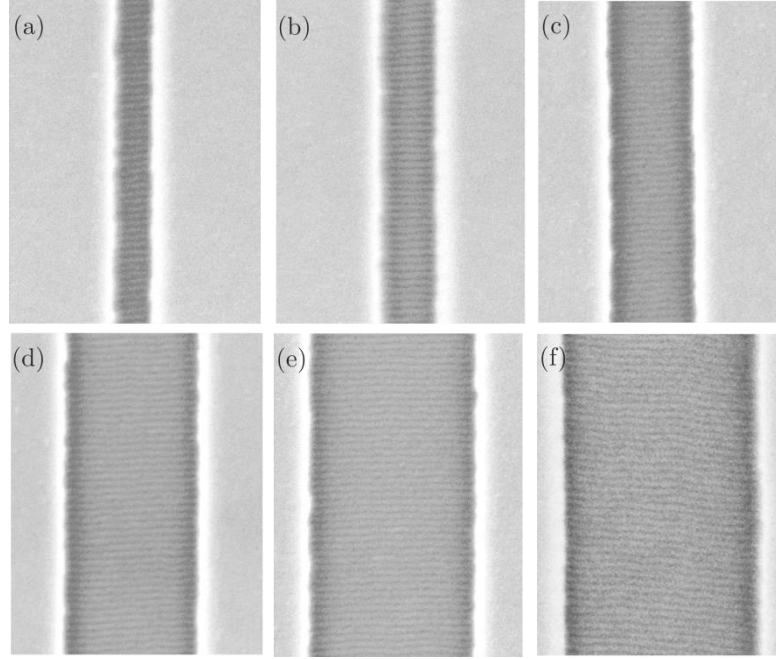


Figure 4.8. PS-*b*-PMMA ($L_0 = 22$ nm) DSA by graphoepitaxy by using separation widths of (a) 100 nm, (b) 160 nm, (c) 250 nm, (d) 400 nm, (e) 500 nm and (f) 600 nm

Above 600 nm separation width, the orientation is no longer maintained, and areas without BCP start to appear. Figure 4.9 shows the DSA defects which appear in guiding patterns above 700 nm separation width.

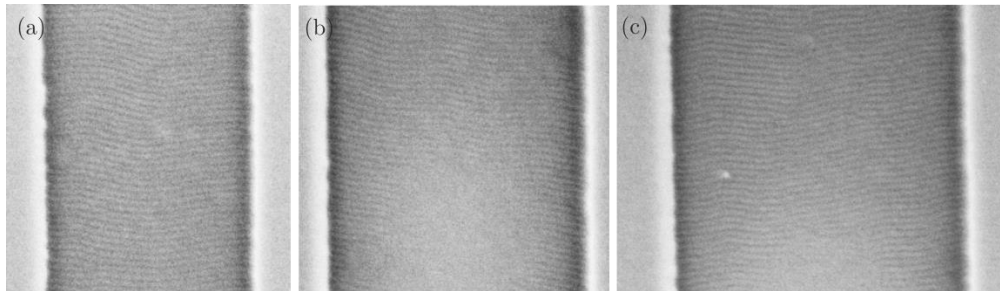


Figure 4.9. PS-*b*-PMMA ($L_0 = 22$ nm) DSA by graphoepitaxy by using separation widths of (a) 700 nm, (b) 900 nm and (c) 1 μ m

As previously discussed, the BCP tends to go inside the trenches due to the topographical confinement effect. It is observed in the SEM image of Figure 4.10. In the zoom-in image, it is observed that the BCP dewetts outside the guiding pattern, whereas inside the guiding pattern presents a well-ordered thick structure. This is in agreement with some works, which demonstrate that the wider the trench separation, the highest the defectivity on the middle of the confinement or outside the guiding pattern, as compared to the lateral order on the trench edges.^{4,29,30}

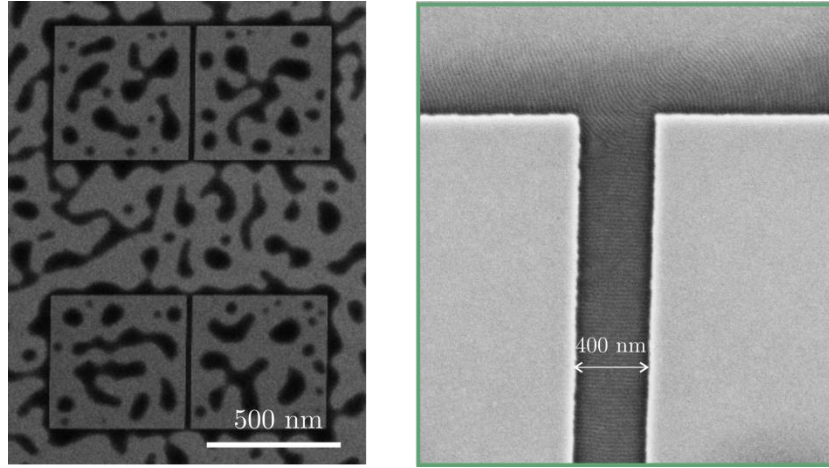


Figure 4.10. PS-*b*-PMMA ($L_0 = 22$ nm) DSA by graphoepitaxy by using separation 400 nm separation width

4.3. Development and implementation of graphoepitaxy on PS-*b*-PMMA by means of photolithography

The graphoepitaxy process has been successfully implemented at IMB-CNM for guiding trench widths up to 600 nm. Therefore, the guiding patterns can be easily defined by means of photolithography since its critical dimension is 350 nm. Hence, the graphoepitaxy process gains more interest, since it presents the added advantages of being a low-cost and time-saving approach.

To define the guiding patterns by means of photolithography, it is necessary first to design and fabricate a photomask. The desired designs for the mask are computerized in a data file. Then, this data is converted to a series of features, and written onto a quartz substrate covered with a layer of chromium. The features are normally written by an e-beam writer on the mask surface. Finally, after the e-beam lithography, the exposed chromium is etched away, leaving the exposed features free in order to let the illumination light system go through.

4.3.1. Materials and methods

4.3.1.1. Description of the graphoepitaxy process

The graphoepitaxy process using photolithography is depicted in Figure 4.11. As observed, the processing steps are the same, being the only differences the materials used to perform the photolithography, and the starting substrates.

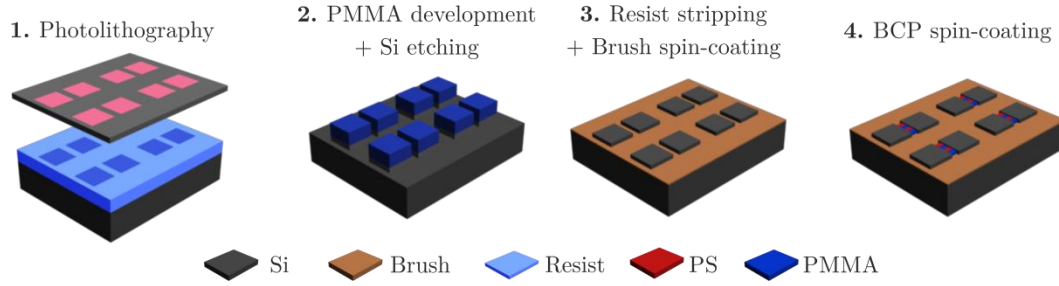


Figure 4.11. Schematic of the graphoepitaxy process for PS-*b*-PMMA by means of photolithography

4.3.1.2. Creation of the topographical guiding patterns

In order to define the topographical patterns into the substrate, the first step consists in the fabrication of the photomask. The software that has been used to define the mask designs is *Cadence*.

The projected reticle presents four quarters (Q1 to Q4) defined with different device designs, in order to use it, not only for DSA, but for other applications. The first area Q1 is depicted in Figure 4.12.

As observed, it consists of an array of features grouped in four identical devices. Then, the length of the trenches and the separation width are varied in columns and rows, respectively. Trench lengths up to 40 μm , and separation widths up to 1 μm have been designed. The dimensions of the guiding patterns for this first quarter are defined in Table 4.3.

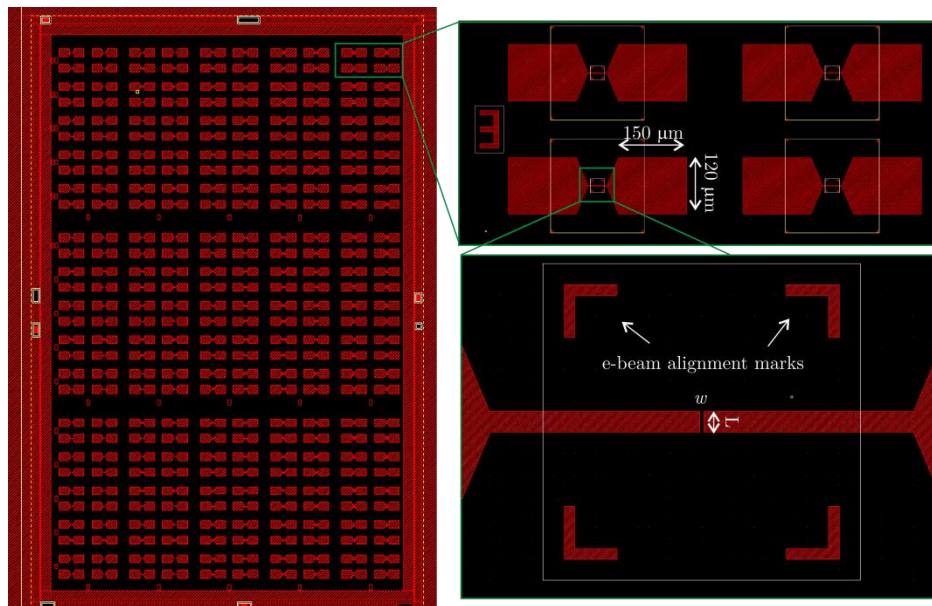


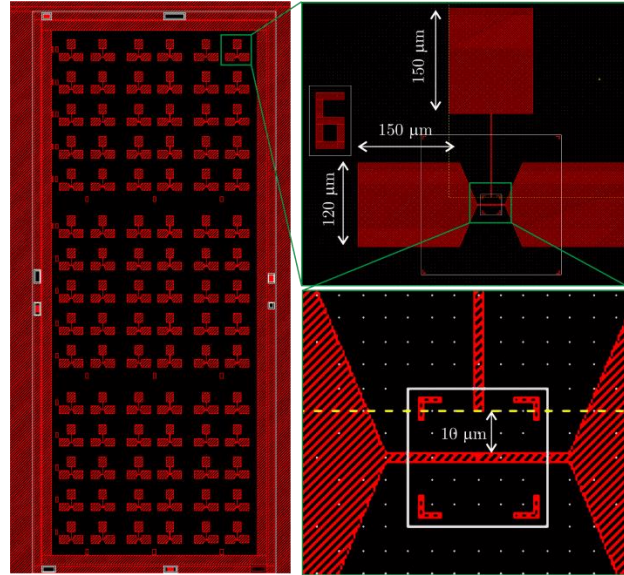
Figure 4.12. Schematic representation of the Q1 area of the reticle used for the photolithography

Table 4.3. Specifications of the geometrical dimensions of Q1 designs as a function of the trench length and separation width

$\begin{matrix} w \text{ (nm)} \\ L \text{ (}\mu\text{m)} \end{matrix}$	0	350	400	450	500	550	600	650	700	750	800	850	900	950	1000
2	A1	A2	A3	A4	A5	A6	A7	A8	A9	A10	A11	A12	A13	A15	A15
5	B1	B2	B3	B4	B5	B6	B7	B8	B9	B10	B11	B12	B13	B14	B15
10	C1	C2	C3	C4	C5	C6	C7	C8	C9	C10	C11	C12	C13	C14	C15
20	D1	D2	D3	D4	D5	D6	D7	D8	D9	D10	D11	D12	D13	D14	D15
40	E1	E2	E3	E4	E5	E6	E7	E8	E9	E10	E11	E12	E13	E14	E15

For further applications on the field, other designs have been defined (Q2 and Q3 depicted in Figure 4.13 and Figure 4.14, respectively).

Designs Q2 are formed of groups of two identical devices defined in three columns by varying $L = 2, 5$ and $10 \mu\text{m}$, and in 15 rows by varying w up to $1 \mu\text{m}$.

**Figure 4.13.** Schematic representation of the Q2 area of the reticle used for the photolithography

Areas Q3 (Figure 4.14), represent more complex designs. On the one hand, in the first two columns (Figure 4.14.a) there are two identical devices with different trench lengths each one ($L = 5, 10, 20$ and μm) repeated in row by varying the separation width, w , up to $1 \mu\text{m}$. On the other hand, in the third column (Figure 4.14.b) devices in which each one presents different trench lengths ($L = 5, 10, 20$ and μm) with three and four gaps in each side, separated a w distance, are represented. As for the previous designs, the separation width is varied in row, up to $1 \mu\text{m}$.

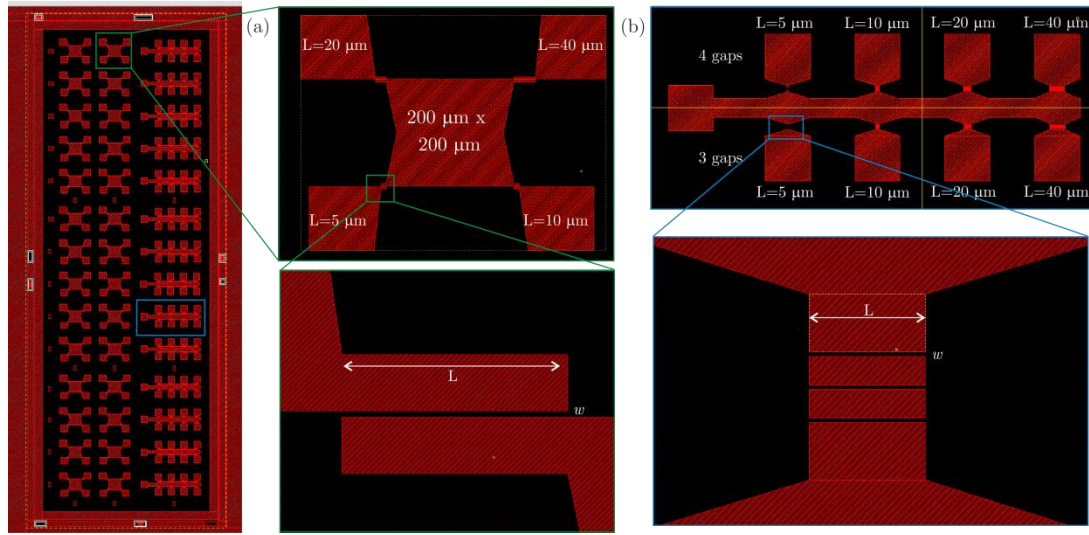


Figure 4.14. Schematic representation of the Q3 area of the reticle used for the photolithography

In the last quarter, Q4, squares, arrays of trenches or circles are defined (Figure 4.15).

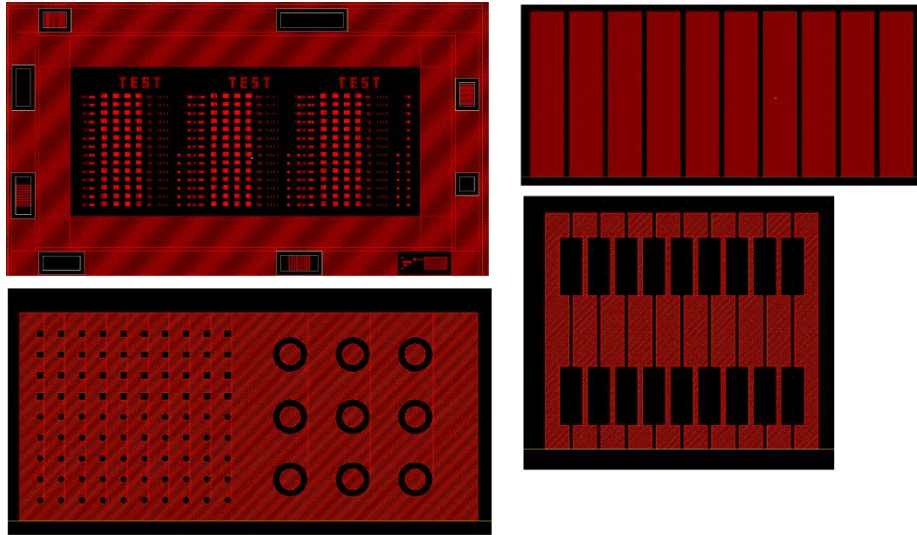


Figure 4.15. Schematic representation of the Q4 area of the reticle used for the photolithography

The starting substrates are 4 inch silicon wafers bearing a native silicon oxide layer ($\{100\}$, p-type silicon wafers of $4\text{--}40 \Omega \cdot \text{cm}$ resistivity). Previously to the photolithography process, 600 nm of a positive-tone resist, *OIR 620-09*, are deposited and annealed at 100°C for 30 s on an automatic coater-developer system, *GAMMA80 Süs*.

The photolithography is performed on a stepper i-line, *NSR 2205i12D* equipment, which has a critical dimension of 350 nm and a maximum exposure area of $22 \times 22 \text{ mm}^2$. The exposure time is 535 ms with a focus of $-0.5 \mu\text{m}$. Then, the wafer is developed by TMAH for 28 s, and annealed at 115°C for 30 s in a hot-plate.

Once the wafers have been exposed and developed, the topographical patterns are finally defined by performing a silicon etching in *DRIE ALCATEL 601E* equipment by using the

same conditions of Table 4.2. Figure 4.16 shows a SEM images of how the guiding patterns look like after silicon etching.

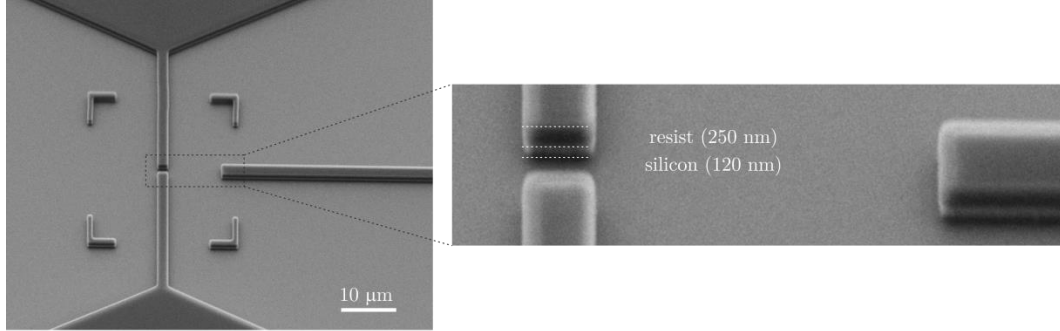


Figure 4.16. SEM cross-section image of the graphoepitaxy guiding pattern created by photolithography after silicon etching

Afterwards, the wafer is cut into small samples (1 x 1 cm²), and the brush layer is deposited and annealed as performed in section 4.2.1.4.

4.3.2. Directed self-assembly by graphoepitaxy results

The DSA experiments have been performed by using the same PS-*b*-PMMA of 22 nm pitch and processing conditions that had been used for the later approach. Figure 4.17 shows the results of the DSA graphoepitaxy process, when the guiding patterns have been defined by photolithography. As observed in the images, the BCP self-assembly behavior is the same as the one shown in Figure 4.8, where the guiding patterns were created by EBL. The maximum trench separation width in which no defects are observed is 750 nm (Figure 4.17.e).

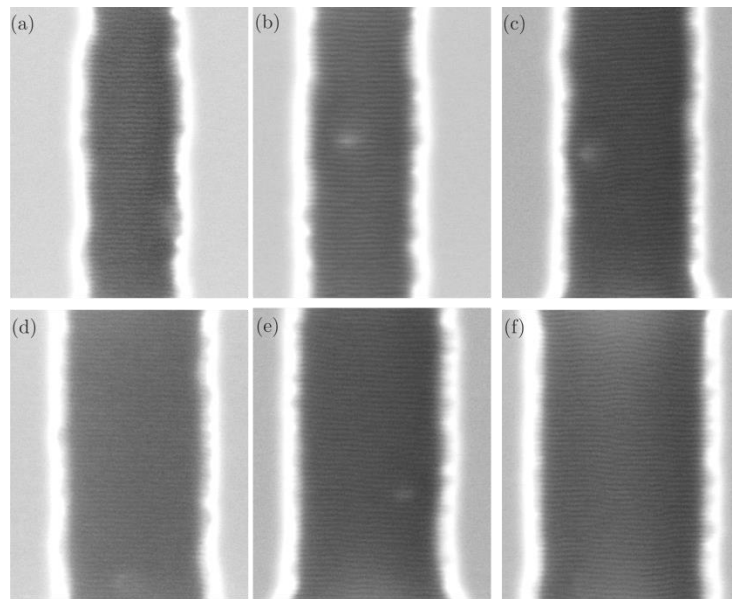


Figure 4.17. PS-*b*-PMMA ($L_0 = 22$ nm) DSA by graphoepitaxy by using separation widths of (a) 450 nm, (b) 500 nm, (c) 650 nm, (d) 700 nm, (e) 750 nm and (f) 850 nm

It is therefore demonstrated, that the presented graphoepitaxy approach can be easily simplified in terms of cost and time, by using a photolithography step instead of EBL. Furthermore, the DSA has been demonstrated, and will be the basis for the design and fabrication of the nanomechanical resonators in *chapter 7*.

4.4. Surface affinity control on topographical guiding patterns

The DSA process by graphoepitaxy is not only governed by the topographical guiding patterns, but also by the affinities toward the underlying substrate.³¹ In order to demonstrate the control on the BCP orientation depending on the substrate conditions, two DSA experiments have been performed by varying the substrate conditions in order to force the BCP to be aligned perpendicular and parallel to the substrate, respectively.

The guiding patterns have been created by IL in collaboration with the *Molecular Foundry*. The starting substrates have been bare silicon and silicon with an 80 nm thick antireflective layer on top. Figure 4.18 shows a schematic representation of both guiding patterns. The dimensions of the trenches are 200 nm width and 80 nm height, they are separated 500 nm from each other.

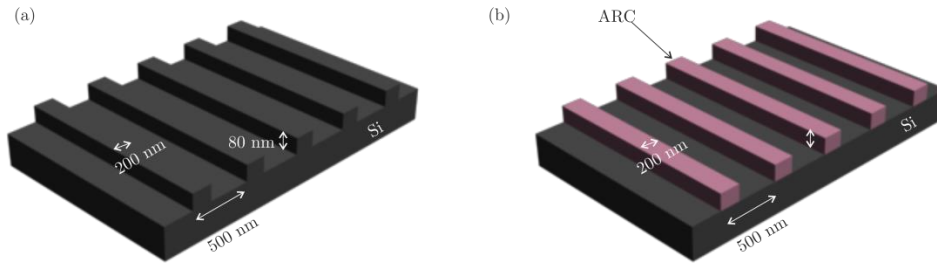


Figure 4.18. Graphoepitaxy guiding patterns made of (a) *silicon* and (b) *silicon + ARC*

Prior to brush deposition, both guiding patterns are cleaned, and the resist is removed by dipping the sample into hot acetone (40°C) for 5 min in an ultrasonic bath and into IPA for 5 more minutes. Then, a 2% PS_{60%}-*r*-PMMA brush solution is deposited on the top of the guiding patterns at the same spin-speed (2000 rpm), in order to coat the whole sample surface as depicted in Figure 4.7.

After removing the non-grafted brush by rinsing the samples with PGMEA for 5 minutes in an ultrasonic bath at 40°C, a 1.5% PS-*b*-PMMA of 22 nm pitch is spin-coated on the top of the guiding patterns at 2000 rpm, and annealed at 230°C for 10 min.

Figure 4.19 shows the results of the DSA graphoepitaxy process on *silicon* (Figure 4.19.a) and on *silicon + ARC* (Figure 4.19.b) guiding patterns. As observed in the images, despite using the same processing conditions and materials, the orientation of the BCP is different depending on the substrate the guiding patterns are made of.

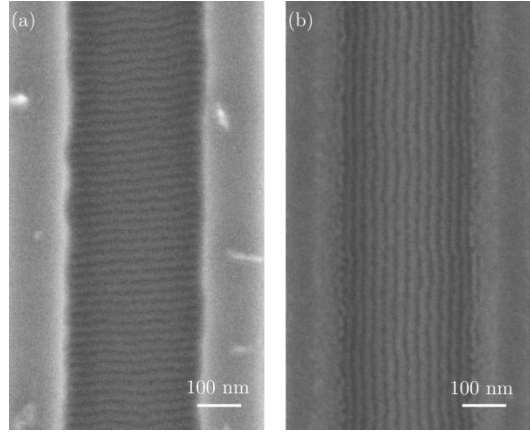


Figure 4.19. PS-*b*-PMMA ($L_0 = 22$ nm) DSA by graphoepitaxy on (a) *silicon* and (b) *silicon + ARC* guiding patterns.

The difference on the BCP orientation occurs because the brush layer does not graft onto the *ARC* layer walls, since it is a carbon-based material. Therefore, in the case where the patterns are created on *silicon + ARC*, the brush is only present at the bottom, and thus the walls do not present a neutral affinity as they do in the samples where the guiding patterns are made of *silicon*.

Figure 4.20 illustrates the DSA process in each situation. When the guiding patterns are made of *silicon* (Figure 4.20.a), the brush is grafted on the whole silicon surface, promoting a neutral affinity for both BCP domains at the walls and at the bottom of the trenches. Therefore, the BCP is oriented perpendicular to the trench orientation. On the other hand, when the guiding patterns are made of *silicon + ARC* (Figure 4.20.b), the brush is only grafted at the bottom of the patterns, promoting there a neutral affinity, whereas the walls are PMMA attractive. In consequence, the BCP tends to be orientated parallel to the trenches.

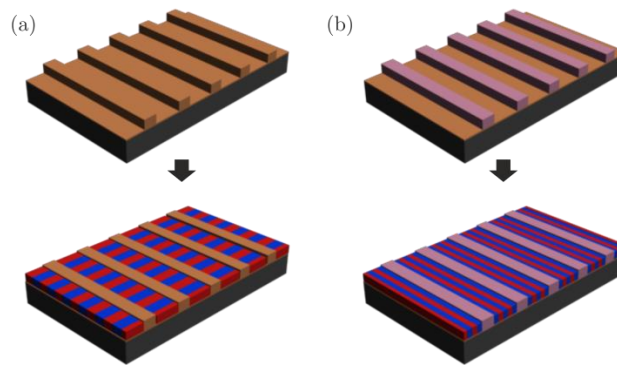


Figure 4.20. Schematic representation of the DSA by graphoepitaxy process when using (a) *silicon* and (b) *silicon + ARC* guiding patterns

As observed in Figure 4.19.b, the density multiplication factor achieved is $11L_0$, which is much more than the one demonstrated for lamellar PS-*b*-PMMA system.³¹ For this system, in order to demonstrate that the BCP domains have the perpendicular morphology through the film thickness down to the substrate, the cross-section of the guiding patterns has been

characterized. To carry out the inspection, the PMMA has been first removed by using soft oxygen plasma at 260W with an oxygen flow of 50 sccm for 18 s.

Figure 4.21 shows the SEM cross-section of the guiding pattern, after removal of the PMMA domain. The cross-section has been obtained by the cleavage of the sample. As it is observed, the brush presents a neutral affinity to both domains of the BCP since the perpendicular morphology is maintained through the film.

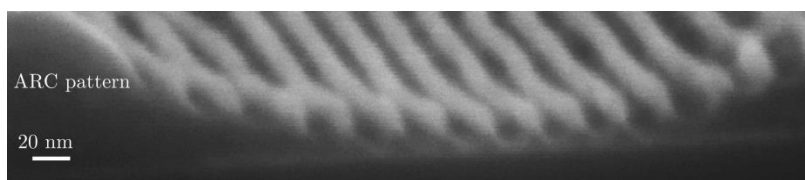


Figure 4.21. SEM cross-section of PS-*b*-PMMA ($L_0 = 22$ nm) DSA by graphoepitaxy on *silicon + ARC* guiding patterns.

4.5. Summary and conclusions

A graphoepitaxy approach to guide the self-assembly of PS-*b*-PMMA BCPs has been presented. Such approach has been designed in order to implement the fabrication of nanowires based on nanomechanical resonators (*chapter 7*).

The guiding patterns have been defined first by e-beam writing in order to demonstrate the viability of the process. Once it has been proved and optimized, the samples have been created at 4 inch wafer scale, and the guiding patterns have been designed by means of photolithography with a critical dimension of 350 nm. From the DSA results, it has been observed, that the BCP shows a good alignment behavior with trench separation widths up to 600 nm, but such alignment is lost at larger widths. Moreover, as reported in the literature, it has been seen that the larger the width of the trenches, the higher the BCP defectivity, being it significantly increased in the center of the trenches.

On the other hand, a way to control the BCP orientation as a function of the substrate used has been demonstrated. Depending on the chemical affinities between the substrate (both walls and bottom) and the BCP domains, the orientation can be parallel or perpendicular to the trench direction.

This graphoepitaxy approach will be later on implemented on high- χ BCP systems (*chapter 5*), by adding an alternative step to enhance the process and adapt it to other chemistries.

4.6. References

1. Park, C., *et al.* Enabling nanotechnology with self assembled block copolymer patterns. *Polymer*. **44**, 6725–6760 (2003).
2. Segalman, R. Patterning with block copolymer thin films. *Mater. Sci. Eng. R Reports* **48**, 191–226 (2005).
3. Darling, S. B. Directing the self-assembly of block copolymers. *Prog. Polym. Sci.* **32**, 1152–1204 (2007).
4. Black, C. T. *et al.* Nanometer - Scale Pattern Registration and Alignment by Directed Diblock Copolymer Self-Assembly. *IEEE Trans. Nanotechnol.* **3**, 412–415 (2004).
5. Hammond, M. R., *et al.* Temperature Dependence of Order, Disorder, and Defects in Laterally Confined Diblock Copolymer Cylinder Monolayers. *Macromolecules* **38**, 6575–6585 (2005).
6. Anandakumar, S. *et al.* Template Synthesis of Cobalt Nanowires Using PS-*b*-PMMA Block Copolymer. *IEEE Transactions on Magnetism* **45**, 4063–4066 (2009).
7. Argoud, M. *et al.* 300mm pilot line DSA contact hole process stability. *Altern. Lithogr. Technol. VI* **9049**, 1–11 (2014).
8. Gharbi, A. *et al.* Contact holes patterning by directed self-assembly of block copolymers: process window study. *J. Micro/Nanolithography, MEMS, MOEMS* **14**, 023508–023508 (2015).
9. Segalman, B. R. A., *et al.* Graphoepitaxy of Spherical Domain Block Copolymer Films. *Adv. Mater.* **13**, 1152–1155 (2001).
10. Hammond, M. R., *et al.* Temperature Dependence of Order, Disorder, and Defects in Laterally Confined Diblock Copolymer Cylinder Monolayers. *Macromolecules* **38**, 6575–6585 (2005).
11. Savas, T. A., *et al.* Large-area achromatic interferometric lithography for 100 nm period gratings and grids. *J. Vac. Sci. Technol. B Microelectron. Nanom. Struct. Process. Meas. Phenom.* **14**, 4167–4170 (1996).
12. Auzelyte, V. *et al.* Extreme ultraviolet interference lithography at the Paul Scherrer Institut. *J. Micro/Nanolithography, MEMS, MOEMS* **8**, 21204–21210 (2009).
13. Jung, Y. S. *et al.* Orientation-Controlled Self-Assembled Nanolithography Using a Polystyrene–Polydimethylsiloxane Block Copolymer. *Nano Lett.* **7**, 2046–2050 (2007).
14. Bitai, I. *et al.* Graphoepitaxy of Self-Assembled Block Copolymers on two-dimensional periodic patterned patterns. *Science*. **321**, 939–943 (2008).

15. Hong, S. W., *et al.* Circular Nanopatterns over Large Areas from the Self-Assembly of Block Copolymers Guided by Shallow Trenches. *ACS Nano* **5**, 2855–2860 (2011).
16. Tavakkoli, K. G. A. *et al.* Templating Three-Dimensional Self-Assembled Structures in Bilayer Block Copolymer Films. *Science*. **336**, 1294–1298 (2012).
17. Kamata, Y. *et al.* Microscopic magnetic characteristics of CoCrPt-patterned media made by artificially aligned self-organized mask. *Japanese J. Appl. Physics, Part 1 Regul. Pap. Short Notes Rev. Pap.* **46**, 999–1002 (2007).
18. Gates, B. D. *et al.* New Approaches to Nanofabrication: Molding, Printing, and Other Techniques. *Chem. Rev.* **105**, 1171–1196 (2005).
19. Savas, T. A., *et al.* Large-area achromatic interferometric lithography for 100 nm period gratings and grids. *J. Vac. Sci. Technol. B Microelectron. Nanom. Struct. Process. Meas. Phenom.* **14**, 4167–4170 (1996).
20. Auzelyte, V. *et al.* Extreme ultraviolet interference lithography at the Paul Scherrer Institut. *J. Micro/Nanolithography, MEMS, MOEMS* **8**, 21204–21210 (2009).
21. Geissler, M. *et al.* Patterning: Principles and Some New Developments. *Adv. Mater.* **16**, 1249–1269 (2004).
22. Cheng, J. Y., *et al.* Nanostructure engineering by templated self-assembly of block copolymers. *Nat. Mater.* **3**, 823–8 (2004).
23. Griffiths, R. A. *et al.* Directed self-assembly of block copolymers for use in bit patterned media fabrication. *J. Phys. D Appl. Phys. J. Phys. D Appl. Phys* **46**, 503001–29 (2013).
24. Park, S. *et al.* Macroscopic 10-terabit-per-square-inch arrays from block copolymers with lateral order. *Science* **323**, 1030–3 (2009).
25. Cheng, J. Y. *et al.* Simple and versatile methods to integrate directed self-assembly with optical lithography using a polarity-switched photoresist. *ACS Nano* **4**, 4815–23 (2010).
26. Jeong, S.-J. *et al.* Soft Graphoepitaxy of Block Copolymer Assembly with Disposable Photoresist Confinement. *Nano Lett.* **9**, 2300–2305 (2009).
27. Moon, H.-S. *et al.* Large-area, highly oriented lamellar block copolymer nanopatterning directed by graphoepitaxially assembled cylinder nanopatterns. *J. Mater. Chem.* **22**, 6307–6310 (2012).
28. Jeong, S.-J. *et al.* Ultralarge-Area Block Copolymer Lithography Enabled by Disposable Photoresist Pre patterning. *ACS Nano* **4**, 5181–5186 (2010).
29. Borah, D., *et al.* Sub-10 nm Feature Size PS-*b*-PDMS Block Copolymer Structures Fabricated by a Microwave-Assisted Solvothermal Process. *ACS Appl. Mater. Interfaces* **5**, 2004–2012 (2013).

30. Jeong, S.-J. *et al.* Ultralarge-Area Block Copolymer Lithography Enabled by Disposable Photoresist Prepatterning. *ACS Nano* **4**, 5181–5186 (2010).
31. Claveau, G. *et al.* Surface affinity role in directed self-assembly of lamellar block copolymers. *Proceeding SPIE* **9779**, 97791F (2016).

Chapter 5

Directed self-assembly of high- χ block copolymers

The increasing demand on the fabrication of ever-smaller structures requires a continuous decrease in the feature size of device components. PS-b-PMMA has a limit in its feature size around 12 nm due to its low χ value. Therefore, BCPs with larger χ values which provide sub-10 nm resolution have to be explored, demonstrating a controlled synthesis and good etching selectivity.

In this chapter, the self-assembly of two high- χ systems is studied and characterized. Then, its implementation to the developed directed self-assembly processes for PS-b-PMMA is also described. Moreover, a novel approach based on a combination technique between chemical and graphoepitaxy is presented, achieving high density multiplication factors.

5.1. Introduction to high- χ block copolymers

DSA based high- χ BCPs offer a complementary solution to conventional DUV or EUV lithography, allowing getting resolutions below 10 nm at a more affordable cost. In general, low- χ BCPs tend to be easier to anneal since the movement of polymer domains encounters lower activation barriers. However, high- χ BCPs are more difficult to direct and orientate by thermal annealing due to the different properties between blocks. Normally, they need an extra top-coat layer or the use of solvent annealing to obtain the perpendicular morphology, which increases processing costs and further complicate an already complex process.

In this chapter, the implementation of chemical epitaxy process based on EBL and subsequent substrate functionalization has been implemented for two different lamellar systems which exhibit a moderate *Flory-Huggins* parameter, yet higher, than PS-*b*-PMMA: PS-*b*-PLA¹⁻⁷ and poly(dimethylsiloxane)-*b*-poly(lactic acid) (PLA-*b*-PDMS-*b*-PLA).⁸⁻¹¹ In particular for these two BCP systems, the synthesis of random copolymers is not trivial and has not been reported in the literature. In addition, neutral layers containing silicon complicate the step of transferring the features to the substrate. Therefore, in order to tune the surface energy between the high- χ system and the substrate, the influence of different random PS-*r*-PMMA copolymers with different compositions has been investigated.

5.2. PS-*b*-PLA systems

5.2.1. PS-*b*-PLA synthesis

PS-*b*-PLA is based on the modification of the common PS-*b*-PMMA system in which the PMMA domains are replaced by another block which allows tuning the *Flory-Huggins* parameter between the two blocks. It exhibits a moderate but higher *Flory-Huggins* parameter, as compared with PS-*b*-PMMA ($\chi = 0.23$ at 298K).¹² Moreover, this BCP system has shown the availability to self-assemble under thermal treatments¹³, avoiding thus the use of complex solvent annealing treatments which increment the processing costs.

The BCP synthesis was performed at the *Laboratoire de Chimie des Polymères Organiques (LCPO)* and *Arkema*. Targeted structures were designed in order to obtain BCPs with overall molecular weight in number, M_n , and dispersity index, PDI , lower than 15 kg/mol and 1.25, respectively, which lead to sub-10 nm lithographic structures. Figure 5.1 shows the two-step synthetic pathway for the synthesis of PS-*b*-PLA. The synthesis of mono-functionalized precursor blocks with predefined molecular weights was performed leading to hydroxyl terminated PS. The controlled growing of the PLA block was then achieved by

using these PS blocks as macroinitiators and by using triazabicyclodecene (TBD) as catalyst for the reaction, thus avoiding the use of non-organic catalysts during synthesis, which simplifies the metallic purification step. The control of the conversion of the PLA growing chains allows the formation of PS-*b*-PLA BCPs with various compositions.

In order to determine the molecular weight of PS domains, Size Exclusion Chromatography (SEC) as well as ^1H Nuclear Magnetic Resonance spectroscopy (NMR) have been used. The obtained results are summarized in Table 5.1. On the other hand, the BCP morphology was determined by small angle X-ray scattering (SAXS).

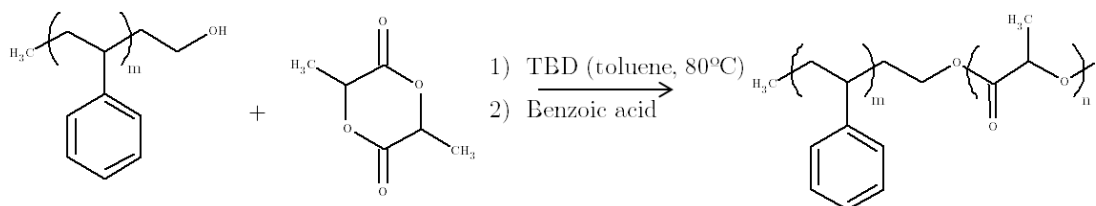


Figure 5.1. Synthetic pathway used for the synthesis of PS-*b*-PLA

Table 5.1. Macromolecular specifications of PS-*b*-PLA BCP. Macroinitiator M_n was determined by SEC using PS standards, BCP M_n and volume fraction by ^1H -NMR, PDI by SEC in THF and the morphology by SAXS

M_n Macroin.	M_n BCP	PDI	Volume fraction (Macroin./PLA)	Morphology
4.6 kg/mol	10.8 kg/mol	1.10	0.48/0.52	Lamellae

5.2.2. PS-*b*-PLA self-assembly

In order to control the self-assembly in thin film configuration, the use of random copolymers grafted onto the substrate is also used since it allows controlling the surface energy between the BCP domains and the substrate. Nevertheless, the synthesis of random copolymers different from PS-*r*-PMMA is not well-established, and it has not been reported in the literature yet.

Therefore, different processing parameters have been studied in order to get the perpendicular lamellae with fingerprint morphology on free-surface, including annealing processing conditions, BCP film thickness and brush layer material. In particular, four brush polymers based on PS-*r*-PMMA have been used by varying the composition of PS. The specifications of these materials are summarized in Table 5.2.

Table 5.2. PS-*r*-PMMA brush layer specifications

Brush material	M_n	PDI	PS Volume fraction
PS-OH	14.5 kg/mol	1.4	1
PS_{60%}-<i>r</i>-PMMA	7.9 kg/mol	1.85	0.59
PS_{70%}-<i>r</i>-PMMA	9.9 kg/mol	1.34	0.70
PS_{48%}-<i>r</i>-PMMA	18.8 kg/mol	1.46	0.48

For each of these brush materials, an annealing temperature range between 100 and 230°C has been used, with annealing times from 10 min to 24 h under a free-oxygen environment. On the other hand, for each situation, a broad study of the BCP self-assembly behavior depending on film thickness has been also conducted.

Figure 5.2 shows a SEM image of PS-*b*-PLA self-assembly with the optimal processing conditions found. The perpendicular morphology has been obtained when using PS-*r*-PMMA with 48% PS content annealed at 230°C for 5 min and with a BCP film thickness of 23.5 nm ($1.2L_0$) annealed at 100°C for 24 h under vacuum conditions. Due to the χ variations with temperature, it is necessary to work at a temperature near to 100°C, which is very close to PS glass transition temperature.

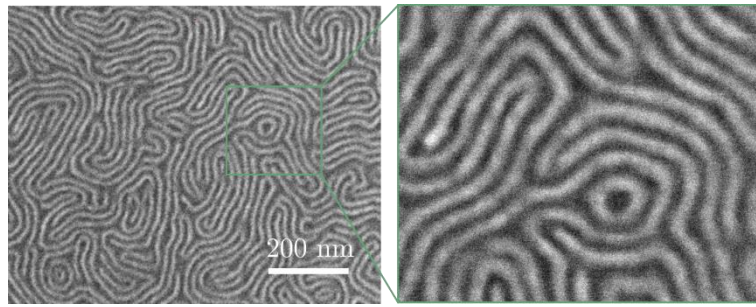


Figure 5.2. SEM image of lamellar PS-*b*-PLA self-assembly for a film thickness of 23.5 nm annealed at 100°C for 24 h under vacuum on top of PS_{48%}-*r*-PMMA

Figure 5.3 shows PS-*b*-PLA self-assembly behavior depending on the content of PS brush layer (the annealing conditions and BCP film thickness are the ones described in Figure 5.2). It is observed that as the PS brush content decreases, the interfacial energies between PS and PLA with the surface become more similar since perpendicular lamellae appear on the surface. When PS_{48%}-*r*-PMMA is used, both interface energies are balanced and thus induce the fingerprint BCP morphology along the sample. As observed, the BCP morphology strongly depends on the brush material composition.

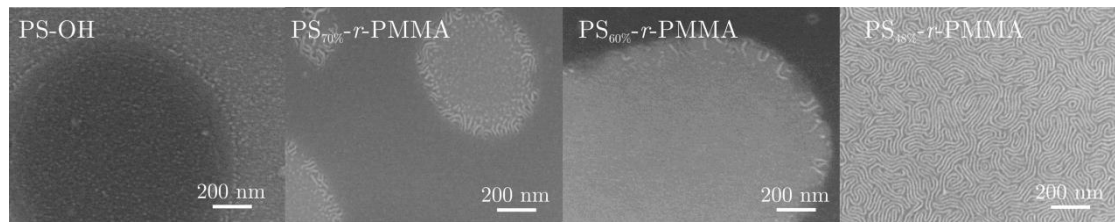


Figure 5.3. SEM images of lamellar PS-*b*-PLA self-assembly for a film thickness of 23.5 nm annealed at 100°C for 24 h under vacuum on top of different PS-*r*-PMMA

On the other hand, Figure 5.4 shows the morphology the BCP takes depending on its film thickness when using PS_{48%}-*r*-PMMA as a brush (the annealing conditions are described in Figure 5.2). It is clearly observed that the morphology is very sensitive to film thickness variations, and thus an accurate film thickness control has to be taken into account for DSA chemical epitaxy processes.

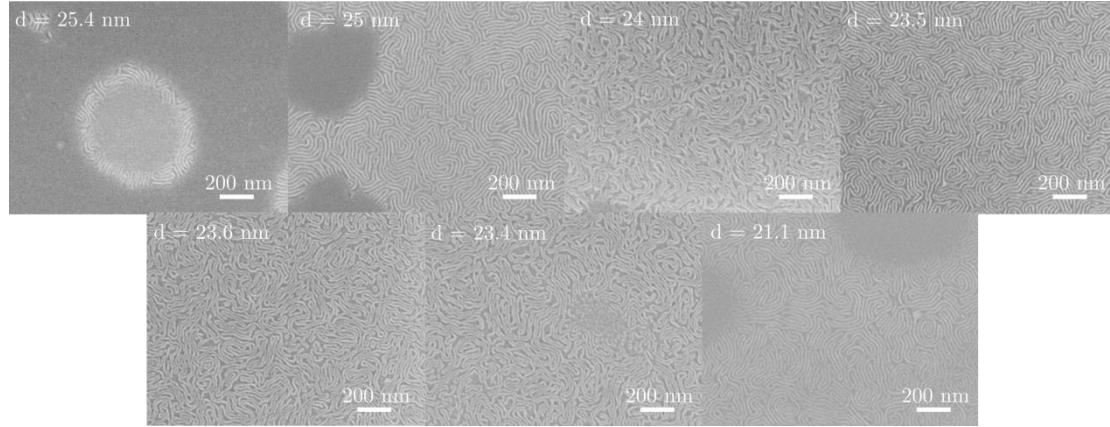


Figure 5.4. SEM images of lamellar PS-*b*-PLA self-assembly annealed at 100°C for 24 h under vacuum on top of PS_{48%}-*r*-PMMA by varying the BCP film thickness

The BCP pitch has been also analyzed by AFM characterization (Figure 5.5). From the Fast Fourier Transform (FFT) image characterization it is observed that the pitch is 21 nm.

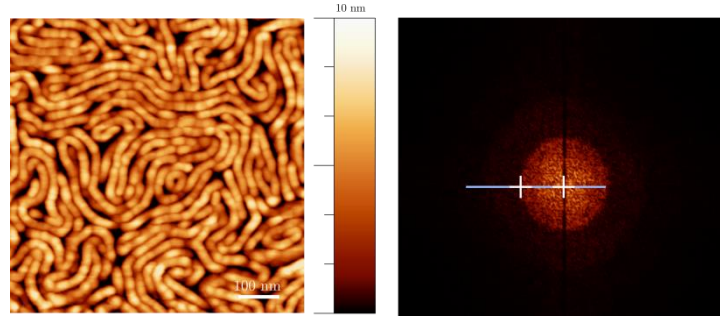


Figure 5.5. AFM characterization of PS-*b*-PLA self-assembled structures under the optimal self-assembly conditions found. The obtained pitch is 21 nm

From the study performed on the PS-*b*-PLA self-assembly on free-surface, it can be concluded that a surface which balances the interface free energies between the domains and the surface has been found, thus allowing to obtain the perpendicular morphology in large areas when using a thermal treatment. Figure 5.2 suggests that PS_{48%}-*r*-PMMA is neutral to both domains of the BCP, thus balancing the free energies between the substrate and the blocks. In contrast, the perpendicular morphology is lost when other brush layers or non-commensurate film thickness are used.

On the other hand, since the BCP annealing time is too long for industrial applications, shorter annealing times have been tried by using a range temperature between 100 and 130°C in a N₂ environment, instead of in vacuum. The shorter annealing time leading to useful results, has been found for an annealing temperature and time of 100°C and 10 minutes, respectively. Figure 5.6 shows a comparison between PS-*b*-PLA self-assembly when it is annealed at the same temperature for 24h under vacuum and for 10 min with continuous nitrogen flow. Although it has been reported that PS-*b*-PLA requires large thermal annealing times to self-assemble¹⁴, the obtained results demonstrate that is possible

to dramatically reduce the thermal annealing times enabling the process to be suitable for an industrial application.

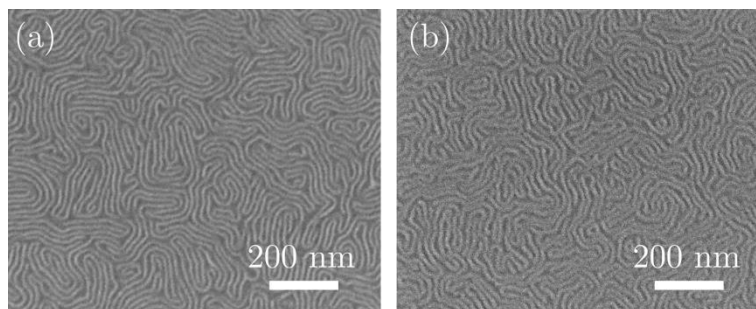


Figure 5.6. SEM images of lamellar PS-*b*-PLA self-assembly annealed at (a) 100°C under vacuum and (b) 100°C for 10 min in a N₂ environment

From the SEM images shown above, it can be observed that PS domains (brighter lines) are immersed in a PLA matrix (darker parts) which seem to be a little bit wider and with an irregular shape. Therefore, the BCP morphology of the film has been further investigated by adding a small amount of PS homopolymer to the PS-*b*-PLA solution. Figure 5.7 shows two PS-*b*-PLA SEM images before and after adding 5% of PS homopolymer. It is seen that after adding the small amount of PS, the brighter domains (PS blocks) become wider, and in consequence a more uniform line/space distribution is obtained. The solvent the BCP is dissolved in, presents higher selectivity to PLA domains.

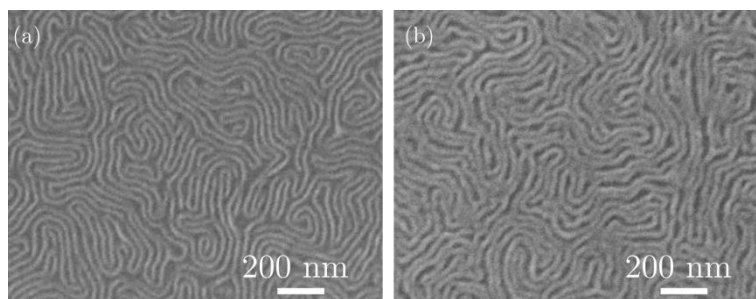


Figure 5.7. PS-*b*-PLA SEM images (a) before and (b) after adding 5% PS homopolymer

In order to explore the influence of the solvent, the PS-*b*-PLA self-assembly behavior has been also characterized as a function of the solvent. Apart from PGMEA, which is the solvent used for the later experiments, 1.5% toluene solution has also been tested. The study has been performed by using the same conditions which PS-*b*-PLA in PGMEA has shown the best self-assembly (PS_{48%}-*r*-PMMA brush, and 100°C for 24h in vacuum for the BCP annealing). Then, experiments as a function of the film thickness have been undertaken. From the characterization of SEM images of Figure 5.8, it can be noticed that the BCP pitch changes depending on which solvent it is dissolved in. It is also confirmed from the FFT AFM image characterization (Figure 5.9) which gives a pitch of 19.5 nm. This characterization has been also corroborated by GISAXS measurements, introduced in *chapter 6*.

This difference in the BCP pitch can be explained by the different solubility of the BCP with PGMEA and toluene. The selectivity of the solvents has been estimated using a solubility parameter study. The closer the solubility parameters of the solute and the solvent are, the larger the solubility will be. Hansen solubility parameters (HSP) developed by *Charles M. Hansen* in 1967¹⁵, represent the total cohesive energy of a solvent or polymer separated in three terms: (i) dispersion, δ_d , (ii) polar, δ_p and (iii) hydrogen bonding forces, δ_h :

$$\delta_t^2 = \delta_d^2 + \delta_p^2 + \delta_h^2, \quad (5.1)$$

To measure the similarity of the HSP of PLA and PS with the HSP of the solvent, the parameter R_a is introduced and defined as the distance between two molecules, representing a measure of how alike the polymer and the solvent are. Then, the smaller R_a the more likely they are to be compatible and the higher the swelling of the polymer:

$$R_a^2 = 4(\delta_{d1} - \delta_{d2})^2 + (\delta_{p1} - \delta_{p2})^2 + (\delta_{h1} - \delta_{h2})^2, \quad (5.2)$$

The distance R_a can be compared to the solubility radius of the polymer, R_θ . The ratio between R_a and R_θ is the relative energy difference (RED), of the system. If $RED > 1$, then there is a low affinity between the polymer and solvent. If it is close or equal to one, the compound will partially dissolve. Table 5.3 shows the solubility parameters for the solvents and polymers involved in the process. From these values, the HSP distance between two molecules can be calculated and then the RED of the system which gives an idea of how suitable the solvent is for the system. Table 5.4 shows the RED calculated for toluene and PGMEA with respect to PS and PLA. From these values it can be concluded that PGMEA is more PLA selective, whereas toluene is nearly neutral with a slight selectivity to PS. Therefore, the different polymer-solvent solubility explains the variance on the BCP pitch. When the polymer is dissolved in PGMEA, it swells more PLA domains making them wider, whereas in toluene there is no swelling, and thus the copolymer pitch is reduced since it is almost neutral for both polymers.

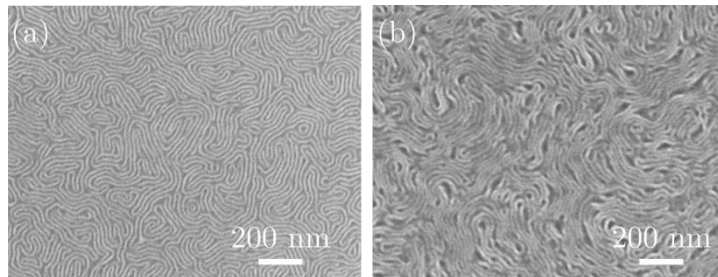


Figure 5.8. PS-*b*-PLA self-assembly as a function of film thickness when using (a) PGMEA, (b) toluene solutions

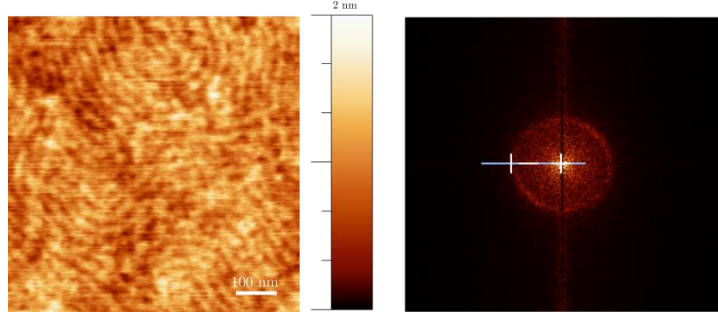


Figure 5.9. AFM characterization of PS-*b*-PLA self-assembled structures when using a toluene solution. The obtained pitch is 19.5 nm

Table 5.3. Average solubility parameters for toluene, PGMEA, PLA and PS¹⁶

Compound	δ_d [MPa ^{1/2}]	δ_p [MPa ^{1/2}]	δ_h [MPa ^{1/2}]
Toluene	18.0	1.4	2.0
PGMEA	15.6	5.6	9.8
PLA	18.6	9.9	6.0
PS	18.5	4.5	2.9

Table 5.4. Relative energy difference calculated for toluene and PGMEA with respect to PS and PLA. PLA and PS radius are 10.7 and 8, respectively¹⁷

Compound	RED _{PLA}	RED _{PS}
Toluene	0.849	0.422
PGMEA	0.621	1.135

5.2.3. PS-*b*-PLA directed self-assembly by chemical epitaxy

Once the self-assembly behavior on free-surface has been optimized, the chemical epitaxy process for PS-*b*-PMMA, presented in *chapter 3*, has been implemented to PS-*b*-PLA. The overall process is the same as the one depicted in Figure 3.2 from *chapter 3*, and the brush used is PS_{48%}-*r*-PMMA. The guiding patterns have been designed for PS-*b*-PLA dimensions, and the oxygen plasma functionalization has been performed with the softer conditions available to not remove the brush but only slightly modify it, which makes the surface more attractive to PLA domains. A 1.5% BCP solution in PGMEA has been spin-coated at 4500 rpm ($d = 23.5$ nm) on top of the chemical guiding patterns and the sample has been annealed at 100°C for 24h under vacuum conditions.

Figure 5.10 shows a SEM image after PS-*b*-PLA DSA process when using a chemical guiding pattern of guiding stripes width equal to the BCP period and $4L_0$ pitch. A chemical contrast between guiding and background regions is observed, although the BCP has not been parallel oriented with respect to the guiding pattern but perpendicularly. On the other hand, and in contrast with PS-*b*-PMMA behavior, darker regions which correspond to modified areas have a strong affinity to the PLA blocks inducing the parallel morphology of the BCP.

Despite having tried several experiments in which the BCP film thickness, the annealing conditions and the BCP composition to change the orientation of the BCP domains with respect to the guiding pattern have been varied, no vertical orientation has been observed. Nevertheless, the DSA results show a considerable progress on high- χ BCPs, since it has been demonstrated a chemical epitaxy DSA in which the BCP has been treated with a thermal annealing instead of using the solvent annealing technique.^{18,2}

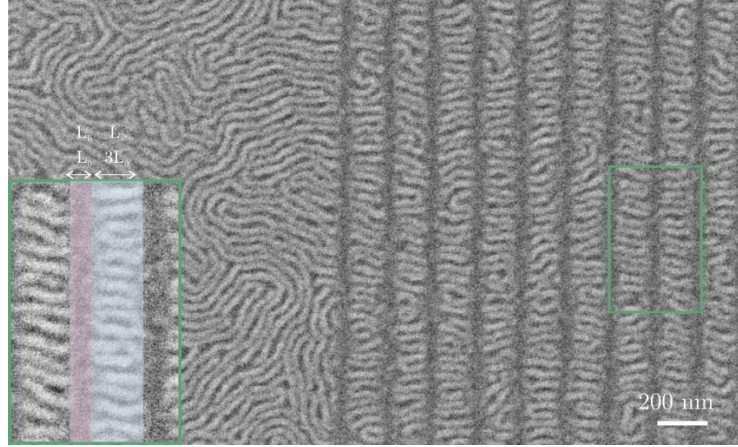


Figure 5.10. SEM image of PS-*b*-PLA DSA for $L_s = L_0$ and $4L_0$ pitch

5.2.4. Experimental determination of surface free energy for PS-*b*-PLA directed self-assembly

In order to chemically characterize the chemical interactions taking place in the DSA chemical epitaxy process of PS-*b*-PLA, the same experimental methodology described in *chapter 3* (Figure 3.14) to determine the surface free energies has been performed.

In the case of PS-*b*-PLA, the chemical guiding patterns are performed on a PS_{48%}-*r*-PMMA brush. Therefore, the contact angle of a PS/PLA 50:50 blend, has been determined on both modified and un-modified brush surfaces. Then, the difference of the surface free energy ($\Delta\gamma_{\text{PS-Brush}} - \Delta\gamma_{\text{PLA-Brush}}$) has been determined by using the *Young's equation* (equation (3.1)). The interfacial tension between PS and PLA ($\gamma_{\text{PS-PLA}} = 5.4 \text{ mN/m}$) has been taken from the literature.¹⁹

Figure 5.11 shows the SEM cross-section images for both un-modified and modified PS_{48%}-*r*-PMMA with the homopolymer blend on top. Table 5.5 depicts the contact angle values, as well as the corresponding interface energies. These values suggest that the surface becomes more PLA attractive when it is chemically modified by oxygen plasma and thus, they corroborate the good chemical contrast observed on the guiding patterns.

Table 5.6. Macromolecular specifications of PLA-*b*-PDMS-*b*-PLA BCP. Macroinitiator M_n was determined by SEC using PS standards, BCP M_n and volume fraction by $^1\text{H-NMR}$, PDI by SEC in THF and the morphology by SAXS

M_n Macroin.	M_n BCP	PDI	Volume fraction (Macroin./PLA)	Morphology
5 kg/mol	12.5 kg/mol	1.2	0.47/0.52	Lamellae

5.3.2. PLA-*b*-PDMS-*b*-PLA self-assembly

In order to guide PLA-*b*-PDMS-*b*-PLA on chemical guiding patterns, a neutral surface has to be found as it has been done for PS-*b*-PLA. The process is challenging due to the fact that PDMS tends to dewet, leading to a non-uniform layer on the substrate.

PLA-*b*-PDMS-*b*-PLA solutions were prepared in a butyl acetate (BA) solution since it shows neutral selectivity to PLA and PDMS. Table 5.7 depicts the calculated relative energy differences for PLA and PDMS in BA compared with toluene and PGMEA. The average solubility parameters for PDMS are $\delta_d = 14.6$, $\delta_p = 4.9$ and $\delta_h = 0^{20}$.

Table 5.7. Relative energy difference calculated for toluene, PGMEA and BA with respect to PLA and PDMS. PLA and PDMS radius are 10.7 and 8.9, respectively^{17,21}

Compound	RED _{PLA}	RED _{PDMS}
Toluene	0.849	0.886
PGMEA	0.621	1.126
Butyl acetate	0.629	0.769

As for PS-*b*-PLA, four different brush layer materials based on PS-*r*-PMMA chemistry have been investigated (Table 5.2) by varying the BCP film thickness and annealing conditions. Figure 5.13 shows the self-assembly behavior of PLA-*b*-PDMS-*b*-PLA on different PS-*r*-PMMA brush materials. The film thickness used is the same for all samples (34 nm) and the BCP has been annealed at 100°C for 24h under vacuum which were the optimal conditions found for PS-*b*-PLA.

As it can be observed from the SEM images, a parallel oriented morphology is observed when PS_{48%}-*r*-PMMA is used as a brush layer due to the fact that there is a very strong affinity between the substrate and one of the domains. For brush layers of 60% and 70% of PS content, some perpendicular lamellae are observed on the surface, but it is not enough to create a total or almost neutral flavor necessary for chemical epitaxy processes. On the other hand, the BCP self-assembly behavior has been also tested directly on 20 nm silicon dioxide layer on silicon, getting some parallel and perpendicular oriented lamellae areas.

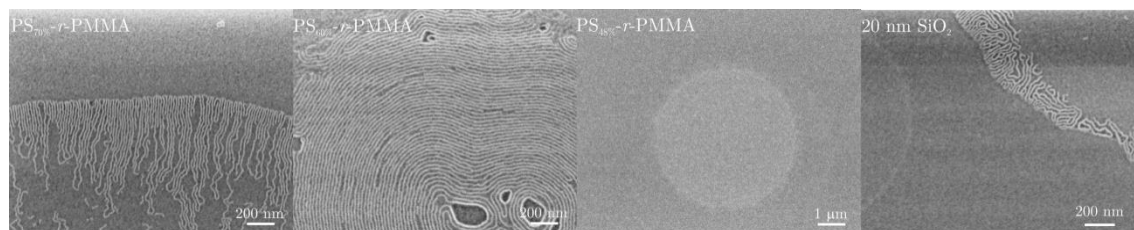


Figure 5.13. SEM images of lamellar PLA-*b*-PDMS-*b*-PLA self-assembly for a film thickness of 34 nm annealed at 100°C for 24 h under vacuum on top of different brush layer materials and 20 nm SiO₂

The BCP self-assembly behavior has shown more perpendicular oriented lamellae regions when PS_{60%}-*r*-PMMA has been used. Therefore, in order to further explore the wetting behavior, a study as a function of BCP film thickness has been performed.

From SEM results shown in Figure 5.14, it is observed that the BCP morphology is, as for PS-*b*-PLA, very sensitive to its film thickness. Nevertheless, despite having studied a broad range of film thicknesses, a large area with perpendicular morphology has not been found. That is, that no neutral layer which enables the balance of surface free energies has been found for this BCP.

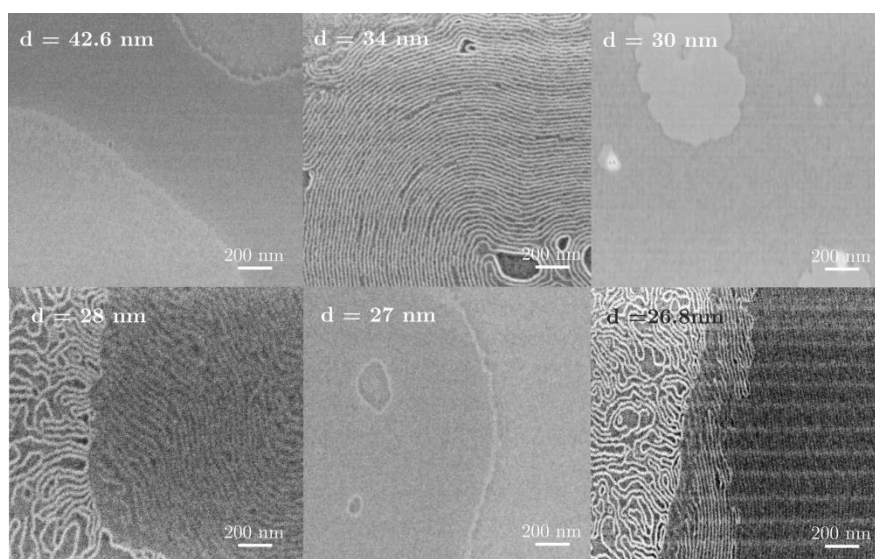


Figure 5.14. SEM images of lamellar PLA-*b*-PDMS-*b*-PLA self-assembly annealed at 100°C for 24 h under vacuum on top of PS_{60%}-*r*-PMMA by varying the BCP film thickness

Since no neutral layer has been found, and in order to change the brush wetting properties, another approach has been tested. PDMS-OH brush (see polymer specifications depicted in Table 5.8) has been spin-coated on PS_{60%}-*r*-PMMA which is the brush that has shown a larger area with fingerprint morphology, and annealed under the same conditions as PS_{60%}-*r*-PMMA was (230°C for 5 min in a N₂ flow). Then the BCP has been spin-coated at 2000 rpm on the top of the brush from a 1.5% solution in BA and annealed at 100°C for 24h in a vacuum oven.

Table 5.8. PDMS-OH brush layer specifications

Brush material	M_n	PDI	PDMS Volume fraction
PDMS-OH	3 kg/mol	2.23	1

Figure 5.15 shows a SEM image of a large area in which the BCP has been oriented perpendicularly to the substrate when PDMS-OH brush has been spin-coated on 8.6 nm of PS_{60%}-*r*-PMMA. Therefore, it can be concluded that it has been found a neutral layer to guide the BCP by using a bi-layer brush approach.

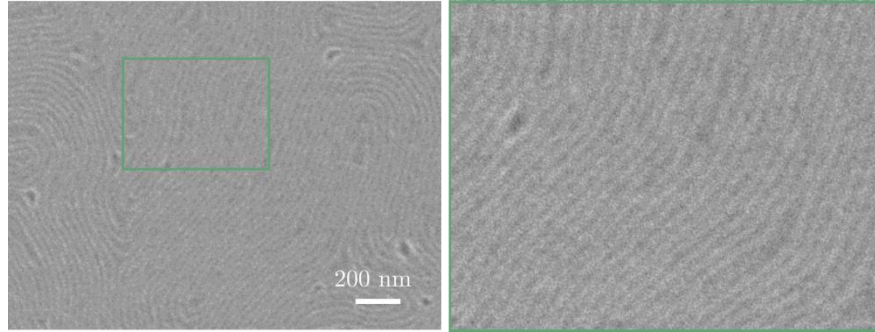


Figure 5.15. SEM image of lamellar PLA-*b*-PDMS-*b*-PLA self-assembly for a film thickness of 34 nm annealed at 100°C for 24 h under vacuum on top of PDMS-OH / PS_{60%}-*r*-PMMA by-layer brush

5.3.3. PLA-*b*-PDMS-*b*-PLA directed self-assembly by chemical epitaxy

The alignment of PLA-*b*-PDMS-*b*-PLA has been investigated on chemical guiding patterns using PS_{60%}-*r*-PMMA brush layer and soft oxygen plasma conditions, although a proper neutral surface has not been found. The BCP has been spin-coated and processed with the optimal conditions found in free-surface (2000 rpm and 100°C for 24h under vacuum). Figure 5.16 shows a SEM image of a DSA pattern. Some degree of dewetting along with some degree of alignment can be observed. This means that, as it has been previously discussed, there exists some chemical contrast on the surface to guide the BCP but not enough to induce the BCP perpendicular morphology in the whole sample, since the surface is not neutral.

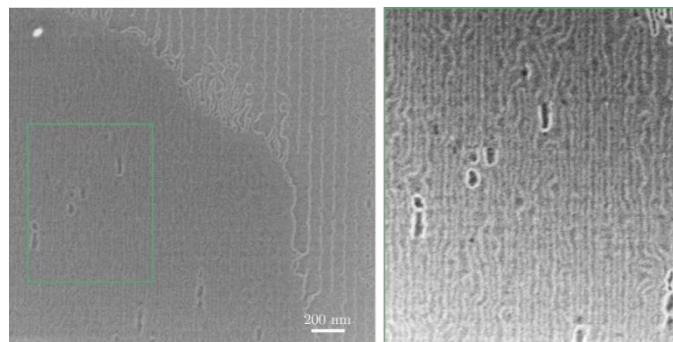


Figure 5.16. SEM images of PLA-*b*-PDMS-*b*-PLA DSA for $L_s = L_0$ and 100 nm pitch

5.3.4. PLA-*b*-PDMS-*b*-PLA directed self-assembly by chemo/graphoepitaxy

As the DSA process based on chemical epitaxy did not work to align PS-*b*-PDMS-*b*-PLA, a graphoepitaxy approach has been implemented in order to study the alignment of the BCP when it is confined. This process, represented in Figure 5.17, is the same as the one described in *chapter 4*. It consists of 6-steps: (i) e-beam writing on PMMA resist, (ii) PMMA development, (iii) silicon etching, (iv) resist removal, (v) polymer brush grafting on silicon, and (vi) BCP spin-coating.

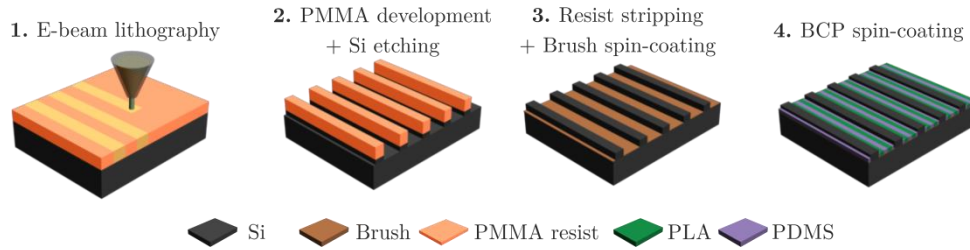


Figure 5.17. Schematic representation of the graphoepitaxy process for PLA-*b*-PDMS-*b*-PLA by means of e-beam lithography

For this BCP, the PS_{60%}-*r*-PMMA brush layer has been used, since it is the one which has shown more neutral affinity with the BCP. After the creation of the topographical guiding patterns, the brush is spin-coated from a 2% PGMEA solution at 5000 rpm in order to graft only the bottom of the trenches. By this way, the bottom will be a neutral surface for both domains, and the silicon walls will be more attractive to PDMS blocks.

Then, the non-grafted brush is removed and a 1.5% BA PLA-*b*-PDMS-*b*-PLA solution is spin-coated at 2500 rpm and annealed at 100°C for 24h in vacuum. Figure 5.18 shows a schematic representation of a silicon trench, in which the brush has been only grafted at the bottom, thus presenting a strong PDMS affinity at the walls. PLA-*b*-PDMS-*b*-PLA DSA by graphoepitaxy results are shown in Figure 5.19 for two different trench widths. As seen from top-view SEM images, a good degree of alignment is achieved, even for trench width of 6L₀.

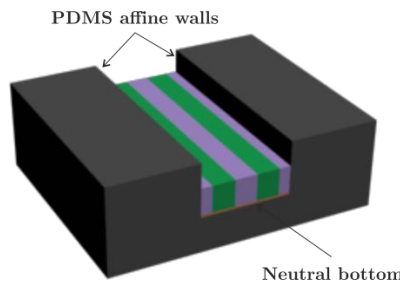


Figure 5.18. Schematic representation of the graphoepitaxy process for PLA-*b*-PDMS-*b*-PLA

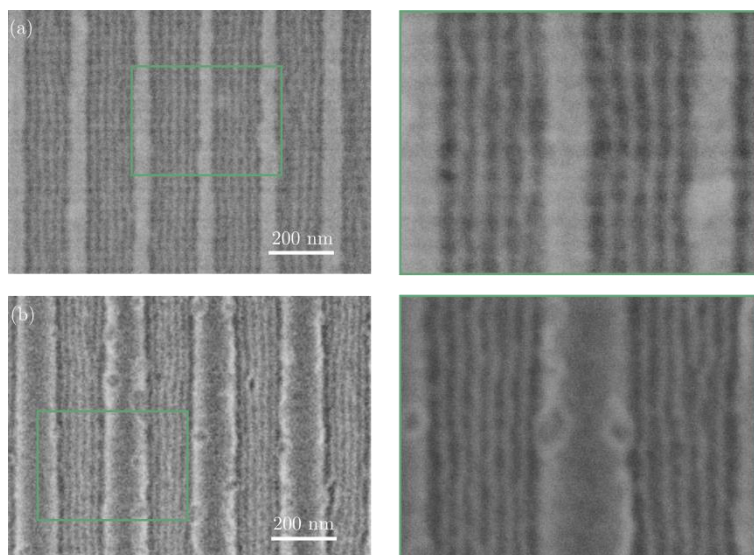


Figure 5.19. SEM images of PLA-*b*-PDMS-*b*-PLA DSA by graphoepitaxy for a guiding pattern of (a) 200 nm pitch and 50 nm trench width and (b) 300 nm pitch and 150 nm trench width, annealed at 100°C for 24h

As previously discussed for PS-*b*-PLA, the annealing times used for BCP were too long for application in industry. Therefore, a wide range of annealing temperatures (100°C to 180°C) and times (10 min to 30 min) have been tested in order to know if there were more suitable conditions with the same alignment results.

Figure 5.20 shows a SEM image with the PLA-*b*-PDMS-*b*-PLA DSA results which present optimal alignment conditions at higher temperatures and lower times. It has been found that by increasing 50°C the annealing temperatures, the time can be reduced to 15 min, which means that the process has potential industrial application.

During the annealing tests, it has been observed that the polymer degrades at temperatures above 150°C. On the other hand, the BCP self-assembly presents a high density of defects when working at 150°C with annealing times below 15 min.

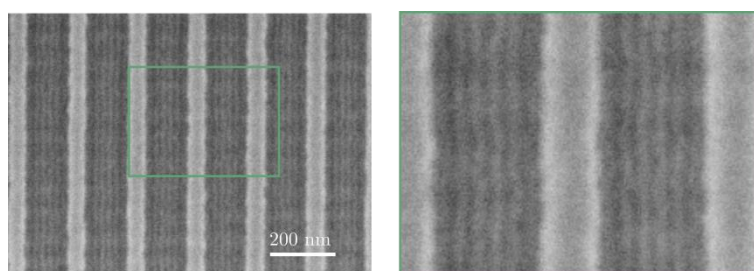


Figure 5.20. SEM images of PLA-*b*-PDMS-*b*-PLA DSA by graphoepitaxy for a guiding pattern of 200 nm pitch and 50 nm trench, annealed at 150°C for 15 min

Nevertheless, despite having shown a good DSA when graphoepitaxy approach is used, there has been observed that the DSA pattern presents some areas in which the BCP shows a parallel orientation due to non-neutrality of the surface (see Figure 5.21).

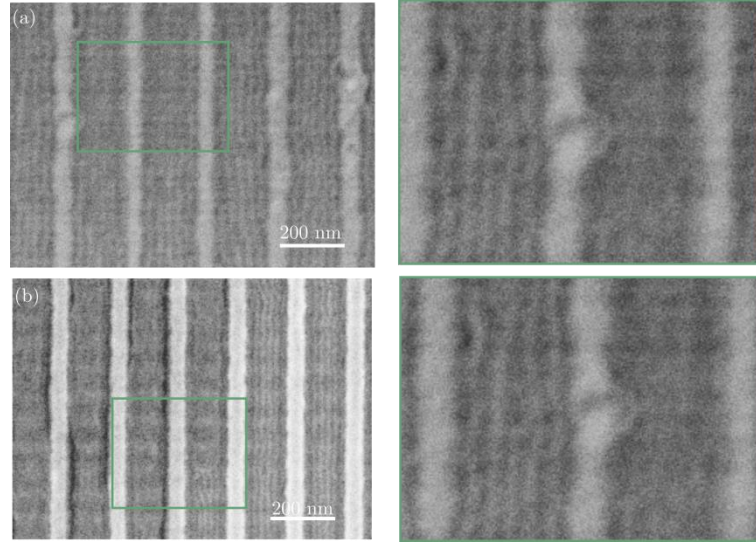


Figure 5.21. SEM images of PLA-*b*-PDMS-*b*-PLA DSA by graphoepitaxy for a guiding pattern of 200 nm pitch and 50 nm trench, annealed at (a) 100°C for 24h and (b) 150°C for 15 min, showing some parallel oriented regions

Therefore, the surface wetting behavior has been further investigated, and in order to slightly change the affinity of the brush at the bottom of the trench an alternative step has been introduced in the overall graphoepitaxy process depicted in Figure 5.17. As observed in the new representation of the process in Figure 5.22, this new step consists in changing the brush affinity before BCP spin-coating, by exposing the sample to a brief dose of oxygen plasma (10 sccm O₂, 150W for 5 s). When doing so, the brush surface is slightly oxidized and therefore there is a change in its chemical affinity.

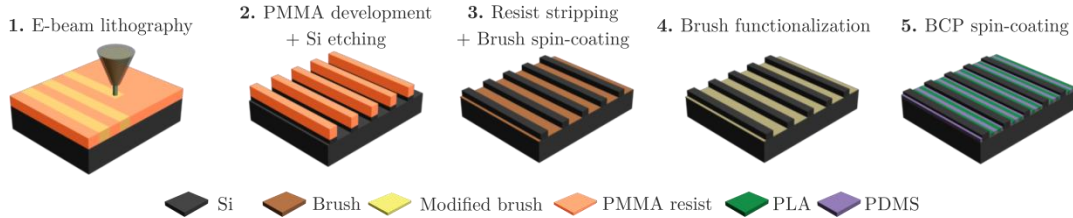


Figure 5.22. Chemo/grapho epitaxy overall process for PLA-*b*-PDMS-*b*-PLA

To directly study the industrial applicability of this process, the experiments have been performed on silicon graphoepitaxy guiding patterns, and then on guiding patterns created at CEA-Leti by using DUV lithography on 30 nm SiARC substrates (see Figure 5.23). Then, the brush grafting, functionalization and BCP spin-coating steps have been performed at IMB-CNM.

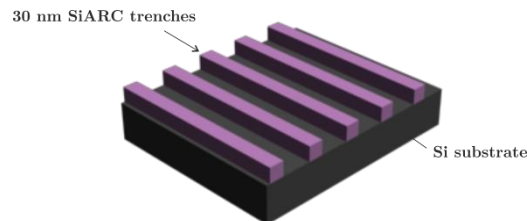


Figure 5.23. Schematics of graphoepitaxy guiding patterns created at CEA-Leti

SEM images of the chemo/grapho epitaxy DSA process are shown in Figure 5.24 for different guiding pattern dimensions resulting in density multiplication factors up to $16L_0$. It can be observed that the BCP shows a good alignment when using this new approach, with very low defectivity. Moreover, it is observed that, in contrast with conventional graphoepitaxy approach, all the patterned area shows a perpendicular morphology, demonstrating thus that the surface is more suitable for the DSA process.

On the other hand, it is seen that the BCP pitch is different depending on the guiding pattern dimensions. As it has been experimentally and theoretically corroborated, BCP tends to adjust its morphology depending on the separation between trenches.^{22,23} Table 5.9 shows the pitch the BCP adapts as a function of the guiding pattern dimensions. As observed, BCP pitch down to 20.9 nm can be obtained.

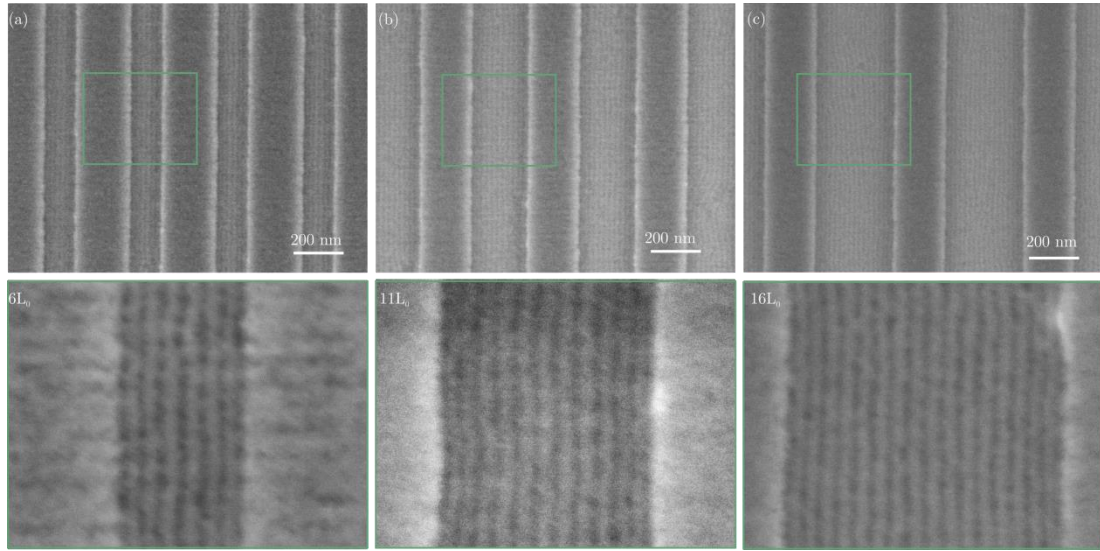


Figure 5.24. SEM images of PLA-*b*-PDMS-*b*-PLA DSA by chemo/grapho epitaxy for guiding pattern trench widths of 230 nm and (a) 135 nm, (b) 235 nm and (c) 335 nm pitch, and annealed at 150°C for 15 min

Table 5.9. PLA-*b*-PDMS-*b*-PLA pitch characterization as a function of guiding pattern dimensions

Guiding width	Trench width	Density mult. factor	BCP pitch
365 nm	230 nm	$6L_0$	22.5 nm
465 nm		$11L_0$	21.4 nm
565 nm		$16L_0$	20.9 nm

In order to study how the BCP behaves at the bottom of the guiding pattern, SEM cross-section characterization has been performed. Despite not having enough resolution, from Figure 5.25, it can be observed that the BCP domains present the perpendicular orientation through the whole film down to the bottom of the guiding pattern. This indicates that there is no wetting layer at the bottom, demonstrating thus the neutrality of the brush for the two BCP domains.

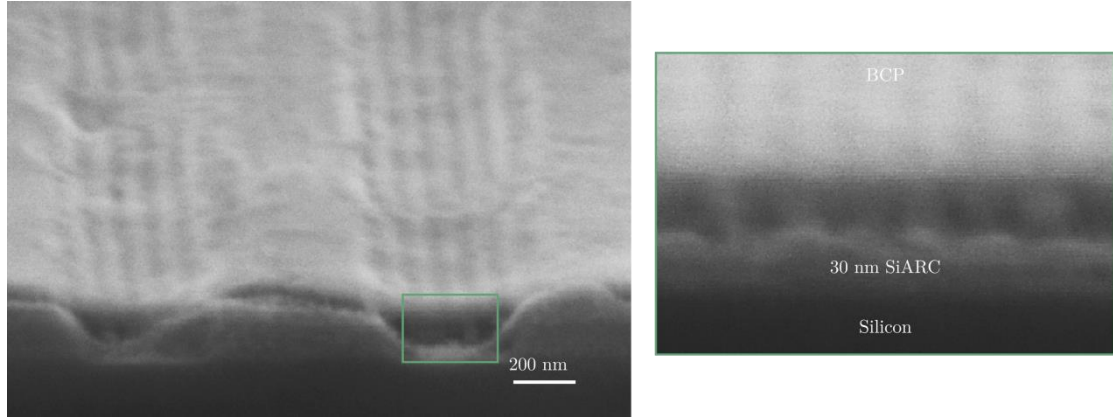


Figure 5.25. SEM cross-section image of PLA-*b*-PDMS-*b*-PLA DSA by chemo/grapho epitaxy for a guiding pattern trench width of 230 nm and 135 nm pitch, annealed at 150°C for 15 min

In order to evaluate the BCP film thickness behavior on the final DSA pattern, two different BCP fillings have been tried. Figure 5.26 shows SEM images, and a schematic representation of three different BCP fillings. As observed from the images, in the three situations there is some BCP alignment, although when the pattern is overfilled (Figure 5.26.c) there are some regions in which the BCP is oriented parallel to the substrate.

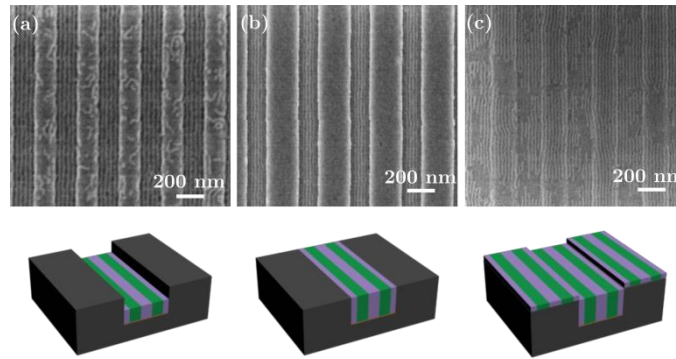


Figure 5.26. Schematic representation of (a) half filled, (b) filled, and (c) overfilled BCP on graphoepitaxy guiding patterns

To determine the BCP filling of the two first samples, they have been characterized by AFM. As observed in Figure 5.27, for the first situation (Figure 5.26.a), there is not enough contrast on the topography image due to the small BCP filling (15 nm). However, when the BCP fills the 30 nm SiARC guiding patterns, there is enough contrast in both topography and phase AFM images.

On the other hand, the high contrast of the phase AFM images reveal that there is no PDMS wetting layer on the top of the guiding patterns, thus allowing the pattern transfer into the substrate.

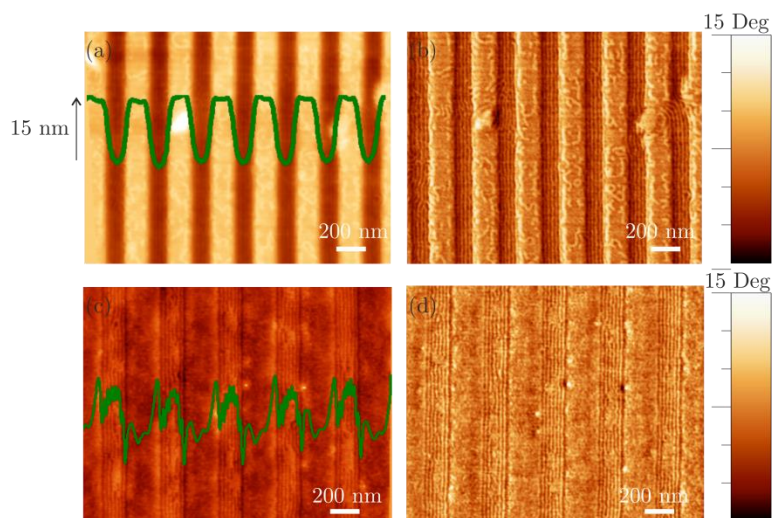


Figure 5.27. Topography and phase AFM images of (a, b) half filled, (c, d) filled BCP on graphoepitaxy guiding patterns

The results presented for PLA-*b*-PDMS-*b*-PLA are very promising for various reasons. First, there has been found a way to get the same BCP orientation on the whole guiding pattern with very high density multiplication factors and with very low defectivity. On the other hand, both the substrates and the processing conditions used, demonstrate that the process is feasible for industrial integration.

5.4. Summary and conclusions

Two different high- χ BCP systems have been designed by macromolecular engineering in order to produce sub-10 nm lithographic structures for line/space patterning. These two BCP systems have been chosen since their segregation strength was expected to be higher than the one corresponding to PS-*b*-PMMA system. This has been confirmed by the study of their self-assembly behavior in thin film configuration. Moreover, for both of them, their self-assembling capabilities have been investigated in order to implement several DSA processes and achieve aligned patterns.

With respect to PS-*b*-PLA, a proper brush layer which balances the interactions between the surface and both BCP domains has been found, thus leading to the perpendicular BCP orientation. Despite working with annealing temperatures very close to the PS glass transition temperature, successful results have been found, which demonstrate that it is possible to reduce the thermal annealing times enabling the process to be suitable for an industrial application. On the other hand, the formation of aligned lines by means of chemical epitaxy has been partially achieved since a chemical guiding pattern contrast has been found, but not strong enough to guide the BCP domains parallel to the guiding stripes.

For PLA-*b*-PDMS-*b*-PLA system, a novel approach has been designed, based on the combination of both chemical and graphoepitaxy methods which has provided large guided areas with density multiplication factors up to 16 L_0 . Furthermore, this BCP has shown very remarkable DSA results with respect to integration capability. Indeed, the integration of this system has shown its ability to define sub-20 nm structures with processing conditions compatible with the industry requirements.

5.5. References

1. Gorzolnik, B., *et al.* Novel functional mesoporous materials obtained from nanostructured diblock copolymers. *Macromol. Symp.* **287**, 127–134 (2010).
2. Vayer, M. *et al.* Perpendicular orientation of cylindrical domains upon solvent annealing thin films of polystyrene-*b*-polylactide. *Thin Solid Films* **518**, 3710–3715 (2010).
3. Phillip, W. A., *et al.* Self-assembled block copolymer thin films as water filtration membranes. *ACS Appl. Mater. Interfaces* **2**, 847–853 (2010).
4. Baruth, A. *et al.* Non-Liftoff Block Copolymer Nanolithography of Magnetic Nanodot Arrays. *APS March Meet. 2011* 3472–3481 (2011).
5. Ha, J.-G., *et al.* Thickness-dependent morphological behavior of dendritic (PS)₂-*b*-PLA copolymer thin films on a SiO₂ substrate. *Chem. Commun.* **48**, 3418–20 (2012).
6. Gu, W. *et al.* Self-assembly of symmetric brush diblock copolymers. *ACS Nano* **7**, 2551–2558 (2013).
7. Keen, I. *et al.* Behavior of Lamellar Forming Block Copolymers under Nanoconfinement: Implications for Topography Directed Self-Assembly of Sub-10 nm Structures. *Macromolecules* **47**, 276–283 (2014).
8. Kricheldorf, H. R., *et al.* Stereocomplexes of A–B–A Triblock Copolymers Based on Poly(L-Lactide) and Poly(D-Lactide) A Blocks. *Macromolecules* **38**, 7018–7025 (2005).
9. Rodwogin, M. D., *et al.*, M. A. Polylactide-poly(dimethylsiloxane)-polylactide triblock copolymers as multifunctional materials for nanolithographic applications. *ACS Nano* **4**, 725–732 (2010).
10. Pitet, L. M., *et al.* Nanostructured supramolecular block copolymers based on polydimethylsiloxane and polylactide. *ACS Macro Lett.* **2**, 1006–1010 (2013).
11. Pitet, L. M. *et al.* Well-organized dense arrays of nanodomains in thin films of poly(dimethylsiloxane)-*b*-poly(lactide) diblock copolymers. *Macromolecules* **46**, 8289–8295 (2013).
12. Zalusky, A. S., *et al.* Ordered nanoporous polymers from polystyrene–polylactide block copolymers. *J. Am. Chem. Soc.* **124**, 12761–12773 (2002).
13. Keen, I. *et al.* Control of the Orientation of Symmetric Poly(styrene)-*b*-poly(D,L-lactide) Block Copolymers Using Statistical Copolymers of Dissimilar Composition. *Langmuir* **28**, 15876–15888 (2012).
14. Keen, I. *et al.* Control of the Orientation of Symmetric Poly(styrene)-*b*-poly(lactide). *Langmuir*, **28** (2012).

15. Hansen, C. M. *The three dimensional solubility parameter and solvent diffusion coefficient*. C. Press (1967).
16. Sato, S., *et al.* Effects of various liquid organic solvents on solvent-induced crystallization of amorphous poly(lactic acid) film. *J. Appl. Polym. Sci.* **129**, 1607–1617 (2013).
17. Auras, R., *et al.* *Poly(lactic acid): Synthesis, Structures, Properties, Processing, and Applications*. John Wiley (2011).
18. Ho, R. M. *et al.* Solvent-induced microdomain orientation in polystyrene-*b*-poly(l-lactide) diblock copolymer thin films for nanopatterning. *Polymer*. **46**, 9362–9377 (2005).
19. Biresaw, G. *et al.* Interfacial tension of poly(lactic acid)/polystyrene blends. *J. Polym. Sci. Part B Polym. Phys.* **40**, 2248–2258 (2002).
20. Ben Soltane, *et al.* Effect of pressure on the swelling and fluxes of dense PDMS membranes in nanofiltration: An experimental study. *J. Memb. Sci.* **435**, 110–119 (2013).
21. Lenz, T. *et al.* Downscaling and Charge Transport in Nanostructured Ferroelectric Memory Diodes Fabricated by Solution Micromolding. *Adv. Funct. Mater.* **26**, 5111–5119 (2016).
22. Wuister, S. *et al.* Lithography assisted self-assembly of contact holes on 300-mm wafer scale. *J. Micro/Nanolithography, MEMS, MOEMS* **11**, (2012).
23. Boots, H. *et al.* Pitch variations of self-assembled cylindrical block copolymers in lithographically defined trenches. *J. Micro/Nanolithography, MEMS, MOEMS* **13**, 33015 (2014).

Chapter 6

Characterization of block copolymer and chemical guiding patterns using synchrotron radiation

In chemical epitaxy DSA it is very important to accurately determine the interactions that take place between the block copolymer domains and the boundaries of the guiding patterns, in order to ascertain the optimal alignment conditions for each chemical epitaxy case. On the other hand, it is also important to determine the BCP morphology and specifications depending on the processing conditions.

In this chapter, the chemical configuration and morphology of different BCPs systems are studied by means of the synchrotron radiation-based X-ray characterization techniques HAXPES (Hard X-ray Photoelectron Spectroscopy) and GISAXS.

6.1. Chemical guiding pattern characterization by X-Ray photoemission techniques

In chemical epitaxy DSA, as demonstrated in *chapter 3*, the interfacial energies between each domain of the copolymer and the chemically patterned surfaces strongly influence the final morphology and microdomain ordering. Therefore, an accurate control of the surface chemistry is needed. Ideally, the background surface should be slightly attractive to one of the BCP domains, and the chemically modified areas should be slightly affine to the other one. Within this framework, to chemically identify the nature of the different surfaces and interfaces, a high-sensitivity characterization method based on photoemission technique has been used.

One technique especially suited for the characterization of buried interfaces is HAXPES.¹ Photoemission is a well-known technique which provides information on the electronic structure of surfaces (identification of elements and their chemical state). Its high sensitivity arises from the small mean free path of the out-coming photoelectrons in solid matter. Using conventional excitation sources with discrete photon energies, kinetic energies below 1500 eV can be achieved, which correspond approximately to 2 nm in probing depth for inorganic materials.

The possibility of acquiring photoemission spectra at higher kinetic energies, as high as 10 keV, has permitted the exploration of the chemical environment of sub-surface regions down to more than 20 nm for polymeric materials (Figure 6.1).²

Working with larger probing depths implies that surface contamination due to exposure to atmosphere is not as critical as compared to measurements performed with conventional XPS equipment. HAXPES reaches its full potential when using synchrotron radiation as excitation source since, in this case, photon energy and thus kinetic energy can be tuned, so that the probing depth can be also varied in a controlled and continuous manner. Nevertheless, the impinging beam can cause an irreversible damage on the surface and therefore, this is a drawback that has to be carefully addressed in any measurement, even for inorganic materials.^{3,4}

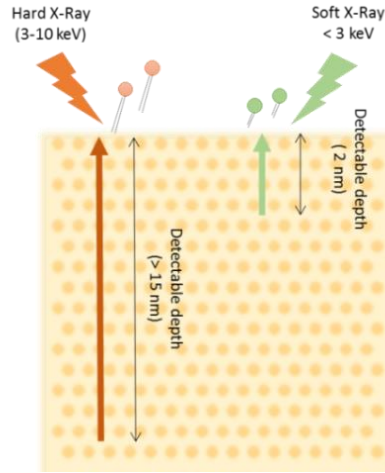


Figure 6.1. Schematic of XPS and HAXPES technique, showing the ability of HAXPES to measure deeper layers

In order to determine the main differences between the different methods developed to create chemical guiding patterns, the resulting surfaces have been characterized by using XPS and HAXPES. In this way, the interactions taking place between the surface and the BCP domains can be determined. Figure 6.2 shows a schematized description of the three approaches to create chemical guiding patterns developed at IMB-CNM, and previously described in *chapter 3*. The DSA processes that have been characterized are sustained on PS-OH brush layers.

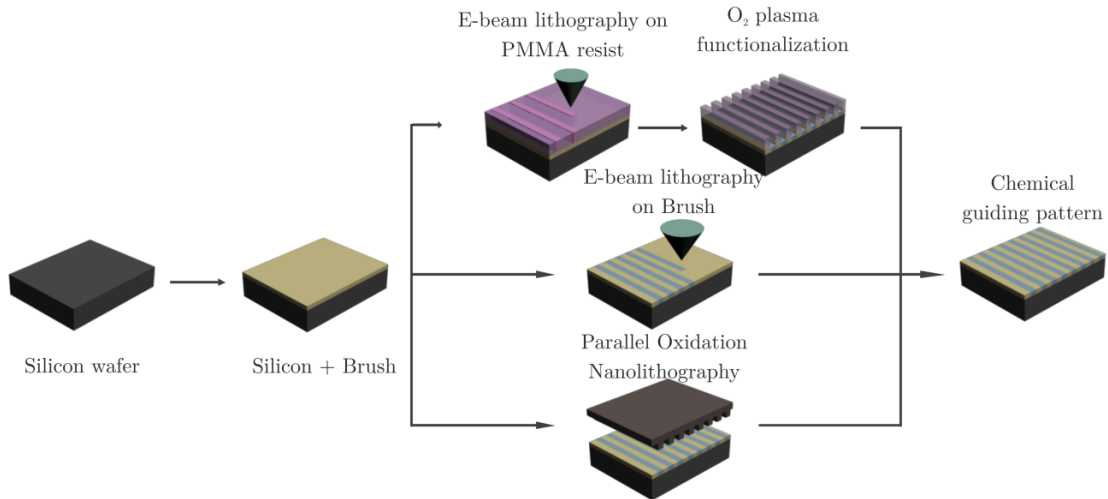


Figure 6.2. Schematized description of the three developed chemical epitaxy methods to DSA BCP. The method on top is the one based on using EBL on a resist and oxygen plasma to chemically functionalize the substrate, while in the other two nanolithography methods (middle and bottom) the guiding patterns are defined without using a resist (direct writing methods)

The HAXPES experiments have been performed at the HIKE end-station located at the KMC-1 beamline at the *BESSY II synchrotron of the Helmholtz Zentrum Berlin für Materialien und Energie* in Berlin (Germany).^{5,6} Monochromatic radiation in the 2020-6000 eV photon energy range has been used for the experiments, impinging the sample surface at grazing incidence. Photoemitted electrons were collected with a *SCIEN TA R4000* high-

resolution hemispherical analyzer at near normal emission, with an upper limit in kinetic energy of 10,000 eV. Experiments were performed in an ultrahigh vacuum chamber with a base pressure in the high 10^{-9} mbar range. To prevent beam damage, measurements were taken at different locations on the sample. In addition, the radiation was stopped when spectra were not acquired. On the other hand, ex-situ XPS experiments have been performed with a *SPECS PHOIBOS 150* hemispherical analyzer located at ICN2 using monochromatic AlK α radiation (1486.6 eV) as excitation source at a base pressure of 10^{-9} mbar.

As compared to the XPS system used, the HAXPES experiments have allowed getting higher energy resolution. Figure 6.3 shows the photoemission spectra of the Si2p line of the underlying silicon wafer taken with 2020 eV photons (lowest photon energy available). Both the signals arising from bulk Si (at 99.3 eV binding energy) and from SiO₂ (at around 104 eV binding energy) are displayed in the spectra. A least-square fit of the Si2p line after a Shirley-type background subtraction gives a spin-orbit splitting of 0.59 eV, the expected 2:1 branching ratio [$2p_{3/2}:2p_{1/2}$ with a nominal value of $(2 \times 3/2 + 1)/(2 \times 1/2 + 1)$] and a FWHM of 0.34 eV, highlighting the actual high resolution at use. Identical results are obtained for SiO₂/Si substrates, indicating the negligible effect of the brush on scattering of photoelectrons.

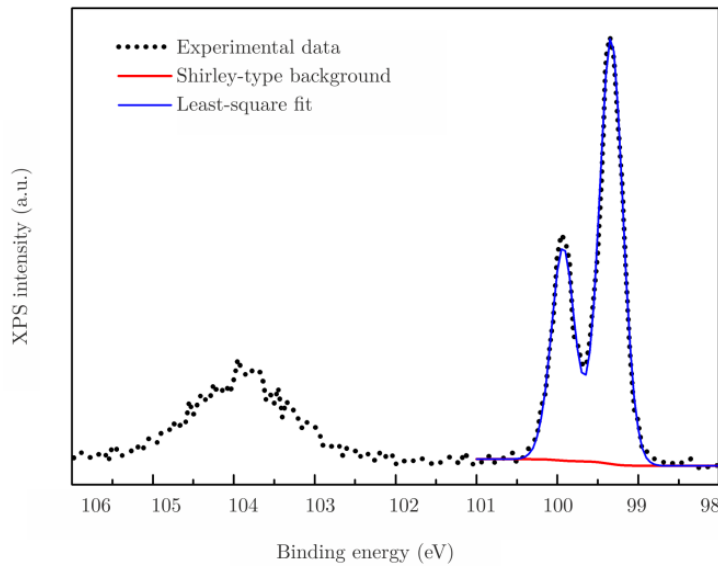


Figure 6.3. Photoemission spectra of the Si2p line taken with 2020 eV photons of a brush/SiO₂/Si sample. The discontinuous line stands for the experimental data while the continuous blue and red lines correspond to a least-square fit and to the chosen background, respectively

6.1.1. Characterization of chemical guiding patterns created by electron beam lithography and oxygen plasma functionalization

The approach based on using EBL and a subsequent oxygen plasma functionalization is the one depicted in section 3.2, and briefly described on the top of Figure 6.2. All the brush annealing processes have been performed within an oxygen free environment, since at the beginning of the research it was observed that the DSA processes did not work when the brush had been annealed in presence of oxygen. Therefore, in order to understand which is the origin of the DSA process efficiency, HAXPES experiments have been performed on unmodified PS-OH brush layers annealed under different conditions (cooled down in oxygen and nitrogen environment, respectively) and on the other hand, on functionalized surfaces.

Figure 6.4.a shows the experimental HAXPES C1s line (continuous black line) of the sample cooled down in nitrogen together with a least-square fit after background subtraction. The most prominent line (continuous red line), with a binding energy of 285.2 eV, corresponds to C-C and C-H sp^3 -like bonding. The continuous blue line in Figure 6.4.a, with a binding energy of 286.5 eV, corresponds to the hydroxyl bonding of the PS-OH. The π - π^* shake-up feature at 291.8 eV, characteristic of a pure PS spectrum (continuous magenta line)⁷, is also observed. Figure 6.4.b compares the zoomed in spectra of the C1s lines corresponding to the sample cooled in air (orange) and that cooled in nitrogen (black), respectively. The figure evidences a small but clear increase in intensity of the region corresponding to hydroxyl bonding for the sample cooled in air. We point out that this minor effect in the C1s line can only be observed because of the high-energy resolution used in the HAXPES experiments and that parallel XPS measurements of samples prepared under the same conditions did not show any significant difference. The higher density of hydroxyl bonding induces higher attraction to PMMA blocks due to the affinity with carbonyl PMMA groups. In this case, the chemical guiding patterns created afterwards on the sample cooled in air will not be effective since the brush is already slightly PMMA affine before the oxygen plasma functionalization. On the other hand, when the sample is cooled down in nitrogen, PS does not undergo oxidation. As a consequence, such sample is slightly affine to PS before functionalization. When chemical guiding stripes are defined on this substrate by oxygen plasma exposure (see Figure 6.5), there is enough chemical contrast to guide the alignment of the BCP. Therefore, it can be concluded that such a small increase in hydroxyl bonding is sufficient to disable the alignment capabilities of the PS-OH brush layer.

On the other hand, Figure 6.4.c shows the C1s HAXPES spectrum taken with 2020 eV photons of the sample cooled in nitrogen after the oxygen plasma treatment. The comparison with Figure 6.4.a evidences an increase in intensity towards higher binding energies in the ca. 286-291 eV region, which corresponds to contributions from different carbon-oxygen bonding configurations, as a result of the effect of the oxygen plasma

exposure on the PS-OH brush layer. The continuous blue line, corresponding to hydroxyl bonding, becomes more intense as compared to Figure 6.4.a Two new features are observed at 287.9 and 290 eV binding energies, which are assigned to the carbonyl (C=O, continuous green line) and carboxyl (O-C=O, continuous pink line) contributions, respectively. Thus, oxygen plasma activates the brush layer surface by creating a distribution of C-O bonding, while annealing and cooling in air induces essentially hydroxylation of the surface.

The combination between optimal processing conditions for grafting the polymer brush layer and an adequate chemical functionalization by oxygen plasma exposure leads to the possibility to generate efficient chemical patterns for guiding the self-assembly of the BCP.

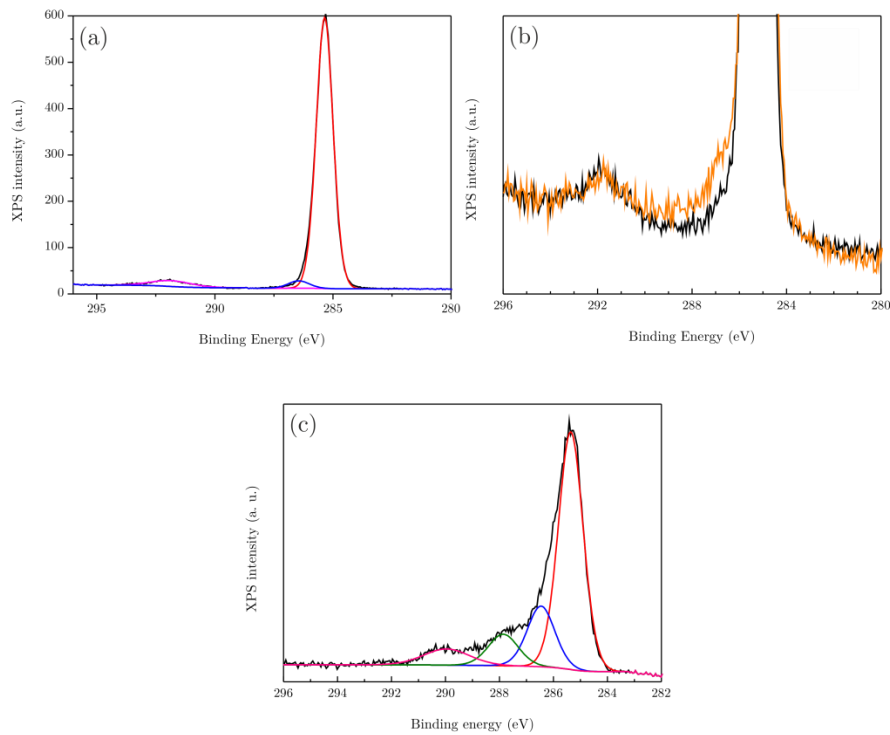


Figure 6.4. HAXPES spectra corresponding to the C1s region of grafted PS-OH samples (a) cooled in nitrogen, (b) cooled in air (orange) and in nitrogen (black) and (c) cooled in nitrogen and exposed to oxygen plasma taken with 2020 eV photon energy

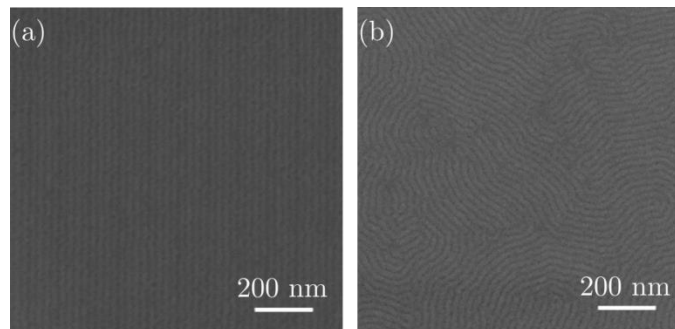


Figure 6.5. SEM images of PS-*b*-PMMA ($L_0 = 28$ nm) DSA for $4L_0$ density multiplication factor when using PS-OH brush layer annealed at (a) 230°C and cooled down in nitrogen and (b) 260°C and cooled down in air

Finally, the interfacial affinity between the PMMA block and both modified and un-modified brush layers has been studied by analyzing samples in which 20 nm PMMA films have been grown in top of modified and un-modified PS-OH.

Figure 6.6.a and b show the C1s HAXPES spectra acquired with 3000 eV photons together with de-convolutions using least-square fits. Both spectra show the characteristic 287.5 (continuous green line) and 290 eV (continuous magenta line) peaks of PMMA, corresponding to O-CH₃ and O-C=O configurations, respectively, with a 1:1 stoichiometric relationship.⁸ The continuous red and blue lines correspond to C-C/C-H bonding and to hydroxyl bonding, respectively, as described in Figure 6.4. The intensity ratio between the C-C, C-H and C-OH contributions (red and blue lines) and the O-C=O contribution (magenta line) increases for the sample exposed to oxygen plasma as compared to un-exposed sample, indicating that for the latter the un-modified brush layer is not uniformly covered by relatively thick PMMA film, as a result of lower affinity between both materials (dewetting effect). However, in the case of the sample exposed to oxygen plasma the modified character of the brush layer triggers a higher affinity to PMMA (wetting).

This is further confirmed when the C1s HAXPES spectra are taken at different photon energies, as shown in Figure 6.6.c and d, where spectra have been acquired at 2700 and 3000 eV, respectively. In the case of the un-exposed sample the mentioned ratio increases strongly between both photon energies, as a result of the increasing contribution of the PS-OH substrate for increasing photon energy and thus of the probing depth, while for the exposed sample the ratio is almost constant indicating a uniformly covered substrate.

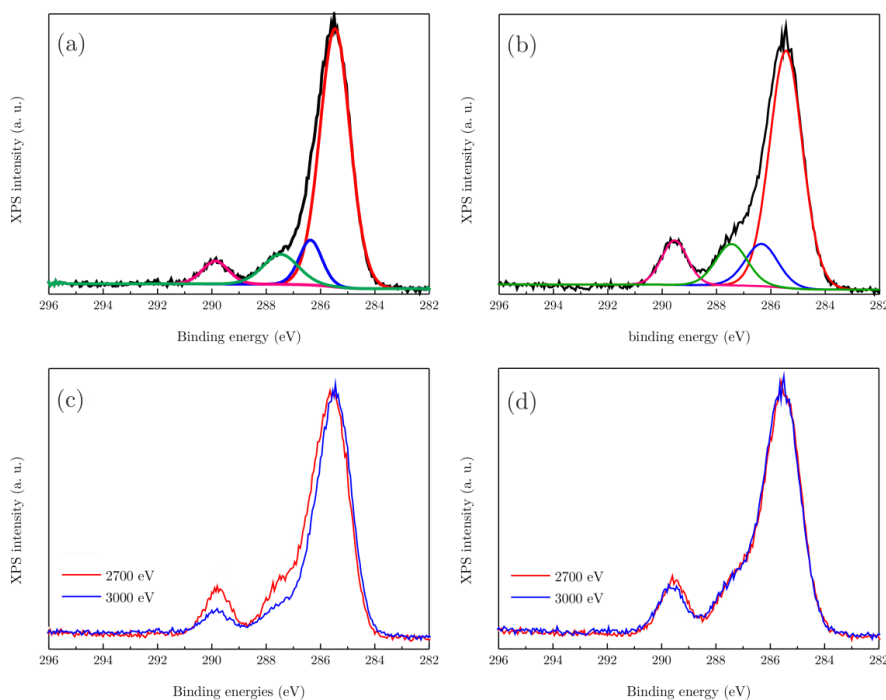


Figure 6.6. HAXPES spectra corresponding to C1s region of PMMA samples on (a) non-modified and (b) modified PS-OH taken with 3000 eV photons. (c) and (d) show a comparison with a lower photon energy (2700 eV)

6.1.2. Characterization of chemical guiding patterns created by direct writing techniques

These two chemical epitaxy approaches correspond to the two direct writing methods described in section 3.6, and schematized on the middle and bottom of Figure 6.2. The first method is based on using EBL to directly expose the sample to an electron beam which modifies the chemical affinity of the brush.⁹ Rather, in the other approach the surface is locally oxidized by means of AFM.¹⁰

Due to the fact that the sample size needed for HAXPES characterization is larger than 0,5 μm , and taking into account that these are low speed writing techniques, both samples have been characterized in a Laboratory-Scale XPS Instrument where the modified areas on the sample are easier to locate. Nevertheless, in order to characterize the different interfaces on samples submitted to oxidation by SPL, the same process has been tried by Parallel Oxidation Nanolithography (PON)¹¹ which allows the oxidation of larger areas. This procedure has been performed in collaboration with the *Instituto de Ciencia de Materiales de Madrid* (ICMM), and it has been performed by contacting a conductive mold with the PS-OH surface while applying a voltage under conditions of high humidity (above 70%). The stamp consists of a 1 cm^2 piece of a DVD replica made with PDMS and coated with 100 nm thick gold film evaporated in high vacuum. The stamp's surface presents parallel hillocks 320 nm wide and spaced 740 nm. The height of the protrusions is 40 nm. To transfer the patterns from the stamp to the substrate, a 35 – 40 V bias voltage for a time ranging between 40 and 180 s has been applied while the stamps has been gently (50 kPa) pressed upon the substrate.

Figure 6.7.a shows a comparison between C1s XPS spectra of four PS-OH surfaces after annealing at 230°C and cooling down in nitrogen (continuous red line), after EBL and PON modification (continuous grey and blue line, respectively) and a freshly cleaved highly-oriented pyrolytic graphite (HOPG) surface (discontinuous black line). The surface modified by EBL shows a relatively large broadening and a strong shift towards lower binding energies, as compared to the sample modified by EBL and oxygen plasma (Figure 6.4.c). Charging effects can be excluded, since in all cases the energies have been referenced to the Si2p_{3/2} peak (99.3 eV) from the buried silicon substrate. The mentioned shift towards lower binding energies denotes the increasing presence of sp² bonding based on the comparison with the results from a freshly cleaved HOPG sample (discontinuous black line), which shows a narrow peak centered at 284.4 eV characteristic of sp² bonding. Such increase in sp² bonding is in line, although not a direct proof, with the cross-linking of PS due to e-beam exposure, as has been reported in the literature^{12–14}, and which contributes to the alignment of the BCP, demonstrated in Figure 6.7.b.

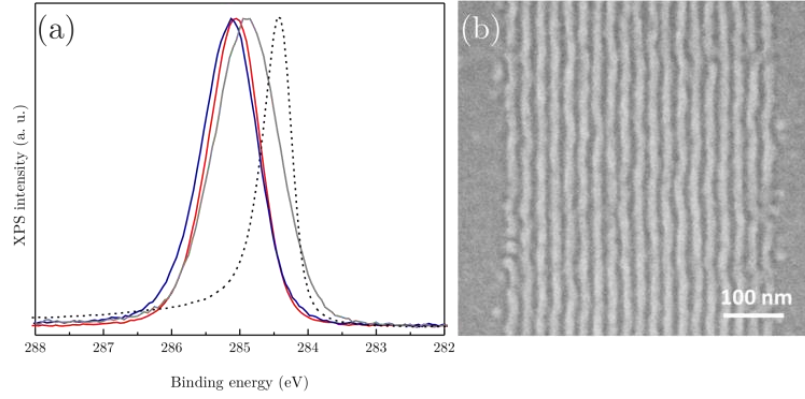


Figure 6.7. (a) C1s XPS spectra region of PS-OH (continuous red line), EBL and PON modified PS-OH (continuous grey and blue lines, respectively) and HOPG (discontinuous black line) using monochromatic 1486.6 eV photons and (b) SEM image of PS-*b*-PMMA DSA ($L_0 = 22$ nm) by EBL direct writing

On the other hand, Figure 6.8.a shows an AFM image of a chemical guiding pattern created by PON. The effect of the brush modification is an effective replication of the DVD pattern with modified regions (brighter in the AFM topography) slightly elevated (1.1 nm). Figure 6.8.b shows the Si1s spectra taken at different photon energies in the 2020-3000 eV range. At 2020 eV (black continuous line) only one feature is observed at about 1844 eV. At higher photon energies two more lines are identified at about 1841 and 1846 eV binding energies, respectively, that become increasingly dominant for increasing photon energies. The 1841 and 1846 eV features correspond to the buried Si/SiO₂ interface. Previous photoemission measurements performed at lower energy resolution using the Si2p line conclude that most of the oxide grown using PON is purely stoichiometric, although contribution from silicon lower oxidation states may be present.¹⁴ In references^{11,14,15} the Si2p spin-orbit splitting is not resolved (compare to Figure 6.3), which can preclude the observation of additional features in the region corresponding to the oxide.

In these experiments, Si1s line has been selected instead because of the higher interfacial sensitivity with photons above 2020 eV as compared to the Si2p line. At 2020 eV the corresponding kinetic energies are about 180 eV and 1920 eV for Si1s and Si2p, respectively, and the minimum mean free path for electrons in matter is at about 100 eV. Thus, we can continuously follow the emergence of the three features as a function of the increasing probing depth from the surface with the Si1s lines. In the case of the Si2p line photon energies above 200 eV should be used, which could not be achieved at the KMC-1 beamline. It can be concluded that the 1844 eV line emerges from a region located on top of the Si/SiO₂ interface, as schematized in Figure 6.8.a. In addition, since the feature at 1844 eV exhibits lower binding energy as compared to the 1846 eV counterpart, it is concluded that the 1844 eV line corresponds to a sub-stoichiometric oxide layer (SiO_x), with partially oxidized silicon. No changes are observed in the C1s spectra taken at the same photon energies, although they do not correspond to the same probing depths, since the associated kinetic energies are above 1735 eV for C1s.

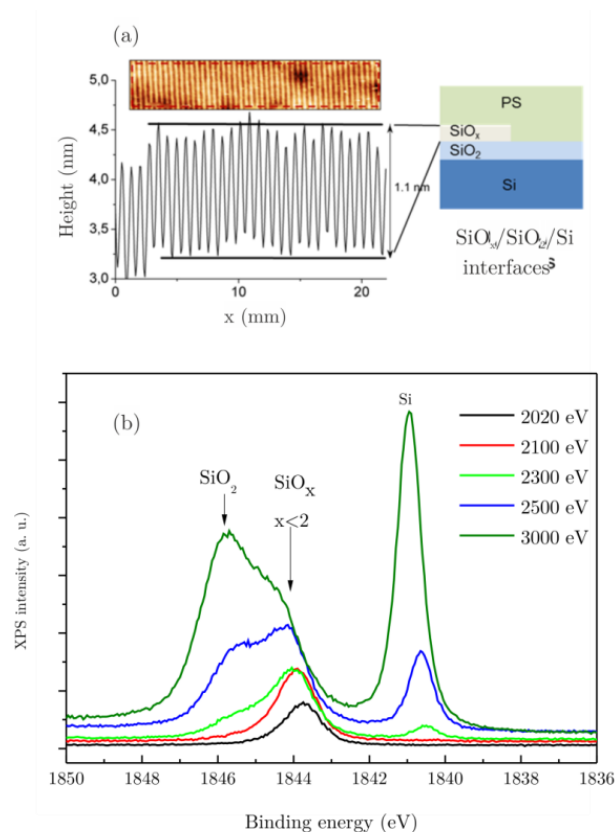


Figure 6.8. (a) AFM topography image and profile of the PS-OH brush surface after PON. A scheme is included showing the different regions and (b) HAXPES spectra of the Si 1s region at different incident energies

After characterizing these guiding patterns, it can be concluded that HAXPES using synchrotron radiation is a powerful spectroscopic tool to explore the chemical properties of surface and buried interfaces of brush layers for BCP DSA, since valuable information as a function of probing depth can be obtained.

Furthermore, it has been found that the choice of the accurate cooling down process after brush annealing is of paramount importance in order to obtain an optimal DSA result. HAXPES characterization shows an increase in intensity on the energy range corresponding to hydroxyl bonds when the brush is cooled down in the presence of oxygen. This is consistent with the change in the chemical affinity of the brush layer with the BCP experimentally observed in DSA.

With regard to the functionalization of the PS-OH brush layers, it has been proven that oxygen plasma exposure activates the brush layers by generating diverse carbon-oxygen bonding which promotes higher affinity to PMMA blocks while electron-beam exposure increases sp^2 bonding promoting higher affinity to PS blocks that might be explained by cross-linking of PS. In the case of parallel oxidation nanolithography, HAXPES provides experimental evidence of the existence of a sub-stoichiometric oxide between the brush layer and the SiO_2/Si substrate.

6.2. Block copolymer morphology and self-assembly characterization by GISAXS

GISAXS is a surface and sub-surface sensitive scattering technique which provides an accurate average structural information of as-received samples, with no need of sample manipulation.¹⁶ In this method, the incident beam is almost totally reflected from the substrate followed by small-angle scattering of the refracted beam by the sample substrate.¹⁷

This technique allows the investigation of surfaces with thicknesses down to the sub-monomolecular range, providing information about the size and shape of nanostructures, as well as about their distribution. On the other hand, GISAXS experiments of polymeric thin films are limited to the use of synchrotron radiation since the scattering cross section is weak in the X-ray regime as compared with metals, because of the low atomic mass involved.^{18,19}

The first examples in which GISAXS was used to characterize nanostructured films date from 1999, in which *Walter et al.* investigated the lateral structures of an ampholytic BCP, finding a good agreement with SPM measurements.²⁰ Since then, a large number of works analyzing the microphase separation in BCP have been reported^{21–23}, including those related with their use in microelectronics industry.²⁴ In this last example, *Ferrarese Lupi et al.* presented a work on high-aspect ratio PS-*b*-PMMA masks for lithographic applications.

The main advantages of GISAXS are that it is a non-destructive technique, and that the measurement is averaged on a large area. On the other hand, it can be used in different environment conditions (vacuum, air, gas atmospheres...). In addition, together with other parallel characterization techniques, it allows corroborating thin films structural information.

This is a technique which has to be used with synchrotron radiation and the obtained information has to be translated from the reciprocal to the real space. Furthermore, it is important to be aware of the radiation damage the sample can suffer, in order to avoid data which is contaminated by damage artifacts. On the other hand, due to the beam size, areas at the nanoscale are sometimes difficult to characterize.

6.2.1. Basis of grazing incidence X-ray technique

X-ray scattering of nanostructures shares the same principle as X-ray diffraction. In GISAXS, the incident X-ray vector is kept at a grazing angle. Due to the small angles used, scattering comes from variations of the mean electronic density, which is simplified by basically considering variations in refractive index.

The geometry employed on the technique gathers the main particularity of GISAXS. Figure 6.9 shows a schematic representation of the GISAXS geometry. The incident X-ray beam of wave vector \vec{k}_i , impinges the surface with a very small incident angle, α_i , (close to the angle of total reflection, α_c) with respect to the sample surface. Then, the scattered intensity of wave vector \vec{k}_f , which makes a scattering angle of Ψ with respect to \vec{k}_i and α_f with respect to the sample surface, is recorded with a two-dimensional (2D) detector. The sample-to-detector distances are normally between 2 and 5 m, and the values of the scattering vector, q , are in the range of 1 to 0.01 nm⁻¹ (features from 1 to hundreds of nanometers can be evaluated by GISAXS).

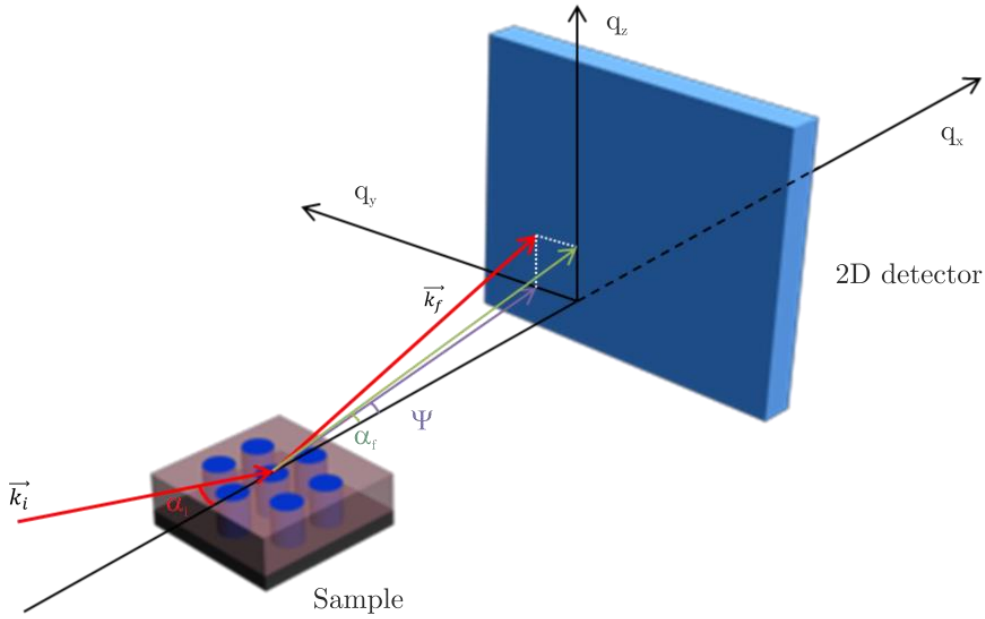


Figure 6.9. Schematic representation of GISAXS scattering geometry

The wave vector transfer, \vec{q} , is defined by the X-ray wavelength, λ , and related with the angular coordinates as described in equation (6.1):

$$\vec{q} = \vec{k}_f - \vec{k}_i = \frac{2\pi}{\lambda} \begin{pmatrix} \cos(\alpha_f) \cos(\psi) - \cos(\alpha_i) \\ \cos(\alpha_f) \sin(\psi) \\ \sin(\alpha_i) \sin(\alpha_f) \end{pmatrix}, \quad (6.1)$$

On the other hand, as previously mentioned, it is necessary to consider the effects of refraction at the surface since the incident angle, α_i , is very small.^{25,26} Scattering originates from variation on the refractive index, which for X-ray is defined by equation (6.2).

$$n = 1 - \delta - i\beta, \quad (6.2)$$

where δ and β represent the dispersion and absorption contributions, respectively.

Arising at the critical angle, α_c , of the polymer there is a characteristic peak called *Yoneda Peak*²⁷, in which the diffuse scattering depends on the material and it is observed at the position $\alpha_i + \alpha_c$ relative to the direct beam on the detector.

$$\alpha_c = \sqrt{2\delta}, \quad (6.3)$$

There is another important peak called *specular peak* which satisfies the condition $\alpha_i = \alpha_f$. This peak can become very intense and therefore, in order to protect the detector against such high intensity, the detector has to be shielded with a beam stopper.

The X-ray penetration depth, Λ , is defined as the depth at which X-ray intensity is attenuated by $1/e$. Therefore, by varying the incident angle, different structures through the film can be characterized. For $\alpha_i, \alpha_c < 1$ and $\alpha_i = \alpha_f$, the equation results in (6.4):

$$\Lambda = \frac{\lambda}{4\pi} \sqrt{\frac{2}{\sqrt{(\alpha_i^2 - \alpha_c^2)^2 + 4\beta^2} - (\alpha_i^2 - \alpha_c^2)}}, \quad (6.4)$$

Once the data has been collected, the data has to be reduced by translating the detector pixels into reciprocal q space. Regarding the data reduction, there are different developed tools which mainly convert to q space and allow line cuts.

Concerning data analysis, as observed in equation (6.1), the intensity distribution in reciprocal space is built as a function of α_i , α_f , and 2θ . Therefore, the analysis of the reciprocal space is typically analyzed within the framework of kinematical approximations, such as the distorted-wave Born approximation (DWBA).^{28,29} An analysis using DWBA results much more complex than the analysis of transmission data, but the basic concepts, form factor, $F(q)$, and structure factor, $S(q)$, are used as well.

6.2.2. Block copolymer self-assembly GISAXS characterization

The morphology of different BCP systems has been analyzed by GISAXS in order to get statistical information about the BCP size and spatial distribution.³⁰⁻³²

The experiments have been performed on the Austrian SAXS beamline at the *Elettra Sincrotrone Trieste* in Italy using a photon energy of 8.05 keV ($\lambda=0.154$ nm). The beam size at the sample position was 200 μm high and 1000 μm wide. Wide strips were used in front of the detector in order to stop the specular beam. All the GISAXS experiments have been performed at incident angles between 0.15° and 0.4° in order to have a wide exploratory analysis angle range.

On the other hand, the 0.15° angle was chosen because it is between the critical angle of the polymer film (0.12°) and that of silicon (0.163°). The scattered intensities have been

recorded with a *Pilatus 1M* detector ($981 \cdot 1043$ pixels of $172 \mu\text{m}^2$ size per pixel) mounted on the SAXS bench at a distance of 1877.824 mm from the sample.

6.2.3. Static GISAXS studies on block copolymer films

The analyzed samples are depicted in Table 6.1. PS-*b*-PMMA samples with different morphologies and molecular weights, as well as the high- χ systems studied in *chapter 5* have been characterized by GISAXS. All the samples have been prepared on $1 \times 1 \text{ cm}^2$ chips bearing a native silicon oxide layer (p-type silicon wafers of $4\text{-}40 \Omega \cdot \text{cm}$ resistivity). Then, in order to obtain the BCP perpendicular morphology, the corresponding brush is spin-coated on the top of the substrate (see Table 6.1).

After having removed the non-reacted brush, the BCP is deposited and annealed to promote its self-assembly. SEM images showing the morphology of the different analyzed BCP samples, taken before GISAXS measurements, are shown in Figure 6.10.

Table 6.1. BCP samples characterized by GISAXS

Sample	Brush	Specifications
PS- <i>b</i> -PMMA	PS _{60%} - <i>r</i> -PMMA	Lamellar
		Lamellar
		Lamellar
	PS _{70%} - <i>r</i> -PMMA	Cylindrical
PS- <i>b</i> -PLA	PS _{48%} - <i>r</i> -PMMA	Lamellar
PLA- <i>b</i> -PDMS- <i>b</i> -PLA	PS _{60%} - <i>r</i> -PMMA + PDMS-OH	Lamellar

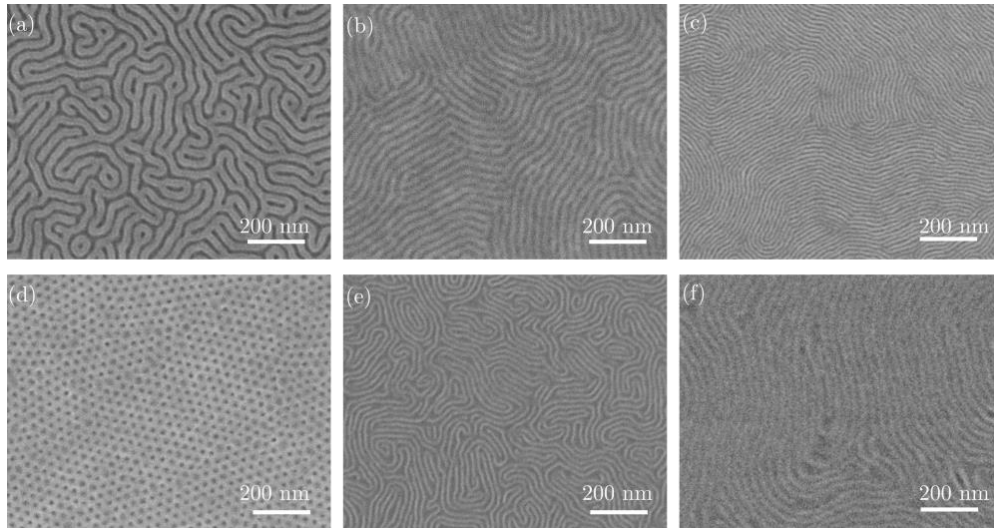


Figure 6.10. SEM images of lamellar PS-*b*-PMMA with (a) $L_0=38 \text{ nm}$, (b) $L_0=28 \text{ nm}$, (c) $L_0=22 \text{ nm}$, (d) cylindrical PS-*b*-PMMA with $L_0=35 \text{ nm}$, (e) lamellar PS-*b*-PLA, and (f) lamellar PLA-*b*-PDMS-*b*-PLA

GISAXS patterns are obtained by following the procedure depicted in Figure 6.11. The image represents the GISAXS detector pixels x and y , in the corresponding axis. Then, the

intensity patterns are obtained by making an horizontal cut of 30 pixels thick in 267 pixel, and translating it into the q space. This pixel corresponds to an angle $\alpha_t = 0.193^\circ$ and $q_z = 0.03 \text{ nm}^{-1}$.

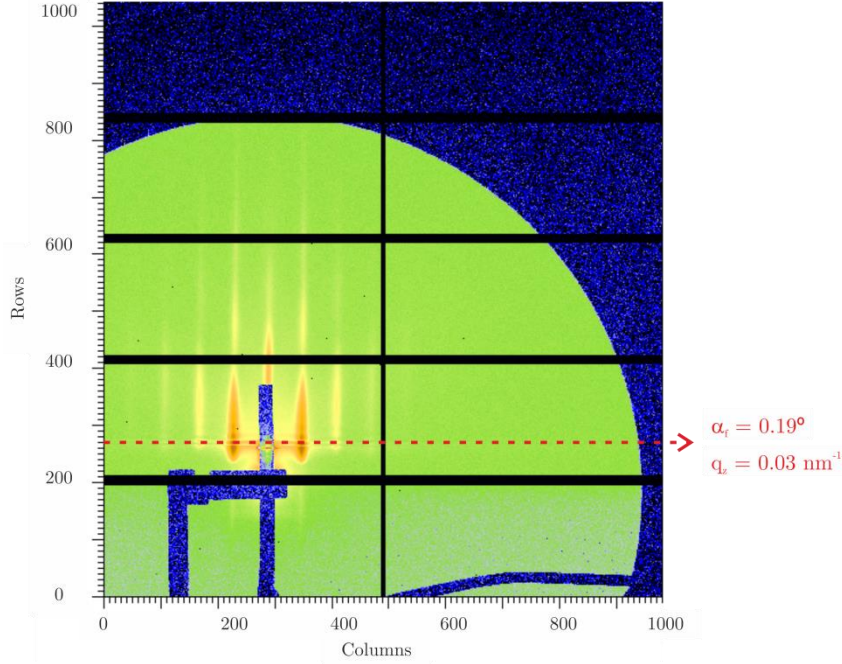


Figure 6.11. Scheme of a GISAXS pattern showing all GISAXS detector sectors. The cuts are performed in the sector in which the center of the reflected beam is located

Figure 6.12 shows the SEM images of the lamellar ($L_0 = 38 \text{ nm}$) and cylindrical PS-*b*-PMMA, and the corresponding GISAXS patterns. Since GISAXS transforms structural parameters in real space into the reciprocal space, the vertical rods are directly related with the d-spacing of the BCP.

For a lamellar and cylindrical BCP, it is related by equations (6.5) and (6.6), respectively.

$$L_0 = \frac{2\pi}{q}, \quad (6.5)$$

$$L_0 = \frac{4\pi}{\sqrt{3}q}, \quad (6.6)$$

For lamellar ($L_0 = 38 \text{ nm}$) and cylindrical BCPs, vertical rods (10 Bragg rod) are equally spaced at an interval of $\Delta q = 0.166$ and 0.203 nm^{-1} , respectively. The corresponding real-space period is thus, 38.27 and 36.01 nm, respectively, which is in agreement with previous SEM measurements.

The L_0 measurements for the other BCP systems, as well as a comparison with the pitch measurement extracted from SEM, are depicted in Table 6.2. The difference between the SEM and GISAXS measurements for the cylindrical BCP is attributed to the change of the PS matrix under the high electron beam inducing its cross-linking.³³

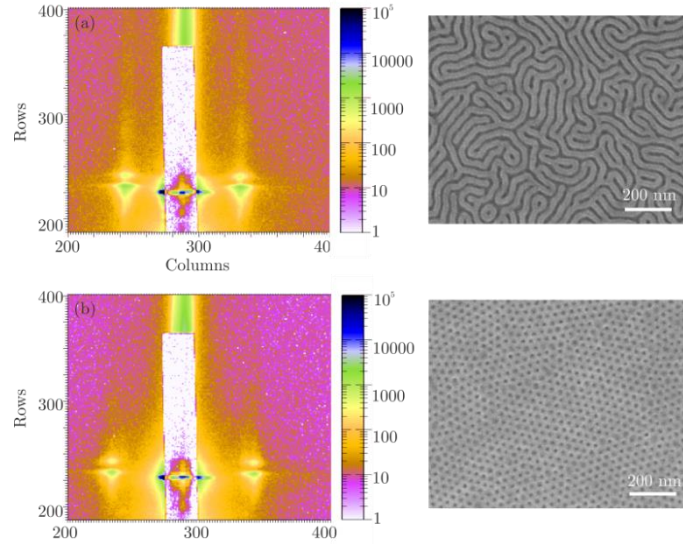


Figure 6.12. GISAXS patterns and SEM images of (a) lamellar and (b) cylindrical PS-*b*-PMMA samples before removing PMMA

Table 6.2. BCP samples characterized by GISAXS

Sample	SEM pitch	GISAXS Pitch	GISAXS Pitch after PMMA etching
PS-<i>b</i>-PMMA	38 nm	38.27 nm	38.70 nm
	28 nm	28.06 nm	28.06 nm
	22.5 nm	23.07 nm	23.06 nm
	35 nm	36.01 nm	36.01 nm
PS-<i>b</i>-PLA	19.5 nm	19.09 nm	-
PLA-<i>b</i>-PDMS-<i>b</i>-PLA	30 nm	29.52 nm	-

On the other hand, in order to have more contrast and get information in the film volume, these samples have been compared with those in which the PMMA domains have been previously removed by exposing the samples to a brief dose of oxygen plasma. Figure 6.13 and Figure 6.14 show the GISAXS patterns and their intensity profiles along the 10 Bragg rod, for the lamellar and cylindrical PS-*b*-PMMA. From the GISAXS patterns of Figure 6.13 it can be seen that there is higher electronic density contrast between PS and PMMA, as compared with the ones in Figure 6.12, due to the PMMA removal. This allows not only the measurement of the 10 Bragg rod, but also of higher order rods.

On the one hand, it is observed that the 10 Bragg position stays unchanged after the PMMA removal (see Table 6.2). On the other, in contrast with Figure 6.14.a, Figure 6.14.b shows the characteristic positions of the 2D hexagonal arrays, representative from the perpendicular oriented cylindrical phase. These peaks are indexed as the (h,k) reflections of a two-dimensional hexagonal lattice (equation (6.7)), and the results obtained are in well agreement with the ones reported in the literature.^{34,35}

$$q = \frac{4\pi\sqrt{h^2+hk+k^2}}{\sqrt{3}L_0}, \quad (6.7)$$

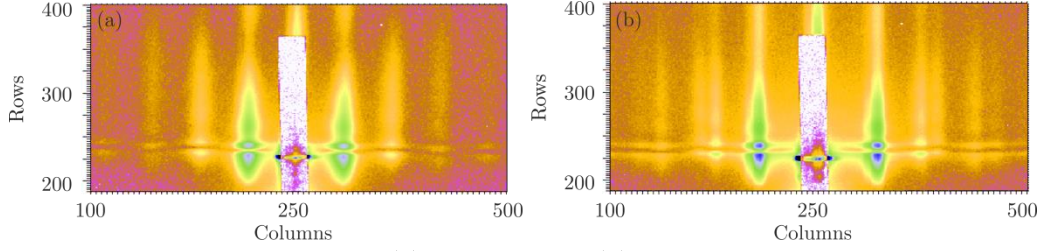


Figure 6.13. GISAXS patterns of (a) lamellar and (b) cylindrical PS-*b*-PMMA samples after removing PMMA by oxygen plasma exposure

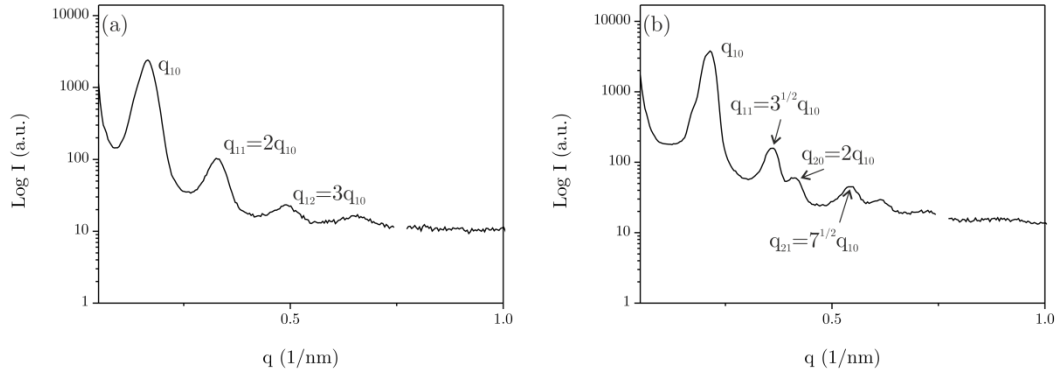


Figure 6.14. GISAXS intensity profile along the 10 Bragg rod for (a) lamellar ($L_0 = 38$ nm) and (b) cylindrical PS-*b*-PMMA

Regarding the high- χ samples, the same analysis procedure described above has been followed. Figure 6.15 shows the GISAXS intensity profiles for PS-*b*-PLA and PLA-*b*-PDMS-*b*-PLA samples. As it is observed, there is enough contrast between the domains to see a sharp primary peak in both cases. Furthermore, for the PLA-*b*-PDMS-*b*-PLA sample the appearance of a higher order rod is observed (Figure 6.15.b).

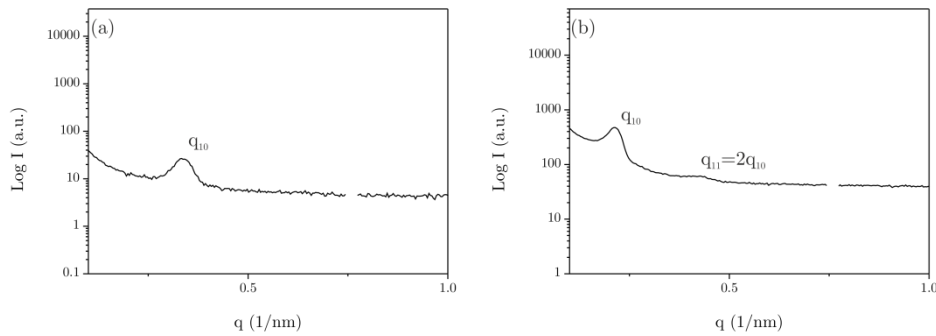


Figure 6.15. GISAXS intensity profile along the 10 Bragg rod for lamellar high- χ (a) PS-*b*-PLA and (b) PLA-*b*-PDMS-*b*-PLA

6.3. Summary and conclusions

In summary, two different techniques to further characterize BCP films and their interactions with the substrate have been presented.

With regard to guiding pattern characterization, it has been demonstrated that HAXPES using synchrotron radiation is a powerful technique to explore the chemical properties of surface and buried interfaces in the DSA process.

The different interactions which take place on the chemically modified guided patterns have been characterized. On the one hand, when the brush is functionalized by using exposure under oxygen, the plasma activates the brush by generating diverse C-O bonding promoting higher affinity to PMMA blocks. On the other hand, when the polymer surface is exposed to direct electron beam exposure, it cross-links as reflected in the increase of sp^2 bonding. In the case of parallel oxidation nanolithography, HAXPES provides experimental evidence of the existence of a sub-stoichiometric oxide between the brush layer and the SiO_2/Si substrate.

Concerning the analysis of BCP films, GISAXS measurements have allowed a well-defined structure characterization of lamellar and cylindrical BCPs. Furthermore, it has been demonstrated the different profiles between lamellar and cylindrical perpendicular oriented BCPs, by selectively removing one of the domains.

6.4. References

1. Wolfgang Drube. Recent advances in Hard X-ray Photoelectron Spectroscopy (HAXPES). *J. Electron Spectros. Relat. Phenomena* **190**, 125–314 (2013).
2. Felicissimo, M. P. *et al.* Determination of vertical phase separation in a polyfluorene copolymer: fullerene derivative solar cell blend by X-ray photoelectron spectroscopy. *J. Mater. Chem.* **19**, 4899–4901 (2009).
3. Subías, G., *et al.* Characterization of the anion-ordering transition in (TMTTF) 2 ReO₄ by x-ray absorption and photoemission spectroscopies. *Phys. Rev. B - Condens. Matter Mater. Phys.* **76**, 1–7 (2007).
4. Fraxedas, J. *et al.* Modulation of surface charge transfer through competing long-range repulsive versus short-range attractive interactions. *J. Phys. Chem. C* **115**, 18640–18648 (2011).
5. Schaefer, F., *et al.* KMC-1: A high resolution and high flux soft x-ray beamline at BESSY. *Rev. Sci. Instrum.* **78**, 1–14 (2007).
6. Gorgoi, M. *et al.* The high kinetic energy photoelectron spectroscopy facility at BESSY progress and first results. *Nucl. Instruments Methods Phys. Res. Sect. A Accel. Spectrometers, Detect. Assoc. Equip.* **601**, 48–53 (2009).
7. Way, W. K., *et al.* Polystyrene by XPS. *Surf. Sci. Spectra* **2**, 67 (1993).
8. Rosencrance, S. W., *et al.* Polymethylmethacrylate by XPS. *Surf. Sci. Spectra* **2**, 71–75 (1993).
9. Evangelio, L. *et al.* Creation of guiding patterns for directed self-assembly of block copolymers by resistless direct e-beam exposure. *J. Micro/Nanolith. MEMS MOEMS*. **14**, 33511 (2015).
10. Fernández-Regúlez, M., Evangelio, L., *et al.* F. Sub-10 nm Resistless Nanolithography for Directed Self-Assembly of Block Copolymers. *ACS Appl. Mater. Interfaces* **6**, 21596–21602 (2014).
11. Albonetti, C. *et al.* Parallel-local anodic oxidation of silicon surfaces by soft stamps. *Nanotechnology* **19**, 435303 (2008).
12. Varlot, K., Martin, J. M. *et al.* Physical and chemical changes in polystyrene during electron irradiation using EELS in the TEM: Contribution of the dielectric function. *J. Microsc.* **191**, 187–194 (1998).
13. Massey, S., *et al.* Chemical Modification of Polystyrene by Low-Energy (<100 eV) Electron Irradiation Studied by Mass Spectrometry. *J. Appl. Polym. Sci.* **108**, 3163–3168 (2008).
14. Klauser, R. *et al.* Oxidation states in scanning-probe-induced Si[₃]N[₄] to

- SiO_x conversion studied by scanning photoemission microscopy. *Appl. Phys. Lett.* **79**, 3143 (2001).
15. Lazzarino, M. *et al.* Atomic force microscope anodic oxidation studied by spectroscopic microscopy. *Appl. Phys. Lett.* **81**, 2842 (2002).
 16. Smilgies, D. M., *et al.* Characterization of Polymer Thin Films with Small-Angle X-ray Scattering under Grazing Incidence (GISAXS). *Synchrotron Radiat. News* **15**, (2002).
 17. Levine, J. R., *et al.* Grazing-incidence small-angle X-ray scattering: new tool for studying thin film growth. *J. Appl. Crystallogr.* **22**, 528–532 (1989).
 18. Müller-Buschbaum, P. *et al.* Determination of micrometer length scales with an X-ray reflection ultra small-angle scattering set-up. *EPL (Europhysics Lett.)* **42**, 517 (1998).
 19. Smilgies, D. M., *et al.* Characterization of Polymer Thin Films with Small-Angle X-ray Scattering under Grazing Incidence (GISAXS). *Synchrotron Radiat. News* **15**, (2002).
 20. Walter, H. *et al.* Lateral structures of thin films of ampholytic diblock copolymers absorbed from dilute aqueous solution at the solid/liquid interface. *Langmuir* **15**, 6984–6990 (1999).
 21. Daillant, J., *et al.* Grazing incidence surface scattering of X-rays. *J. Chem. Soc., Faraday Trans.* **92**, 505–513 (1996).
 22. Müller-Buschbaum, P. *et al.* Correlated Roughness, Long-Range Correlations, and Dewetting of Thin Polymer Films. *Macromolecules* **31**, 3686–3692 (1998).
 23. Xu, T. *et al.* Scattering Study on the Selective Solvent Swelling Induced Surface Reconstruction. *Macromolecules* **37**, 2972–2977 (2004).
 24. Ferrarese Lupi, F. *et al.* High Aspect Ratio PS-b-PMMA Block Copolymer Masks for Lithographic Applications. *ACS Appl. Mater. Interfaces* **6**, 21389–21396 (2014).
 25. Jackson, J. D. *Classical Electrodynamics*. (John Wiley and Sons, 1999).
 26. Peng, Q., *et al.* Nanoscopic patterned materials with tunable dimensions via atomic layer deposition on block copolymers. *Adv. Mater.* **22**, 5129–5133 (2010).
 27. Yoneda, Y. Anomalous Surface Reflection of X Rays. *Phys. Rev.* **131**, 2010–2013 (1963).
 28. Sinha, S. K., *et al.* X-ray and neutron scattering from rough surfaces. *Phys. Rev. B* **38**, 2297–2311 (1988).

29. Baumbach, G. T., *et al.* The influence of specular interface reflection on grazing incidence X-ray diffraction and diffuse scattering from superlattices. *Phys. B Condens. Matter* **198**, 249–252 (1994).
30. Smilgies, D., *et al.* Characterization of polymer thin films with small-angle X-ray scattering under grazing incidence (GISAXS). *Synchrotron Radiat. News* **15**, 35–42 (2002).
31. Busch, P., *et al.* Structure of Thin Films of Lamellar Poly(styrene-*b*-butadiene) Diblock Copolymers As Revealed by Grazing-Incidence Small-Angle Scattering. *Macromolecules* **40**, 630–640 (2007).
32. Hexemer, A. *et al.* Advanced grazing-incidence techniques for modern soft-matter materials analysis. *IUCrJ* **2**, 106–125 (2015).
33. Freychet, G. *et al.* Removal of poly(methyl methacrylate) in diblock copolymers films studied by grazing incidence small-angle X-ray scattering. *J. Polym. Sci. Part B Polym. Phys.* **54**, 1137–1144 (2016).
34. Ferrarese Lupi, F. *et al.* High Aspect Ratio PS-*b*-PMMA Block Copolymer Masks for Lithographic Applications. *ACS Appl. Mater. Interfaces* **6**, 21389–21396 (2014).
35. Fleury, G. *et al.* Development and integration of systems with enhanced resolutions based on Si-containing block copolymers for line space applications. **9425**, 94250Z (2015).

Chapter 7

Pattern transfer of block copolymers and application in device fabrication

The nanoscale BCP mask features formed on the substrate after self-assembly present very poor contrast etching and are easily damaged after plasma processing. Therefore, an accurate pattern transfer method is required.

This chapter introduces a method based on the use of atomic layer deposition (ALD) to enhance the etching contrast between PS and PMMA, and thus perform the pattern transfer of the features into the substrate. It has been characterized by Peak Force tapping AFM which has made possible to access the local mechanical properties of single BCP domains.

On the other hand, the application of BCP DSA in microelectronics is presented, with the fabrication of a novel nanomechanical resonator made by graphoepitaxy and infiltrated material by ALD.

7.1. Conventional atomic layer deposition

7.1.1. Introduction

Atomic layer deposition (ALD) is a vapor phase deposition technique which can produce thin, highly uniform and conformal films of a variety of materials. It is based on sequential, self-limiting and surface controlled vapor phase reactions capable of achieving a control on the film growth at the nanometer or sub-nanometer scale.^{1,2} The film formation mechanism consists of consecutive atomic layers grown from the surface at relatively low temperatures.

The number of ALD applications has been significantly increased over the past few years, especially due to the constantly decrease of the IC device size. ALD is a very suitable method for the fabrication of nanostructures with high aspect ratio, because it offers functional material layers with high quality, uniformity and conformality.³ On the other hand, ALD has been also used for biomedical applications, for the creation of biomedical coatings, and for optical sensors.⁴

In contrast to chemical vapor deposition (CVD), the precursors are not injected simultaneously in the reactor; they are instead inserted as a series of sequential pulses. In each pulse, the precursor reacts with the surface until the reaction is completed. Therefore, the amount of material deposited on a surface depends on the interactions between the precursor and the surface.⁵

The ALD surface reaction mechanisms are depicted in Figure 7.1, and as observed, it consists on the sequential use of self-terminating gas-solid reactions. The following 4-steps are involved: (i) the first precursor (A, red) is introduced in the chamber, and it reacts with the reactive sites of the surface until they are consumed, (ii) the remaining reactant molecules and the secondary reaction products are evacuated, (iii) the second precursor (B, green) is inserted into the reactor, and after the reaction (iv) the chamber is purged. This mechanism represents one ALD cycle, and in each reaction cycle a certain amount of material to the surface is added, until the desired thickness is achieved.

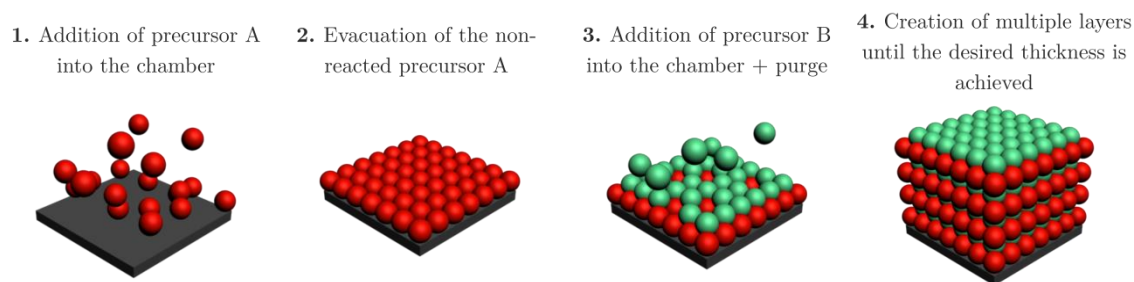


Figure 7.1. ALD surface reaction mechanism

ALD processes have been developed for a wide range of inorganic materials, like oxides, nitrides, sulphides, selenides and others.⁵ However, among all the processes published in the literature, the synthesis of Al_2O_3 from trimethylaluminum (TMA) and water is the mostly known. The reactants are very reactive and thermally stable, which means that the self-limited growth of alumina can be achieved in a wide range of temperatures.⁵

The reaction mechanism sequence is described in Figure 7.2. First the TMA precursor chemisorbs on the substrate reacting with the adsorbed hydroxyl groups, until the surface is passivated (TMA does not react with itself, thus the reaction leads to one layer). Next, the non-reacted precursor and the secondary products (CH_4) are pumped out of the chamber, normally by using argon or nitrogen as purge gases, leaving a surface covered with AlCH_3 groups (reaction (7.2)). Afterwards, the water vapor is pulsed into the chamber and reacts with the methyl groups of the surface forming Al-O bridges and hydroxyl surface groups. Finally, the chamber is purged with argon or nitrogen, and the secondary products are pumped away (reaction (7.3)). The overall stoichiometry reaction is (7.1), and it is often described by two half-reactions (7.2) and (7.3).

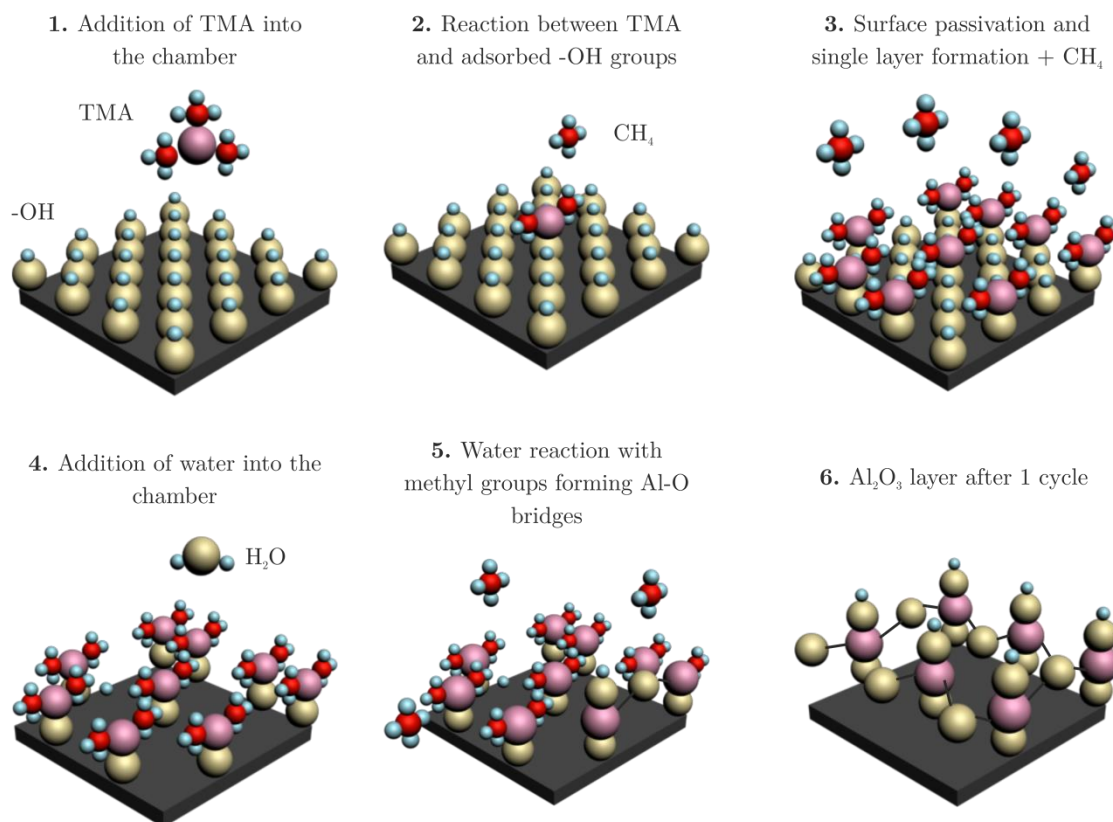
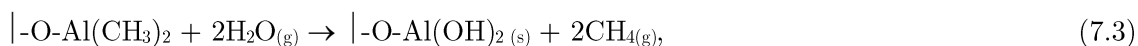
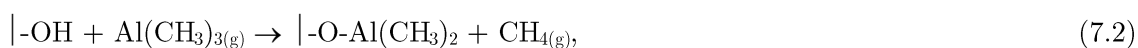


Figure 7.2. Al_2O_3 reaction mechanism sequence

When ALD is used with polymer surfaces, it has been demonstrated that precursors can infiltrate and react to modify significantly their mechanical properties.⁶ In particular, PMMA presents a characteristic bonding structure (hydroxyl and carbonyl) which allows the ALD film nucleation and growth. A possible mechanism for the reaction between TMA and PMMA is presented in Figure 7.3. The PMMA carbonyl groups react with the TMA molecules forming an acetal group by transferring the methyl to the carbon. Then, the water, reforms the carbonyl not in the ester form but in the ketone form.

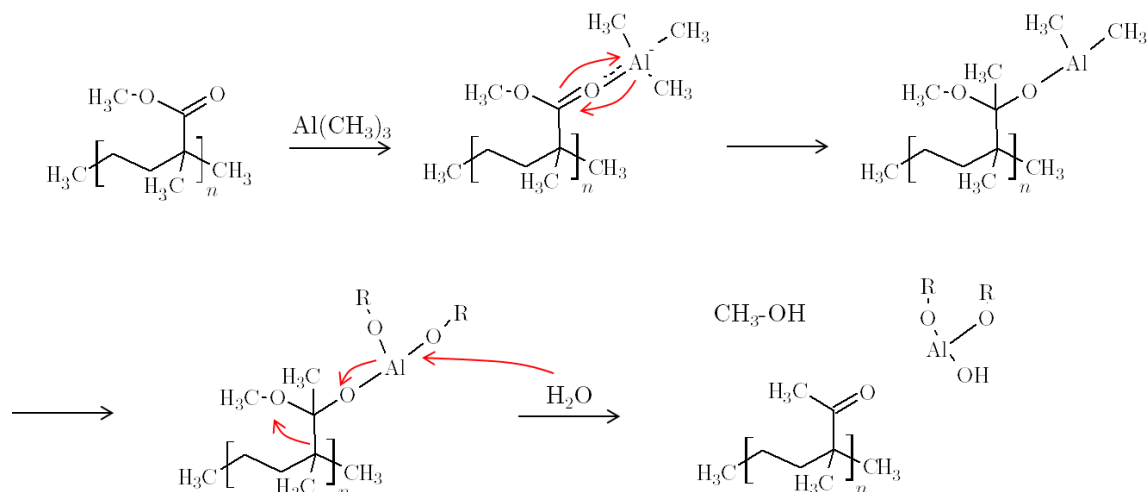


Figure 7.3. Possible mechanism for the reaction between TMA (Lewis acid) and PMMA carbonyl groups (Lewis base), followed by the reaction with water (R denotes PMMA)⁶

The ability of controlling the reactions between the precursors and polymers, is being used on the field of BCP DSA, to enhance the etching BCP properties, by selectively depositing the material in only one of the domains.^{6,7}

7.1.2. Use of atomic layer deposition for block copolymer pattern transfer

To take advantage of the nanostructures offered by BCP DSA, accurate pattern transfer techniques are needed. Normally, to enhance the etch resistance of the BCP film to oxygen plasma, the pattern is transferred to an intermediate hard mask layer.^{8,9} However, in order to avoid the complication on the fabrication process and the associated additional costs, selective deposition by means of ALD is used.¹⁰⁻¹²

The ALD technique provides a powerful nanofabrication technique for BCP DSA pattern transfer, since it enhances the etching contrast between BCP domains, and thus allows obtaining high-aspect ratio nanostructures. ALD organometallic precursors exhibit higher chemical affinity to one of the domains, thus allowing the selective deposition on one of the blocks. The etching contrast between domains is enhanced because for each cycle, there is a selective deposition by ALD, which produces a selective growth of material on top of the preferential domain.

The use of ALD has been performed with TMA precursor and water, to selectively grow Al_2O_3 on top of PMMA domains of a PS-*b*-PMMA BCP. As discussed in the previous section, it has been reported that Al_2O_3 is selectively deposited on PS-*b*-PMMA BCP samples, due to the preferential chemical interactions between the TMA molecules and the carbonyl moieties along the PMMA chains.^{11–14}

7.1.2.1. Materials and methods

The ALD process has been performed on self-assembled PS-*b*-PMMA samples, as depicted in Figure 7.4. The whole process consists of 5-steps: (i) PS-*b*-PMMA self-assembly, (ii) selective alumina deposition on PMMA domains, (iii) PS removal, (iv) silicon etching and (vi) ALD mask removal.

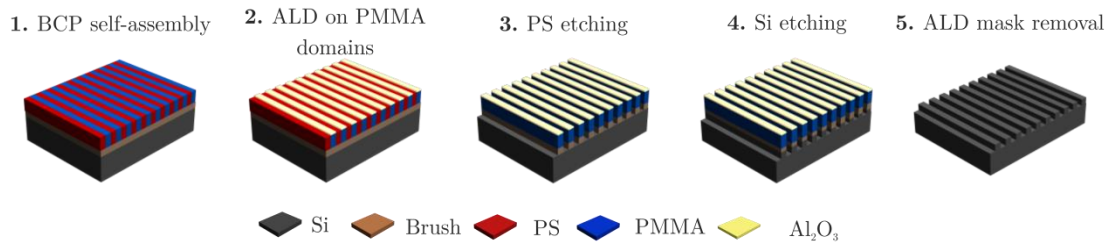


Figure 7.4. Schematic of ALD on PMMA domains of PS-*b*-PMMA sample

After the PS-*b*-PMMA ($L_0 = 28$ nm) BCP is self-assembled, Al_2O_3 is selectively deposited on top of PMMA domains by using five ALD cycles. The ALD process has been performed in a *Savannah* equipment from *Cambridge Nanotech*.

The alumina is synthesized using binary reactions of TMA (*Aldrich*, 97%) and water within the polymer films. The deposition is performed at 85°C as follows: first, the chamber is stabilized with nitrogen for 10 min. Then, the precursor, TMA, is admitted into the reactor for 60 s. Afterwards, the chamber is purged with nitrogen for further 60 s, and the water is admitted in the reactor for 60 s. Finally, this sequence is repeated for five cycles.

7.1.2.2. PS-*b*-PMMA pattern transfer results

After PS-*b*-PMMA self-assembly, the alumina is deposited on top of the material for five cycles, and the obtained results are shown in Figure 7.5.

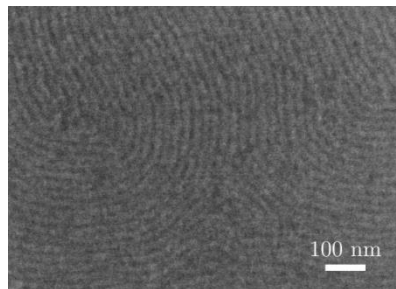


Figure 7.5. SEM image of PS-*b*-PMMA self-assembly after five cycles of ALD deposition

After selectively depositing the alumina on PMMA domains, an oxygen plasma exposure at 300W and 50 sccm of oxygen flow is performed to remove the PS domains (Step 3 of Figure 7.4). The PS etching has been studied for different times, and the obtained results are shown in Figure 7.6. As observed, the higher the etching time, the more damaged the BCP structure is. From the SEM images it is observed that the optimal etching time is 5 s. Nevertheless, the hard mask used to transfer into the silicon would not withstand the etching, since it is easily damaged when exposing to slightly higher times of oxygen plasma.

This occurs because the alumina is only deposited on the top of PMMA domains, but it is not infiltrated through the whole domain. Therefore, when exposing the sample to oxygen plasma, the PS domains start to be removed because the PMMA is protected by the alumina (step 2 of Figure 7.7). Afterwards, as the PMMA domains are not protected by the alumina in the edges but only on the top, they also start to be etched. Consequently, as the PMMA etching speed is faster than for PS, the whole PMMA domains (now not protected by the alumina) are removed (step 3 of Figure 7.7), and only a thin PS layer remains on the surface (step 4 of Figure 7.7).

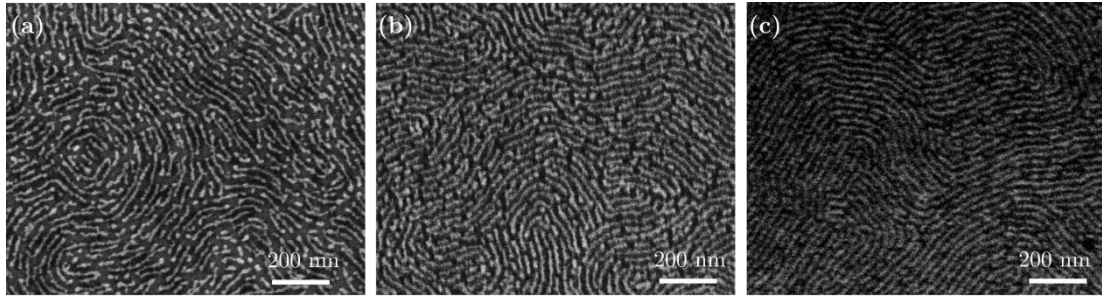


Figure 7.6. SEM image of PS-*b*-PMMA self-assembly after three cycles of ALD deposition and oxygen plasma exposure for (a) 60 s, (b) 30 s and (c) 5 s etching times

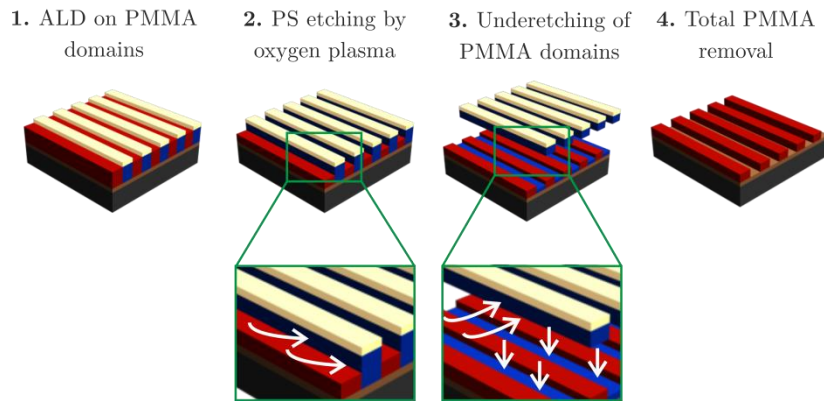


Figure 7.7. Schematic representation of the PS etching process during oxygen plasma exposure

7.2. Sequential Infiltration Synthesis

7.2.1. Introduction

SIS offers an alternative ALD mechanism which allows the infiltration of the precursors into the polymer.^{7,10–12,15,16} On the BCP field, it is used to selectively infiltrate one BCP domain, and use this protective component as a hard mask to pattern transfer.

Moreover, the thermal budget of SIS is low and it shares the same conventional ALD reaction mechanism. However, whereas ALD implies surface reactions, SIS uses functional moieties within the bulk of the polymer. As a consequence, when samples are exposed to SIS conditions, not only the polymer top domains are covered but the whole polymer domains are infiltrated, resulting in an improvement of resist hardness.

7.2.2. Use of sequential infiltration synthesis for pattern transfer

As observed in the previous section, the conventional ALD mechanism does not protect the whole PMMA domains and therefore, it cannot act as a hard mask for pattern transfer since it is under-etched after some seconds of oxygen plasma exposure. As an alternative solution SIS, which has been demonstrated to lead to high-aspect-ratio features in a substrate, is used.^{7,11,12,16–18}

It has been reported that the mechanism which takes place during the reaction between TMA and PMMA in the SIS process involves two-step reaction.¹² In the first step (7.4), TMA reacts with the carbonyl groups of PMMA and form a physisorbed complex ($\text{C=O} \cdots \text{Al}(\text{CH}_3)_3$), which slowly reacts to form a permanent O-Al bond (7.5).



It has been found out that TMA purge times are crucial for the infiltration process, since longer purge times reduces the SIS growth. On the other hand, longer TMA exposure times, enhance the alumina formation, since the intermediate complex concentration is maintained, and it allows the slow reaction of the chemisorbed species.^{11,12}

7.2.2.1. Materials and methods

The overall process describing the SIS mechanism is shown in Figure 7.8. As observed, it has the same processing steps as the one described for the conventional ALD deposition (Figure 7.4).

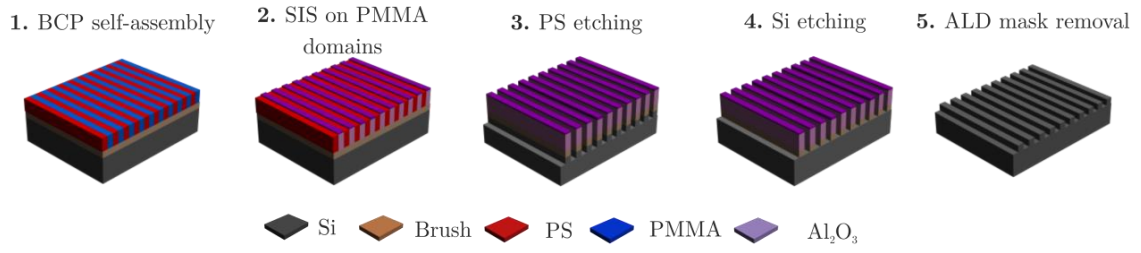


Figure 7.8. Schematic of SIS on PMMA domains of PS-*b*-PMMA sample

After PS-*b*-PMMA self-assembly, the SIS is performed in the same ALD equipment, but by varying the processing conditions in order to induce the diffusion of the alumina into the PMMA domains.

The infiltration is performed at 85°C as follows: first, the chamber is purged and the TMA is admitted at a $P=0.5$ torr for 80 s. Then, the non-reacted gases are evacuated with nitrogen for 30 s, and the water is introduced into the chamber for further 80 s. Finally, the chamber is purged for 30 s. This sequence is then repeated for several cycles.

The main differences between conventional ALD and SIS, are the pressure reached inside the chamber after the precursor admission, the time the precursor is inside the chamber, and the purge time. It has been reported that in order to obtain an optimal SIS process, it is recommended to work at higher pressures and shorter purge times.^{10,16}

7.2.2.2. PS-*b*-PMMA pattern transfer results

After trying the optimal SIS conditions on a self-assembled PS-*b*-PMMA sample, it was found that the optimal number of cycles when using these conditions was 5. Figure 7.9 shows PS-*b*-PMMA self-assembly SEM images before and after SIS, for a lamellar ($L_0 = 38$ nm) and a cylindrical ($L_0 = 35$ nm) BCP.

As observed in the images, the infiltration is performed on the PMMA domains, as better revealed on the cylindrical SEM images. The cylindrical BCP has a PS/PMMA composition of 60:40, so that the BCP morphology consists of PMMA cylinders immersed in a PS matrix. In Figure 7.9.b it is observed that the cylinders (PMMA domains) exhibit higher contrast compared with Figure 7.9.a, due to the alumina infiltration.

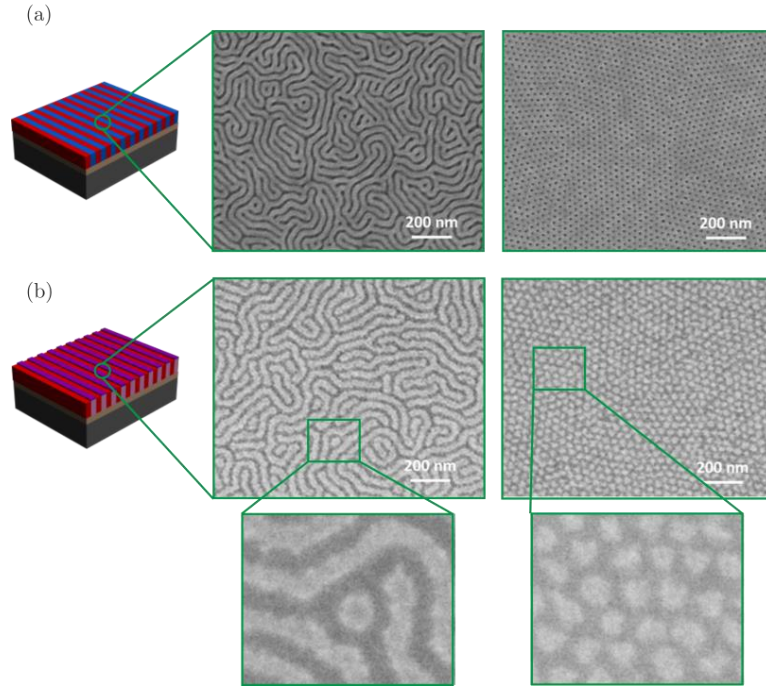


Figure 7.9. SEM images of lamellar ($L_0 = 38$ nm) and cylindrical ($L_0 = 35$ nm) BCP (a) before and (b) after 5 cycles of SIS

In order to explore the degree of infiltration in the PMMA domains, the samples have been exposed to oxygen plasma at 300W with a 50 sccm oxygen flow, for 18 s to etch the PS block. Afterwards, it has been performed a silicon etching by using the conditions depicted on Table 7.1 for 60 s to etch 15 nm silicon.

Table 7.1. Silicon etching conditions for PS-*b*-PMMA pattern transfer

[SF ₆]	20 sccm
[C ₄ F ₈]	30 sccm
Power Source	220 W
Chuck Power	20 W
Time	60 s
Pressure	2 Pa
Temperature	20°C
Silicon etched	15 nm

Figure 7.10 and Figure 7.11 show top-view and cross-section SEM images, respectively, of the PS-*b*-PMMA silicon pattern transfer, after being removed the infiltrated PMMA hard mask. As observed from the images, the features have been successfully transferred to the substrate, thus demonstrating the viability of the method to obtain high-aspect ratio nanostructures. There has been performed an EDX characterization, and the presence of alumina has not been detected. However, since the alumina mask is hard to remove by oxygen plasma, a thin alumina layer can remain on top of etched silicon.

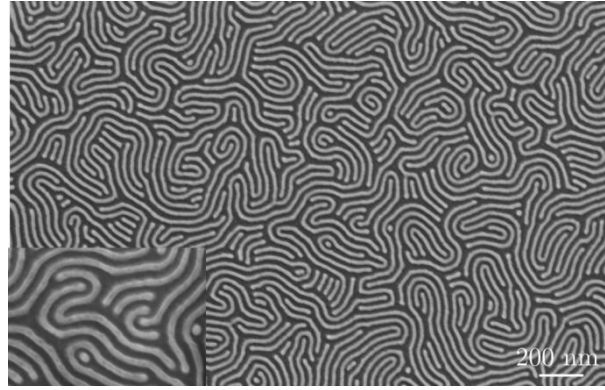


Figure 7.10. SEM image of lamellar ($L_0 = 38$ nm) BCP after pattern transfer the features into the silicon by using an infiltrated PMMA mask

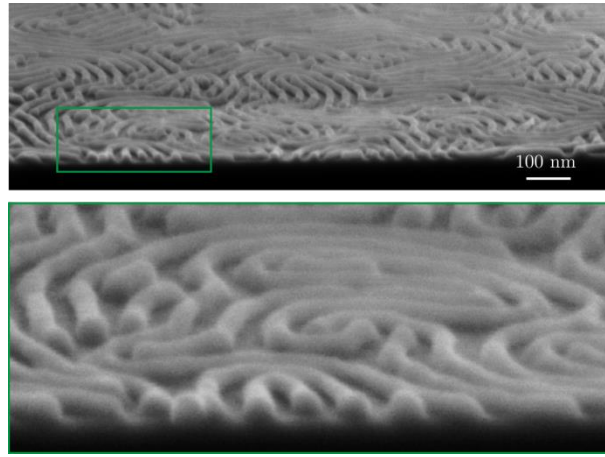


Figure 7.11. Cross-section SEM image of lamellar ($L_0 = 38$ nm) BCP after pattern transfer the features into the silicon by using an infiltrated PMMA mask. The lower image corresponds to the zoomed part region (green) of the image above

7.2.2.3. High- χ block copolymers pattern transfer results

In order to demonstrate the applicability of the SIS process to other material systems, the procedure depicted in Figure 7.8 has been tried on two high- χ systems: PS-*b*-PLA and poly(1,1-dimethyl silacyclo-butane)-*b*-poly(methyl methacrylate) (PDMSB-*b*-PMMA).

PDMSB-*b*-PMMA samples have been provided by LCPO, and it consists of a cylindrical BCP where PMMA cylinders are immersed in a PDMSB matrix. Figure 7.12 shows the PDMSB-*b*-PMMA self-assembly after SIS and PS etching, and it is observed that after the process the PMMA cylinders have been infiltrated as the ones for PS-*b*-PMMA in Figure 7.9.b.

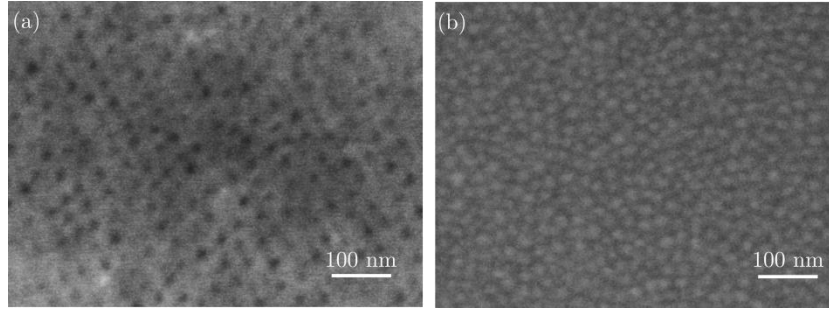


Figure 7.12. SEM images of PDMSB-*b*-PMMA self-assembly (a) before and (b) after SIS and PS etching

On the other hand, the SIS process has been used for PS-*b*-PLA, where the selective infiltration takes place with the PLA block in a similar mechanism as the PMMA does, due to the carbonyl groups present on the PLA molecular structure. As observed in Figure 7.13.b, after an oxygen plasma etching, the PS domains are etched away, and the PLA infiltrated mask resists, allowing thus a subsequent pattern transfer. On the other hand, the morphology the BCP takes when it is dissolved in PGMEA, reveals that the wider domains are the ones infiltrated corresponding to the PLA, as previously discussed in *chapter 5*.

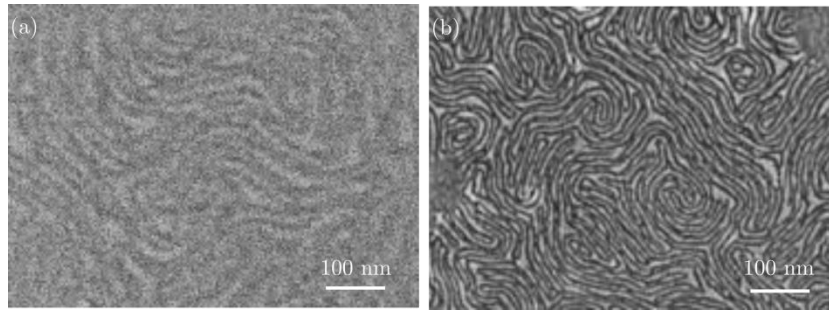


Figure 7.13. SEM images of PS-*b*-PLA self-assembly (a) before and (b) after SIS and PS etching

7.3. Local nanomechanical properties of PS-*b*-PMMA self-assembly

7.3.1. Introduction

In order to characterize the enhancement on the mechanical properties when the BCP films are covered and infiltrated with alumina, the *Peak Force* quantitative nanomechanical mapping (QNM) technique was used.

With this technique, it is possible to reliably quantify the Young's modulus, E , of materials with high spatial resolution and surface sensitivity. This is achieved by the acquisition of a large number of force-distance curves to calculate the mechanical properties at each point.¹⁹

When probing ultrathin films, the film thickness is in the order of magnitude of the indentation performed. Therefore, the tip also feels the substrate and as a consequence, the mechanical properties are dominated by the substrate, resulting in a larger apparent

modulus compared to the bulk ones.²⁰ To avoid this effect, it is widely accepted to limit the indentation depth to less than 10% of the film thickness.^{21,22}

Figure 7.14 shows a force-separation curve obtained with a single approach (blue) and withdraw (red) on a PS reference sample. The deformation parameter is obtained from a portion of the approach curve (blue). In order to determine the Young's modulus from the curve, the curve is fitted to the Derjaguin-Muller-Toporov (DMT) model (modified Hertzian model that also takes adhesive forces into account)²³, which provides the reduced modulus, E^* , as a function of the applied force, the maximum adhesion, F_{adh} , force and the instantaneous sample deformation, d_{sample} (equation (7.6)).

$$F = \frac{4}{3}E^*\sqrt{Rd_{sample}^3} + F_{adh}, \quad (7.6)$$

where the relation between the reduced modulus and the sample modulus is approximately $E = 0.88E^*$, if it is assumed that the tip modulus is larger than the sample modulus (when using silicon-based tips with polymer surfaces).

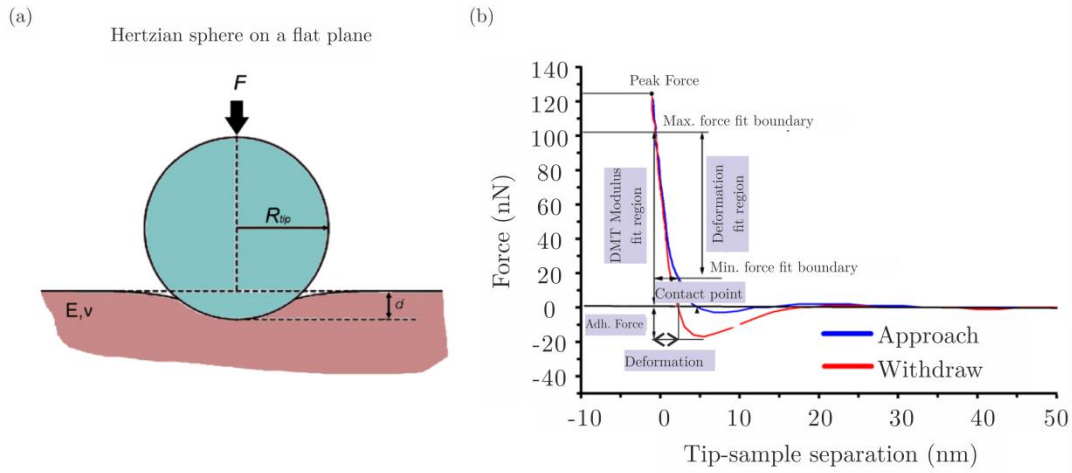


Figure 7.14. (a) Hertz contact model for a spherical indenter and (b) typical force plot of a PS reference sample of $E = 2.7$ GPa obtained with a cantilever of $k = 42$ N/m

Finally, the tip radius values have been obtained by using a calibration kit from *PELCO*.²⁴ The tip radius is calculated from the height profile when scanning a mica substrate with attached Au spherical nanoparticles with a nominal radius of 5 nm.

7.3.2. Optimal Indentation Conditions

The surface imaging has been obtained by using an AFM (*Dimension Icon*, *Bruker*) operating in Peak Force tapping mode, by using standard tapping cantilevers with a nominal radius of 7 nm and with a nominal spring constant of 26 N/m.

By calibrating the optical lever sensitivity, cantilever spring constant and tip radius, the force-distance curve can be obtained with information about the Young's modulus, adhesion force, sample deformation and dissipated energy.

In order to obtain a detectable deformation, the correct cantilever spring constant has to be selected. For sample Young's modulus in the 1 GPa to 10 GPa range, force constants in the order of about 25 N/m are indicated. In the experiments, the applied force set points have been in the range between 10 and 25 nN, to get an optimal deformation for a reliable fit (1-2 nm) avoiding plastic deformation.¹⁴

Figure 7.15.b shows the Young's modulus map for a PS film ($E = 2.7$ GPa) at various Peak Force set points to identify the optimal indentation conditions. From the force-distance graph (Figure 7.15.c) it is observed that when the deformation reaches 2.1 nm, the value of the modulus does not change with respect to the force applied, matching the nominal value of the reference.

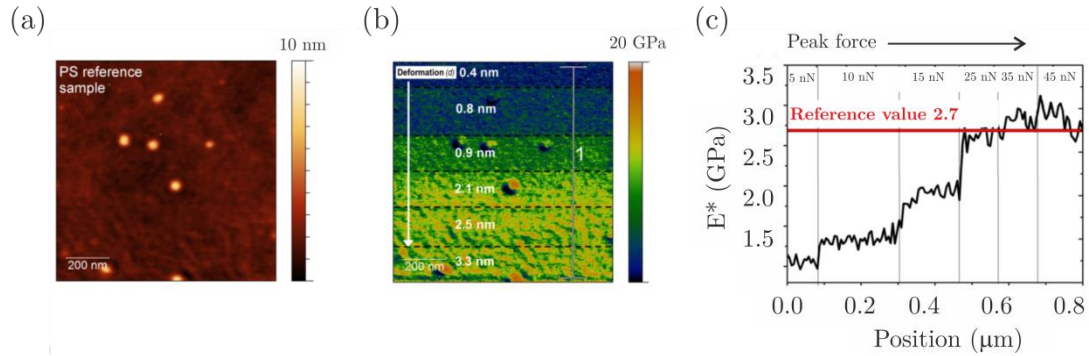


Figure 7.15. (a) AFM topography image and (b) reduced modulus of a PS reference film. The value of the sample reduced modulus, E^* , is plotted along the position in (c)

7.3.3. Characterization of PS-*b*-PMMA thin films

Once the deformation range has been obtained, a PS-*b*-PMMA thin film of 38 nm pitch has been characterized after self-assembly. Its specifications are depicted in Table 7.2.

Table 7.2. Specifications of PS-*b*-PMMA

Sample	M_n	Morphology	Thickness	E^*_{PS}	E^*_{PMMA}
PS- <i>b</i> -PMMA	79 kg/mol	Lamellar	43 nm	1.97 ± 0.21 GPa	3.10 ± 0.73 GPa

The experiments have been performed by keeping constant the deformation between 1 and 4 nm and with a standard silicon tip. AFM topography, adhesion, modulus and deformation channels are presented in Figure 7.16.b-e. From the images, it is observed that PS is softer and deforms more resulting in a higher adhesion. The value of E^* reported in Table 7.2, is obtained by fitting the modulus distribution to two Gaussians, each one representing the modulus distribution of each phase (Figure 7.16.j).

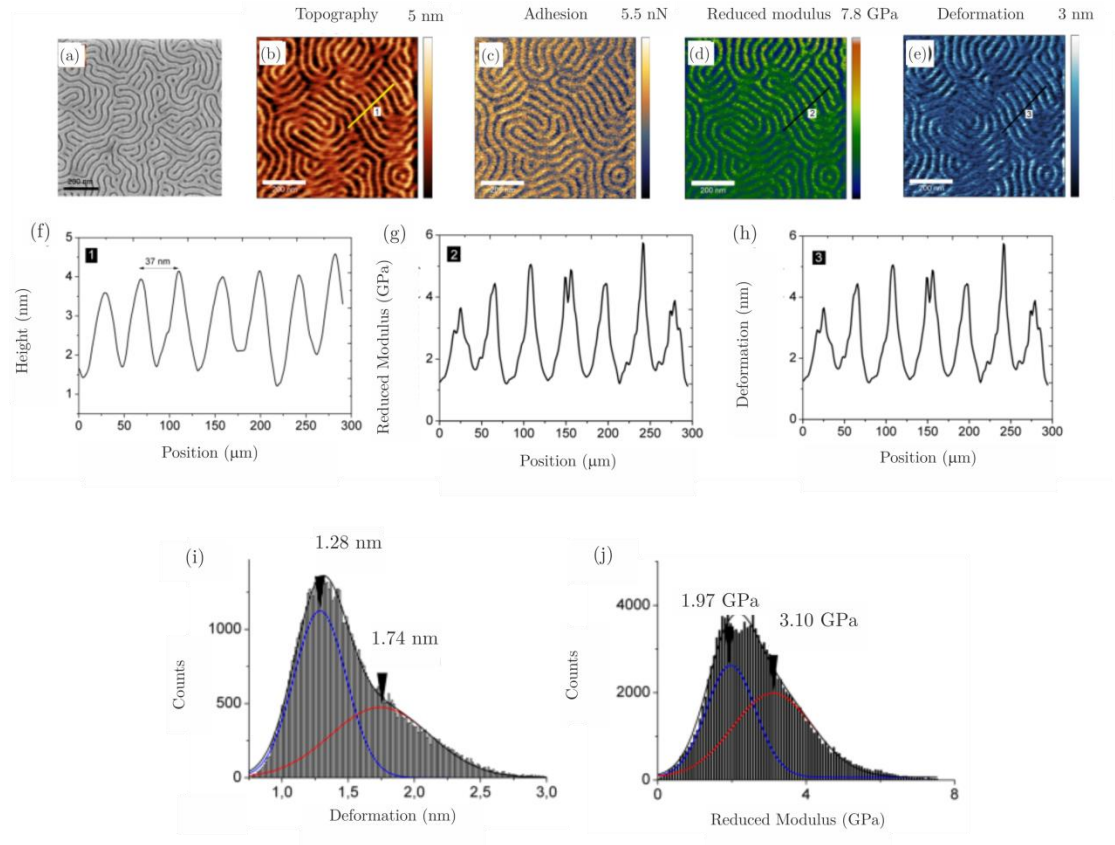


Figure 7.16. (a) SEM image of PS-*b*-PMMA ($L_0 = 38$ nm) self-assembly, and (b) height, (c) adhesion, (d) reduced modulus, and (e) deformation maps of the sample acquired by peak force at 30 nN set-point. Detailed profiles of (f) height, (g) reduced modulus and (h) deformation. For deformation and elastic maps, the corresponding Gaussian fitting of the data histograms (i) and (j), respectively

7.3.4. Characterization PS-*b*-PMMA thin films after atomic layer deposition

In order to compare the enhancement of mechanical properties with self-assembled layers after ALD, the BCP reference sample has been compared to self-assembled layers exposed to 3, 6 and 9 ALD cycles.

Figure 7.17.a-d shows AFM topography images of PS-*b*-PMMA samples before and after different alumina cycles deposition. Figure 7.17.e shows an histogram with the height distribution of the sample, after 9 ALD cycles. The height difference observed is approximately 2.70 nm. However, to this value, 1.35 nm have to be subtracted due to the initial height difference between phases, and 0.40 nm due to the deformation. This leads to 0.95 nm of alumina that remains on top of PMMA after 9 ALD cycles.

On the other hand, Figure 7.20 shows the reduced modulus maps and the corresponding data histograms of PS-*b*-PMMA samples before and after different alumina cycles deposition. From the graphs, it is clearly observed how stiffness increases locally only on PMMA domains (from 3 to 10 GPa), while the PS elastic response remains unchanged.

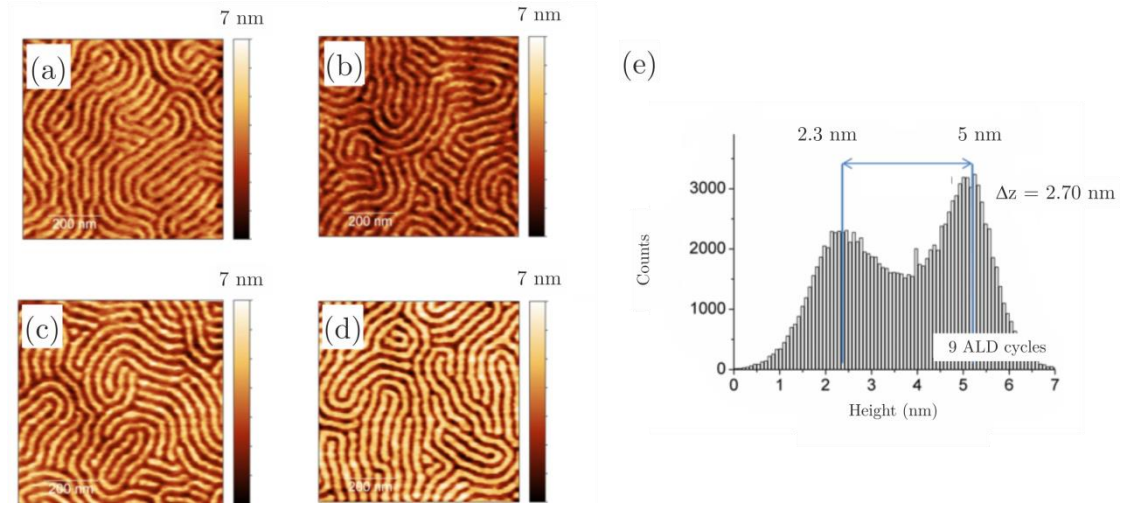


Figure 7.17. AFM topography images of (a) PS-*b*-PMMA, (b) PS-*b*-PMMA + 3 ALD, (c) PS-*b*-PMMA + 6 ALD and (d) PS-*b*-PMMA + 9 ALD. An histogram showing the height distribution of sample PS-*b*-PMMA + 9 ALD, is presented in (e)

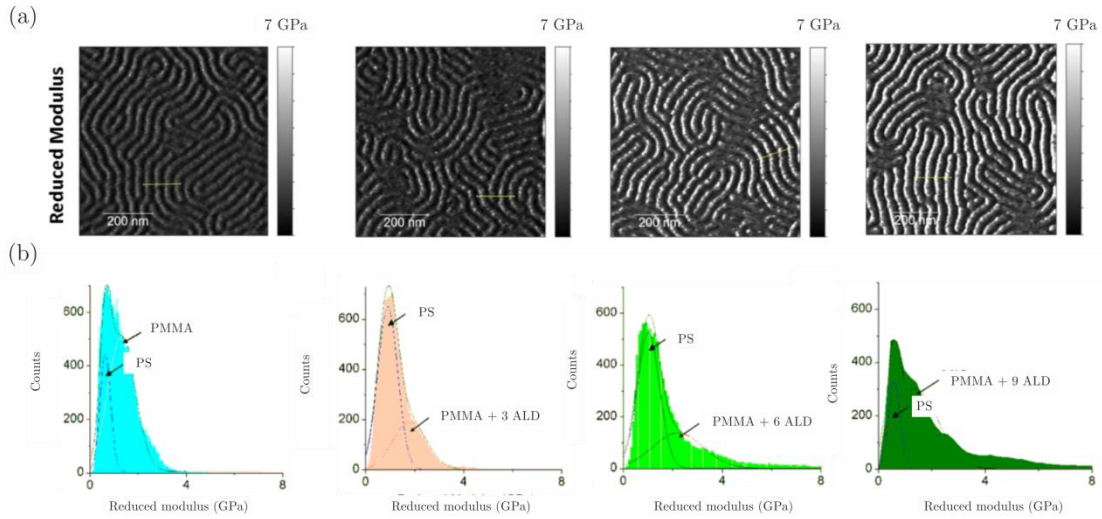


Figure 7.18. (a) AFM elastic maps of PS-*b*-PMMA, PS-*b*-PMMA + 3 ALD, PS-*b*-PMMA + 6 ALD and PS-*b*-PMMA + 9 ALD, and (b) the corresponding data histograms

From the mechanical properties characterization, it is concluded that with an accurate tip calibration, and by adjusting the indentation conditions, it is possible to differentiate between PS and PMMA domains in terms of modulus and adhesion forces. Moreover, the average modulus found for PS and PMMA are in agreement with the ones found in the literature. On the other hand, this technique has the unique capability of recognizing local stiffening induced by the deposition of alumina, as demonstrated in samples exposed to various ALD cycles.^{14,25}

7.3.5. Characterization of PS-*b*-PMMA thin films after sequential infiltration synthesis

In order to characterize the difference on the mechanical properties between PS-*b*-PMMA treated with ALD and SIS, infiltrated PS-*b*-PMMA samples are studied.

However, as a first step, infiltrated PS/PMMA blends are investigated on different brush layer materials because after annealing the film dewetts and form micrometer-scale droplets which present the advantage of not needing high lateral resolution. The preparation of the films has been performed by following the procedure described in Figure 3.14, by using PS-OH and PS-*r*-PMMA with 60 and 70% PS content, as brush layers.

As shown in SEM images of Figure 7.19.a-c, the higher the content in PS in the brush, the larger the PS droplets which incorporate smaller PMMA droplets.

On the other hand, the contrast in the SEM cross-section image (Figure 7.19.d), reveals the extent of SIS within PMMA (80-90 nm). The infiltration thickness is less than 200-300 nm, as already reported previously for similar infiltration conditions.²⁶

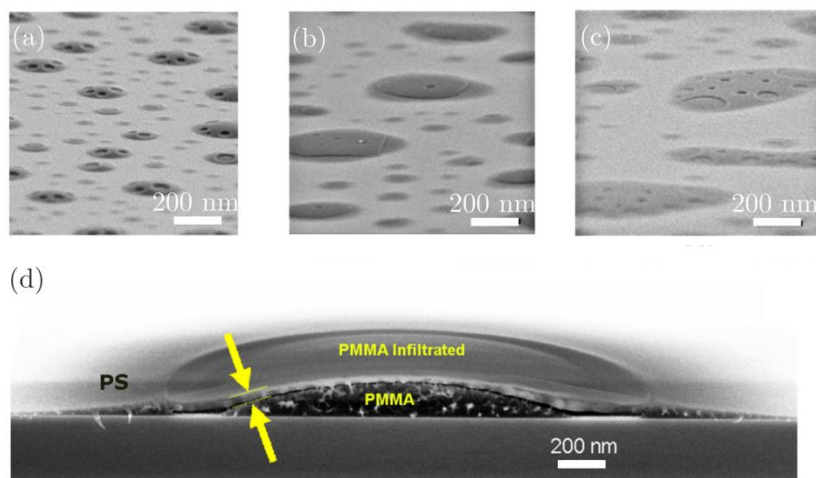


Figure 7.19. SEM images of PS/PMMA droplets on top of (a) PS-OH, (b) PS_{60%}-*r*-PMMA and (c) PS_{70%}-*r*-PMMA and (d) SEM cross-section image of a PS/PMMA droplet on PS-OH after SIS

Then, the local mechanical properties of hPS, hPMMA and homopolymer blend after 5 cycles of SIS are investigated. The results are shown in Figure 7.20. As observed from the modulus profiles, the PMMA modulus increases from 3 to 5.3 GPa after SIS. On the contrary, the PS surface stiffness is less affected changing from 2.6 to 2.2 GPa.

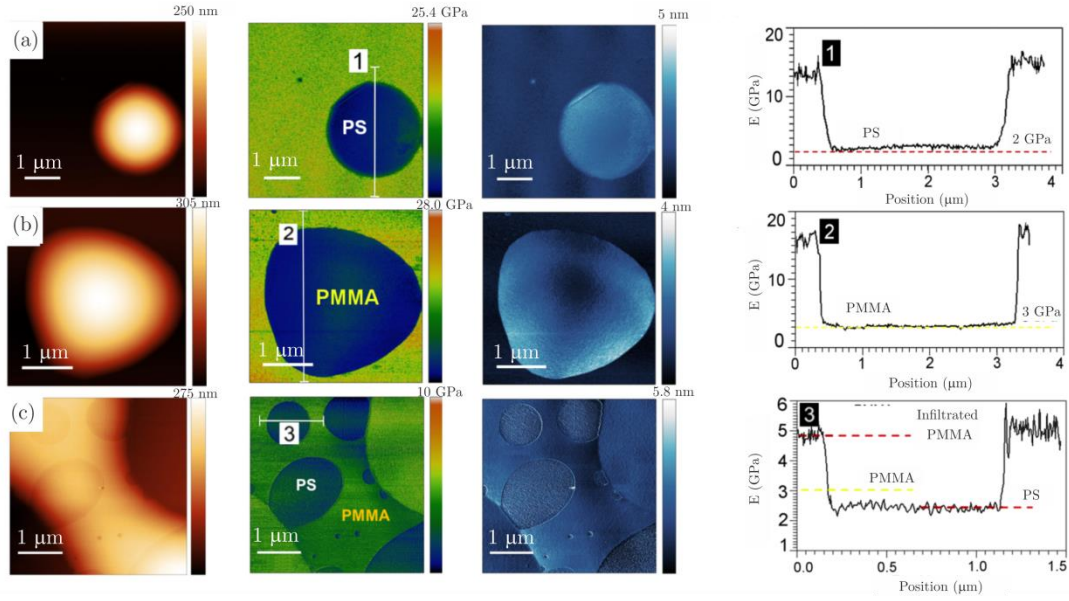


Figure 7.20. Topography, reduced modulus, deformation maps and reduced modulus profiles of (a) PS droplet, (b) PMMA droplet, and (c) infiltrated PS/PMMA droplet

Figure 7.21 shows the results of PS-*b*-PMMA ($L_0 = 38$ nm) characterization after five cycles of SIS. As observed from the results, there is a modest increase in stiffness on the PMMA domains, after SIS (3.6 GPa). The obtained stiffness is likely to have been due to the creation of an hybrid material in which the alumina is dispersed into a polymeric material.¹¹

On the other hand, and compared to the sample exposed to ALD, it has been found that the amount of alumina deposited on the top of PMMA domains is lower because during SIS the alumina is not only deposited on top of PMMA but also infiltrated.

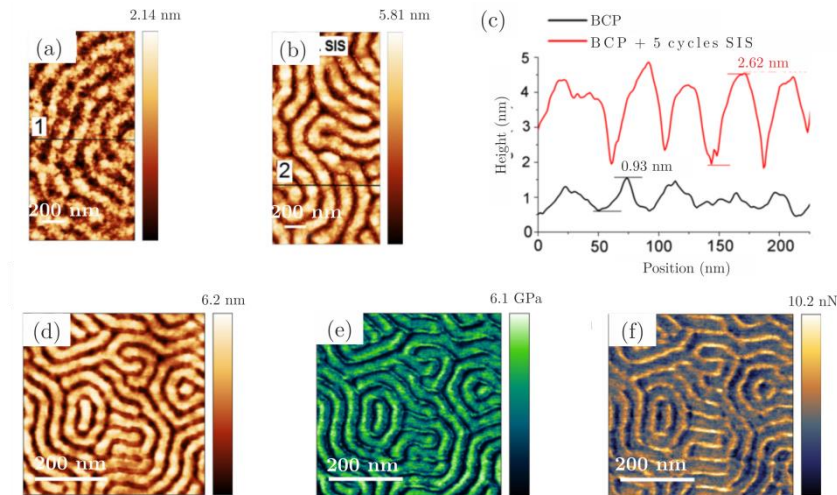


Figure 7.21. AFM topography images of (a) PS-*b*-PMMA and (b) PS-*b*-PMMA + 5 cycles SIS and (c) the corresponding profile; (d-f) represent the topography, modulus and adhesion map, respectively, acquired in Peak Force tapping mode

7.4. Fabrication of nanomechanical devices based on metallic oxide nanowires

As a final objective of the thesis, the fabrication of nanomechanical resonators made of infiltrated polymer as structural material is targeted. The nanofabrication approach is based on using SIS to modify the etching and mechanical properties of the nanowires, together with the DSA of BCP by graphoepitaxy to create the arrays.

Nanomechanical resonators based on suspended nanowires are excellent building blocks since high resonant frequencies can be achieved by reducing the dimensions of the nanowires. Nanowires with sub-10 nm section can show ultrahigh sensitivity when used for the development of mass sensors. Moreover, additional effects arise at such dimensions, like single charge transport effects and quantum phenomena. Recent works at IMB-CNM, demonstrate the realization of a single-hole transistor made of a nanocrystalline suspended p-type silicon nanowire²⁷, and the onset of enhanced piezoresistive effects²⁸.

The fabrication of nanomechanical resonators by combining DSA and SIS, allows achieving nanobeam dimensions dictated by half of the BCP pitch. Up to now, nanowires based mechanical resonators have been made of silicon, silicon nitride, carbon nanotubes or 2D materials.²⁸⁻³¹ However, an optimal nanofabrication process in terms of accuracy and scalability is still lacking.

The fabrication process has been performed at the Molecular Foundry (*Lawrence Berkeley National Laboratory*) in Berkeley, CA, EEUU. The Molecular Foundry is supported by the Department of basic energy science, through the Nanoscale Science Research Center program, and it represents a national user facility for nanoscale science which provides users access to expertise and instrumentation in a collaborative, multidisciplinary environment. The Molecular Foundry is organized in seven interdependent research facilities and provides access to state-of-the-art instrumentation, unique scientific expertise and specialized techniques to help users address challenges in nanoscience and nanotechnology.

7.4.1. Materials and methods

7.4.1.1. Description of the fabrication method

The fabrication process to define the nanowire based mechanical resonators is described in Figure 7.22, and it consists on the following steps: (i) fabrication of the topographical guiding patterns on a SOI substrate, (ii) brush layer deposition, (iii) PS-*b*-PMMA self-assembly, (iv) SIS on PMMA domains, (v) PS and brush etching, and (vi) silicon oxide underetching.

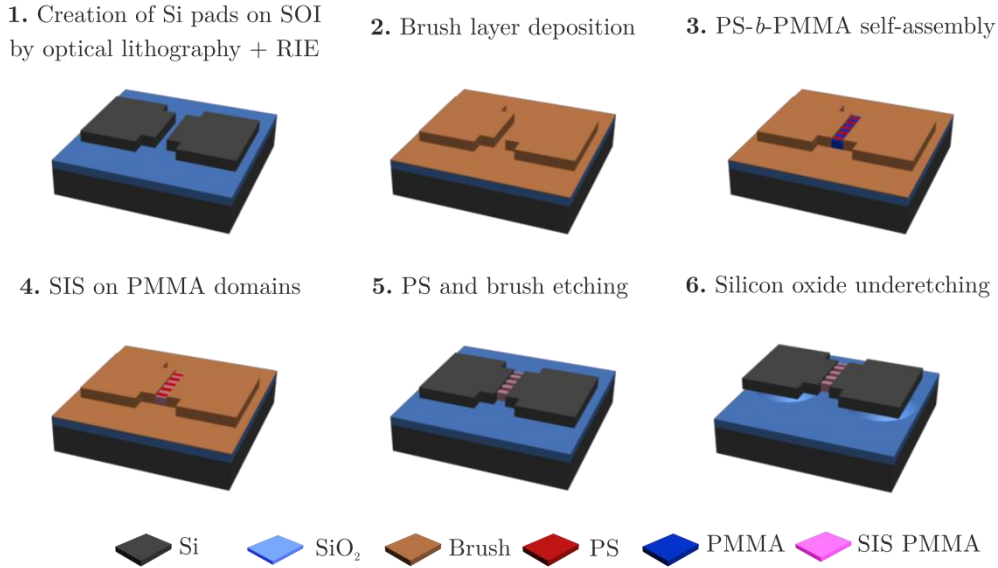


Figure 7.22. Schematic of the nanofabrication process of a device based on an array of identical nanobeams made by DSA and SIS

The creation of the topographical guiding patterns has been performed at the IMB-CNM cleanroom facility by following the process depicted in Figure 4.11 in *chapter 4* on SOI substrates (120 nm silicon on 400 nm SiO₂). After photolithography and development steps, 120 nm of silicon have been etched down to the SiO₂ layer by using the etching conditions depicted in Table 4.2.

7.4.1.2. Brush and block copolymer materials

The BCP and brush materials used in the experiments are summarized in Table 7.3. The brush is deposited on the guiding patterns from a 2% PS_{60%}-*r*-PMMA solution at 1500 rpm, and annealed at 230°C for 5 min, covering the whole surface. Then, the sample is dipped in PGMEA for 5 min at 40°C in an ultrasonic bath. Finally, 0.5% PS-*b*-PMMA solution is spin-coated at 2500 rpm, and annealed at 230°C for 10 min.

Table 7.3. Specifications of PS-*b*-PMMA and brush materials (* BCP blend formed of a mixture of 38 nm and 22 nm BCP pitch (40:60))

Chemical nature	M _n	PDI	PS fraction	Pitch
PS _{60%} - <i>r</i> -PMMA	7.9 kg/mol	1.85	60%	-
PS- <i>b</i> -PMMA	79 kg/mol	1.09	50%	38 nm
	Blend*			28 nm
	42.3 kg/mol	1.1		22 nm

7.4.1.3. Directed self-assembly by graphoepitaxy process

The same graphoepitaxy experiments performed with PS-*b*-PMMA of 22 nm pitch and described in *chapter 4*, have been replicated at the Molecular Foundry, and the results have been the same as those presented in Figure 4.8.

On the other hand, the process has been also tried with two more BCP, showing good alignment for the 28 nm pitch BCP (Figure 7.23).

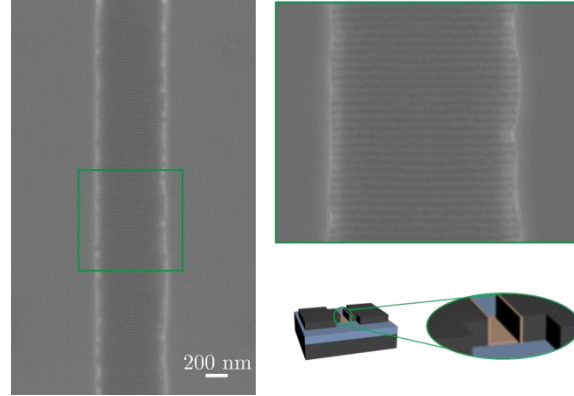


Figure 7.23. PS-*b*-PMMA ($L_0 = 28$ nm) DSA by graphoepitaxy by using 600 nm separation width

7.4.1.4. Optimization of sequential infiltration synthesis in free-surface

In parallel to the DSA optimization, the SIS process has been optimized in a new ALD tool at the Molecular Foundry (*Maxima SMD VI*). The process optimization has been performed on PS-*b*-PMMA samples on free-surface for two materials: Al_2O_3 and ZnO.

Sequential infiltration synthesis with Al_2O_3

In order to optimize the SIS process, a first test has been performed on PS-*b*-PMMA of 38 nm pitch, and based on the obtained results, the precursor pulse, the temperature and the purge time have been varied. This sequence is illustrated in Figure 7.24.

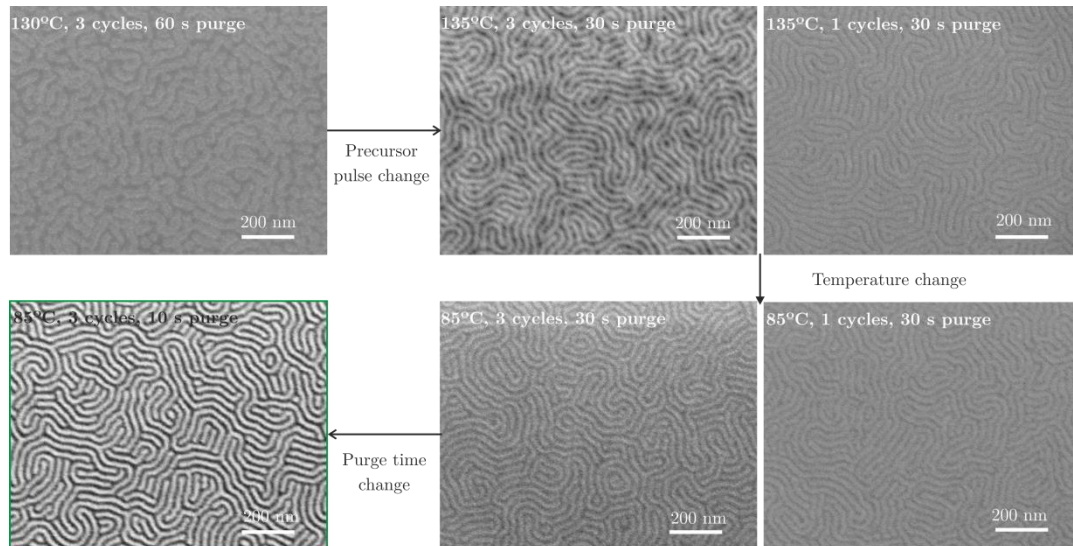


Figure 7.24. Sequence followed to optimize the SIS with Al_2O_3 on PS-*b*-PMMA ($L_0 = 38$ nm)

Once the optimal SIS conditions have been found, they have been transferred to the other two BCP ($L_0 = 22$ nm and 28 nm). Then, the SIS process has been characterized as a function of the different experimental parameters (number of cycles, purge times, BCP film

thickness and BCP molecular weight). All the experiments have been performed by using the optimal conditions (85°C, 3 cycles and 10 s of purge) and by varying only the parameter of study.

Figure 7.25 shows the SIS dependence as a function of the number of cycles. As observed from the SEM images, one cycle is not enough to infiltrate the whole PMMA domains, therefore poor contrast is observed. On the other hand, for cycles above 5, alumina deposition is started to be seen on the fingerprint morphology.

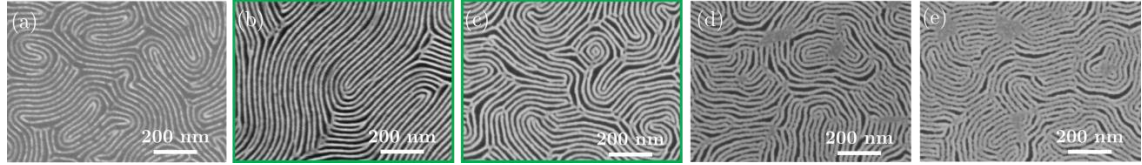


Figure 7.25. SIS with Al_2O_3 on PS-*b*-PMMA ($L_0 = 22$ nm) as a function of the number of cycles: (a) one, (b) three, (c) five, (d) seven and (e) nine (SEM images have been taken after PS removal)

Figure 7.26 shows the SIS results when varying the purge time after the precursor reaction inside the chamber. As revealed in the images, the best results are obtained for purge times of 10 s. Above this time, the SIS is not so efficient and partially infiltrated areas appear, in accordance with the literature.¹¹

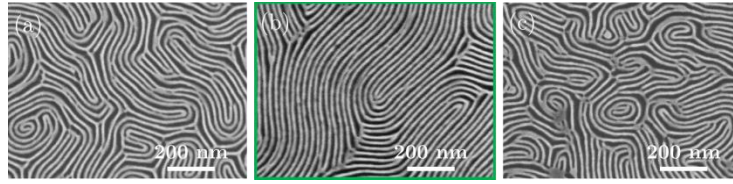


Figure 7.26. SIS with Al_2O_3 on PS-*b*-PMMA ($L_0 = 22$ nm) as a function of the purge time: (a) 5 s, (b) 10 s and (c) 30 s (SEM images have been taken after PS removal)

Then, BCP of different film thickness have been infiltrated. Since the orientation of the lamellae depends on the BCP thickness, there are some samples (Figure 7.27.c-d) which show some parallel oriented lamellae before the SIS process. The results after SIS are shown in Figure 7.27, and for the two perpendicular oriented samples (Figure 7.27.a-b), a decrease in contrast in the thickest BCP sample (Figure 7.27.b) is observed. On other hand, it is observed, that the alumina is deposited on the parallel oriented lamellae (Figure 7.27.c-d).

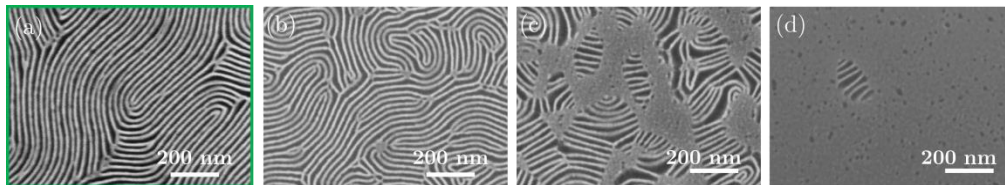


Figure 7.27. SIS with Al_2O_3 on PS-*b*-PMMA ($L_0 = 22$ nm) as a function of BCP film thickness (SEM images have been taken after PS removal)

On the other hand, the SIS with Al_2O_3 has been performed on three molecular weight BCPs by using the optimal conditions described above. As revealed in the SEM images of Figure 7.28, there is no influence on the process when varying the BCP chain length within the chosen values (from 22 to 38 nm).



Figure 7.28. SIS with Al_2O_3 on PS-*b*-PMMA as a function of BCP chain length: (a) 38 nm, (b) 28 nm, and (c) 22 nm (SEM images have been taken after PS removal)

Finally, in order to demonstrate the influence of the purge time and the temperature on the final BCP structure, the sample infiltrated at 85°C, with 1 SIS cycle and 10 s purge time from Figure 7.25.a, has been compared with a sample processed under the same conditions but with higher purge times and higher temperature. Figure 7.29.a and Figure 7.29.b, show the difference on the infiltration depending on the purge time. As observed, and as demonstrated before, the higher the purge times, the less infiltrated the sample is (it is revealed by the poor contrast on the SEM image). On the other hand, when comparing Figure 7.29.a and Figure 7.29.c, in which the temperature has been increased to 135°C, it is observed that the infiltration process works much better, driving to the same results as those in which the sample is infiltrated for 3 cycles at 85°C.

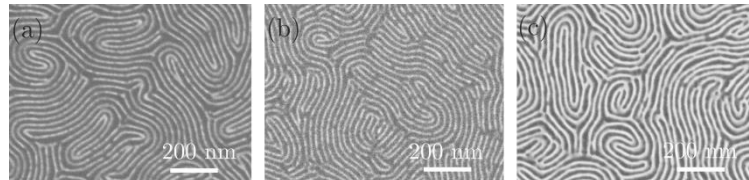
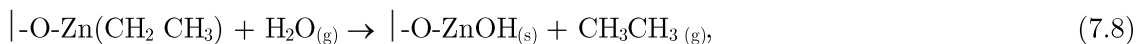
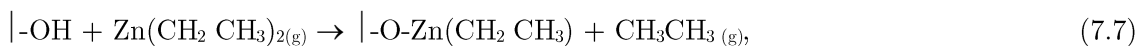


Figure 7.29. SIS with Al_2O_3 on PS-*b*-PMMA for 1 cycle and (a) 85 °C, 10 s purge time, (b) 85°C, 30 s purge time, and (c) 135°C, 10 s purge time

Sequential infiltration synthesis with ZnO

In addition to Al_2O_3 , the infiltration using another oxide of interest, namely ZnO, has been also performed. This material has been chosen due to its many advantageous properties, such as thermal and electrical stabilities and optical transparency.^{32,33} Moreover, it presents a wide band gap of 3.37 eV, a large exciton binding energy of 60 meV, and its structure leads to large piezoelectricity.³⁴⁻³⁶

The ALD process for ZnO uses diethylzinc (DEZ) and water as precursors. The reaction mechanism process consists of the reactions (7.7) and (7.8).



In order to infiltrate ZnO into the PMMA domains, the process has been tried by using the same processing conditions found for Al_2O_3 . As observed in Figure 7.30, the SEM images after PS etching reveal that the infiltration has failed, and almost all the BCP film has been removed.

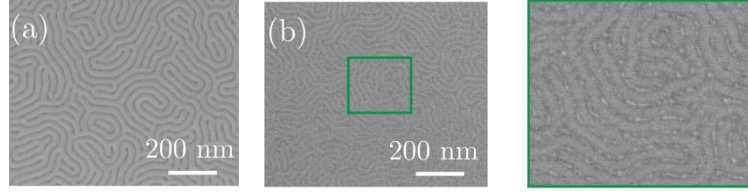


Figure 7.30. SEM images of PS-*b*-PMMA ($L_0 = 38$ nm) + 3 cycles of SIS (ZnO) (a) before and (b) after PS etching

Therefore, in order to promote the ZnO infiltration, different approaches have been tried. On the one hand, the activation and slightly oxidization of the surface has been tested, before the SIS process, by exposing the sample to a short time of oxygen plasma or UV. As observed, in Figure 7.31, the process has not worked, and only some infiltrated regions remain after PS etching.

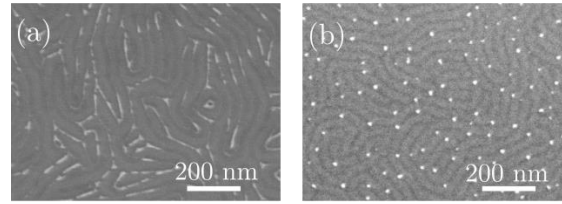


Figure 7.31. SEM images of PS-*b*-PMMA ($L_0 = 38$ nm) with smooth (a) oxygen plasma and (b) UV exposure, + 3 cycles of SIS (ZnO) after PS etching

Another approach that has been tried consists in infiltrating one Al_2O_3 cycle before 3 ZnO SIS cycles, in order to activate the surface and promote the ZnO growth on an alumina layer. The process has been performed at 85°C with 10 s of purge time, and the result obtained is presented in Figure 7.32. As observed in the images, the process works when the surface is first infiltrated with alumina. Moreover, the higher contrast shown in Figure 7.32.a, if compared with Figure 7.25.a, reveals that there is ZnO infiltration. Moreover, in the SEM cross-section image, Figure 7.32.b, two contrasted phases corresponding to Al_2O_3 and ZnO, are observed.

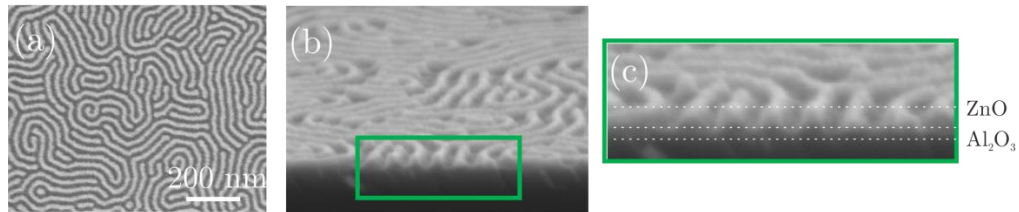


Figure 7.32. (a) Top-view and (b) cross-section SEM image and (c) inset of PS-*b*-PMMA ($L_0 = 38$ nm) with one Al_2O_3 and three ZnO cycles after PS etching

Finally, in order to demonstrate the ZnO infiltration without using Al_2O_3 activation, since the temperature has demonstrated to increase the reaction speed, the procedure has been tried at higher temperatures (Figure 7.33). On the other hand, by keeping constant the temperature at 85°C , the experiment has been performed by changing the order of the precursors introduction in the chamber. That is, the water has been introduced first, and then, the DEZ (Figure 7.34). As observed in both figures, the increasing temperature enhances the SIS process, and a thin infiltrated PMMA layer remains on the substrate after PS etching. On the other hand, the infiltration enhances more when the sequence of introducing the precursors inside the chamber is inverted. The reason behind is that water reacts more with PMMA carbonyl groups than DEZ does, and therefore leaves more reactive sites when DEZ is introduced in the chamber.

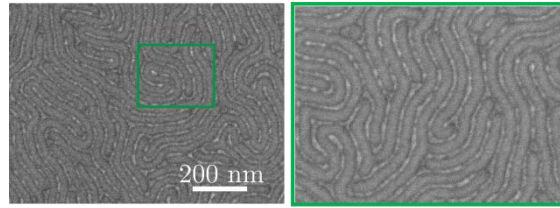


Figure 7.33. SEM image of PS-*b*-PMMA ($L_0 = 38$ nm) with three ZnO cycles at 135°C after PS etching

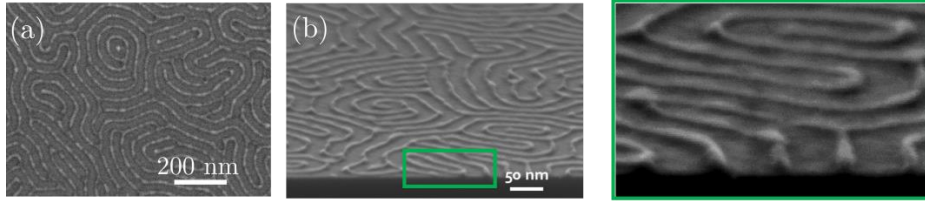


Figure 7.34. SEM image of PS-*b*-PMMA ($L_0 = 38$ nm) with three ZnO cycles at 85°C by inverting the introduction of precursors into the chamber

7.4.2. Nanomechanical resonators fabrication results

Once the SIS process on free-surface is optimized for both Al_2O_3 and ZnO materials, it is combined with the DSA by graphoepitaxy to fabricate the nanobeams. Figure 7.35 shows the DSA results for PS-*b*-PMMA of 28 nm pitch after infiltration, before and after PS etching. On the other hand, Figure 7.36 shows a SEM 30° tilted image of Figure 7.35.b. As observed, the beams are already suspended after PS etching, since the infiltration does not diffuse through the whole PMMA domains down to the bottom.

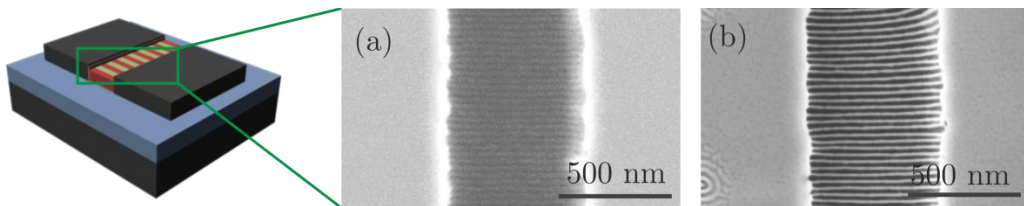


Figure 7.35. SEM images of PS-*b*-PMMA ($L_0 = 28$ nm) with three Al_2O_3 cycles at 85°C (a) before and (b) after PS etching

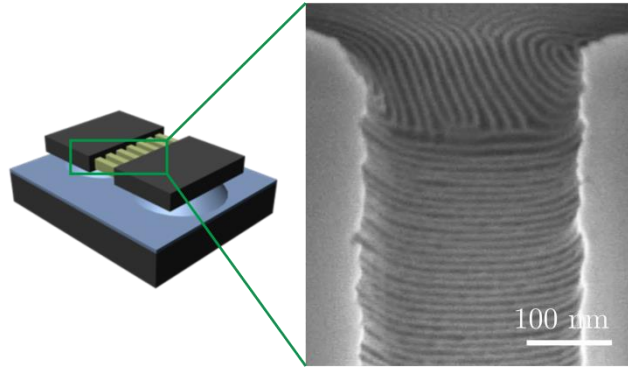


Figure 7.36. SEM 30° tilted image of PS-*b*-PMMA ($L_0 = 28$ nm) with three Al₂O₃ cycles at 85°C after PS etching

The PS etching step has to be accurately controlled since the nanowires tend to crosslink between them at longer oxygen plasma exposures. Figure 7.37 shows this effect after 10 min of oxygen plasma etching.

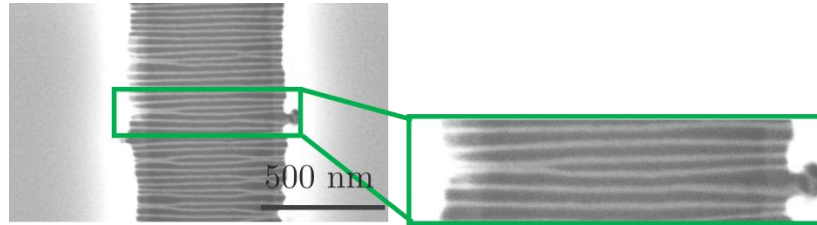


Figure 7.37. SEM image of PS-*b*-PMMA ($L_0 = 28$ nm) with three Al₂O₃ cycles at 85°C after 10 min PS etching

To corroborate that the nanowires are suspended after the optimal PS etching removal time (Figure 7.35.b), a SEM cross-section at 90° has been taken. As observed in Figure 7.38, the Al₂O₃ infiltrated nanowires are already suspended after the PS etching since the infiltration does not reach the bottom of the PMMA domain. Therefore, there is no need to go further and etch the SiO₂ under-layer to suspend them.

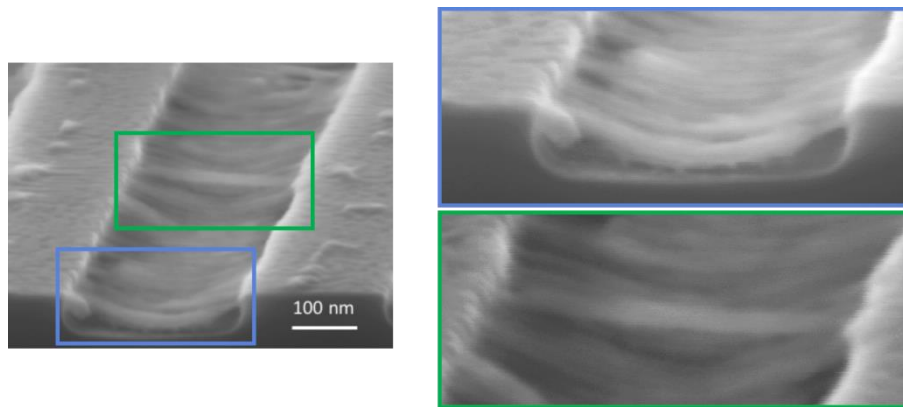


Figure 7.38. SEM image of PS-*b*-PMMA ($L_0 = 28$ nm) with three Al₂O₃ cycles at 85°C after 2 min PS etching showing the suspended infiltrated nanowires

Finally, the same procedure has been tried not with alumina, but with the optimal infiltration conditions found for ZnO. As observed in Figure 7.39, after the PS etching, very few nanowires stand after PS etching. However, the remaining can be used to measure some of their properties.

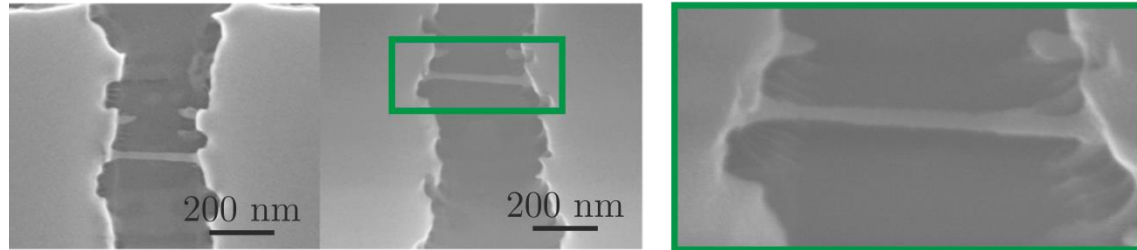


Figure 7.39. SEM image of PS-*b*-PMMA ($L_0 = 28$ nm) with three ZnO cycles at 85°C after 2 min PS etching showing the suspended infiltrated nanowires

In order to enhance the results shown in Figure 7.39 it is possible to increase the number of ZnO infiltration cycles, or repeat the procedure increasing also the temperature.

7.5. Summary and conclusions

A reliable method to pattern transfer BCPs has been implemented for BCP DSA. Moreover, the difference between the conventional ALD process and SIS has been presented and corroborated by an extensive study on the mechanical properties of the BCP after the treatments. The difference between processing conditions is depicted in Table 7.4.

Table 7.4. Optimal processing conditions for ALD and SIS

Conditions	ALD	SIS
Temperature	85°C	85°C
Precursor time in the chamber	60 s	80 s
Purge time	60 s	30 s
Cycles	5 cycles	5 cycles

The SIS process has been tried not only for PS-*b*-PMMA materials, but also for high- χ systems. It has been demonstrated that the infiltration process in PLA domains has a similar mechanism as for PMMA, due to the carbonyl groups found in PLA molecular structure.

Apart from Al₂O₃, ZnO has been also tried as infiltrating material. However, due to the reactivity of the precursors with the PMMA molecules, the infiltration procedure needs to be performed at higher temperatures and with a higher number of cycles. On the other side, it has been observed, that the change on the order the precursors are introduced into the chamber enhances the infiltration process.

From the mechanical characterization, it has been found that ALD and SIS enhance the stiffness of PMMA domains, while PS remains almost constant. Furthermore, it has been demonstrated that in ALD, there is only material deposition whereas in SIS not only deposition, but infiltration as well. This is also demonstrated in the etching tests performed with both techniques.

On the other hand, the application of BCP DSA and SIS has been combined to fabricate nanomechanical resonators which can be used on the development of mass sensors. It has been demonstrated that DSA, in combination with SIS, is a powerful technique in that field, since it provides the resolution of half of the BCP pitch, by using a simple and affordable process. However, further work has still to be performed on the fabrication process optimization and nanowire characterization.

7.6. References

1. A. M. Shevjakov, *et al.* Chemistry of High-Temperature Materials. *Proc. 2nd USSR Conf. High Temp. Chem. Oxides* **26–29**, 149–155 (1965).
2. Suntola, T. *et al.* Method for producing compound thin films. US Patent (US4058430) (1977).
3. McDaniel, M. D. *et al.* Atomic layer deposition of perovskite oxides and their epitaxial integration with Si, Ge, and other semiconductors. *Appl. Phys. Rev.* **2**, 41301 (2015).
4. Purniawan, A., *et al.* TiO₂ ALD nanolayer as evanescent waveguide for biomedical sensor applications. *Procedia Eng.* **5**, 1131–1135 (2010).
5. Puurunen, R. L. Surface chemistry of atomic layer deposition: A case study for the trimethylaluminum/water process. *J. Appl. Phys.* **97**, 121301 (2005).
6. Parsons, G. N. *et al.* Mechanisms and reactions during atomic layer deposition on polymers. *Coord. Chem. Rev.* **257**, 3323–3331 (2013).
7. Peng, Q., *et al.* Nanoscopic patterned materials with tunable dimensions via atomic layer deposition on block copolymers. *Adv. Mater.* **22**, 5129–5133 (2010).
8. Krishnamoorthy, *et al.* Nanoscale patterning with block copolymers. *Mater. Today* **9**, 40–47 (2006).
9. Huda, M., *et al.* Pattern Transfer of 23-nm-Diameter Block Copolymer Self-Assembled Nanodots Using CF₄ Etching with Carbon Hard Mask (CHM) as Mask. **737**, 133–136 (2013).
10. Tseng, Y.-C., *et al.* Enhanced Block Copolymer Lithography Using Sequential Infiltration Synthesis. *J. Phys. Chem. C* **115**, 17725–17729 (2011).
11. Biswas, M., *et al.* Kinetics for the Sequential Infiltration Synthesis of Alumina in Poly(methyl methacrylate): An Infrared Spectroscopic Study. (2015).
12. Biswas, *et al.* New Insight into the Mechanism of Sequential Infiltration Synthesis from Infrared Spectroscopy. (2014).
13. Tseng, Y. C., *et al.* Enhanced block copolymer lithography using sequential infiltration synthesis. *J. Phys. Chem. C* **115**, 17725–17729 (2011).
14. Lorenzoni, M., Evangelio, L., *et al.* Assessing the Local Nanomechanical Properties of Self-Assembled Block Copolymer Thin Films by Peak Force Tapping. (2015).
15. Darling, S. B., *et al.* Sequential infiltration synthesis for advanced lithography. (2012).
16. Peng, Q., *et al.* A route to nanoscopic materials via sequential infiltration synthesis on block copolymer templates. *ACS Nano* **5**, 4600–4606 (2011).

17. Johnston, D. E. Plasma etch transfer of self-assembled polymer patterns. *J. Micro/Nanolithography, MEMS, MOEMS* **11**, 31306 (2012).
18. Ruiz, R. *et al.* Image quality and pattern transfer in directed self assembly with block-selective atomic layer deposition. *J. Vac. Sci. Technol. B, Nanotechnol. Microelectron. Mater. Process. Meas. Phenom.* **30**, 06F202 (2012).
19. Young, T. J. *et al.* The use of the PeakForce TM quantitative nanomechanical mapping AFM-based method for high-resolution Young's modulus measurement of polymers. *Meas. Sci. Technol.* **22**, 125703 (2011).
20. Cappella, B. *et al.* Nanomechanical properties of polymer thin films measured by force-distance curves. *Thin Solid Films* **516**, 1952–1960 (2008).
21. Du, B., *et al.* Study of Elastic Modulus and Yield Strength of Polymer Thin Films Using Atomic Force Microscopy. *Langmuir* **17**, 3286–3291 (2001).
22. Oommen, B. *et al.* Effects of nanoscale thickness and elastic nonlinearity on measured mechanical properties of polymeric films. *Thin Solid Films* **513**, 235–242 (2006).
23. Cappella, B. *et al.* Force-distance curves by atomic force microscopy. *Surf. Sci. Rep.* **34**, 1–104 (1999).
24. Vesenska, J., *et al.* Colloidal gold particles as an incompressible atomic force microscope imaging standard for assessing the compressibility of biomolecules. *Biophysical Journal* **65**, 992–997 (1993).
25. Lorenzoni, M. *et al.* Nanomechanical properties of solvent cast PS and PMMA polymer blends and block co-polymers. *Proc. SPIE* **9423**, 942310–942325 (2015).
26. Tseng, Y.-C. *et al.* Enhanced polymeric lithography resists via sequential infiltration synthesis. *J. Mater. Chem.* **21**, 11722–11725 (2011).
27. Llobet, J. *et al.* Resonant tunnelling features in a suspended silicon nanowire single-hole transistor. *Appl. Phys. Lett.* **107**, 1–6 (2015).
28. Sansa, M., *et al.* High-sensitivity linear piezoresistive transduction for nanomechanical beam resonators. *Nat. Commun.* **5**, 4313 (2014).
29. Eichler, A. *et al.* Nonlinear damping in mechanical resonators made from carbon nanotubes and graphene. *Nat. Nanotechnol.* **6**, 339–342 (2011).
30. Gil-Santos, E. *et al.* Nanomechanical mass sensing and stiffness spectrometry based on two-dimensional vibrations of resonant nanowires. *Nat. Nanotechnol.* **5**, 641–645 (2010).
31. Fong, K. Y., *et al.* Frequency and phase noise of ultrahigh silicon nitride nanomechanical resonators. *Phys. Rev. B.* **85**, 1–5 (2012).

32. Ott, A. W. *et al.* Atomic layer-controlled growth of transparent conducting ZnO on plastic substrates. *Mater. Chem. Phys.* **58**, 132–138 (1999).
33. Kowalik, I. A. *et al.* Structural and optical properties of low-temperature ZnO films grown by atomic layer deposition with diethylzinc and water precursors. *J. Cryst. Growth* **311**, 1096–1101 (2009).
34. Wang, Z. L. ZnO nanowire and nanobelt platform for nanotechnology. *Mater. Sci. Eng. R Reports* **64**, 33–71 (2009).
35. Wang, C. Y. *et al.* ZnO-CNT composite nanotubes as nanoresonators. *Phys. Lett. Sect. A Gen. At. Solid State Phys.* **375**, 2171–2175 (2011).
36. Korir, K. K., *et al.* Piezoelectric properties of zinc oxide nanowires: an *ab initio* study. *Nanotechnology* **24**, 475401 (2013).

General conclusions

The thesis contributes to the development of directed self-assembly of block copolymers as a fabrication method for the next generation of nanoelectronic devices and circuits.

The primary achievement has been the development, implementation and characterization of a chemical epitaxy process for PS-*b*-PMMA systems.

- The DSA chemical epitaxy process is based on creating a chemical nanoscale contrast on a polymeric brush layer by oxygen plasma functionalization.

The optimal processing conditions for brush and BCP preparation, guiding pattern definition by EBL and oxygen plasma functionalization, have been established. This has entailed the study of different brush layer compositions and BCP annealing conditions, required for each specific system.

It has been successfully implemented to lamellar forming PS-*b*-PMMA BCPs of the following periods: 38 nm, 28 nm and 22 nm. Density multiplication factors up to 7 have been achieved by means of using wide guiding stripes. It has been demonstrated that the use of wide guiding stripes is of prime importance in chemical epitaxy since it allows relaxing the lithography requirements in terms of resolution, enabling furthermore, the process integration to high- χ systems.

It has been investigated the role of the interface energies between the brush and the BCP domains by a novel experimental method based on using homopolymer blends. The contact angle between two phases in droplets formed by homopolymer blend dewetting experiments on brush layers is related with the affinity strength. The experimental data has been fitted in a DSA model to simulate the chemical epitaxy process, and a good experimental correlation has been obtained. From simulation results it is proposed that, along with the difference on surface free-energies, a relevant parameter to define the efficiency of the guiding patterns to obtain standing lamellae oriented parallel to the guiding patterns is the responsiveness of the brush layer, which is related with the brush density.

Along with the characterization and development of a chemical epitaxy approach, other complementary methods and exploratory investigations have been addressed.

- It has been studied the self-assembly behavior of two novel high- χ materials: PS-*b*-PLA and PLA-*b*-PDMS-*b*-PLA.

With respect to PS-*b*-PLA, a proper brush layer which balances the interactions between the surface and the BCP domains has been found, thus leading to the perpendicular BCP orientation on the whole surface. Moreover, the self-assembly behavior has been studied by using short thermal annealing times, demonstrating thus, its easy industrial applicability. A DSA chemical epitaxy process for PS-*b*-PLA has been partially achieved. A chemical contrast to force the alignment of the domains has been observed, but not strong enough to guide them parallel to the guiding stripes.

Regarding the PLA-*b*-PDMS-*b*-PLA system, a DSA process has been implemented using a novel approach based on the combination of grapho and chemical epitaxy, showing large areas with high density multiplication factors. Furthermore, this BCP has shown very remarkable DSA results with respect to integration capability.

- Two new chemical epitaxy processes based on direct writing techniques have been designed and implemented for PS-*b*-PMMA material systems. The guiding patterns on the two processes have been created by locally oxidizing the surface with AFM nanolithography, and by exposing the sample directly to the electron beam. The development of these methods has allowed simplifying the processing sequence steps, since the use of resists is avoided, and obtaining guiding patterns of higher resolution (smaller linewidth).
- It has been implemented a sequential infiltration synthesis (SIS) to enhance the etch resistivity between PS and PMMA. This process improves the pattern transfer into the substrate. It has been demonstrated for PS-*b*-PMMA, for high- χ systems and for two different infiltration materials, Al₂O₃ and ZnO. The combination of BCP DSA by graphoepitaxy and SIS has been applied to the design and fabrication of nanomechanical resonators for mass sensing applications. As the nanowires are created directly from the infiltrated polymer domain, the advantage of this process is that nanowires of very small cross-section can be obtained.
- Two techniques to further characterize BCP films and their interactions with the substrate have been presented.

It has been demonstrated that Hard X-ray Photoelectron Spectroscopy (HAXPES) using synchrotron radiation is a powerful technique to explore the chemical properties of the surface and buried interfaces in the DSA process.

Three chemical guiding patterns have been characterized, and the subsequent modifications performed on the brush polymer have been identified. It has been demonstrated that when the brush is exposed to oxygen plasma, it generates C-O bonding, promoting higher affinity to PMMA domains. In case of Parallel Oxidation Nanolithography (PON), it has been seen that a sub-stoichiometric oxide appears between the brush and the substrate. When the polymer is exposed to electrons, the cross-linking of PS molecules is what induces the BCP alignment.

Characterization by Atomic Force Microscopy (AFM) using the peak force quantitative nanomechanical mode has made possible to access the local mechanical properties of the single BCP domains, surpassing the limitations of standard nanoindentation methods. Quantitative information about the average modulus of PS and PMMA on PS-*b*-PMMA films has been obtained. This technique has been also applied to PS-*b*-PMMA infiltrated BCPs, showing the unique capability of the method in recognizing local stiffening induced by the deposition and infiltration of alumina, as well as its evolution in terms of thickening and stiffening as a function of the numbers of ALD cycles.

In summary, the research performed within this thesis contributes significantly to the DSA community, since it demonstrates a feasible industrial implementation of a new chemical epitaxy approach for PS-*b*-PMMA BCPs, as well as the chemical mechanism which drives their DSA. Moreover, a broad study on new novel BCPs has been performed, providing a general overview of the major drawbacks and advantages of their implementation in the industry, as well as a possible DSA fabrication process to their integration. The fabrication process of a nanomechanical resonator has been presented by combining the DSA technology with SIS.

Conclusions generals

Aquesta tesi contribueix al desenvolupament de l'auto-assemblatge dirigit de copolímers de bloc com a mètode de fabricació per a la futura generació de dispositius i circuits nanoelectrònics.

La principal contribució ha estat el desenvolupament, implementació i caracterització d'un mètode de guiatge basat en la modificació química de la superfície per als copolímers de bloc basats en PS-*b*-PMMA.

- El procés de guiatge per modificació química de la superfície, es basa en crear un contrast químic nanomètric a una capa de polímer, a través de la seva modificació amb plasma d'oxigen.

S'han establert les condicions de procés òptimes per a la preparació de la capa de copolímer de bloc i la corresponent definició dels patrons de guiatge per litografia amb feix d'electrons i modificació amb plasma d'oxigen. Això ha comportat realitzar un profund estudi amb diferents polímers i condicions de recuit, requerides per a cada sistema.

S'ha demostrat, la implementació del copolímer laminar PS-*b*-PMMA amb les següents longituds de cadena: 38 nm, 28 nm i 22 nm, i s'han obtingut factors de multiplicació fins a 7, utilitzant línies àmplies de guiatge. S'ha demostrat que l'ús de línies amples de guiatge és molt important en l'estudi de l'auto-assemblatge dirigit de copolímers de bloc per modificació química de la superfície, perquè això permet relaxar els requeriments litogràfics en termes de resolució, permetent alhora, la integració dels sistemes d'alta χ .

S'ha investigat el paper de les energies d'interfície entre la capa de polímer "brush" i els dominis del copolímer, mitjançant un nou mètode basat en l'ús d'una mescla d'homopolímers. Mitjançant la mesura de l'angle de contacte entre les dues fases d'una gota formada per una mescla d'homopolímers, és possible determinar l'afinitat química. Les dades experimentals s'han ajustat a un model d'auto-assemblatge dirigit per simular el procés, i s'ha obtingut una bona correlació. Dels resultats de les simulacions s'ha conclòs que juntament amb la diferència d'energies d'interfície, la densitat de la capa de "brush" juga un paper important a l'hora de definir l'eficiència del patró de guiatge per obtenir làmines perpendiculars al substrat i paral·leles a les línies de guiatge.

Juntament amb la caracterització i desenvolupament del mètode de guiatge basat en modificació química de la superfície, també s'han dut a terme altres investigacions.

- S'ha estudiat el mecanisme d'auto-assemblatge de dos materials d'alta χ : PS-*b*-PLA i PLA-*b*-PDMS-*b*-PLA.

Respecte al sistema PS-*b*-PLA, s'ha trobat una capa neutra de polímer “brush”, la qual balança les interaccions entre la superfície i els dominis del copolímer. Això ha donat lloc a una orientació perpendicular del copolímer de bloc a tota la superfície. A més, el procés d'auto-assemblatge s'ha demostrat utilitzant temps curts de recuit tèrmic, demostrant així, la seva fàcil aplicabilitat industrial. El procés d'auto-assemblatge dirigit de copolímers de bloc per epitàxia química, s'ha aconseguit de manera parcial, ja que s'ha observat contrast químic a la superfície, però no suficientment fort com per guiar el polímer de manera paral·lela a les línies del patró.

En referència al sistema PLA-*b*-PDMS-*b*-PLA, s'ha demostrat la implementació d'un nou procés d'auto-assemblatge dirigit, basat en mètodes químics i topogràfics de guiatge, en àrees grans i amb alts factors de multiplicació. A més, aquest copolímer de bloc ha demostrat l'obtenció de resultats d'auto-assemblatge dirigit molt exitosos, amb respecte a la seva capacitat d'integració.

- S'han dissenyat dos mètodes de guiatge químics basats en tècniques de litografia que no requereixen l'ús de resina. Aquests s'han implementat pel copolímer de bloc PS-*b*-PMMA. Els patrons de guiatge han estat creats mitjançant la oxidació local de la superfície mitjançant litografia per AFM, i per mitjà de l'exposició directa de la superfície de polímer “brush” al feix d'electrons. El desenvolupament d'aquests mètodes, ha permès simplificar el nombre de passos de la seqüència del procés de fabricació, ja que no requereixen l'ús de resina. A més, permeten obtenir patrons de guiatge d'alta resolució.
- Per tal de millorar la resistència al gravat entre el PS i el PMMA, s'ha implementat un procés basat en la infiltració de materials per mitjà de la tècnica d'ALD. Aquest procés permet millorar el procés de transferència al substrat. S'ha demostrat pel sistema, PS-*b*-PMMA i per dos sistemes d'alta χ , amb dos materials d'infiltració diferents, Al₂O₃ i ZnO. La combinació d'aquesta tècnica i la de guiatge dirigit mitjançant patrons topogràfics, s'ha aplicat al disseny i fabricació de raonadors nanomecànics per aplicacions de sensors de massa. Com que els nanofils són creats directament amb polímer infiltrat, l'avantatge del procés és que la mida d'aquests fils ve determinada per la meitat de la longitud de cadena del copolímer.

- S'han presentat dues tècniques per caracteritzar més profundament les pel·lícules primers de copolímers de bloc i les seves interaccions amb el substrat.

S'ha demostrat que la tècnica HAXPES utilitzant radiació sincrotró, és una tècnica molt adequada per determinar i estudiar les propietats químiques de la superfície i interfícies en el procés d'auto-assemblatge dirigit.

Mitjançant la caracterització de tres patrons de guiatge químics, s'han identificat les diferents modificacions químiques realitzades a la superfície del “brush”. S'ha demostrat que quan el “brush” s'exposa a un plasma d'oxigen, es generat enllaços C-O, els quals promouen l'alta afinitat de la superfície al bloc de PMMA. En el cas de PON, s'ha observat la presència d'un òxid subestequiomètric entre la capa de “brush” i el substrat. Quan el polímer és exposat al feix d'electrons, hi ha un entrelligament de les molècules de PS, el qual indueix l'alineament del copolímer.

La caracterització per AFM utilitzant el mode de *peak force quantitative nanomechanical mapping*, ha permès la caracterització de les propietats mecàniques de cadascun dels dominis del copolímer, sobrepassant les limitacions dels mètodes de nanoidentació estàndards. S'ha obtingut informació quantitativa sobre el mòdul de Young del PS i PMMA, al sistema PS-*b*-PMMA. Aquesta tècnica també s'ha aplicat a sistemes infiltrats, i ha permès reconèixer els canvis en la rigidesa dels materials induïts per la deposició i infiltració d'alúmina, així com l'evolució del gruix i rigidesa en funció del nombre de cicles d'ALD.

En resum, la recerca que s'ha dut a terme en el marc de la tesi, contribueix significativament a l'estudi de l'auto-assemblatge dirigit dels copolímers de bloc, ja que s'ha demostrat una implementació industrial factible per a un nou procés basat en epitàxia química. A més, s'ha realitzat un ampli estudi sobre la implementació i integració del procés amb nous materials. D'altra banda, s'ha presentat també el procés de fabricació d'un ressonador nanomecànic mitjançant la tècnica descrita i la tecnologia d'infiltració de materials.

Annexes

Annex I. Acronyms List

AFM	Atomic force microscopy
ALD	Atomic layer deposition
ARC	Antireflective coating
ATRP	Atom-transfer polymerization
BA	Butylacetate
BCP	Block copolymer
CAR	Chemically amplified resist
CD	Critical dimension
CMOS	Complementary metal-oxide-semiconductor
CVD	Chemical vapor deposition
DEZ	Diethylzinc
DGL	Ginzburg-Landau theory
DMT	Derjaguin-Muller-Toporov
DPP	Discharge produced plasma
DSA	Directed self-assembly
DUV	Deep ultraviolet
EBL	Electron beam lithography
EUV	Extreme ultraviolet
FEM	Focus Energy matrix
FFT	Fast Fourier Transform
FIB	Focused ion beam

GISAXS	Grazing-incidence small-angle X-ray scattering
HAXPES	Hard X-ray high kinetic energy photoelectron spectroscopy
HF	Hydrofluoric acid
hPS	Homopolymer polystyrene
HSP	Hansen solubility parameters
IC	Integrated circuit
ICP	Inductively coupled plasma
IL	Interference lithography
IPA	Isopropanol
ITRS	International technology roadmap for semiconductors
LAO	Local anodic oxidation
LER	Line edge roughness
LPP	Laser produced plasma
LWR	Line width roughness
MEMS	Micro electromechanical system
MIBK	Methyl isobutyl ketone
NA	Numerical aperture
NEMS	Nano electromechanical system
NGL	Next generation lithography
NIL	Nanoimprint lithography
NMP	Nitroxide-mediated polymerization
NMR	Nuclear Magnetic Resonance spectroscopy
ODT	Order-disorder transition

OTS	Octadecyltrichlorosilane
OWRK	Owens, Wendt, Rabel and Kaelble
PDI	Polydispersity index
PDMS	Polydimethylsiloxane
PGMEA	propylene glycol monomethyl ether acetate
PLA	Poly(lactide acid)
PLA-<i>b</i>-PDMS-<i>b</i>-PLA	poly(dimethylsiloxane)- <i>b</i> -poly(lactic acid)
PMMA	Polymethyl methacrylate
PON	Parallel Oxidation Nanolithography
PS	Polystyrene
PS-<i>b</i>-PB	Poly(styrene- <i>b</i> -butadiene)
PS-<i>b</i>-PEO	Poly(styrene- <i>b</i> -ethylene oxide)
PS-<i>b</i>-PLA	Poly(styrene- <i>b</i> -D,L-lactide)
PS-<i>b</i>-PMMA	Poly(styrene- <i>b</i> -methyl methacrylate)
PS-OH	Hydroxyl terminated polystyrene
PS-<i>r</i>-PMMA-OH	Random hydroxyl terminated poly(styrene- <i>b</i> -methyl methacrylate)
QNM	Quantitative nanomechanical mapping
RAFT	Reversible addition-fragmentation chain transfer
RED	Relative energy difference
RIE	Reactive ion etching
SAM	Self-assembled monolayer
SAXS	Small angle X-ray scattering
SCFT	Self-consistent field theory

SEC	Size Exclusion Chromatography
SEM	Scanning electron microscopy
SIS	Sequential infiltration synthesis
SOC	Spin-on-carbon
SPL	Scanning probe lithography
SPM	Scanning probe microscopy
SSL	Strong segregation limit
STM	Scanning tunneling microscopy
TBD	triazabicyclodecene
TMA	Trimethylaluminum
WSL	Weak segregation
XPS	X-Ray Photoelectron Spectroscopy
X-PS	Cross-linkable polystyrene

Annex 2. Scientific contributions

List of publications

Laura Evangelio, Marta Fernández Regúlez, Xavier Borrisé, Matteo Lorenzoni, Jordi Fraxedas, Francesc Pérez Murano, “*Creation of guiding patterns for directed self-assembly of block copolymers by resistless direct e-beam exposure*”, J. Micro/Nanolith. MEMA MOEMS, 14 (3)m 033511 (2015)

Marta Fernández Regúlez, Laura Evangelio, Matteo Lorenzoni, Jordi Fraxedas, Francesc Pérez Murano, “*Sub-10 nm resistless nanolithography for directed self-assembly of block copolymers*”, ACS Applied Materials & Interfaces, 6 (23), 21596-21602 (2014)

Matteo Lorenzoni, Laura Evangelio, Marta Fernández-Regúlez, Célia Nicolet, Christophe Navarro, Francesc Pérez-Murano, “*Sequential Infiltration of Self-Assembled Block Copolymers: A Study by Atomic Force Microscopy*”, J. Phys. Chem. C, 121, 3078-3086 (2017)

Matteo Lorenzoni, Laura Evangelio, Sophie Verhaeghe, Célia Nicolet, Christophe Navarro, Francesc Pérez-Murano, “*Assessing the local nanomechanical properties of self-assembled block co-polymers thin films by peak force tapping*”, Langmuir, 31 (42) 11630-11638 (2015)

Matteo Lorenzoni, Laura Evangelio, Sophie Verhaeghe, Célia Nicolet, Christophe Navarro, Alvaro San Paulo, Gemma Rius, Francesc Pérez-Murano, “*Nanomechanical properties of solvent cast PS and PMMA polymer blends and block copolymers*”, J. Micro/Nanolith. MEMS MOEMS, 14 (3)m 033509, (2015)

Laura Evangelio, Federico Gramazio, Matteo Lorenzoni, Michaela Gorgoi, Francisco Miguel Espinosa, Ricardo García, Francesc Pérez-Murano and Jordi Fraxdas, “*Identifying the nature of surface chemical modification for directed self-assembly of block copolymers*”, In preparation

Laura Evangelio, Marta Fernández-Regúlez, Weihua Li, Célia Nicolet, Christophe Navarro, Jordi Fraxedas, Marcus Müller and Francesc Pérez-Murano, “*Directed self-assembly of block copolymers by chemical epitaxy using wide guiding stripes*” In preparation

Laura Evangelio, Marta Fernández-Regúlez, Célia Nicolet, Christophe Navarro, Guillaume Fleury and Francesc Pérez-Murano, “*Use of ALD Sequential Infiltration Synthesis to improve the patterns transfer on Directed Self-Assembly high-chi block copolymers*” In preparation

Conference contributions

“Use of ALD Sequential Infiltration Synthesis to improve the pattern transfer on Directed Self-Assembly high-chi PS-b-PLA block copolymers”

Laura Evangelio, Marta Fernández-Regúlez, Xavier Chevalier, Celia Nicolet, Ian Cayrefourcq, Christophe Navarro and Francesc Pérez-Murano

SPIE Advanced Lithography 2017, February 2017, San Jose, California (EEUU)

Oral Presentation

“Control of interface energies for implementing directed self-assembly of block copolymers in a 300 mm CMOS processing line”

Laura Evangelio, Marta Fernández-Regúlez, Patricia Pimenta-Barros, Maxime Argoud, Xavier Chevalier, Celia Nicolet, Ian Cayrefourcq, Christophe Navarro, Raluca Tiron, Marcus Müller and Francesc Pérez-Murano

SPIE Advanced Lithography 2017, February 2017, San Jose, California (EEUU)

Poster Presentation

“Control of interface energies for implementing directed self-assembly of block copolymers in a 300 mm CMOS processing line”

Laura Evangelio, Marta Fernández-Regúlez, Patricia Pimenta-Barros, Maxime Argoud, Xavier Chevalier, Celia Nicolet, Ian Cayrefourcq, Christophe Navarro, Raluca Tiron, Marcus Müller and Francesc Pérez-Murano

2nd DSA Symposium, October 2016, Grenoble (France)

Oral Presentation

“Use of atomic layer deposition for improving pattern transfer in directed self-assembly of PS-b-PMMA”

Laura Evangelio, Matteo Lorenzoni, Marta Fernández-Regúlez, Steven Gottlieb, Francesc Pérez-Murano

SR-ALD Workshop, ALBA Synchrotron, June 2016, Cerdanyola del Vallès (Spain)

Oral Presentation

“Use of atomic layer deposition for improving pattern transfer in directed self-assembly of PS-b-PMMA”

Laura Evangelio, Matteo Lorenzoni, Marta Fernández-Regúlez, Steven Gottlieb, Francesc Pérez-Murano

Nanoselect, June 2016, Sant Feliu de Guíxols (Spain)

Oral presentation

“Role of interface energies in the directed self-assembly of block copolymers in wide chemical patterns”

Laura Evangelio, Weihua Li, Matteo Lorenzoni, Jordi Fraxedas, Marcus Müller and Francesc Pérez-Murano

EUPOC 2016 on Block copolymers, May 2016, Lago di Garda (Italy)

Oral presentation

“Creation of chemical guiding patterns for DSA of block copolymers by high resolution resistless nanolithography methods”

Laura Evangelio, Marta Fernández-Regúlez, Xavier Borrisé, Matteo Lorenzoni, Jordi Fraxedas, Francesc Pérez-Murano

1st International Symposium on DSA, October 2015, Leuven (Belgium)

Poster presentation

“Enabling density multiplication in directed self-assembly of block copolymers by chemical surface modification using wide guiding stripes”

Laura Evangelio, Weihua Li, Matteo Lorenzoni, Marcus Müller, Francesc Pérez-Murano

1st International Symposium on DSA, October 2015, Leuven (Belgium)

Poster presentation

“Determination of the interfacial energies in chemical guiding patterns for directed self-assembly of block co-polymers”

Laura Evangelio, Matteo Lorenzoni, Jordi Fraxedas, Francesc Pérez-Murano

International Conference on Micro and Nano Engineering (MNE), September 2015, The Hague (Netherlands)

Oral presentation

“Characterization of buried interfaces of grafted polymer films using high kinetic energy photoemission”

Laura Evangelio, Matteo Lorenzoni, Federico Gramazio, Francesc Pérez-Murano, Jordi Fraxedas

II ALBA User’s Meeting, June 2015, Barcelona (Spain)

Poster presentation

“Assessing the local nanomechanical properties of self-assembled block copolymers thin films by Peak Force tapping.”

Matteo Lorenzoni, Laura Evangelio, Célia Nicolet, Christophe Navarro, Francesc Pérez-Murano

European Conference on Surface Science, September 2015, Barcelona (Spain)

Oral presentation

“Characterization of buried interfaces of grafted polymer films using high kinetic energy photoemission”

Laura Evangelio, Matteo Lorenzoni, Federico Gramazio, Francisco Espinosa, Ricardo García, Francesc Pérez-Murano, Jordi Fraxedas

European Conference on Surface Science, September 2015, Barcelona (Spain)

Oral presentation

“Directed self-assembly of block copolymers by chemical surface modification”

Laura Evangelio, Marta Fernández-Regúlez, Matteo Lorenzoni, Francesc Pérez-Murano, Jordi Fraxedas

1st Scientific Meeting of BNC-b Students, May 2015, Barcelona (Spain)

Oral Presentation

“Formation of chemical guiding patterns for DSA of block copolymers by high resolution resistless nanolithography methods”

Laura Evangelio, Marta Fernández-Regúlez, Xavier Borrisé, Matteo Lorenzoni, Jordi Fraxedas, Francesc Pérez-Murano

European Materials Research Society, May 2015, Lille (France)

Oral presentation

“Enabling density multiplication in directed self-assembly of block copolymers by chemical surface modification using wide guiding stripes”

Laura Evangelio, Weihua Li, Matteo Lorenzoni, Marcus Müller, Francesc Pérez-Murano

European Materials Research Society, May 2015, Lille (France)

Oral presentation

“Nanomechanical properties of different phases in assembled block copolymers thin films”

Matteo Lorenzoni, Laura Evangelio, Célia Nicolet, Christophe Navarro, Alvaro San Paulo, Francesc Pérez-Murano

European Materials Research Society, May 2015, Lille (France)

Poster presentation

“Creation of guiding patterns for directed self-assembly of block co-polymers by resistless direct e-beam exposure”

Laura Evangelio, Marta Fernández-Regúlez, Xavier Borrisé, Matteo Lorenzoni, Jordi Fraxedas, Francesc Pérez-Murano

SPIE Advanced Lithography 2015, February 2015, San Jose, California (EEUU)

Poster presentation

“Challenges and opportunities of scanning probe lithography for creation of guiding patterns used in directed self-assembly of block co-polymers”

Laura Evangelio, Matteo Lorenzoni, Marta Fernández-Regúlez, Marcus Kaesner, Yana Krivoschapkina, Ivo W. Rangelow, Francesc Pérez-Murano

SPIE Advanced Lithography 2015, February 2015, San Jose, California (EEUU)

Oral presentation

“Nanomechanical properties of solvent cast PS and PMMA polymer blends and block co-polymers”

Matteo Lorenzoni, Laura Evangelio, Celia Nicolet, Christophe Navarro, Francesc Pérez-Murano

SPIE Advanced Lithography 2015, February 2015, San Jose, California (EEUU)

Poster presentation

“Density multiplication in directed self-assembly of block co-polymers by chemical surface modification using wide guiding stripes”

Laura Evangelio, Marta Fernández-Regúlez, Weihua Li, Matteo Lorenzoni, Jordi Fraxedas, Marcus Müller, Francesc Pérez-Murano

SPIE Advanced Lithography 2015, February 2015, San Jose, California (EEUU)

Poster presentation

“Directed Self-Assembly of block copolymers by chemical surface modification”

Laura Evangelio, Marta Fernández-Regúlez, Jordi Fraxedas, Francesc Pérez-Murano

Nanolito Workshop in Nanolithography, October 2014, Zaragoza (Spain)

Oral presentation

“AFM nanolithography for block copolymer directed self-assembly”

Laura Evangelio, Marta Fernández-Regúlez, Jordi Fraxedas, Francesc Pérez-Murano

European Conference on Surface Science, September 2014, Antalya (Turkey)

Oral presentation

“AFM nanolithography for block copolymer directed self-assembly”

Laura Evangelio, Marta Fernández-Regúlez, Jordi Fraxedas, Francesc Pérez-Murano

1st SNM Workshop, July 2014, Barcelona (Spain)

Oral presentation

“Creation of chemical guiding patterns for directed self-assembly of block co-polymers by AFM lithography”

Laura Evangelio, Marta Fernández-Regúlez, Jordi Fraxedas, Francesc Pérez-Murano

SPIE Advanced Lithography 2014, February 2014, San Jose, California (EEUU)

Poster Presentation

“Block co-polymer multiple patterning direct self-assembly on PS-OH brush layer and AFM based nanolithography”

Marta Fernández-Regúlez, Laura Evangelio, Jordi Fraxedas, Francesc Pérez-Murano

Nanoimprint and Nanoprint Technology 2013, October 2013, Barcelona (Spain)

Poster Presentation

“AFM nanolithography for creating guiding patterns for directed self-assembly of block co-polymers”

Marta Fernández-Regúlez, Laura Evangelio, Jordi Fraxedas, Francesc Pérez-Murano

International Conference on Micro and Nano Engineering 2013, London (United Kingdom)

Oral Presentation

“Block co-polymer multiple patterning direct self-assembly on PS-OH brush layer and AFM based nanolithography”

Marta Fernández-Regúlez, Laura Evangelio, Jordi Fraxedas, Francesc Pérez-Murano

Euronanoforum 2013, CRANN/Intel DSA Workshop , June 2013, Dublin (Ireland)

Oral Presentation